VST FAKULTÄT FÜR VERFAHRENS- UND SYSTEMTECHNIK

Optimization of low-impact hydropower devices

Dissertation
for the award of the degree

Doktoringenieur (Dr.-Ing.)

by Olivier Cleynen
born March 19, 1983, in Brussels (Belgium)
accepted by the Faculty for process and systems engineering
of the University Otto von Guericke of Magdeburg

Reviewers: Prof. Dr.-Ing. Dominique Thévenin
Prof. Dr.-Ing. Christian-Toralf Weber
Prof. Roberto Revelli

Submitted October 15, 2021
Graduation colloquium on April 12, 2022

Optimization of low-impact hydropower devices

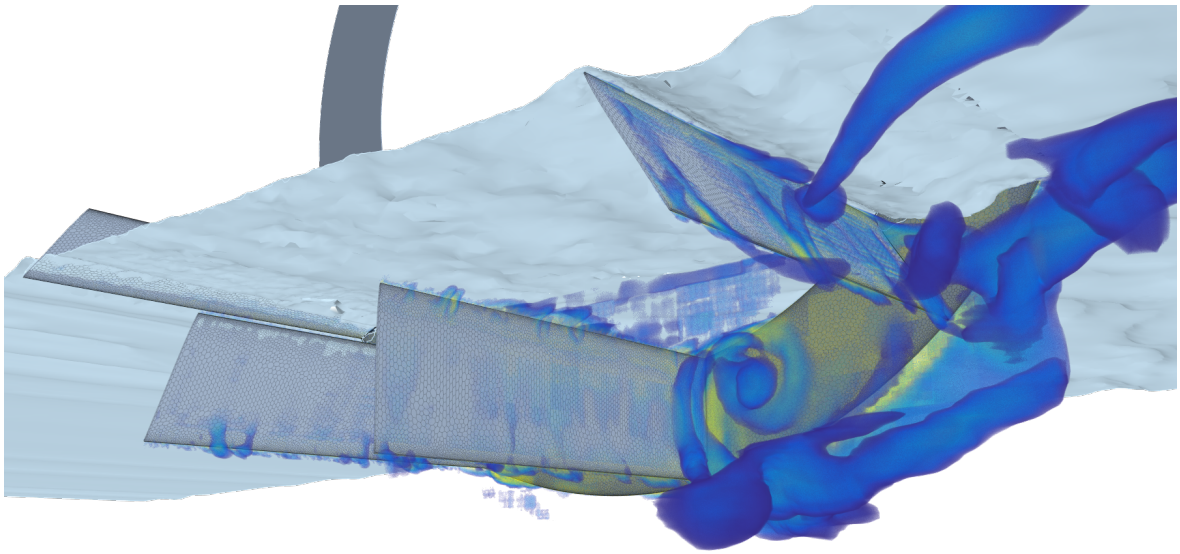

OTTO VON GUERICKE UNIVERSITÄT MAGDEBURG

Dissertation for the award of the degree
Doktoringenieur (Dr.-Ing.)
from the Faculty for process and systems engineering
of the University Otto von Guericke of Magdeburg
Submitted October 15, 2021

Olivier Cleynen

Contents

Abstract

This thesis focuses on the optimization of low-impact hydropower devices in general, and free-stream water wheels in particular.

A theoretical analysis of the achievable performance in floating or bypass hydropower installations is first carried out. A model is developed by which to quantify the maximum available hydraulic power, and measure efficiency. Its use is demonstrated with a practical example, where the performance of a small-scale power plant is benchmarked against reference values anchored in physical principles. These results are obtained at a very low computational cost.

Computational fluid dynamics (CFD) simulations of free-stream water wheels are then set up. A two-dimensional model is exploited to describe their most important power characteristics in a systematic study. Two conflicting performance requirements are identified: generating high power per unit submerged frontal area ($C_{\mathrm{P\ wet}}$), and high power unit frontal rotor area ($C_{\mathrm{P\ rotor}}$). The decomposition of the net power output in terms of the contribution of individual blades allows for an improved understanding of the dynamics of the machine.

Two sets of experimental measurements are used, by which the adequacy of the numerical simulations can be assessed.

Finally, two optimizations steered by a genetic algorithm are carried out in order to optimize the design of the free-stream water wheel on the basis of two-dimensional simulations. The first features extremely wide ranges of parameters; as a result, it is shown that operators constrained in installation width or area should adopt high-radius, high-depth wheels, while operators constrained in rotor size or installation depth should deploy low-radius, low-depth wheels. The second optimization focuses on improving the quality of power delivery; the resulting design recommendation features shortened blades. After the investigation of 2 400 different wheel configurations, the results indicate that the optimal free-stream water wheel design features fully-immersed blades which produce power in a continuous fashion for most of the power stroke. This shows that lift, in addition to drag, contributes to energy conversion mechanism for these machines. Last, a preliminary assessment of three-dimensional effects is finally given, highlighting areas where further research is needed.

Zusammenfassung

Diese Arbeit konzentriert sich auf die Optimierung von Wasserkraftanlagen, die sich gering auf die Flussfauna auswirken, und schwimmende Wasserrädern im Besonderen.

Eine theoretische Analyse der erreichbaren Leistung in schwimmender oder Bypass Wasserkraftanlage wird zuerst durchgeführt. Ein Modell wird entwickelt, das eine Quantifizierung der maximal verfügbaren Hydraulikleistung und die Messung des Wirkungsgrades ermöglicht. Seine Verwendung wird an einem Praxisbeispiel erläutert, in welchem die Leistung eines Kleinwasserkraftwerks mit in physikalischen Prinzipien verankerten Referenzwerten verglichen wird. Diese Ergebnisse werden mit sehr geringem Rechenaufwand erreicht.

Anschließend werden numerische Strömungssimulationen (CFD) von schwimmenden Wasserrädern erstellt. Ein zweidimensionales Modell wird genutzt, um ihre wichtigsten Leistungseigenschaften in einer systematischen Studie zu beschreiben. Es werden zwei widersprüchliche Leistungsanforderungen identifiziert: Erzeugung einer hohen Leistung pro Einheit untergetauchter Stirnfläche ($C_{\mathrm{P\ wet}}$) und einer hohen Leistung pro Einheit Rotorstirnfläche ($C_{\mathrm{P\ rotor}}$). Die Zerlegung der Nettoleistung in den Beitrag einzelner Schaufeln ermöglicht ein besseres Verständnis der Dynamik der Maschine.

Es werden zwei experimentelle Messreihen verwendet, mit denen die Angemessenheit der numerischen Simulationen beurteilt werden kann.

Abschließend werden zwei durch einen genetischen Algorithmus gesteuerte Optimierungen durchgeführt, um die Auslegung des Freilaufwasserrades auf Basis zweidimensionaler Simulationen zu optimieren. Der erste bietet extrem breite Parameterbereiche. Als Ergebnis wird gezeigt, dass Betreiber, die mit einer begrenzten Installationsbreite oder -fläche arbeiten müssen, Räder mit großem Radius und großer Tiefe verwenden sollten, während Betreiber, die mit einer begrenzten Rotorgröße oder Eintauchtiefe arbeiten müssen, Räder mit geringem Radius und geringer Tiefe einsetzen sollten. Die zweite Optimierung konzentriert sich auf die Verbesserung der Qualität der Leistungsabgabe; die daraus resultierende Designempfehlung weist verkürzte Schaufeln auf. Nach der Untersuchung von 2 400 verschiedenen Radkonfigurationen zeigen die Ergebnisse, dass das optimale schwimmende Wasserraddesign vollständig eingetauchte Schaufeln aufweist, die für den größten Teil des Arbeitshubs kontinuierlich Leistung erzeugen. Dies zeigt, dass der Auftrieb zusätzlich zum Strömungswiderstand zum Energieumwandlungsmechanismus dieser Maschinen beiträgt. Schließlich wird eine vorläufige Bewertung der dreidimensionalen Effekte gegeben, die Bereiche aufzeigen, in denen weitere Forschung erforderlich ist.

Co-authors, collaborators, technical and financial resources

The work presented in this thesis was carried out in collaboration with many people, whose contributions are acknowledged along the text, and are summarized here.

Dominique Thévenin, Stefan Hoerner, Emeel Kerikous, Sebastian Engel and Dennis Powalla have co-authored the four main journal articles which this thesis builds upon [63, 73, 103, 109]. Stephanie Müller, Dennis Powalla and Abhishekkumar Shingala are the first authors of three further articles presenting results obtained in the scope of this work [78, 106, 111]. Rohit Patil, Abhisheik Joshi and Aman Jain, as student assistants, have contributed directly to producing numerical and experimental results used in this work.

The water channel of the laboratory in Magdeburg, in which experiments were carried out, was engineered by Stefan Hoerner. The construction and rigging of the experimental apparatus used by the author has been in great part carried out by Michael Haarmann (Firma CATLAB) and Dirk Meinecke (from the LSS laboratory). Stephan Mertens, from project partner company Sibau Genthin GmbH, has helped with continuous sharing of technical information and advice.

Most of the computations in this work were carried out on the *Neumann* cluster of the University of Magdeburg (172 16-core nodes, 10 TFLOPS), in part financed by the laboratory.

Stefan Hoerner and Dominique Thévenin have been instrumental in obtaining the funds which supported the author's work in the laboratory. These mainly take the form of financial support provided by the *Fluss-Strom* project financed by the *Bundesministerium für Bildung und Forschung* (German Federal Ministry of Education and Research) under the project number 1714, for which the author is very thankful.

Finally, the author's gratitude goes towards his mentees Stephanie Müller [66], Artem Skrypnik [71], Annemarie Lehr [72], Farook Hussain [75], Leyla Orunova [80], Jenny Wahrlich [82], Dennis Powalla [92], Abhishekkumar Shingala [107] and Sergei Sukhorukov [108], as well as towards the students of the fluid dynamics course he taught on behalf of the laboratory, for the many contributions they made to his understanding of fluid mechanics.

This PhD thesis is dedicated to Françoise and Michèle Boulanger.

Introduction

It is now widely accepted that the exploitation of air and water flows in the environment must be part of the solution to our current global energy production challenge. Currently, the bulk of this contribution comes from high-head hydraulic installations and axial wind turbines. Nevertheless, research is also being carried out to optimize unconventional devices in air or water (for example Wells, Savonius or Darrieus turbines) suited to small-scale electrical production. These are relevant not only because they give access to untapped potential (in Germany, all sites with large hydroelectric potential are exploited already, and onshore wind power is no longer growing steadily), but also because they allow for decentralized, low-impact production of electricity.

The topic of this thesis concerns the exploitation of water currents with low-power, low-footprint devices. Conventional micro-hydro ($< 100\,\mathrm{kW}$) and pico-hydro ($< 5\,\mathrm{kW}$) installations are associated with high global sustainability ratings [23, 47]. In particular, devices operating without additional damming or modification to channel beds have an extremely low impact on fauna and flora and are most likely to meet the most stringent environmental regulations in Europe or even Germany. Because they feature high availability and can be installed with relative ease near populated areas, machines installed in floating installations may make a valuable contribution towards increasing electrification or decentralizing existing power networks.

The work in this thesis was carried out in large part with funding from project *Fluss-Strom*, financed by the German Federal Ministry of Education and Research, which supported research in this area. The laboratory for fluid dynamics of the University of Magdeburg took up the task of optimizing the configuration of a floating water wheel, building on prior experience acquired optimizing related devices [25, 32, 48].

The present thesis thus focuses on the optimization of low-impact hydropower devices in general, and free-stream water wheels in particular. It is divided in four parts.

Chapter 1 focuses on the power potential of low-density hydropower devices. Indeed, these machines are designed to operate in flows significantly larger than themselves, at the surface of river flows or in bypass channels. Exploiting this energy potential to its fullest requires careful consideration of the boundary conditions, and a model is presented accordingly, by which to quantify the available power and measure efficiency.

Chapter 2 introduces computational fluid dynamics (CFD) simulations of free-stream water wheels. The challenges associated with calculating the flow in these machines are presented, before a two-dimensional model is exploited to describe their most important power characteristics.

Chapter 3 presents two sets of experimental measurements, by which the adequacy of the numerical simulations can be assessed.

Finally, chapter 4 is focused on optimizing the design of free-stream water wheels to maximize their power output. Two optimizations covering a very large range of parameters are presented, guided by genetic algorithms; they result in the publication of broadly-applicable design guidelines. A first assessment of three-dimensional effects is finally given, highlighting areas where further research is needed.

Chapter 1

Energy budget for low-density hydropower

1.1 Introduction

This thesis focuses on the performance of low-power, low-density hydraulic devices: machines of relatively small size, capable of producing hydropower without radically altering their environment. These machines would typically include vertical- and horizontal-axis turbines immersed below floating structures in rivers, or operating as bypasses to the main river flow.

The complex nature of fluid flows within these machines (three-dimensional, turbulent, featuring free surfaces) makes it difficult to predict *a priori* their power potential. The final stages of the design of such turbomachines are in practice carried out using Computational Fluid Dynamics (CFD) simulations and experimental measurements. For such flows involving moving parts and free surfaces, considerable computational resources and time budgets are required. In addition, models accounting for two interacting phases (air and water), and especially the inherent uncertainties associated with the Reynolds-averaging (RANS) of the momentum equations in CFD, require devoting additional resources to calibration and validation of simulation results. These challenges will be amply demonstrated in chapters 2 and following.

While these advanced methods provide detailed descriptions of fluid flow, they are not easily used to obtain insight needed for a fist, broad scientific and engineering study. In the field of wind turbine design, for example, any preliminary work will begin with the use of the actuator theory popularized by Betz, Joukowski and contemporaries, in order to obtain estimates for power potential and later quantify efficiency. In the case of small-scale hydraulic installations with an unrestricted outlet, equivalent tools are available in the literature, as covered later in section 1.3. This chapter purposes to do the same for the case of hydraulic devices operating in free-stream flows significantly larger than themselves.

In this way, tools will be proposed to quantify the performance of machines expected to harvest both hydrokinetic and potential energy from flowing water. For example, given one installation site, how to quantify the energy potential using the minimum possible amount of information? What fundamental characteristics of the installation and of the machine affect this potential? At which rotor operating speed would it be fulfilled? Answering those questions leads first to distinguish between the notions of efficiency and power non-dimensionalization through coefficients. Then, a comparatively simple analytical model will be proposed, which allows for fast computations of the energy budget in all types of free-stream installations. Finally, in section 1.5, a worked-out example will be given to demonstrate usage of the model in practice.

Sections 1.2 to 1.4 of this chapter were published in a peer-reviewed journal article (reference [63]): O. Cleynen, S. Hoerner, and D. Thévenin. "Characterization of hydraulic power in free-stream installations". In: *International Journal of Rotating Machinery* 2017 (2017). DOI: 10.1155/2017/9806278.
Section 1.5 of this chapter was published in a peer-reviewed journal article between the submission and the publication of this Thesis (reference [109]): O. Cleynen, D. Powalla, S. Hoerner, and D. Thévenin. "An efficient method for computing the power potential of bypass hydropower installations". In: *Energies* 15.9 (2022). DOI: 10.3390/en15093228.

1.2 Parameters for hydropower performance evaluation

Several approaches can be taken for quantifying the performance of hydraulic power devices. The following criteria and notation, illustrated in figure 1.1, are used in the present analysis:

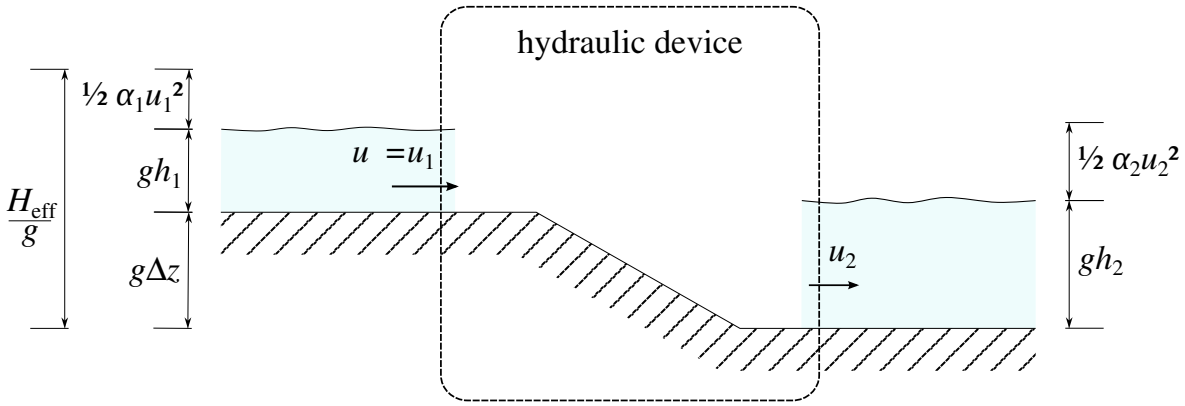

Figure 1.1: Notation for describing an arbitrary hydraulic installation, including the effective head H_{eff} introduced by P. F. Pelz [33] and described in section 1.3 of this paper.

Figure previously published in [63]

Hydraulic power $\dot{W}_{\text{hydraulic}}$ is the time rate at which water affected by the machine is losing or gaining specific mechanical energy e:

$$\dot{W}_{\text{hydraulic}} \equiv \int (\Delta e)\ \mathrm{d}\dot{m} \tag{1.1}$$

in which the integral is performed over the surface of a control volume enclosing the device;
where the sign of Δe is measured from the reference frame of the fluid (and thus usually negative – a loss);
and where $\dot{m}$ stands for mass flow ($\mathrm{kg\,s^{-1}}$).

In the case of a machine with uniform inlet and outlet properties, Δe can be evaluated as

$$\Delta e = \Delta \left[g(z+h) + \frac{1}{2}u^2 \right] \tag{1.2}$$

where g is the gravitational acceleration ($\mathrm{m\,s^{-2}}$);
z is the local altitude of the river bed, positive upwards (m);
h is the height of the water surface relative to the bed, positive upwards (m);
and u is the local flow velocity ($\mathrm{m\,s^{-1}}$).

In that case, and when the mass flow through the machine $\dot{m}$ is easily identified, hydraulic power (1.1) is simply evaluated as

$$\dot{W}_{\text{hydraulic}} = \dot{m}\ \Delta \left[g(z+h) + \frac{1}{2}u^2 \right] \tag{1.3}$$

Nevertheless, in the case of a device operating within a wide channel (such as a tidal turbine), it may be impossible to identify a single mass flow rate $\dot{m}$ corresponding

to a streamtube with uniform properties, and $\dot{W}_{\text{hydraulic}}$ needs to be evaluated with integral (1.1), which requires extensive knowledge of the velocity field.

The hydraulic power transmitted to or from the device can have an extremum value for a given set of constraints. The existence and value of this maximum or minimum depend on the parameters which are assumed given, i.e. on the chosen operational scenario. The purpose of the present chapter is to study and determine best design and operating conditions.

The energy flow through a hydraulic machine can be conceptualized as shown in figure 1.2. The performance of a hydraulic machine is then evaluated using the following three efficiencies.

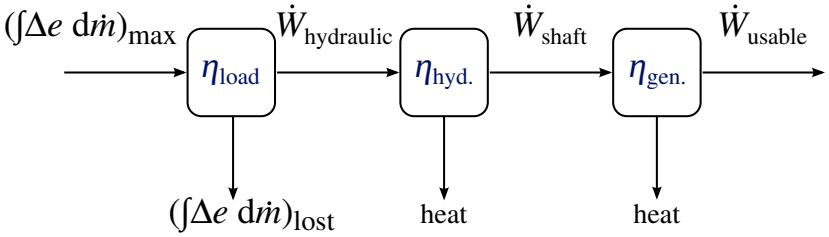

Figure 1.2: A conceptual representation of the energy flow through a machine operating in arbitrary conditions. The usable power $\dot{W}_{\text{usable}}$ is maximized when the three efficiencies $\eta_{\text{generator}}$, $\eta_{\text{hydraulic}}$ and η_{load} are equal to one. The definition of what constitutes the *maximum* value of $\int \Delta e \, \mathrm{d}\dot{m}$ depends on the operating constraints, as discussed later.

Figure previously published in [63]

When there exists an extremum hydraulic power (see later discussion), then a device's ability to reduce the energy of the water is measured with the *load efficiency* η_{load}:

$$\eta_{\text{load}} \equiv \frac{\dot{W}_{\text{hydraulic}}}{\dot{W}_{\text{hydraulic max.}}} \tag{1.4}$$

The hydraulic power extracted from the water is in part converted to (useful) mechanical shaft power, while viscous effects cause the other part to be washed down the flow, ultimately translating into heat. A measure of the conversion effectiveness is already known as the *hydraulic efficiency* $\eta_{\text{hydraulic}}$:

$$\eta_{\text{hydraulic}} \equiv \frac{\dot{W}_{\text{shaft}}}{\dot{W}_{\text{hydraulic}}} \tag{1.5}$$

Because of the high specific heat capacity of water, losses converted into heat do not translate into easily-measurable temperature changes, in particular for free surface flows and for such low-power installations. In practice a direct experimental measurement of the hydraulic efficiency of such an installation is therefore very difficult.

Lastly, the shaft power is converted into usable form, usually electricity, in a process whose effectiveness is measured with the ***generator efficiency*** $\eta_{\text{generator}}$:

$$\eta_{\text{generator}} \equiv \frac{\dot{W}_{\text{usable}}}{\dot{W}_{\text{shaft}}} \tag{1.6}$$

Therefore, the usable power developed by a hydraulic installation can be expressed as follows:

$$\dot{W}_{\text{usable}} = \eta_{\text{generator}}\ \eta_{\text{hydraulic}}\ \eta_{\text{load}}\ \dot{W}_{\text{hydraulic max.}} \tag{1.7}$$

Differing definitions for the efficiency may be constructed; for example a different turbine efficiency may be devised to relate the shaft power to the flow wake impact [26]. Nevertheless, this thesis focuses on the energy conversion process. The three efficiencies in eq. 1.7 are independent but may be affected together. For instance, the rotating speed of the impeller would impact both $\eta_{\text{generator}}$ and $\eta_{\text{hydraulic}}$. In this chapter, the focus is on hydrodynamics and $\eta_{\text{generator}}$ is not further considered.

Power, be it hydraulic, shaft or useful power, can be non-dimensionalized by comparing it to a partly arbitrary reference power: this ratio is named *power coefficient* C_{P} (sometimes named "harvesting factor" in the literature). A commonly-accepted definition [29], used as well in this thesis, is:

$$C_{\text{P}} \equiv \frac{\dot{W}}{\frac{1}{2}\,\rho\,S\,U_\infty^3} \tag{1.8}$$

where ρ is the fluid density ($\mathrm{kg\,m^{-3}}$);
S is a reference surface area, as discussed below ($\mathrm{m^2}$);
and U_∞ is the free-stream (faraway) velocity ($\mathrm{m\,s^{-1}}$).

Typically, the reference area S in eq. 1.8 is the frontal inlet area of the device, although, as will be seen in chapter 2, other definitions are sometimes more suitable. In this manner, $C_{\text{P hydraulic}}$, $C_{\text{P shaft}}$ and $C_{\text{P useful}}$ designate the power coefficients associated to each of the powers defined in figure 1.2.

Other selections of reference powers for the denominator of eq. 1.8 can be used, such as those proposed by Y. Li [41], M. Denny [14], or that put forth by P. F. Pelz [33], discussed below and re-written here with our notation:

$$C_{\text{P}} \equiv \frac{-\dot{W}}{\frac{4}{5}\dot{m}\left(g h_1 + \frac{\alpha_1}{2}u_1^2 - g\Delta z\right)} \tag{1.9}$$

At this point, it is important to stress out that the efficiency values η introduced previously have an unambiguous definition and fulfill the condition $\eta \leq 1$. On the other hand, the power coefficient is merely a non-dimensional parameter with a partly arbitrary character. As a result, the value of C_P might well exceed 1. A given machine may be attributed different values for the maximum power coefficient $C_{\text{P max.}}$, either because the underlying assumption in defining the optimum case, or the definition of C_{P}, may differ. These are the only reasons why Pelz's limit described later in eq. 1.11 does not converge towards the 16/27 classical result (see remarks p. 24) when $g \to 0\,\mathrm{m\,s^{-2}}$ and $\Delta z \to 0\,\mathrm{m}$.

1.3 Optimum for flatbed installations by Pelz

In order to connect our new developments with established results from the literature, the analysis starts by considering an obstructed channel. P. F. Pelz first developed (2011, [33]) an expression for an extremum hydraulic power $\dot{W}_{\text{hydraulic max.}}$ with the following constraints:

1. A full obstruction of the upstream fluid flow;
2. An entirely unobstructed downstream flow;
3. A limited outlet width.

Thus, in this model, condition 2 turns the outlet water height h_2 into a control variable, while condition 1 sets the mass flow $\dot{m}$, and condition 3 the outlet width b_2, as input constants. The whole mass flow $\dot{m}$ always passes through the device.

To analyze the system, Pelz defines an energy budget termed *effective head* $H_{\text{eff.}} \equiv h_1 + \alpha_1 u_1^2/2g - \Delta z$, using the notations shown in figure 1.1 and in the nomenclature. Pelz then shows that the hydraulic power available to an installation fed with rectangular ducts can be maximized if two conditions are met. They constrain the Froude number at exit $[\text{Fr}]_2 \equiv u_{2,\text{ av.}}/\sqrt{gh_2}$, and the volume flow per unit width at exit $q_2 \equiv \dot{\mathcal{V}}_2/b_2 = u_{2,\text{ av.}} h_2$, leading to following conditions:

$$q_{2,\text{opt.}} = \left(\frac{g}{\alpha_2}\right)^{\frac{1}{2}} \left[\frac{2}{5} H_{\text{eff.}}\right]^{\frac{3}{2}} \tag{1.10a}$$

$$[\text{Fr}]_{2,\text{opt.}} = 1 \tag{1.10b}$$

The maximum hydraulic power that may be extracted from a flow of given $H_{\text{eff.}}$ when $\eta_{\text{hydraulic}} = 1$ is then, written in our notation:

$$\dot{W}_{\text{hydraulic max, Pelz}} = -\rho b_2 \left(\frac{g^3}{\alpha_2}\right)^{\frac{1}{2}} \left[\frac{2}{5} H_{\text{eff.}}\right]^{\frac{5}{2}} \tag{1.11}$$

This optimum, which can be re-written as $\dot{W}_{\text{hydraulic max, Pelz}} = -\dot{m} g \frac{2}{5} H_{\text{eff.}}$, is a benchmark by which to evaluate the performance of hydraulic machines working with a fully-controlled stream, i.e. in installations where the fluid is guaranteed to enter the device, and where the outlet flow can be discharged with any chosen water level height h_2. Indeed, during performance evaluations of such devices the mass flow rate $\dot{m}$ is a direct input variable [53].

The removal of condition 1 (full flow obstruction, with the entire stream passing through the device) has been later explored by Pelz & Metzler [37]: a model is then obtained for the performance of channel hydraulic devices installed on the bottom of channels and with lateral flow bypass.

Even if these theoretical findings are useful in specific settings, many hydraulic devices exist for which conditions 2 and 3, necessary for the derivation of the above optimum, do not apply. Such devices may include floating installations operating in wide and/or deep channels e.g. operated away from navigation lanes or where the tidal power potential is highest [43]. In that case:

- The mass flow $\dot{m}$ flowing through the device is not readily known because it is a function of the operating conditions;
- It cannot be assumed that an unobstructed, steeply-sloped bed at altitude z_2 is available at the outlet to receive the water leaving the machine. Instead, the outlet boundary condition will be conditioned by the water level altitude $\{z_2 + h_2\}$ of an existing body of water (e.g. a reservoir) independent of the device operation.

A machine operating in such conditions would therefore attain a maximum hydraulic power different from that quantified in eq. 1.11. For such a case, constraining the value of $\dot{m}$ as input variable, as in [18], would result in grossly over-estimated power calculations. The purpose of the next section is to determine a realistic prediction of optimal operation.

1.4 Efficiency and optimal speed of surface-constrained installations

1.4.1 Maximum power in unobstructed channel flow

A model is developed here to evaluate the performance of a hydraulic power device operating in a wide channel and constrained by a given outlet water altitude $\{z_2 + h_2\}$. This model is based on the classical actuator disk models developed by Froude, Betz, Joukowski and other scientists (described e.g. by van Kuik et al. in 2014 [50]). Building on top of this classical theory, the effects of altitude change and duct pressure loss will be included in the analysis. This model assumes uniform inlet and outlet velocities, however advances made in the modeling of wakes [51] and wall effects [39] may lift this restriction in the future.

In the most general case a hydraulic machine can be described as shown in figure 1.3; water incoming at 1 and leaving at 2 sees its momentum changed by the three forces $\vec{F}_{\text{actuator}}$ (by the power-producing moving parts modeled by an actuator surface), $\vec{F}_{\Delta p_{\text{alt.}}}$ (due to altitude change), and $\vec{F}_{\text{loss}}$ (due to internal friction effects):

$$\vec{F}_{\text{actuator}} + \vec{F}_{\Delta p_{\text{alt.}}} + \vec{F}_{\text{loss}} = \dot{m}\,(\vec{u}_2 - \vec{u}_1) \tag{1.12}$$

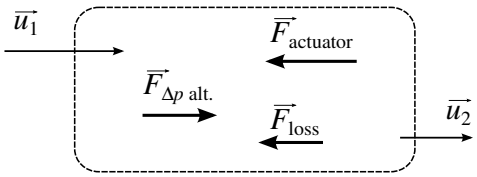

Figure 1.3: A hydraulic machine in the most generic case: the fluid momentum is altered by the combined action of forces $\vec{F}_{\text{actuator}}$, $\vec{F}_{\Delta p_{\text{alt.}}}$ and $\vec{F}_{\text{loss}}$.

Figure previously published in [63]

When one considers the machine as a "black box", the hydraulic power production can be described as a one-dimensional phenomenon. Here for clarity, the machine is arranged so that all forces and velocities are aligned with the horizontal direction, x.

In an ideal machine designed for this environment, water would be guided to and from an actuator surface, across which hydraulic power is extracted from the fluid (figure 1.4). The velocity changes of the fluid are matched with cross-sectional area changes along the flow, so that the pressure distribution within the device can be traced as in figure 1.5 and quantified as follows.

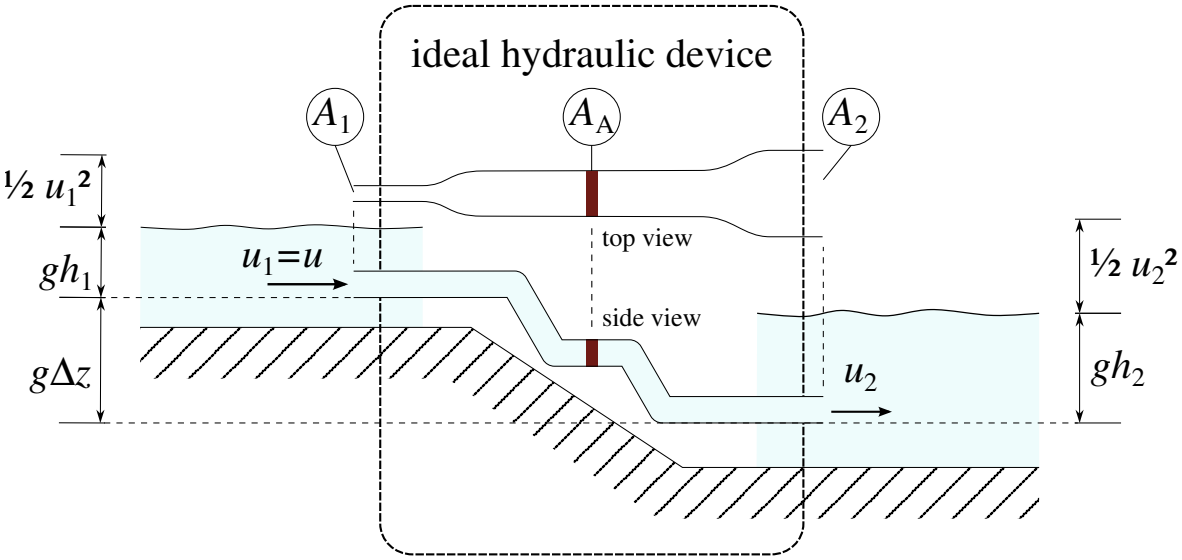

Figure 1.4: Cross-section of an arbitrary ideal hydraulic installation. The water streamtube expands from cross-sectional area A_1 to A_A, with a corresponding increase in pressure. The actuator surface of area A_A extracts hydraulic power from the fluid with a resulting pressure drop; the streamtube then expands again so the outlet pressure reaches p_2. The altitude of the inlet, outlet and actuator surface do not affect the machine's performance and are never specified. In this model, neither h_1 nor h_2 are affected by the power extracted by the device, since it occupies only a small part of the channel.

Figure previously published in [63]

The force exerted by the ideal actuator can be expressed in two different ways, one as a function of the rate of change of momentum of the water:

$$\begin{aligned} F_\mathrm{actuator} &= \dot{m}\,(u_2 - u_1) - F_{\Delta p_\mathrm{alt.}} - F_\mathrm{loss} \\ &= \rho u_\mathrm{A} A_\mathrm{A}(u_2 - u_1) + \rho g A_\mathrm{A}\Delta(z+h) - F_\mathrm{loss} \end{aligned} \tag{1.13}$$

where u_1 and u_2 are the inlet and outlet velocities ($\mathrm{m\,s^{-1}}$);
u_A is the flow velocity through the actuator ($\mathrm{m\,s^{-1}}$);
and A_A is the frontal area of the actuator surface ($\mathrm{m^2}$).

and the other as a function of the kinetic energy change across the actuator surface:

$$\begin{aligned} F_\mathrm{actuator} &= A_\mathrm{A}\,(p_+ - p_-) \\ &= \rho A_\mathrm{A}\left[\frac{1}{2}\left(u_2^2 - u_1^2\right) + g\Delta(z+h)\right] - F_\mathrm{loss} \end{aligned} \tag{1.14}$$

where p_+ and p_- are the pressures upstream and downstream of the actuator surface, as shown in figure 1.5 (Pa).

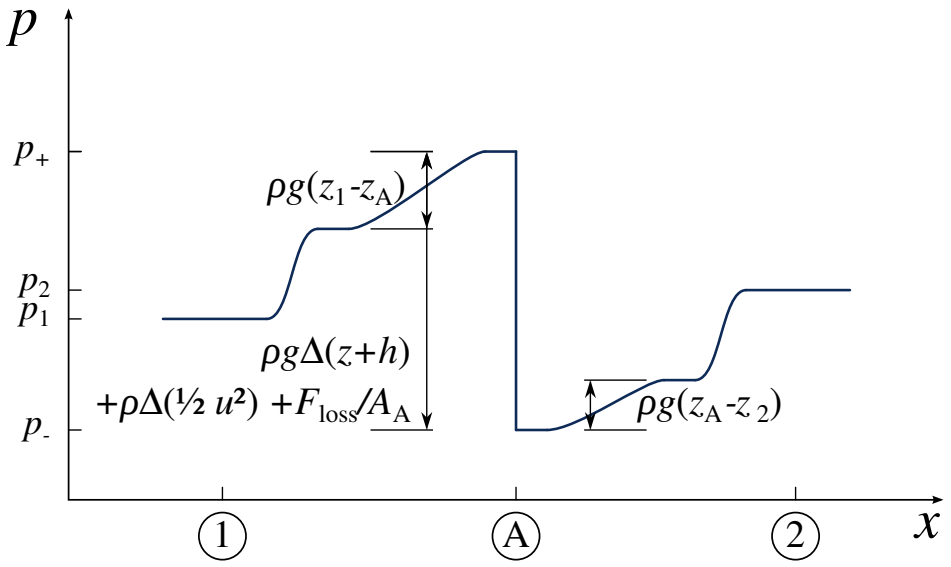

Figure 1.5: Pressure distribution within the arbitrary ideal machine described in figure 1.4. The pressure p_1 of the inlet water is raised twice; first as its velocity is reduced from u_1 to u_A, then as the altitude is varied by $z_1 - z_\mathrm{A}$. Similarly, downstream of the actuator, the fluid pressure is raised twice so that flow conditions 2 at the outlet may be attained. The pressure drop across the actuator surface A, described in eq. 1.14, corresponds to the lumped contributions of net water level altitude change $\Delta(z+h)$, velocity change $\frac{1}{2}\Delta u^2$, and losses due to drag F_loss.

Figure previously published in [63]

In this analysis the sign convention is as described in figure 1.3, i.e. $\Delta(z+h) < 0$ when the water level drops, and F_loss is always negative; thus, whenever hydraulic power is produced by the device, $F_\mathrm{actuator} < 0$.

Equating eqs. (1.13) and (1.14) gives an expression of u_A as a function of u_1 and u_2; this allows to express the hydraulic power as:

$$\dot{W}_\mathrm{hydraulic} = \rho A_\mathrm{A} \frac{1}{2}(u_2 + u_1)\left[\frac{1}{2}\left(u_2^2 - u_1^2\right) + g\Delta(z+h) - \frac{F_\mathrm{loss}}{\rho A_\mathrm{A}}\right] \tag{1.15a}$$

$$\dot{W}_\mathrm{hydraulic} = \rho A_\mathrm{A} u_\mathrm{A}\left[2u_\mathrm{A}^2 - 2u_\mathrm{A}u_1 + g\Delta(z+h) - \frac{F_\mathrm{loss}}{\rho A_\mathrm{A}}\right] \tag{1.15b}$$

This expression reduces as expected to that of Betz et al. in the case where either $\Delta(z+h)$ or g tend to zero. Similarly, when $u_1{=}u_2$, i.e. no kinetic energy is withdrawn from water, the power tends towards $\dot{W}_\mathrm{hyd.}{=}\rho A_\mathrm{A} u_1 g\Delta(z+h)$, as expected of a high-head hydropower installation.

In order to maximize power, a compromise must be made at the actuator surface: higher actuator velocities increase the mass flow, but reduce kinetic energy harvest; while lower actuator velocities increase kinetic energy recovery at the cost of decreased mass flow. This compromise is additionally affected by the (usually negative) potential energy term $g\Delta(z+h)$ and the losses F_loss due to friction.

In this paper, the optimum is determined according to following constraints:

1. A known device actuator surface area;

2. A known water surface altitude drop independent of the device.

Here, condition 1 constrains the actuator surface area A_A, while condition 2 constrains the water level drop $\Delta(z+h)$ as input variables; therefore, the main control variable becomes the cross-actuator velocity u_A. Alternative boundary conditions describing e.g. a bypass flow [20] may be added in the future.

In the view of these restrictions, eq. 1.15b is non-dimensionalized by using the power coefficient defined in eq. 1.8 and the ratio u_A/U_∞, which is equal to u_A/u_1 in our case. Additionally, a non-dimensional *drop coefficient* K_D is defined to express the effect of both the water level drop and the friction losses, lumped together:

$$K_\mathrm{D} \equiv -\frac{\rho g \Delta(z+h) - \frac{F_\mathrm{loss}}{A_\mathrm{A}}}{\frac{1}{2}\rho U_\infty^2} \tag{1.16}$$

In this manner, the hydraulic power equation is obtained as:

$$C_{\mathrm{P\ hydraulic}} = 4\left(\frac{u_\mathrm{A}}{U_\infty}\right)^3 - 4\left(\frac{u_\mathrm{A}}{U_\infty}\right)^2 - K_\mathrm{D}\left(\frac{u_\mathrm{A}}{U_\infty}\right) \tag{1.17}$$

The solution of eq. 1.17 is plotted in figure 1.6, in which it is seen that unfavorable (negative) values of K_D decrease not only the maximum hydraulic power attainable by the machine (this was obviously expected), but also the optimum actuator speed needed to attain it. For $K_\mathrm{D} < -1$, the power coefficient is always positive (the device turns into a pump and does not extract any energy from the fluid); for $K_\mathrm{D} < -4/3$, the power curve no longer features an extremum outside of the standing condition ($u_\mathrm{A} = 0$).

The value of u_A/U_∞ that produces extremum values for the hydraulic power (i.e. setting $\eta_\mathrm{load} = 1$), as well as an explicit expression for this extremum, can be found by differentiating eq. 1.17 with respect to u_A/U_∞ and selecting the roots relevant to this study. For clarity, those are expressed as a function of a factor $T \equiv \frac{1}{3}\left[1 + \frac{3}{4}K_\mathrm{D}\right]^{\frac{1}{2}}$, obtaining:

$$\frac{u_{\mathrm{A\ opt.}}}{U_\infty} = \frac{1}{3} + T \tag{1.18}$$

$$C_{\mathrm{P hydraulic\ extremum}} = -\frac{8}{27} + 4T^3 - \frac{4}{3}T - \left(\frac{1}{3} + T\right)K_\mathrm{D} \tag{1.19}$$

In the case where there is neither altitude drop nor friction loss, the drop coefficient K_D is brought to zero and $T \to 1/3$: then, $u_{\mathrm{A\ opt.}} \to \frac{2}{3}U_\infty$; and the absolute value of the power coefficient tends towards 16/27, a classical value known as the *Betz-Joukowski limit* [50], and from hereon simply referred to as the Betz limit.[1]

The relationship between the optimum actuator velocity and the drop coefficient value (eq. 1.18) is plotted in figure 1.7. An optimum only exists for $K_\mathrm{D} > -4/3$, since standing

[1] Bergey [8] and van Kuik in 2006 [17] propose attributing this result to F. W. Lanchester as well. Van Kuik et al. in 2014 [50], however, show that although he expanded Froude's work to reach the result $|C_{\mathrm{P\ extremum}}| = 16/(27Q^2)$, Lanchester failed to conclude definitely on the value of the factor Q that he introduced [3]. The author of the present thesis adds that those considerations focus only on the name given to the end result. Actuator theory and the search for associated optimal velocity predate Betz and his contemporaries by two centuries — for example, Parent implicitly obtained $u_\mathrm{A}/U_\infty|_{\mathrm{opt.}}$=2/3 in 1704 [1].

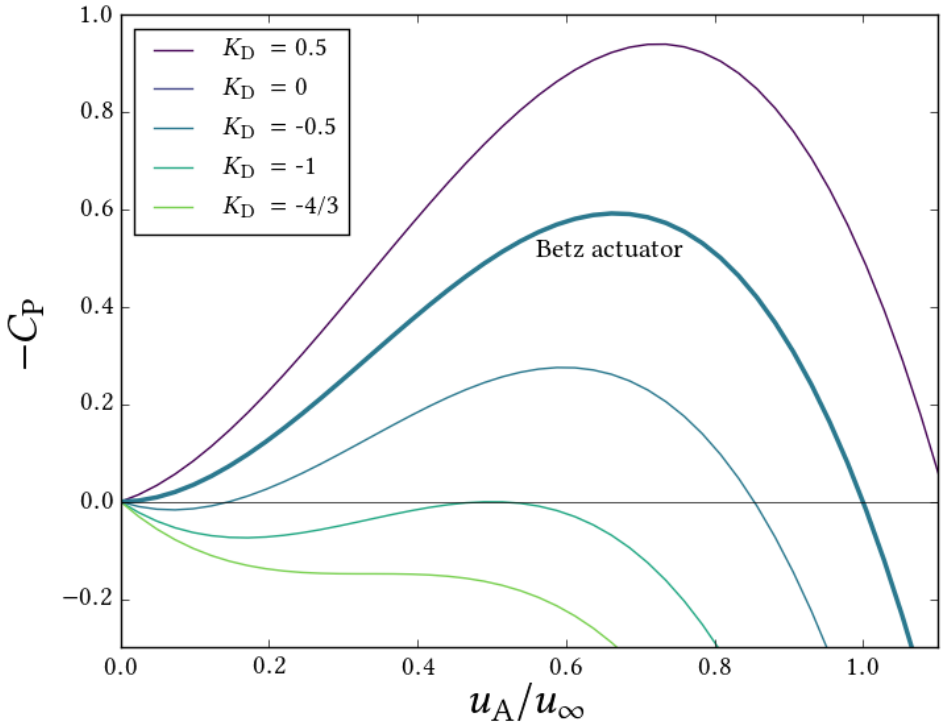

Figure 1.6: Power curves for an ideal actuator surface machine, for different values of the drop coefficient K_D. The case $K_D = 0$ corresponds to the well-known solution for an actuator surface without any loss, now associated with Betz & Joukowski. Positive values of K_D correspond to increased pressure drop across the device; increasingly negative values of K_D may occur due to increasing pressure losses. Note that negative $C_{P\ hyd.}$ values (or $-C_{P\ hyd.} \geq 0$, above the straight horizontal line in this figure) correspond to hydraulic power being extracted by the device, which is obviously the objective.

Figure previously published in [63]

conditions are found to be best when $K_D \leq -4/3$. The machine can only extract hydraulic power when $K_D > -1$. The optimum value $u_{A\ opt.}$ increases monotonically with K_D: more favorable drop coefficients always shift the optimum velocity ratio upwards. This remains true even in the hypothetical case where $u_{A\ opt.} > U_\infty$, as the energy expenditure required to accelerate the flow through the device (in eq. 1.15a, $\dot{m}(u_2^2 - u_1^2) > 0$) is compensated by the resulting increase in mass flow. In a free-stream unchanneled installation (e.g. a floating or bed-bound tidal or river turbine), it is expected that $\Delta(z + h) = 0$ and such devices will therefore always operate at $-1 < K_D \leq 0$.

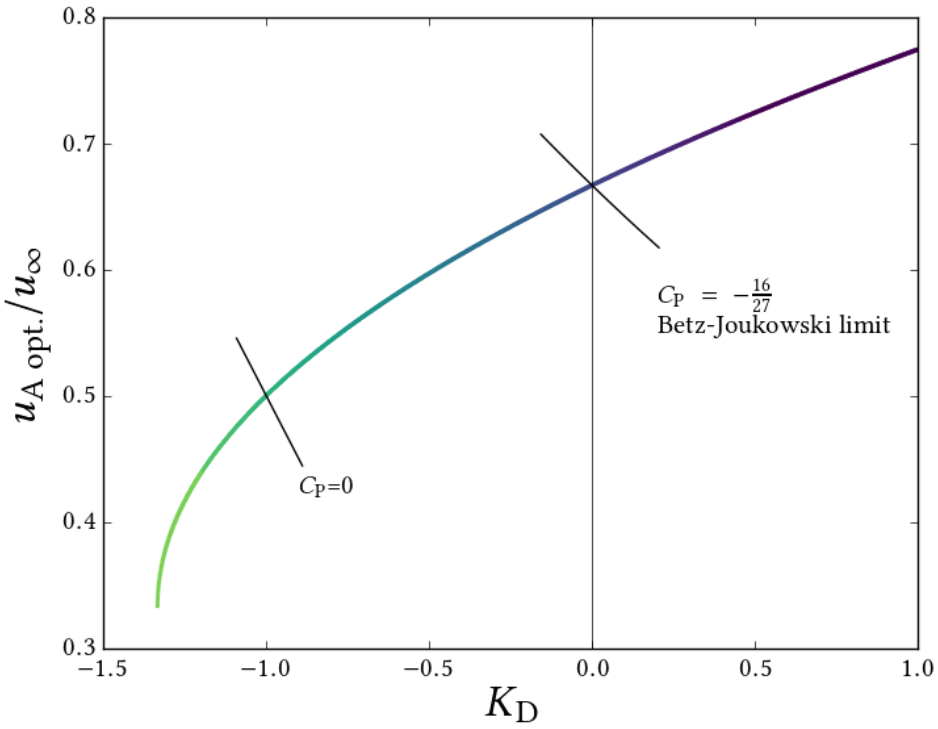

Figure 1.7: Optimum non-dimensional actuator velocity $u_{\mathrm{A\ opt.}}/U_\infty \equiv u_\mathrm{A}/U_\infty|_{\eta_\mathrm{load}=1}$ as a function of the drop coefficient K_D. The curve colormap is matched to that of figure 1.6. For values below -1, the hydraulic power coefficient becomes positive, and no energy can be extracted; below -4/3, an optimum actuator velocity no longer exists, since the best efficiency is obtained for standing conditions.

Figure previously published in [63]

1.4.2 Performance improvements through ducting

The developed model can now be expanded to account for the effect of ducting around a free-stream device. A suitable stationary duct positioned around a power-producing device can result in three distinct benefits:

1. An increase in $\eta_\mathrm{hydraulic}\eta_\mathrm{generator}$, through the optimization of the flow velocity distribution or rotation speed;
2. An increase in power density, obtained through the reduction in the size of the moving parts for a given volume footprint of the device;
3. An increase of power, obtained through the increase of the frontal area by the use of a stationary duct.

The first of those cannot be described in general terms for a generic hydraulic machine, and is best studied with the help of experimental and CFD techniques. The last two, however, can be examined by extending the model described above, in order to obtain tentative quantitative descriptions based on sensible hypotheses, and especially a broad qualitative characterization of the phenomenon.

A duct may increase the flow velocity locally, but will always impede the overall flow through and around the device; thus, in order to determine the optimal duct size (that

which will maximize power or power density), its effectiveness must be coupled back with the drop coefficient K_{D}.

A very simple duct drag model, in the line of classical hydrodynamic theory, links net drag force F_{loss} to the frontal area $S{=}A_{\mathrm{f}}$ and to the square of the actuator flow velocity u_{A} (a more complex duct drag model is also described in [63]). The proportionality constant is termed *loss coefficient* K_{D2}:

$$K_{\mathrm{D2}} \equiv \frac{-F_{\mathrm{loss}}}{\frac{1}{2}\ \rho\ u_{\mathrm{A}}^2\ S} \tag{1.20}$$

In turn the effect of altitude drop is described with a *static drop coefficient* K_{D0}:

$$K_{\mathrm{D0}} \equiv \frac{-\rho g \Delta(z+h)}{\frac{1}{2}\ \rho\ U_{\infty}^2} \tag{1.21}$$

An underlying expectation in defining those terms is that for a device of known geometry, neither K_{D0} nor K_{D2} are significantly affected by the device scale, the actuator speed or the hydraulic power.

The drop coefficient K_D of eq. 1.16 can now be re-written as:

$$K_{\mathrm{D}} = K_{\mathrm{D0}} - K_{\mathrm{D2}} \frac{A_{\mathrm{f}}}{A_{\mathrm{A}}} \left(\frac{u_{\mathrm{A}}}{U_{\infty}}\right)^2 \tag{1.22}$$

The actuator speed ratio that maximizes the load efficiency, $u_{\mathrm{A\ opt.}}/U_{\infty}$, can now be described as a function of K_{D0} and K_{D2}. The case where $A_{\mathrm{f}}{=}A_{\mathrm{A}}$ (corresponding to the central case, $R = 1$, in figure 1.9 further down) is presented in figure 1.8, where it is seen, as expected, that increases in the value of the loss coefficient lead to a decrease in the optimum velocity ratio and inevitably reduce the power output.

In a final effort to describe more realistic configurations, the geometry of the duct is parametrized using a *size ratio* parameter R comparing the frontal area A_{f} of the device to that of the actuator, A_{A} (see also figure 1.9):

$$R \equiv \frac{A_{\mathrm{A}}}{A_{\mathrm{f}}} \tag{1.23}$$

Then, eq. 1.17 can be re-formulated using eqs. (1.22) and (1.23) as:

$$C_{\mathrm{P\ hydraulic}} = \left[4 + \frac{K_{\mathrm{D2}}}{R^2}\right] \left(R\frac{u_{\mathrm{A}}}{U_{\infty}}\right)^3 - 4\left(R\frac{u_{\mathrm{A}}}{U_{\infty}}\right)^2 - K_{\mathrm{D0}}\left(R\frac{u_{\mathrm{A}}}{U_{\infty}}\right) \tag{1.24}$$

Since only the factor $\left(R\frac{u_{\mathrm{A}}}{U_{\infty}}\right)$ appears in eq. 1.24 when the loss coefficient K_{D2} is zero, any increase in u_{A} generated by ducting is exactly compensated by a decrease in the size ratio R, so that the power coefficient is unaffected. In practice however, $K_{\mathrm{D2}} > 0$ and losses to friction are a function not merely of the free-stream velocity U_{∞}, but also of the actuator operating velocity u_{A}.

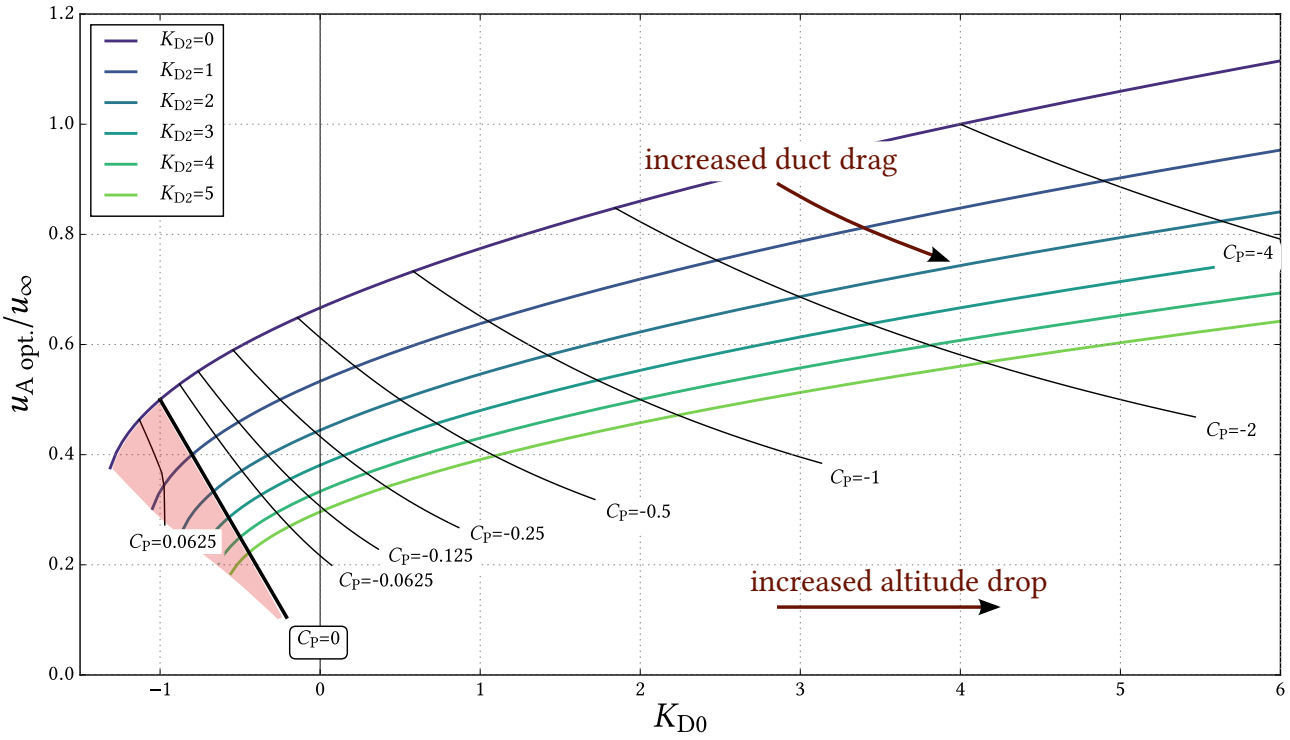

Figure 1.8: The optimum velocity ratio $u_{\text{A opt.}}/U_\infty \equiv u_\text{A}/U_\infty|_{\eta_\text{load}=1}$ as a function of the static drop coefficient K_{D0} and loss coefficient K_{D2} in a device for which $A_\text{f}{=}A_\text{A}$. Isocurves for various values of $C_{\text{P hyd.}}$ are also shown; the area highlighted in red, where the hydraulic power is positive (i.e. received by the water), is merely of theoretical interest. This diagram presents the solutions to eq. 1.24 in which eq. 1.25 is inserted, when $R{=}1$.

Figure previously published in [63]

Expression (1.24) is maximized, yielding $\eta_\text{load}{=}1$, when the adjusted actuator velocity ratio $R\frac{u_\text{A}}{U_\infty}$ reaches the value:

$$\left(R\frac{u_\text{A}}{U_\infty}\right)_{\text{opt.}} = \frac{4+\left[16+12K_{\text{D0}}+3K_{\text{D0}}\frac{K_{\text{D2}}}{R^2}\right]^{\frac{1}{2}}}{12+3\frac{K_{\text{D2}}}{R^2}} \tag{1.25}$$

This optimum reduces to that of eq. 1.18 when $K_{\text{D2}}{=}0$, and to the value $\frac{2}{3}$ predicted by Betz when both $K_{\text{D0}}{=}0$ and $K_{\text{D2}}{=}0$. Inserting this eq. 1.25 into eq. 1.24 gives us an expression for the optimum power coefficient $C_{\text{P hyd. opt.}}$ as a function of the size ratio for any given duct.

We are now able to characterize and visualize the effect of ducting on free-stream hydropower installations. This is perhaps best done by differentiating between two cases, illustrated in figure 1.9. Compared to the reference configuration (a duct without any change in cross-section) shown in the middle ($R = 1$):

- In case 1, a duct with known characteristic loss coefficient K_{D2} is used in the design phase to reduce the actuator size A_A for a given inlet frontal area A_f. In this case, R is reduced with the intent of increasing the power density $\frac{1}{R}C_{\text{P hyd}}$;

- In case 2, a duct with known K_{D2} is added on an existing device with fixed actuator area A_A. In that case, $1/R$ is increased with the intent of increasing the overall power $\dot{W}_{\text{hydraulic}}$.

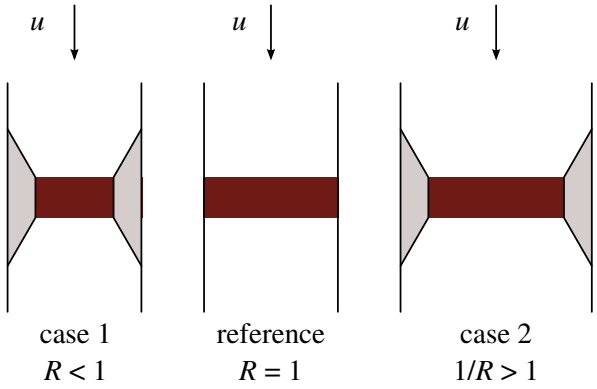

Figure 1.9: Conceptual schematic to describe the ducting of an actuator device. A duct can be used either to reduce the size of the actuator for a given frontal surface (case 1, left), or to increase the frontal area of a machine with an existing actuator (case 2, right). Both processes are described mathematically by reducing the value of parameter R below 1.

Figure previously published in [63]

The effect of both modifications, which amount to the same physical effect, can be observed in figures 1.10 & 1.11, which represent how the power coefficient and power density evolve as R is varied, for various values of K_{D2}.

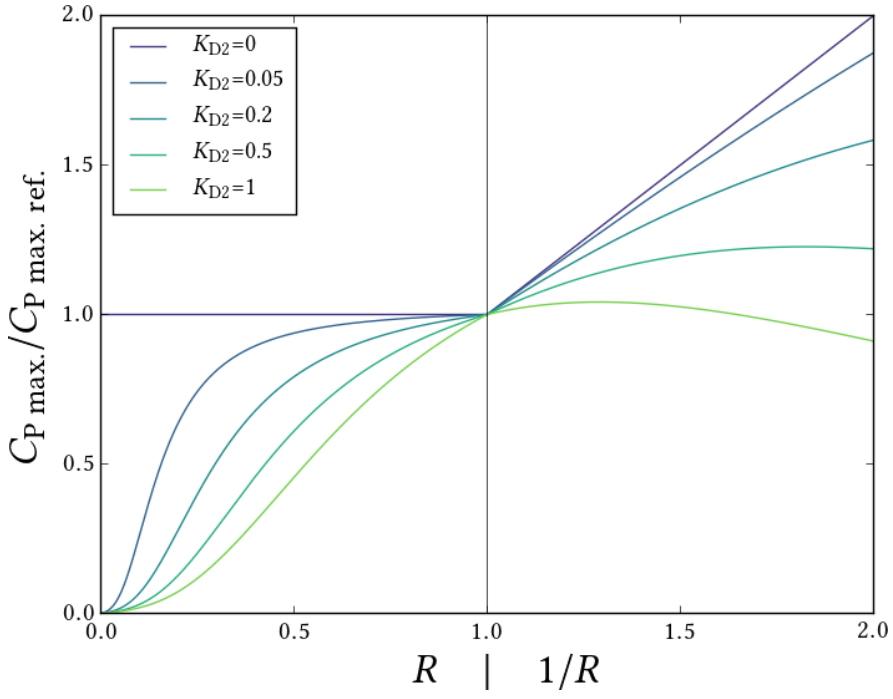

Figure 1.10: The ratio of maximum power coefficient $C_{\text{P hyd. max.}}$ to a reference value $C_{\text{P hyd. max. ref.}}=C_{\text{P hyd. max.}}|_{R=1}$, shown as a function of the duct size ratio. The abscissa represents R from values 0 to 1, and $1/R$ from 1 onward.
The curves are drawn for various values of K_{D2} when K_{D0}=0.25.

Figure previously published in [63]

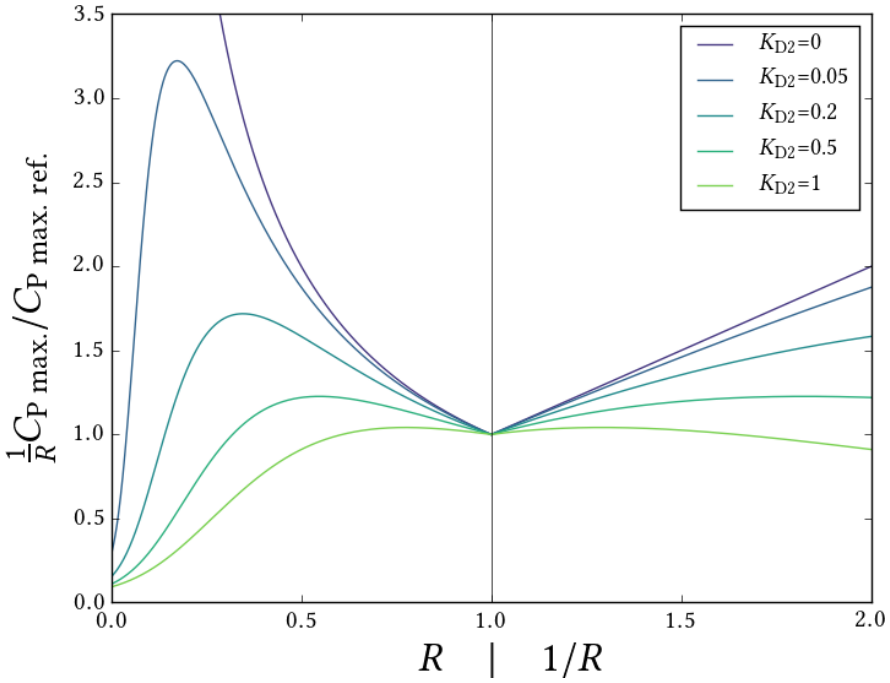

Figure 1.11: The ratio of maximum power density $\frac{1}{R}C_{\text{P hyd. max.}}$ to its reference value $\frac{1}{R}C_{\text{P hyd max.}}|_{R=1}$, shown as a function of the duct size ratio. The abscissa represents R from values 0 to 1, and $1/R$ from 1 onward.
The curves are drawn for various values of K_{D2} when K_{D0}=0.25.

Figure previously published in [63]

It is readily seen from these figures that low loss coefficients are associated to a high increase in power density through the use of ducting; the ratio R (size of actuator relative to frontal surface) then features an optimum value plotted in figure 1.11. Nevertheless, high K_{D2} values result in cases where adding a duct results in neither power nor power density increase (i.e. $R_{\text{opt.}}$=1) in that configuration. As expected, unless the frontal area is increased, the use of ducting can only result in a power coefficient decrease.

The geometrical features of the power and power density curves displayed in figures 1.10 & 1.11 are also affected by the value of the drop coefficient K_{D0}. This dependence can be visualized in figure 1.12, in which the value $R_{\text{opt.}}$ of the size ratio which maximizes the power density $\frac{1}{R}C_{\text{P hyd. max.}}/C_{\text{P hyd. ref.}}$ is plotted as a function of K_{D0} and K_{D2}.

From figure 1.12 it is seen that for any one value of K_{D0} (a property of the operating environment), increasing values of the loss coefficient increase the optimum size ratio, i.e. the relative size of the actuator that will maximize power density. For each value of K_{D0}, there exists a loss coefficient value above which $R_{\text{opt.}}$=1: in that case, the ducting can only reduce performance.

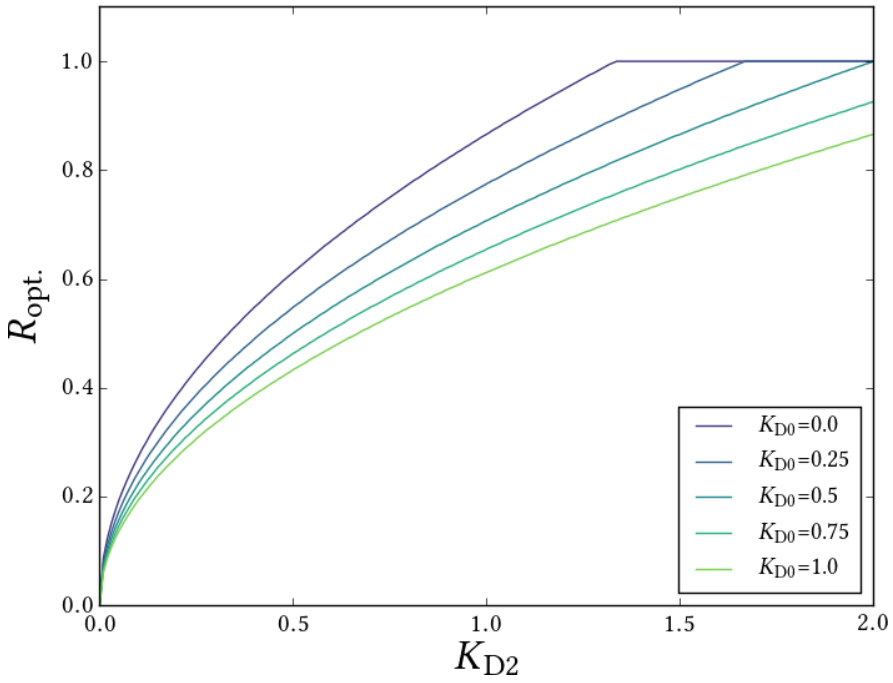

Figure 1.12: The optimum actuator size ratio $R_{\text{opt.}}$ (that will result in maximum hydraulic power density $\frac{1}{R}C_{\text{P hyd max.}}/C_{\text{P hyd. ref.}}$), plotted as a function of the loss coefficient K_{D2} for various values of the static drop coefficient K_{D0}.

Figure previously published in [63]

1.5 Example: application to a water vortex power plant

An example demonstrating the use of the model developed in this chapter is now given, focusing on a water vortex power plant (WVPP), a small-scale hydropower device designed for installation along rivers.

1.5.1 Context

Water vortex power plants are hydropower devices which use a Francis turbine (radial inlet, vertical outlet), but without the use of any guide vanes; instead, their turbine inlet consists of an open-air, spiral-shaped basin. This type of device is suited for combinations of modest flow rates (in the order of $1\,\mathrm{m^3\,s^{-1}}$) and modest hydraulic head (in the order of $1\,\mathrm{m}$). Recent research interest in this type of device has focused on their compatibility with fish river migration.

As part of the research project *Fluss-Strom* which has funded most of the work presented in this thesis, the dynamics of a 26 m-long WVPP have been investigated. The constructor of the device markets it as the "*Fisch-Freundliches Wehr*", for use as fish migration corridors bypassing dams and large weirs. Work has gone towards erecting a full-scale laboratory installation at the Teschnische Universität Dresden (fig. 1.13), suited to biological investigations with live fish [76, 77, 91, 95]. Numerical investigations have also been carried out, as presented further below.

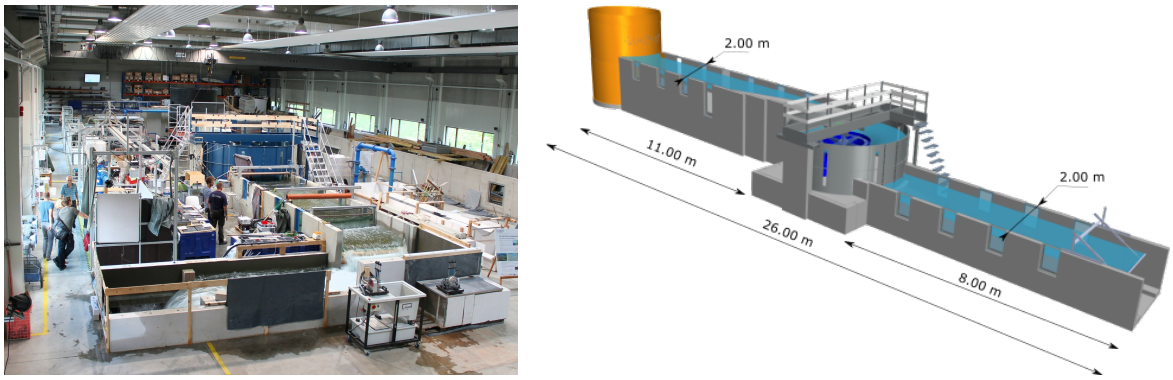

Figure 1.13: Left: photograph of the WVPP installation in the laboratory of the Teschniche Universität Dresden. The water flows from the background towards the viewer, with the blue turbine basin visible in the center. Right: computer drawing of the device with its main dimensions. The flow is from top left to bottom right, with the turbine basin in the center. The settling tank at inlet is depicted in yellow, and the turbine itself is displayed in dark blue.

Drawing reproduced from Powalla et al. 2021 [106], with geometry provided by Ecoligent GmbH. Figure later published in [109]

In the Dresden laboratory, water is picked up by pumps whose discharge goes through a settling tank before being fed to the WVPP. Water then flows through the free-surface installation, before overflowing an outlet weir, back into the inlet of the pumps. Observation of the dynamics of the installation in Dresden during testing reveals that its behavior is not simple. The system is controlled by prescribing the volume flow (provided by the pumps) and turbine rotation speed; the water levels in the inlet and outlet channels are part of the response.

The need for a model by which to analyze the installation's behavior can be prompted with the following observation. The plant in Dresden is first operated with a given volume flow and turbine rotation speed. Then, the turbine speed is reduced. This increased restriction to the flow causes the water in the upstream channel to "back up", and within the following minute, the water level there has increased significantly. As a result, the turbine's load increases, which, together with the change in rotation speed, causes the power output to change.
From the point of view of the experimental scientist, and of the device's future operator, is this change desirable? Is more hydraulic power now available to the turbine? Can the former power output (which occurred for a higher turbine speed and identical volume flow) be meaningfully compared with the new one? Is the turbine more efficient in one of the two cases? Should the expression for efficiency take the increase in inlet cross-sectional area into account?

In the literature, the turbine power of such devices is sometimes non-dimensionalized as an "efficiency", formulated as $\dot{W}_{\text{shaft}}/(\dot{m}g\Delta h)$, as would be done with a high-head cross-flow installation. In this case however, the device is intended for use as a *bypass* to the main river flow; the mass flow that is not captured by the WVPP is lost and will pass through the main river flow instead. The denominator in the expression above (the power that corresponds to an "efficiency" of 100 %) is therefore a fleeting amount that is affected by the device's operation, making comparison of different operating points difficult.

These introductory questions prompted by observation of the Dresden laboratory installation can be answered by addressing two more general questions: against which

maximum may we compare the measured performance of the installation? And, to this purpose, how to express power and efficiency in a meaningful way, so they may be compared across different scales and operating conditions?

1.5.2 Limitations of full flow simulations

As part of the same *Fluss-Strom* research project, a series of numerical investigations of the same WVPP have been carried out at the University of Magdeburg; these include Bachelor's and Master's theses mentored by the author [66, 72, 92, 108], as well as conference talks [57, 67] and journal articles co-authored by the author [78, 106]. The main focus of this research is the device's compatibility with fish migration (further work currently underway in the laboratory to develop increasingly capable fish behavior models using these simulations), but a secondary objective, of concern in the present work, is the quantification of its hydropower potential.

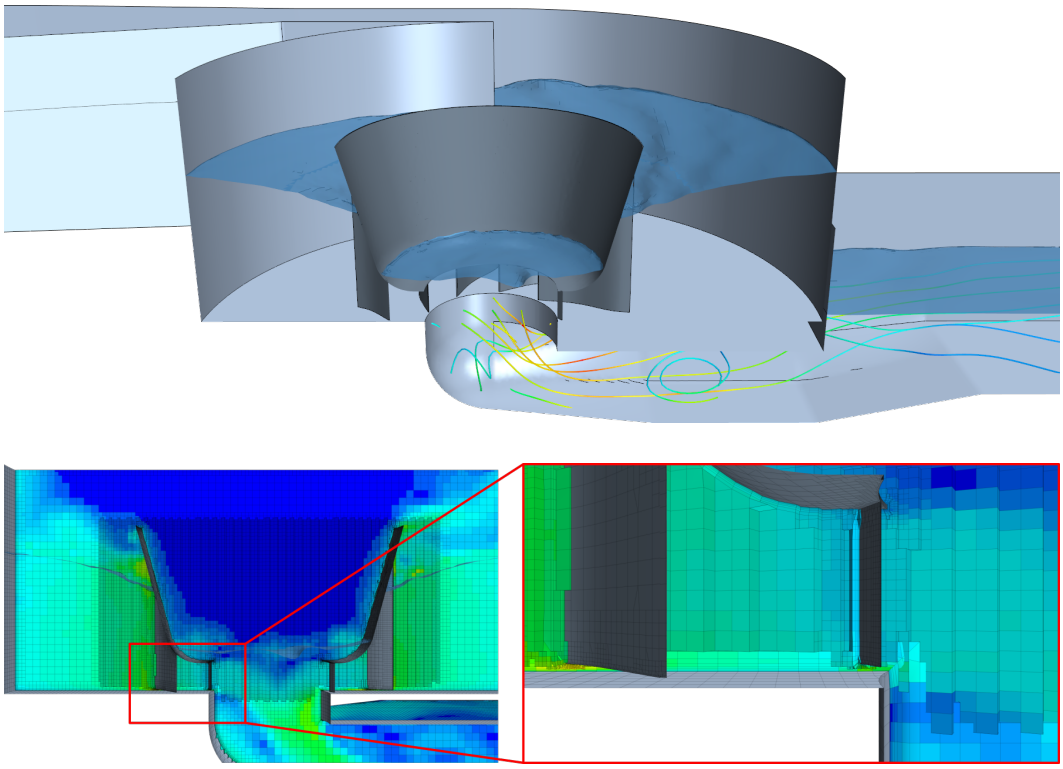

Figure 1.14: Views from complete simulations of the flow in the WVPP. Top: the device has been sectioned longitudinally so as to display the water level and turbine position in the WVPP. A few streamlines colored according to velocity are visible in the outlet of the turbine. Bottom: view of the mesh structure in the turbine basin. The cells are colored according to velocity; local refinement is implemented in areas where high gradients are expected. Full details of this simulation are published in Powalla et al. 2021 [106].

Simulations prepared by Dennis Powalla as part of [106], and run by Sergei Sukhorukov as part of [108]. Figure later published in [109]

A family of numerical fluid flow simulations is now available to reproduce the flow in the WVPP (figure 1.14). These simulations are based on a Reynolds-averaged Navier-Stokes (RANS) approach and have been validated with experimental measurements in the Dresden laboratory. The properties of the simulations are detailed in [78, 106] and are

not discussed here (numerical simulations of comparable flows are extensively described in the following chapter of this thesis); nor are the ethohydraulic properties of the device, which are not of concern for the present work. Instead, the emphasis is here placed on the computational costs involved in running those simulations: obtaining a single reading for the turbine power in [106] uses up 19 000 CPU-hours. The reasons for this high cost are, firstly, that the inherent physics of the flow are challenging to describe numerically (an account of those is given in section 2.2 p. 45 of the next chapter), and secondly, that the simulations must be run for long periods of simulated time (of the order of 45 s) in order to account for the device's long response times, allowing for the volume flows or water levels to stabilize.

It therefore follows that a three-dimensional, two-phase CFD simulation accounting for the plant's complete geometry cannot currently be used to map out the behavior of the WVPP across a large range of volume flows, inlet heights, and outlet heights. Instead, a simpler model is needed in order to evaluate the potential power available to the plant, by which its efficiency can be quantified across many conditions.

1.5.3 Model for the energy budget of a water vortex power plant

Here, the WVPP is analyzed with the lens of the model presented in section 1.4, in order to quantify the available power at various regimes. The underlying hypothesis is that the machine is installed a a bypass to a weir or traditional hydraulic dam, as depicted in figure 1.15; it is assumed the inlet and outlet water heights h_1 and h_2 are unaffected by its operation. The mass flow rate $\dot{m}$ is a priori unknown.

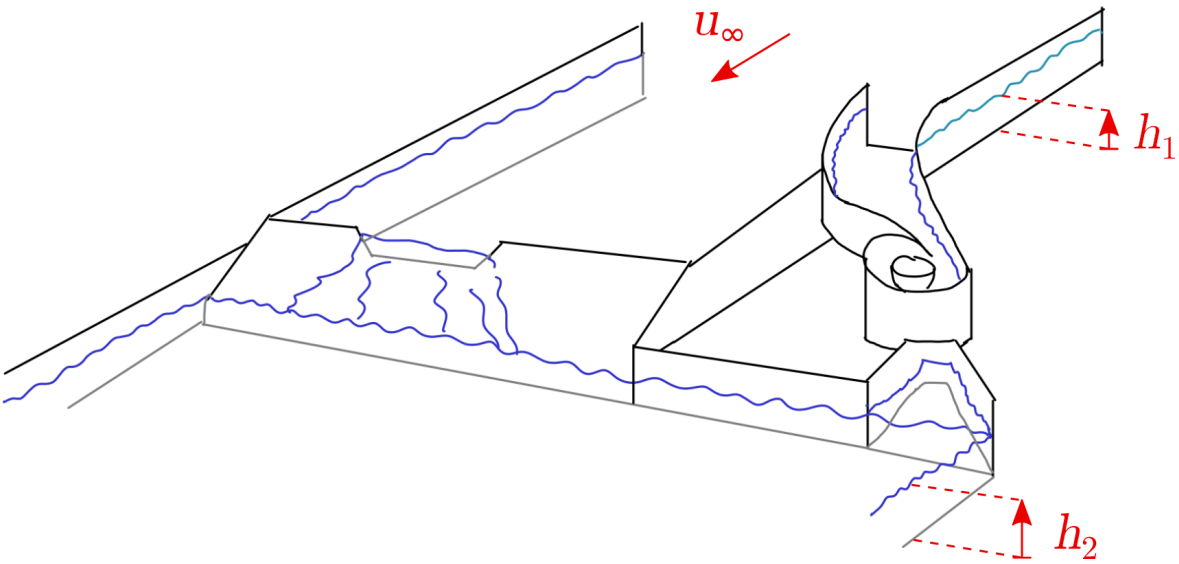

Figure 1.15: Drawing of the WVPP in the type of installation it has been designed for: as the bypass to the main flow of a river. The hypotheses used to quantify its hydraulic power potential are that heights h_1 and h_2 remain independent of its operation. These heights are formally described in figure 1.4 p. 22.

Figure later published in [109]

In order to quantify and non-dimensionalize power, reference values are chosen. The cross-section of the WVPP's inlet is used as a reference area $A_f = L_{\text{width inlet}} h_1$, and a

representative upstream river velocity U_∞ is used as a reference velocity. The turbine power is non-dimensionalized as the power coefficient from definition 1.8, which, together with definitions 1.4 & 1.5, becomes:

$$C_{\mathrm{P\ hydraulic}} = \frac{\dot{W}_{\mathrm{hydraulic}}}{\frac{1}{2}\rho A_\mathrm{f} U_\infty^3} = \frac{1}{\frac{1}{2}\rho A_\mathrm{f} U_\infty^3}\ \eta_{\mathrm{load}}\ \dot{W}_{\mathrm{hydraulic,\ max}} \tag{1.26}$$

$$C_{\mathrm{P\ shaft}} = \frac{\dot{W}_{\mathrm{shaft}}}{\frac{1}{2}\rho A_\mathrm{f} U_\infty^3} = \frac{1}{\frac{1}{2}\rho A_\mathrm{f} U_\infty^3}\ \eta_{\mathrm{hydraulic}}\ \eta_{\mathrm{load}}\ \dot{W}_{\mathrm{hydraulic,\ max}} \tag{1.27}$$

In these equations 1.26 & 1.27, the reference power in the denominator, $\frac{1}{2}\rho A_\mathrm{f} U_\infty^3$, is a partly arbitrary quantity, so that C_P is not expected to reach any value in particular. Nevertheless, for any given inlet boundary condition, higher power coefficient values unambiguously indicate higher power. When h_1 is increased, the reference power grows in proportion, reflecting the device's increased ability to capture mass flow $\dot{m}$ in the inlet. The device's *performance* is quantified separately, using η_{load} and $\eta_{\mathrm{hydraulic}}$.

Now, the hydraulic power available to the device is quantified using eq. 1.24, which is reproduced here:

$$C_{\mathrm{P\ hydraulic}} = \left[4 + \frac{K_{\mathrm{D2}}}{R^2}\right]\left(R\frac{u_\mathrm{A}}{U_\infty}\right)^3 - 4\left(R\frac{u_\mathrm{A}}{U_\infty}\right)^2 - K_{\mathrm{D0}}\left(R\frac{u_\mathrm{A}}{U_\infty}\right) \tag{1.28}$$

In this equation, the two parameters which must be quantified to assess the power potential are K_{D0} and K_{D2} from eqs. 1.21 & 1.20, reproduced here:

$$K_{\mathrm{D0}} \equiv \frac{-\rho g \Delta(z+h)}{\frac{1}{2}\rho U_\infty^2} \tag{1.29}$$

$$K_{\mathrm{D2}} \equiv \frac{-F_{\mathrm{loss}}}{\frac{1}{2}\rho u_\mathrm{A}^2 A_\mathrm{f}} \tag{1.30}$$

The static drop coefficient K_{D0} is already known, since it is determined entirely by the device's installation settings. The loss coefficient K_{D2}, however, is the result of the flow: some reference measurement or numerical simulation is needed in order to estimate its value, and thus predict the device's internal losses during operation.

To this purpose, a CFD simulation is prepared, based on the simulations presented in Powalla et al. 2021 [106]. The full details of the flow are not of interest here; instead, what is needed is only a measure of the device's internal energy losses. The simulation is therefore greatly simplified, as shown in figure 1.16. The global inlet and outlet are set to total pressure boundaries with a static pressure distribution. The modeling of two-phase flow is abandoned, prescribing instead a perfectly flat slip wall for each of the upstream and downstream channel ceilings. The turbine is removed and is replaced with a cylindrical outlet in the upstream channel, and a disc-shaped inlet in the downstream channel. Coupling of mass flow and total pressure between these two surfaces is implemented, with some under-relaxation for increased stability.

The resulting, highly-simplified simulation features 2.6 million cells; after a crude initialization, a stable flow field is obtained after 52 s of simulated time, marching with a time step of 0.02 s. This is obtained at the expense of only 550 CPU-hours, making the computation well within reach of an ordinary desktop computer.

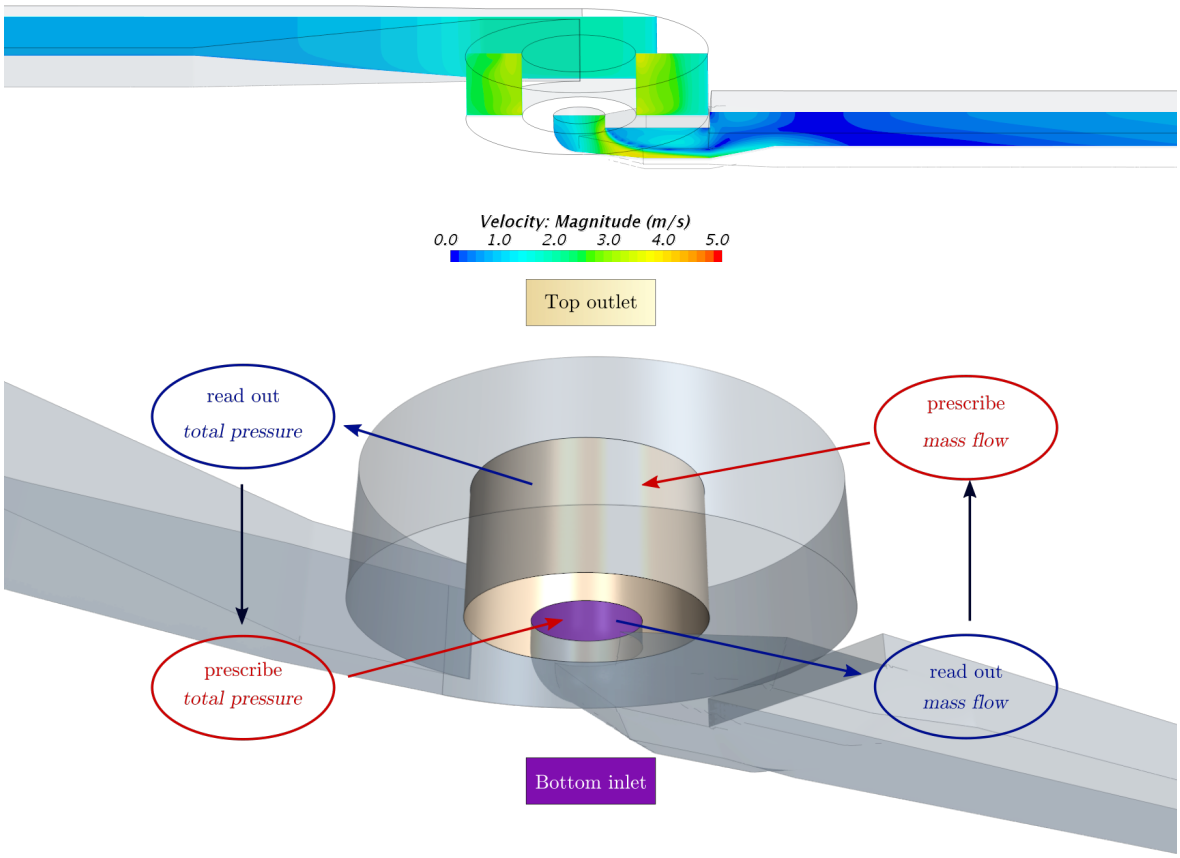

Figure 1.16: Main features of a simplified simulation for the WVPP, based on the family of simulations depicted in figure 1.14, but with much of the sophistication removed: the flow is now water only, and the turbine is no longer present. Top: a cross-section of the weir is shown, with plane sections colored according to velocity. Bottom: coupling mechanism between the upper and lower parts of the weir. Water exits the top part of the weir in the yellow cylinder-shaped "top outlet", a surface with a prescribed mass flow boundary condition. The mass-flow-averaged total pressure is read out from this surface, and in turn, this value is prescribed as a boundary condition for the "bottom inlet" (purple disc in the throat of the device). The resulting mass flow in this "bottom inlet" is read out and serves to prescribe the mass flow in the "top outlet".

Figure later published in [109]

In this simulation, since the flow is unobstructed by the presence of a turbine, the mass flow is governed by the dissipation losses associated with the transit of water through the complete installation. The mass flow $\dot{m}$ is the only output from the simulation required to quantified F_{losses}, the force representative of all such losses in the model, by quantifying the difference between the fluid's momentum at inlet and outlet (eq. 1.13 p. 22). With F_{losses}, the loss coefficient K_{D2} is quantified, and with it, the power curve of the installation can be drawn, quantifying the hydraulic power available to the turbine as a function of the mass flow.

For the case of the WVPP installed in the laboratory in Dresden, the performance is quantified as follows. The machine features $\Delta z{=}{-}0.875\,\text{m}$ and $L_{\text{width inlet}}{=}L_{\text{width outlet}}{=}2\,\text{m}$.

The upstream reference velocity is chosen as $U_\infty{=}1.2\,\text{m}\,\text{s}^{-1}$. In the outlet of the turbine chamber leading to the outlet channel, a cross-section is selected arbitrarily as an actuator surface, with area $A_{\text{A}}{=}0.817\,\text{m}^2$. The choice of that "abstracted turbine" cross-section is a simple matter of convenience and does not affect results. Here, it is expected that this section will likely remain unaffected by modifications of interest in

later studies, such as changes to the turbine basin geometry or to the diameter of the throat.

The operating boundary conditions are chosen as h_1=0.825 m and h_2=0.7 m. These values result in an inlet area A_f=1.65 m^2 and a corresponding actuator-to-inlet area ratio R=0.495. The static drop coefficient is then given, before the simulation is run, as K_{D0}=13.625.

The simulation is run until the flow has stabilized to a satisfactory level. The mass flow then reaches a value of 953 kg s^{-1} (this is the sole output of the simulation).

The effect of all momentum losses in the system is summed up as the single force F_{loss}=−16.09 kN (eq. 1.13 p. 22). In this manner, the loss coefficient (eq. 1.20) is finally obtained as K_{D2}=14.329. Using the mass flow, the relative actuator velocity (adjusted for relative area) is computed as $R\ u_A/U_\infty$=0.481 (the fastest the water can ever flow through the device given these boundary conditions). The available power curve, plotted using the obtained K_{D0} and K_{D2} values, is plotted in figure 1.17.

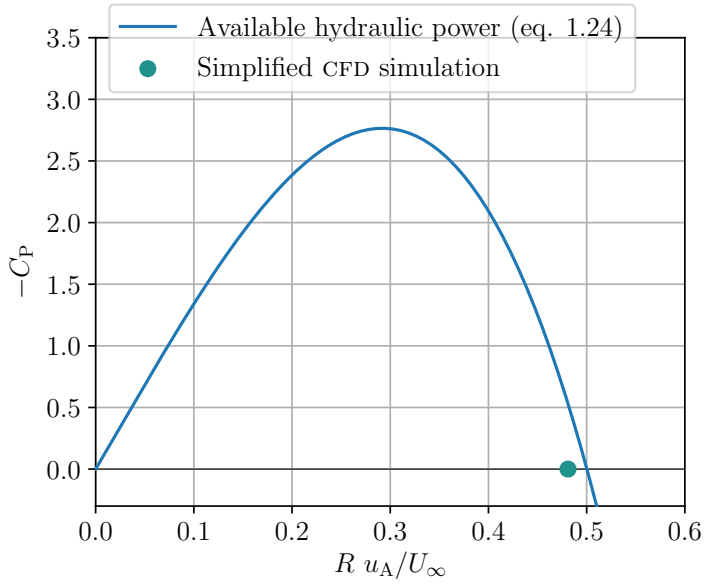

Figure 1.17: Power coefficient of the WVPP when h_1=0.83 m & h_2=0.7 m, as predicted using a single, simplified CFD simulation. The vertical axis is the power coefficient C_P based on the frontal area A_f (eq. 1.26), and the horizontal axis is the adjusted actuator velocity (non-dimensional inlet velocity, directly proportional to the mass flow). A single dot on the zero-y axis stands for the value read out from the simplified CFD simulation, while the power curve is the solution to equation 1.24, calibrated with the K_{D2} value obtained from the simulation.

Figure later published in [109]

In this figure 1.17, a single point is shown for the single simulation used to generate the curve. A discrepancy between that point and the corresponding prediction according to the power curve is observed. This difference is attributed to non-uniformities in the flow (particularly at the outlet), which are neglected in the intentionally simple post-processing of the simulation.
The power curve in figure 1.17 features a maximum of $C_{P\ hydraulic}$=2.76 at an adjusted speed $(R\ u_A/U_\infty)_{opt}$=0.29 (corresponding to $\dot{m}_{C_{P\ hydraulic\ max}}$=574 kg s^{-1}). This information, available before any detail about the turbine is specified, already provides information useful for its design, for example in determining velocity triangles or sizing mechanical components.

In order to check the validity of the model, further simplified simulations are run, in which the coupling between the upper and lower regions of the simulations is modified: each time, only a specified fraction of the total pressure read out in the top outlet is prescribed in the bottom outlet. The mass flow is therefore reduced by the (fictive) force exerted by the actuator. The result of these simulations are displayed in figure 1.18 together with the previously-obtained power curve. Additionally, the turbine shaft power coefficient obtained from a complete, moving-turbine simulation of a corresponding case is displayed as a single, orange-colored point.

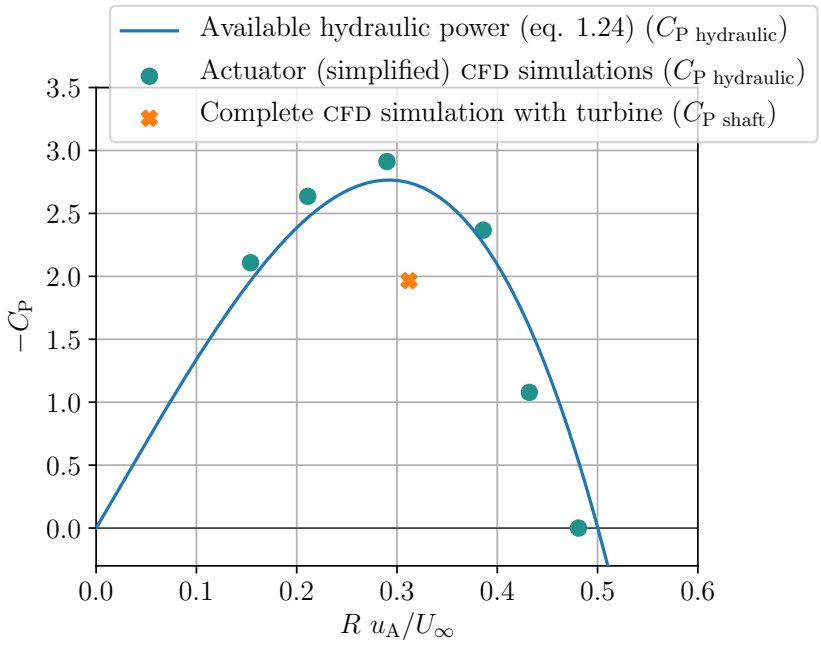

Figure 1.18: Modeled power curve for the WVPP. The right-most data point and the blue curve are these from figure 1.17. The other green points are generated using further simplified simulations from which energy is extracted summarily in the main basin. The orange cross indicates the turbine shaft power coefficient obtained in a complete CFD simulation for conditions very close (h_1=0.85 m, h_2=0.74 m) to those used when plotting the power curve.

Figure later published in [109]

In figure 1.18, the agreement between the values obtained in the actuator simulations and the curve prediction built on a single, unobstructed-flow simulation is, for the purposes of this work, deemed excellent. The curve plotted is not a best-fit model, but indeed the solution of equation 1.24, built on the assumption that the losses internal to the WVPP can be well-described using a single, constant loss coefficient.
In this same figure, the single data point corresponding to a complete simulation (two-phase CFD with rotating turbine) falls well below the curve, at 71 % of $C_{\mathrm{P\ hydraulic\ max}}$. In this case, the product of the load and hydraulic efficiencies, which account together for the not-quite-optimal mass flow, free-surface effects in the device, and dissipation losses within and around the turbine, is $\eta_{\mathrm{load}}\eta_{\mathrm{hydraulic}}$=71 %.

The same model can be used to evaluate performance in different situations. For example, in recent work, a series of four complete simulations of the WVPP were run, with boundary conditions adjusted so that the inlet and outlet heights would be set to respectively h_1=0.64 m and h_2=0.56 m. Each time, the rotation speed ω of the turbine

is varied, and the power of the turbine is extracted. These two properties are presented together in figure 1.19.

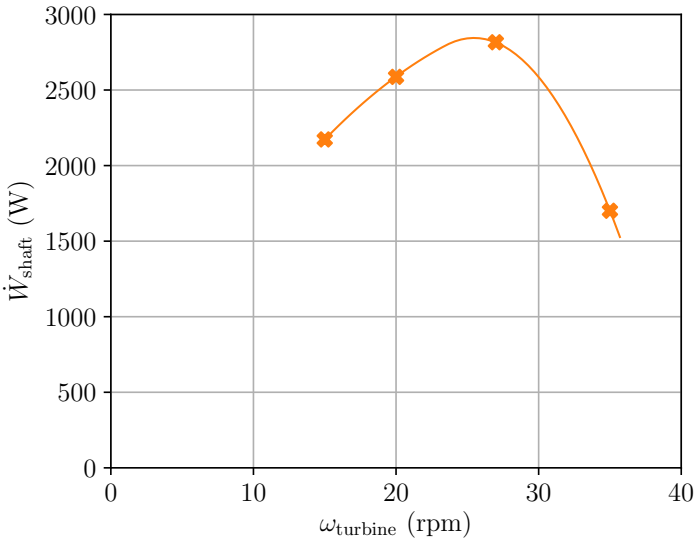

Figure 1.19: Four turbine shaft power readings carried out in full CFD calculations of the WVPP, with h_1=0.64 m and h_2=0.56 m. Both axes are dimensional (power in W and rotation speed in revolutions per minute). In these four simulations, the mass flow decreased steadily as the turbine speed was increased.

Data post-processed from simulations prepared by Dennis Powalla as part of [106], and run by Sergei Sukhorukov as part of [108]. Figure later published in [109]

The model developed in this chapter allows for the non-dimensionalization of these values, and their comparison to a maximum theoretical reference point. For this, a new, simplified (single-phase, turbine-less) simulation is run. The changed inlet height modifies the value of R to 0.641 and the boundary conditions to K_{D0}=13.03. Using the mass flow obtained in the simulation, the loss coefficient is quantified as K_{D2}=16.23. These results make it possible to transform the figure 1.19 above into the two figures 1.20 & 1.21, which present the power coefficient and product of efficiencies for each of the simulations, together with the theoretical limit for these.

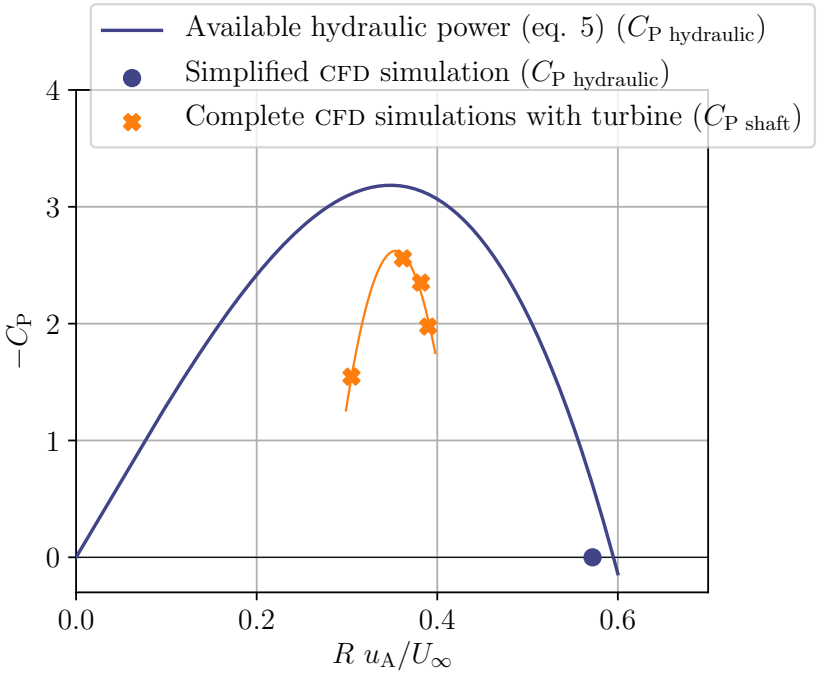

Figure 1.20: The turbine shaft power readings from figure 1.19, this time non-dimensionalized as per the model developed in this chapter (orange crosses). In addition, a single simplified simulation has been run (rightmost circle data point), and the corresponding power curve has been drawn.

Figure later published in [109]

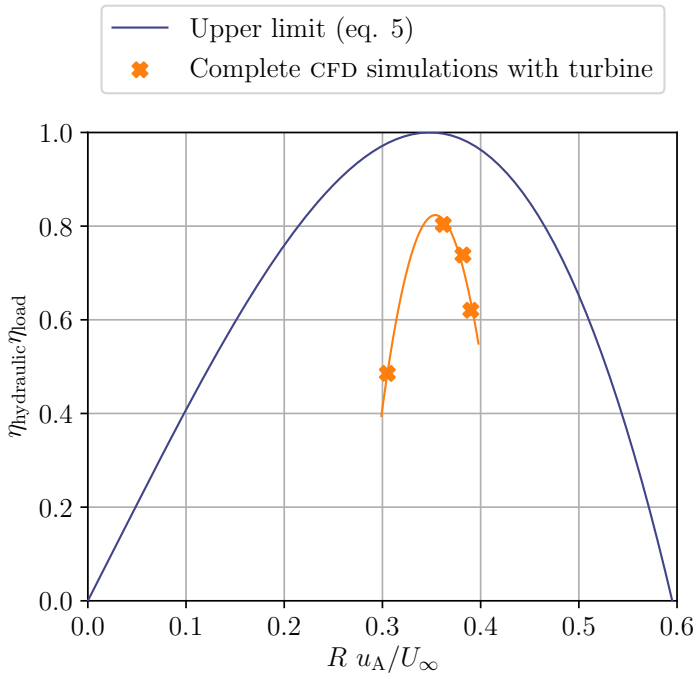

Figure 1.21: The data from figure 1.20, this time presented so that the efficiency of the power extraction (the product of the load efficiency η_{load} and hydraulic efficiency $\eta_{\mathrm{hydraulic}}$) is quantified; the reference power for this is the maximum of the power curve.

Figure later published in [109]

Finally, the model can be used to answer the questions formulated at the start of this section pp. 32-33 in a quantitative manner. The simulations in figure 1.20 were subjected to an inlet height of 0.825 m; what happens if this height is raised to 1.2 m? The answer is obtained by running one additional simplified CFD simulation. Once the property fields are have been initialized with values from the previous case, a converged flow state is obtained after 12 s of simulated time and an expense of 190 CPU-hours. The resulting available power curve is plotted together with that from fig. 1.20 in figure 1.22.

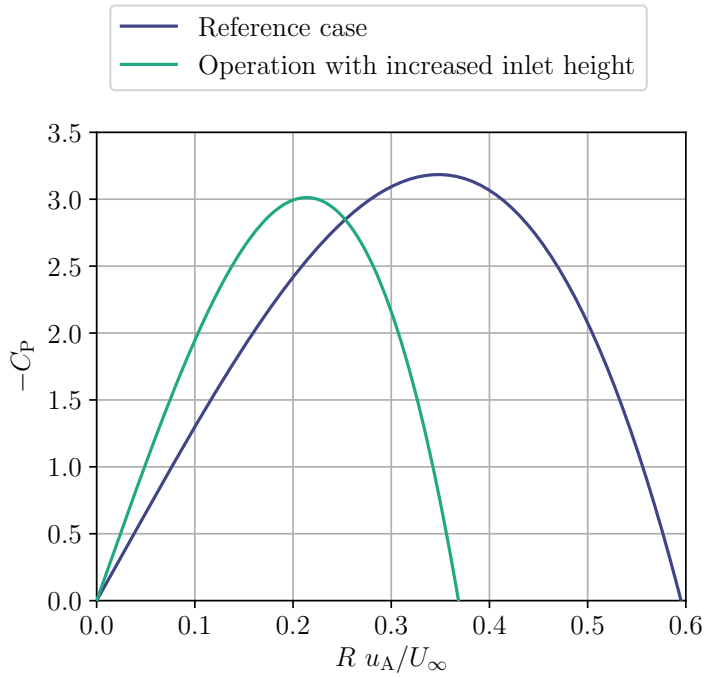

Figure 1.22: Power curves of the WVPP for two cases: the blue curve, already plotted in figure 1.20, is for when h_1=0.825 m; while the green curve is for the same installation when h_1=1.2 m. Each curve is based on a single reading from a simplified CFD simulation.

Figure later published in [109]

Using the information in figure 1.22, the answers are summarized as follows. The inlet height has been increased by 45 %, and the available power has increased almost in proportion (the maximum power coefficient is decreased by only 5 %), by 38 %. In order to have access to this additional power, the turbine must operate so that the inlet velocity is strongly reduced (from $0.35U_\infty$ down to $0.21U_\infty$). A quick re-dimensionalization of these results indicates that the maximum available power $\dot{W}_{\text{hydraulic max}}$ goes from 4.54 to 6.25 kW, while the corresponding mass flow $\dot{m}_{\text{opt}}$ reduces from 571 down to 512 $\text{kg}\,\text{s}^{-1}$; these new values become the reference point by which to quantify the installation's efficiency.

It is therefore seen that the model developed in the first part of this chapter can be used to answer questions that, although simple, have no obvious immediate answer. In this case, increasing the inlet height increases the load on the turbine, but also the internal dissipative losses in the plant; if the inlet velocity were to be kept constant, these losses and the increased momentum abandoned in the outlet (where velocity would increase by virtue of mass conservation) would reduce the power available to the turbine. From the

point of view of the operator, the change in conditions is only desirable if the turbine and generator are able to operate efficiently at a reduced flow rate.

If the power characteristics of the WVPP were of further interest, models better suited to predicting its losses could naturally be developed, using more sophistication. Here, the approach was voluntarily kept as simple as possible, focusing on illustrating the capabilities of a model which was developed to cover a much more general class of devices — including turbomachines such as these described in the upcoming chapters, operating in floating installations.

1.6 Conclusions

This chapter has presented a theoretical analysis of the achievable performance in floating or bypass hydropower installations, a first, essential step towards developing high-efficiency systems.

A one-dimensional model describing the fluid flow through hydraulic devices was presented: a tool able to characterize the performance of machines operated in conditions where the mass flow rate is a control variable and the outlet water height cannot be controlled. This corresponds for instance to a small turbine or water wheel installed in a large river, or to a machine operating in a cascading flow alongside a dam. In the model, the device operating speed required to attain full load efficiency, and the corresponding maximum hydraulic power, can be quantified independently of the hydraulic efficiency.

The model is able to account for the effects (both desirable and undesirable) of ducting, i.e. the use of deflectors to increase the frontal area of devices. When adding a duct to a machine of given frontal area operating at 100 % load efficiency, the model specifies the conditions required to generate an increase in power density.

Usage of the model is demonstrated with the case of a mid-scale hydropower device, a 26 m-long water vortex power plant (WVPP). In order to characterize the installation's power budget, two properties need to be quantified: the static drop coefficient K_{D0}, a function of the boundary conditions only, and the loss coefficient K_{D2}, a measure of the device's hydraulic flow resistance. It is shown that a simplified CFD simulation with a single output (the mass flow rate) is sufficient to obtain a useful value for K_{D2}.

In this manner, the power available to the machine can be quantified given any set of boundary conditions. It becomes possible to evaluate the device's real-life performance, benchmarking it against reference values anchored in physical principles. The model can be used to provide design guidance, and compare sets of boundary conditions one against the other easily, providing answers that are not easily obtained using intuition or even experiments. These results are obtained for a computing cost several orders of magnitude smaller than those associated with a full description of the flow using CFD methods, which also require experimental validation to provide reliable results, as discussed next.

Chapter 2

Computational simulation of a free-stream waterwheel

2.1 Introduction

From this chapter onward, this thesis focuses on the study of one specific kind of hydropower device: the free-stream water wheel, a wheel operated at the surface of a tidal or river flow, on a floating installation.

From an engineering point of view, a water wheel possesses undeniably appealing characteristics: it may be thought as a drag-based turbomachine, similar to a horizontal-axis Savonius turbine, in which the blade return path takes place in a fluid 800 times less dense than water. Nevertheless, closer examination of a typical such machine in operation also reveals striking weaknesses: blade entry and exit from the water bring strong disturbances, the fluid flow within the machine is highly unsteady and to some degree chaotic, and the power delivery features high-amplitude, high-frequency oscillations.

In *breastshot* water wheels, operated with a sizable water height difference between inlet and outlet, the incoming and outgoing flow conditions are well controlled. This type of machine eventually dominated water wheel technology at the start of the 20$^{\text{th}}$ century [2, 4]; recent guidelines and updated theory regarding their design were recently obtained using modern techniques [53, 69].

Free stream water wheels, however, operate in uncontrolled, un-dammed free-surface flows; they represent a puzzling design for which classical techniques in turbomachine theory, such as velocity triangles, do not always help. For example, because of the unconstrained movement of the free surface it is difficult to determine a priori or sometimes even control the fluid velocity at given positions in the vicinity of the rotor, which complicates the search for a blade geometry which would facilitate entry and exit from the water.

The literature concerning *free-stream* water wheels is much sparser than for their breastshot counterparts [81]. Experimental work has already been carried out to quantify the performance of one specific, simple stream wheel as part of the Hylow project [19, 28], but without the search for an optimum design.
Numerical studies have also been published; unfortunately many are missing critical information [30, 34], are not reproducible [38, 93], or even feature inconceivable flow fields [83]. Some studies present simplified models featuring single-phase flow, with the water surface arbitrarily "flattened" as a slip-wall boundary condition [24, 35, 44, 45, 62, 94].

In spite of this, it is clear that computational fluid dynamics (CFD) tools are able to capture the full complexity of hydrokinetic devices operating near the free surface [49, 58, 61]. Reynolds-averaged Navier-Stokes (RANS) models backed by experimental measurements were already used to study Dethridge wheels [59, 60] as well as breastshot wheels [70, 79], perhaps most successfully by Nishi et al. [42, 52, 68, 100, 101].

A potential therefore exists to approach the problem of free-stream waterwheel design with numerical tools, enabling a systematic exploration of the effect of design parameters on their performance.

The aim of this chapter is to describe a method by which the performance of free-stream water wheels can be not only evaluated as a whole, but also understood in terms of the fluid mechanics occurring at the blade level. For this, a series of 30 CFD simulations will

be carried out, showing how the influence of selected design parameters and operating conditions can be characterized. The methods described here will later be used to optimize and describe broad design guidelines for this type of machine.

Sections 2.4 and 2.5 of this chapter were published in a peer-reviewed journal article (reference [73]): O. Cleynen, E. Kerikous, S. Hoerner, and D. Thévenin. "Characterization of the performance of a free-stream water wheel using computational fluid dynamics". In: *Energy* 165 (2018), pp. 1392–1400. DOI: 10.1016/j.energy.2018.10.003

2.2 Numerical models for simulation of hydrokinetic power devices

2.2.1 Fluid flow physics

The physics of the fluid flow through low-impact hydropower devices, and in particular hydrokinetic devices, have the following main properties:

Turbulent River flow, which serves as incoming flow for such machines, is always turbulent ($[\mathrm{Re}]_{\text{river width}} \approx 10^8$). Yokosi (1967, [5]), shows that the Kolmogorov power laws apply well to river flow, with length scales covering 100 m down to 1 mm in the horizontal plane (20 m to 1 mm in the vertical plane), based on measurements in a 100 m-wide river.

The flow patterns in such machines is also turbulent, at the very least in their wakes. Water wheel blades with 0.5 m depth are likely to generate large-scale vortices at $[\mathrm{Re}]_{\text{blade depth}}=5 \cdot 10^5$, which will dissipate down to structures less than 0.1 mm in size.

Low energy density Water flowing in a typical river possesses low amounts of specific kinetic energy ($e_k \approx 2\,\mathrm{J\,kg^{-1}}$); rivers in plains feature low gradients (on the order of 0.3 %). Those make for feeble energy conversion potentials, and make low-impact hydropower devices particularly sensitive to dissipation losses.

Two-phase Describing water flow near the surface involves predicting movement of both water and atmospheric air, even if only the flow of water (being 800 times more dense) is of practical importance for the operation of the machine. The atmosphere above the river essentially acts as a flexible isopressure boundary condition for the water, the position of which varies in time.
The degree of freedom brought by the air-water interface translates into the possibility for surface wave propagation. This propagation features very little dissipation; however, it can affect the spatial distribution of available hydraulic energy as a function of time. It may also interact with the dynamics of the machine (e.g. synchronizing with characteristic frequencies, as observed later in sec. 4.2.3 p. 90).

Given the size of the devices of interest here, the influence of surface tension is insignificant; compressibility effects are likewise negligible.

Unsteady The movement of a rotor obviously translates into some form of unsteady boundary condition for the flow. The movement of the free surface, especially when affected by the entry and exit of solid blades, also translates into significant unsteadiness.

Large-scale Hydrokinetic devices operated in a free stream affect river flow in a spatial domain many times larger than themselves (with the water diverting its path upstream, to the sides and below the device, as resistance is added to the flow through the machine). Correctly predicting performance for such machines requires reproducing boundary conditions adequately, in order not to create artificially high blockage ratios. Correspondingly, settling times in the order of several seconds at least are required for the flow to develop, before proper analysis can be conducted.

2.2.2 Main numerical models

In this work, CFD simulations of free-stream water wheels are carried out. The resources of the laboratory for fluid dynamics of the University of Magdeburg, where this research is carried out, include access to the industrial simulation software package Star-CCM+ by Siemens, and to a share of a high-performance computing cluster (106 TFLOPS).

In the scope of this work, a tentative objective was that a three-dimensional simulation run on ∼100 cores complete with a computing time in the order of one week. With this in mind, and with consideration of the physics of the problem described above, a series of choices is made for models with which to simulate the flow, presented below.

The velocity field $\vec{V}$ at some point in time is calculated incrementally, with its change over each timestep computed by solving a discretized form of a momentum balance equation, while respecting the constraint of a mass balance equation. The momentum equation here is the incompressible version of the Reynolds-averaged Navier-Stokes (RANS) equation,

$$\rho \frac{\mathrm{D}\vec{V}}{\mathrm{D}t} = \rho\vec{g} - \vec{\nabla}p + (\mu + \mu_T)\vec{\nabla}^2\vec{V} \tag{2.1}$$

where μ_T is the turbulent (or eddy) viscosity, which lumps together all the effects of turbulence (fluid movement in time and spatial scales too small to be captured by the simulation) as one local dissipative, viscous-like effect. The distribution of μ_T is calculated indirectly using two turbulence models, which solve for k, the turbulent specific kinetic energy (in $\mathrm{J\,kg^{-1}}$), and either ϵ, the turbulent dissipation rate (in $\mathrm{J\,kg^{-1}\,s^{-1}}$) , or ω, the specific turbulent dissipation rate ($\omega \equiv \epsilon/k$, in $\mathrm{s^{-1}}$).

The equations for these three variables take a form similar to the Navier-Stokes equations: an advective term is equated to other terms (here all terms are generically named T) whose values are calculated according to local flow properties, with the help of partly-arbitrary constants calibrated with experiments. The k-ϵ model, summarized in 1972 by Jones and Launder [6], and well presented by Leschziner [56], solves for two scalar equations in the form of:

$$\frac{\mathrm{D}k}{\mathrm{D}t} = T_{\text{mean diffusion}} + T_{\text{turbulent diffusion}} + T_{\text{generation}} - \epsilon \tag{2.2}$$

$$\frac{\mathrm{D}\epsilon}{\mathrm{D}t} = T_{\text{generation by mean strain}} + T_{\text{generation by turbulent straining}} + T_{\text{diffusive transport}} + T_{\text{destruction}} \tag{2.3}$$

In turn, the k-ω model, formulated by Wilcox in 1988 [10] and again well presented in Leschziner [56], solves for eq. 2.2 as well as an equation for ω with two partly-arbitrary constants C in the form of:

$$\frac{\mathrm{D}\omega}{\mathrm{D}t} = C_1\ \omega + C_2\ \omega^2 + T_{\text{mean diffusion}} + T_{\text{turbulent diffusion}} \tag{2.4}$$

From both k, and either ϵ or ω, the turbulent viscosity is then recovered by these models with the help of a partly-arbitrary constant C_μ as:

$$\mu_T = \rho\ C_\mu \frac{k^2}{\epsilon} = \rho\ C_\mu \frac{k}{\omega} \tag{2.5}$$

In all simulations presented in this thesis, use is made of the SST model (formulated by Menter in 1994 [11] and again well presented by Leschziner [56]), which blends both turbulence models. The k-ω model is used near walls up to $y^+ \approx 70$, and the k-ϵ model is used beyond that. Both models are blended with a weighted function; some limiters are applied, and wall functions are used where wall meshing is too coarse to resolve wall gradients. This approach has progressively become the state-of-the-art standard for engineering simulations with the scale and purpose of these in this work, and indeed, has been used with success to describe turbulent flows near free surfaces in machines similar to these studied in this chapter [49, 61]. The adequacy of the models, and of the default values for the constants that were used throughout this thesis, are from here on no longer discussed.

In principle, two interacting fluids (water and air) are flowing through the domain of interest and so two sets of equations could be solved simultaneously for the entire domain. However, liquid water is 800 times denser than atmospheric air, and the two fluids do not mix significantly in the applications of interest here. Therefore, a *single* set of flow equations is solved for both fluids, using the volume-of-fluid method (VOF, formulated in 1976 by Noh & Woodward [7] and 1981 by Hirt & Nichols [9]). In this method, in each cell, the share of volume occupied by water is quantified with a fraction O_{water} (ranging from 0 to 1), and used as a weight function to quantify the density and viscosity used in eqs. 2.1-2.4:

$$\rho = O_{\text{water}}\rho_{\text{water}} + (1 - O_{\text{water}})\rho_{\text{air}} \tag{2.6}$$

$$\mu = O_{\text{water}}\mu_{\text{water}} + (1 - O_{\text{water}})\mu_{\text{air}} \tag{2.7}$$

In turn, the volume fraction of water is simply convected through the domain in a conservative manner:

$$\frac{\mathrm{D}O_{\text{water}}}{\mathrm{D}t} = 0 \tag{2.8}$$

Using this model greatly reduces the required computational cost. It has the disadvantage that in cells where a mix of air and water is present, only the dynamics of an "average" fluid are computed. This is not only formally incorrect; it also prevents the description of surface waves, drops and bubbles at a scale smaller or equal to the local cell size. To mitigate those effects, the mesh is refined near the interface (cf. upcoming paragraphs).

To summarize, in the main flow field, six main coupled, non-linear equations are solved for every time step: the three components of the RANS (eq. 2.1), a mass conservation equation ($\vec{\nabla} \cdot \vec{V} = 0$), and two turbulence property equations (two among eqs. 2.2-2.4). In addition, the VOF equation (2.8), the blending function of the SST model, wall models, as well as accessory linking equations (e.g. eqs. 2.5-2.7), are solved, at a comparatively lower cost. The details of the numerical implementation, such as discretization schemes, coupling techniques, and multigrid approaches, are not described here.

2.2.3 Spatial discretization

A final important set of choices in the numerical tools concerns meshing. Given the physics described above in section 2.2.1, in particular the range of length scales to be covered, a coarse structured mesh is used for the faraway field, with local refinements near the interface and in the regions of interest (e.g. near the blade tips and along the surface of the blades).

The rotation of the rotor brings in additional challenges. Since a re-meshing of the complete field for each time step would be prohibitively expensive, some form of mesh rotation (together with the rotor) relative to a static background is required. One approach is to use a direct interface, in which the faces of cells at the edges of two disjointed meshes communicate with one another; nevertheless, this could not be implemented reliably in Star-CCM+ 11.04 and 12.02. Instead, the overset method is used in all simulations presented here. In this method, the rotating mesh is superimposed on a background mesh, and several rows of cells on the edges of each overlap one another; the software solves flow equations for both groups, and interpolates between them.

In the simulations presented in this thesis, some of the most important considerations regarding the implementation of the mesh movement are as follows:

- Some information loss due to interpolation occurs continuously in the overlap zone, and across time steps in cells where the flow motion does not align with the mesh motion. These losses increase with mesh size.
- Since the rotating mesh crosses the horizon plane, it carries with its rotation the locally-refined areas surrounding the air-water interface. This calls for regular re-meshing; a time-intensive process (in Star-CCM+ 12.02, the meshing is a largely serial process) which again results in losses of information through interpolation.
- In order to avoid numerical divergence, the edge layers of each mesh, across which exchange of information takes place during the flow equation solving, must have sizes with same order of magnitude. At the same time, to reduce computational costs, a finer mesh is desirable in the water than in the air (where not only the fluid movement is of little interest, but the velocities are also typically higher).

The combination of these factors leads to numerical divergence issues in areas where finer cells are moved together with the rotor over coarse background cells.

- Another requirement to avoid numerical divergence is to maintain low cell-to-cell velocities (in other words, to maintain low cell Courant numbers). This tends to favor small time steps and large overlap cell sizes in cases where the tip speed ratio, the free stream velocity or the radius of the wheel are relatively large.

- In simulations which are limited by the number of cells, such as three-dimensional simulations, an interesting technique is to only model wheel blades in the lower rotor region, where they interact with water. To achieve this, the mesh is reset in its original position at time intervals equal to the time interval separating the passing of two blades. In turn, this means the blade-passing time interval must correspond to an integer number of solver time steps — and so the choice of a time step is again affected.

Most of these considerations translate into contradicting requirements, with various compromises to be made as the radius, depth, tip-speed ratio and free-stream velocity of simulations is varied: trial and error is used to determine practical combinations of mesh size distribution and time steps. The regular re-meshing of simulations according to flow field properties, and resetting of mesh positions when needed, is implemented during the simulation runs through Java macros (Java being the language in which the Star-CCM+ graphical user interface is written).

2.3 Three-dimensional CFD model of a water wheel

The first numerical simulation of a free-stream water wheel undertaken in this work investigates the performance of a wheel whose geometry was proposed by the company Sibau Genthin GmbH, a partner in the research project *Fluss-Strom* which funded part of this work. The wheel has twelve blades, a diameter of 2.4 m, a width of 3.5 m, and a depth of 0.5 m. The design is intended for electrical production, installed on an anchored, floating twin-hull structure.

As a first exploratory investigation, the rotor of the wheel is modeled in Star-CCM+. It is placed at the center of a large (30 m long, 3.7 m deep) domain, as shown in figure 2.1. The hulls of the floating installation are not simulated. Because the wheel is positioned perfectly perpendicular to the incoming flow, the flow is expected to be largely symmetrical. For this reason, only one half of the domain is simulated, with a symmetry plane set-up across the rotation axis, in the middle of the rotor.

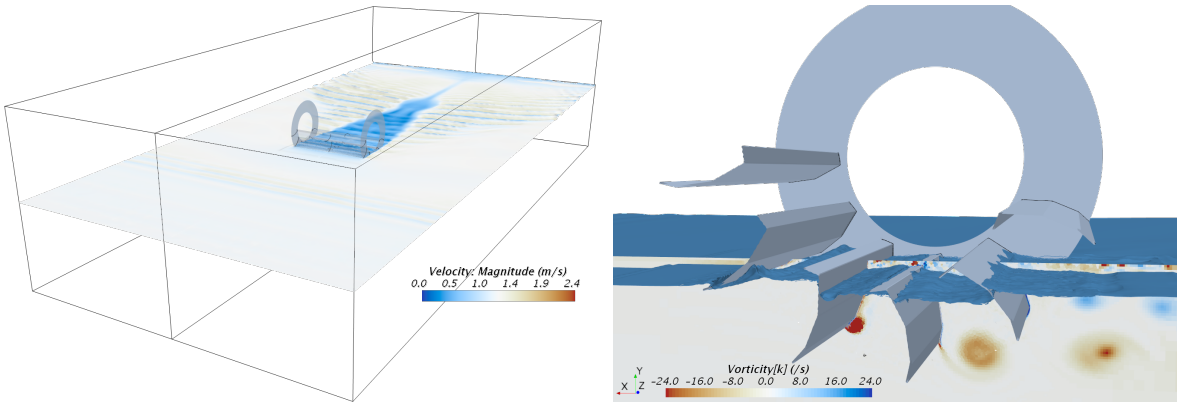

Figure 2.1: Left: the complete simulated flow domain (with flow from the foreground to the background). The flow field has been mirrored along the symmetry plane which is setup across the center of the axis of the wheel, so that the flow is only solved for one half of the domain showed here. The water surface is colored according to velocity, with the color scale centered around the inlet velocity, U_∞=1.2 m s^{-1} (white color).
Right: close-up view of the flow field in the wheel, with flow from left to right. Only the right half of the wheel (the half of the domain for which the flow is solved) is shown. Under the water surface, on an x-y plane longitudinal with the flow, magnitude of the vorticity in the z-direction (along the axis of the wheel) is shown.

The simulation is configured according to the considerations listed in sections 2.2.2 & 2.2.3 above. A structured mesh is used as a stationary background, on top of which a rotating cylindrical mesh containing the wheel is rotated. Figures 2.2 & 2.3 display the mesh structure in longitudinal and cross-flow planes. The "overset" technique implemented in Star-CCM+ activates the cells of one mesh or the other, depending on location; it automatically defines an overlap region in which information exchange occurs. The meshes are refined near the water-air interface, near the blades' tips (where high velocity gradients are expected), in the water immediately surrounding the rotor, and all along the mesh overlap region (where uniform mesh sizes are required for numerical stability). Regular re-meshing of the rotating mesh is implemented, ensuring that highly-refined regions (conducive to high computational costs) are not carried out of the water with the movement of the rotor. In order to reduce the total number of cells in the simulation, only six of the rotor's twelve blades are modeled; every time the rotor has completed 30° of rotation (the angle separating any two blades), the rotor is reset back into its original position. Ultimately, the number of cells attained 4.2 million.

As per the considerations listed in section 2.2.2 above, an unsteady, incompressible, implicit segregated RANS solver was used, with Volume-of-Fluid (VOF) and k-ω-SST solvers. The discretization was first-order in time, and the time step (selected so that 30° of mesh rotation would be covered by an integer number of time steps) was $1.7 \cdot 10^{-3}$ s. Boundary conditions were set to mass flow inlet & outlet, slip walls along the domain floor, side wall and ceiling, and a symmetry plane midway across the wheel's axis. The simulation, run on the high-performance cluster *Neumann* of the University of Magdeburg, progressed at a cost of 2 800 CPU-hours per simulated second. The power curve stabilized after 11 s at a value of 5.3 kW (for the complete wheel), corresponding to a wet-area power coefficient (def. 1.8) of 0.34.

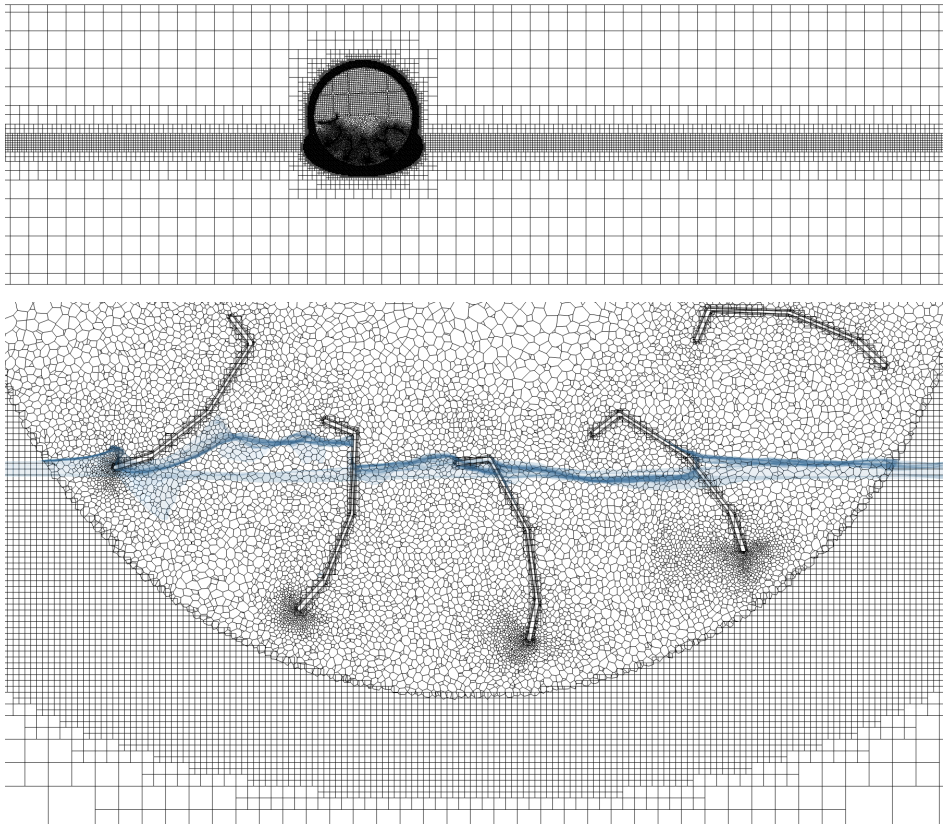

Figure 2.2: The mesh structure of the three-dimensional simulation in the longitudinal plane.
Top: longitudinal cross-section along the complete, 30 m-long domain, showing the different levels of refinement applied near the free surface, in sections where high gradients are expected, and in the area of overlap between the static and rotating meshes.
Bottom: close-up view of the longitudinal section through mesh, near the blades of the wheel. Close to the blades, the size of the cells is approximately 6 mm; at the periphery of the rotating mesh, cells are approximately 16 mm wide. In addition, prism layers of cells are applied to the surface of the blades. The water surface in between the plane and the viewer is represented with a light semi-transparent surface.

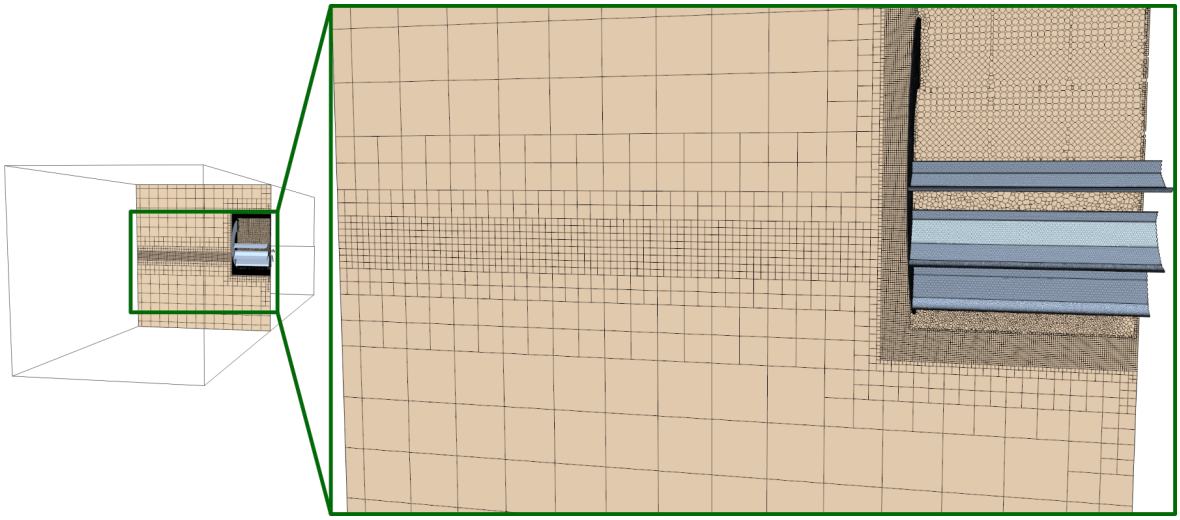

Figure 2.3: A plane section through the mesh, in a plane perpendicular to the main flow direction and passing through the axis of the wheel. Visible are the refinement areas near the free surface, near the blades, and in the overlap region between the static and the rotating meshes.

Because of this extremely high computational cost (obtaining a single reading for power with this setup involves approximately three weeks of waiting and computing time on the Neumann cluster), it is clear that this approach, based on a three-dimensional description of the flow in a full-scale machine, is unsuited to the systematic study of parameters that is needed to characterize, for the first time, the performance of free-stream water wheels. For this reason, and because the mechanism of power production in such machines is predominantly two-dimensional, most of the numerical work carried out on this thesis is henceforth built on 2D simulations, which involve computational resources that are several orders of magnitude smaller. Once a characterization of power (in section 2.4) and a full optimization (in sections 4.2 & 4.3) will have been carried out in 2D, three-dimensional effects will be chiefly studied again in section 4.5 p. 123.

2.4 Two-dimensional CFD model of a water wheel

The two-dimensional simulation setup that constitutes the basis for much of the numerical results obtained in this thesis made of a longitudinal plane through the three-dimensional simulation presented above.

From here on, the mesh consisted of a trimmed, 35 m-long 115k-cell static part, and a 35k-cell rotating component. In an effort to reproduce free-stream conditions despite the limitations of two-dimensional flow, the water depth was set to 12.5 m, so that the blockage brought by the wheel (diameter 2.4 m) never exceeded 4 % of the water inlet cross-sectional area. Boundary conditions were set to velocity inlet (with steady inlet water height), mass flow outlet, and slip-wall at the channel bed floor. In order to reduce the Courant number and kinematic instabilities within the air phase, and after verifying that this in no way affected the wheel power nor the behavior of the water phase, the viscosity of the air was arbitrarily increased by a factor 10 (this restriction could later be abandoned in simulations presented in the following chapters). All other settings were carried over from the three-dimensional simulations. A view of the flow in such a simulation, centered on the region near the wheel, is presented in figure 2.4. Observation of the flow shows that separation occurs immediately at the tip of the blades, with a shear layer appearing in the wake of the wheel. The vortical patterns shed periodically by the wheel are clearly revealed by displaying the vorticity field in figure 2.4.

In order to assess mesh size dependence, the mesh density of a single simulation was increased by a factor 1.33, 1.67 and 2.22 relative to the reference case; this work was performed by Rohit Patil under mentorship of the author. The time-averaged shaft power over one cycle —the main parameter of interest in this study— was observed to vary by respectively $-3\,\%$, $-2.2\,\%$, and $-0.1\,\%$ relative to the case with the coarsest mesh. The grid convergence index of the coarsest mesh with 95 % confidence interval, calculated according Richardson Extrapolation methodology described by Roache [12], was 5 %; this coarsest mesh resolution was used for the rest of the study. The time step ($1.1 \cdot 10^{-3}$ s on average) was adjusted to allow an integer number of steps per blade period, and small enough to prevent divergence at the interface between meshes; its influence over the results was not further investigated.

Java macros (an interface standard to the Star-CCM+ software) were used to configure and control the 30 different simulations investigated in this chapter, and re-mesh them

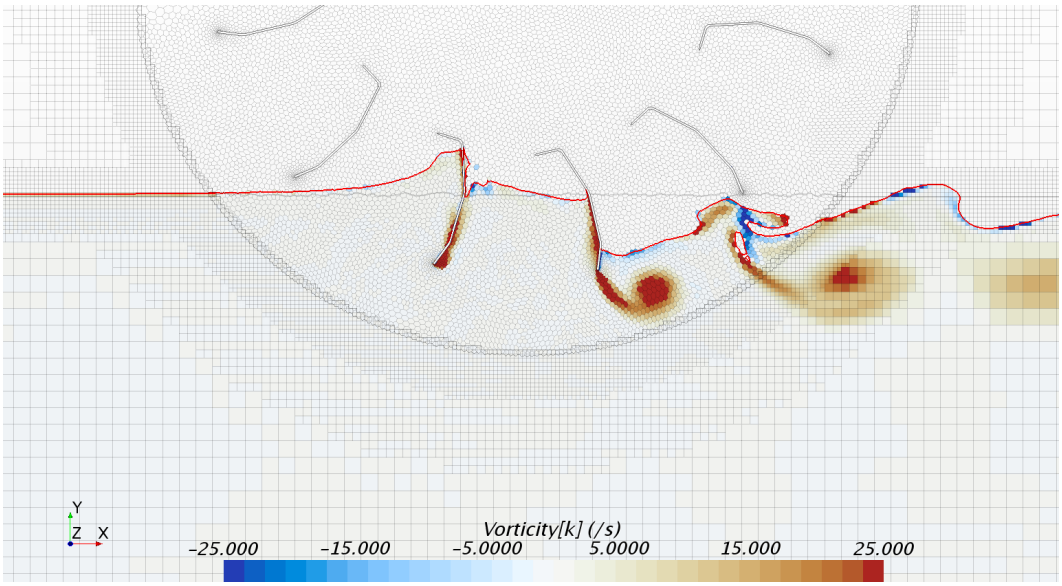

Figure 2.4: Vorticity field in the water phase of the simulated water wheel, for n_b=12, λ=0.6, U_∞=2 m s^{-1}, f_{wet}=0.25. The interface between two fluids is represented by a red isoline of 0.9 volume fraction of water, and shows air entrainment below the departing blade. The magnitude of vorticity in the field (in the direction across the 2D plane) is shown as a scalar field, with blue and red indicating clockwise and anticlockwise rotation respectively (the color scale is saturated at $\pm$25 s^{-1}). The mesh structure is displayed in the background. A video of this unsteady simulation is provided as supplementary material to reference [73].

Figure previously published in [73]

at appropriate intervals. The main output of each simulation –the power developed by each blade as a function of time– was exported automatically and post-processed with Python scripts. With two CPU cores of an ordinary desktop computer attributed to each simulation, the progress rate reached approximately 5 s per week.

In spite of the low blockage effect, the very large fluid volume, and the subcritical ($[Fr]_\infty$=0.2) inflow, the altitude of the water surface was in every case observed to rise slowly during the simulation throughout the entire domain, at a rate increasing with the wheel shaft power. As a result, the water wheel immersion depth was not a fully-controlled input. The output of the simulations thus had to be extracted late enough that enough blades had passed through the water to provide a realistic operating environment, but early enough that the water level rise was still insignificant. In practice it was determined that analyzing data along the full stroke of the third to fifth blades to enter the water was the compromise which yielded the most realistic results. In work that followed the publication of the present results in [73], ultimately leading to running thousands of further simulations (as detailed later in chapter 4), this problem was completely solved by prescribing velocity rather than mass flow in the simulation outlet boundary.

2.5 Performance analysis of the two-dimensional free-stream water wheel

2.5.1 Parameters for quantifying water wheel performance

The most important performance characteristic of a water wheel is obviously its power output, typically non-dimensionalized as the power coefficient C_{P} (eq. 1.8 p. 19).

In maximizing power, two competing objectives may be pursued. One may attempt to maximize wet-area performance, i.e. power per unit area exposed to water. This may lead towards wheels with very large diameters and numerous blades that are only lightly immersed in the water, translating into very low power densities. Conversely, one may attempt to maximize power per unit area *of the rotor*, thus obtaining compact machines featuring lower power-specific production costs, perhaps at the cost of decreased wet-area performance. The two metrics of interest are therefore:

- Wet-area performance. This is measured using the wet-area (or simply "wet") power coefficient, in which S is the area exposed to water (immersed depth times rotor width):

$$S \equiv S_{\mathrm{wet}} = L_{\mathrm{wet}}\ L_{\mathrm{width}} \tag{2.9}$$

$$C_{\mathrm{P\ wet}} \equiv \frac{\dot{W}}{\frac{1}{2}\rho S_{\mathrm{wet}} U_\infty^3} \tag{2.10}$$

$$C_{\mathrm{P\ shaft,\ wet}} \equiv \frac{\dot{W}_{\mathrm{shaft}}}{\frac{1}{2}\rho S_{\mathrm{wet}} U_\infty^3} \tag{2.11}$$

  In zero-height-drop installations, as considered here, the upper limit to $C_{\mathrm{P\ wet}}$ is 16/27, the Betz limit (other cases are studied extensively in chapter 1 and are henceforth no longer discussed);

- Rotor-area performance. This is measured using the rotor-area (or simply "rotor") power coefficient, in which S is the projected frontal area of the rotor (rotor diameter times rotor width):

$$S \equiv S_{\mathrm{rotor}} = 2\ R\ L_{\mathrm{width}} \tag{2.12}$$

$$C_{\mathrm{P\ rotor}} \equiv \frac{\dot{W}}{\frac{1}{2}\rho S_{\mathrm{rotor}} U_\infty^3} \tag{2.13}$$

$$C_{\mathrm{P\ shaft,\ rotor}} \equiv \frac{\dot{W}_{\mathrm{shaft}}}{\frac{1}{2}\rho S_{\mathrm{rotor}} U_\infty^3} \tag{2.14}$$

  The upper limit to $C_{\mathrm{P\ rotor}}$ in zero-drop cases is $2(L_{\mathrm{wet}}/R)(16/27)$.

In chapter 1, energy transfers had been measured from the point of view of the fluid, resulting in negative power coefficient values when power was extracted. From hereon, since the focus is on the design of only one kind of machine, the sign convention is inverted, with positive $\dot{W}$ and C_{P} values indicating power production by the machine (the desirable outcome, as per common language conventions).

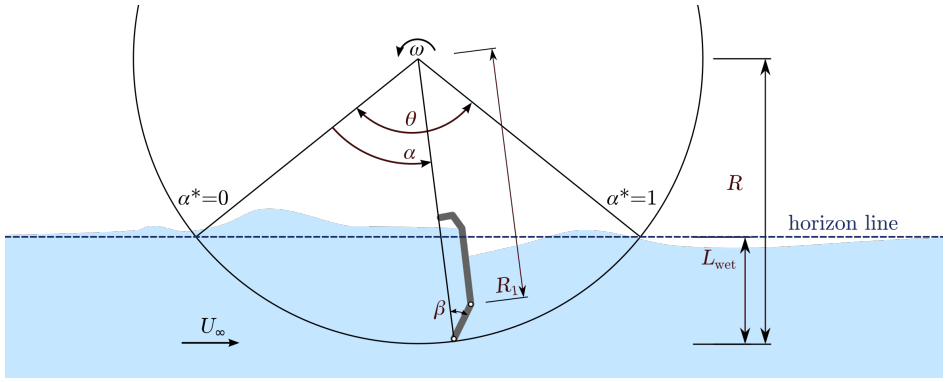

Figure 2.5: Nomenclature for basic dimensions used in the paper. The position and stroke angles α and θ, as well as the immersion depth L_{wet}, are measured relative to the horizon line, independently of the local water surface height.

Figure previously published in [73]

The rotation velocity ω is non-dimensionalized as the classical *tip-speed ratio*:

$$\lambda \equiv \omega R / U_\infty \tag{2.15}$$

where ω is the rotor rotational speed ($\mathrm{rad\,s^{-1}}$).

The blade geometry is characterized as shown in figure 2.5. Three values for the blade tip angle β are considered; the pivot point for this angle is positioned at $R_1 = 0.9R$ for this entire study. Other aspects of the blade geometry are not further considered.

The maximum immersion depth at which the wheel enters the water relative to the free-stream water height, named L_{wet}, can be non-dimensionalized as the *wet radius fraction* f_{wet}:

$$f_{\text{wet}} \equiv \frac{L_{\text{wet}}}{R} \tag{2.16}$$

The wet radius fraction, in turn, influences the length of the power stroke (the path along which a blade may deliver power to the shaft). This parameter can be described using the *stroke angle* θ, measured in the reference case where the water surface remains entirely undisturbed by the wheel (as $U_\infty \to 0$). From geometry (see figure 2.5), one rapidly obtains:

$$\theta \equiv 2\cos^{-1}(1 - f_{\text{wet}}) \tag{2.17}$$

Using this angle, the position of a blade tip within the stroke path can be tracked with the *non-dimensional stroke angle* $\alpha^\star$:

$$\alpha^\star \equiv \frac{\alpha}{\theta} \tag{2.18}$$

The specific flow characteristics, such as upstream water build-up or turbulent wake, will in practice cause the blade to leave and enter the water at different positions; nevertheless, the points at which $\alpha^\star$=0 and $\alpha^\star$=1 always correspond to landmark positions regardless of the duration and path length associated to the blade power stroke.

The *single-blade wet power coefficient* is here written C_{Pb}; when averaged over several blades it is noted with a tilde: $\tilde{C}_{\mathrm{Pb}}$.

Finally, it is proposed that the number of blades n_{b} be parametrized as the *equivalent blade number* n_{e}, which represents the average number of blades which dip below the horizon at any given time:

$$n_{\mathrm{e}} \equiv \frac{n_{\mathrm{b}}\ \theta}{2\pi} \tag{2.19}$$

Using these parameters, the power developed by any free-stream water wheel can be deconstructed in terms of the contribution of a single blade as it sweeps through the stroke angle, and non-dimensionalized for critical comparison. A single curve displaying $n_{\mathrm{e}}\tilde{C}_{\mathrm{Pb}}$ as a function of $\alpha^\star$ is then enough to represent not only the power dynamics at the blade level, but also the net power produced by the entire wheel. The time-averaged wheel power coefficient, noted with a bar as $\overline{C}_{\mathrm{P\ rotor\ wet}}$, is then recovered as the net area below the curve:

$$\overline{C}_{\mathrm{P\ rotor,\ wet}} = \int_0^{2\pi} n_{\mathrm{b}}\ \tilde{C}_{\mathrm{Pb}}\ \frac{1}{2\pi}\,\mathrm{d}\theta \tag{2.20}$$

$$= \int_0^{\frac{2\pi}{\theta}} n_{\mathrm{e}}\ \tilde{C}_{\mathrm{Pb}}\ \mathrm{d}\alpha^\star \tag{2.21}$$

2.5.2 Results and analysis

Procedure

The effect of four main parameters was investigated across a series of 30 simulations: the immersion depth, the free-stream velocity, the blade tip angle, and the number of blades of the wheel.

From each of the simulations, the power curves of the third to fifth blades to enter the water were extracted, synchronized (overlaid) and averaged out, as shown in figure 2.6. The resulting blade-averaged power curve was then filtered with a low-pass 30 Hz filter in order to suppress non-meaningful artifacts resulting from the averaging, such as multiple peaks appearing instead of a single one. The averaged curve obtained in this manner, non-dimensionalized in a $n_{\mathrm{e}}\tilde{C}_{\mathrm{Pb}}$ vs. $\alpha^\star$ graph, is produced systematically for analysis in the later sections.

Furthermore, for each case, this blade-averaged power curve was repeated several times at a time interval corresponding to the time $\Delta t_\delta \equiv 2\pi/\omega n_{\mathrm{b}}$ separating two blades. The sum of all these repeated curves (a net power curve with characteristic period Δt_δ) was used as the basis signal for computing the time-averaged net power and the amplitude of its oscillations.

The idealized net power curve reconstructed in this manner features slight differences when compared to the net power curve extracted directly from the simulation, as shown in figure 2.6 (compare top and bottom). However, it features a unique frequency –unlike the original signal–, so that the power developed over one period can be extracted reproducibly across all simulations for systematic comparison. After the issues with boundary conditions were solved in later work (the results of which are presented in

chapter 4), this procedure was no longer needed, and the wheel power output was considered directly.

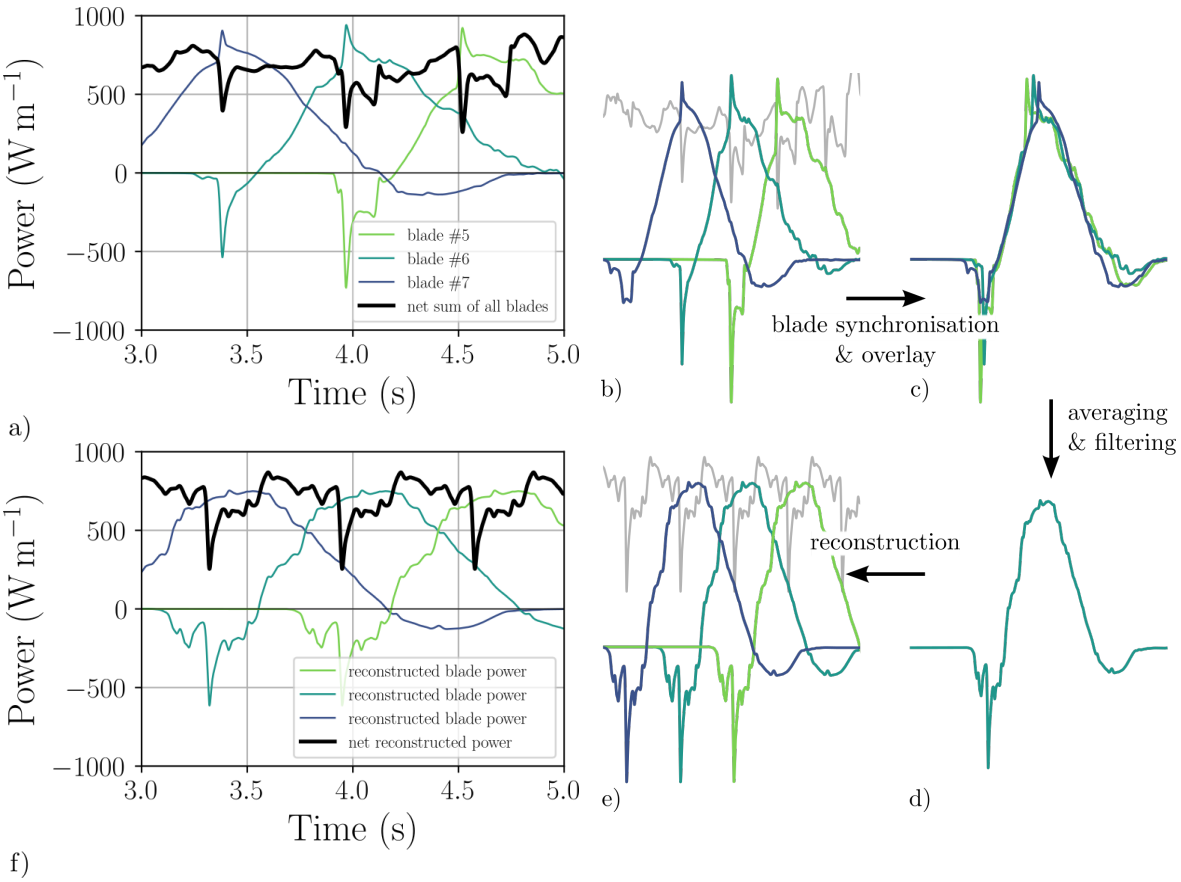

Figure 2.6: Power curves are extracted directly from the simulation (a and b). These curves are synchronized (c) and averaged-out (d). A final equivalent power curve is finally obtained by repeating this blade-averaged power curve with a determined frequency (e and f). Data shown here corresponds to a case configured with $\lambda = 0.5$, $f_{\text{wet}} = 0.33$, $U_\infty = 2\,\text{m}\,\text{s}^{-1}$ and $n_\text{b} = 12$. Since the simulations are two-dimensional, the power values are per unit width. After resolving the dissatisfactory behavior of the outlet boundary conditions in later work, the results of which are presented in chapter 4, this method was no longer necessary.

Figure previously published in [73]

Immersion depth

The power characteristics of the simulated wheel were first monitored for three different immersion depths, at f_{wet} =0.17, 0.25 and 0.33. For each depth, a simulation was run for each of three tip speed ratios, the values of which (λ=0.5, 0.6 and 0.65) favor relatively high rotation speeds, a generally positive characteristic for electrical power generation.

The time-averaged power characteristics are plotted in figure 2.7. It is readily observed that greater immersion depths lead to higher power outputs; however, the power increase is not proportional to the increase in the wet area ($\overline{C_{\text{P wet}}}$ ultimately decreases). Also, an increase in the amplitude of the power oscillations is observed.

An analysis at the blade level, with the help of figure 2.8, provides insights as to the mechanisms underlying these trends. Generally, blade power curves display a negative

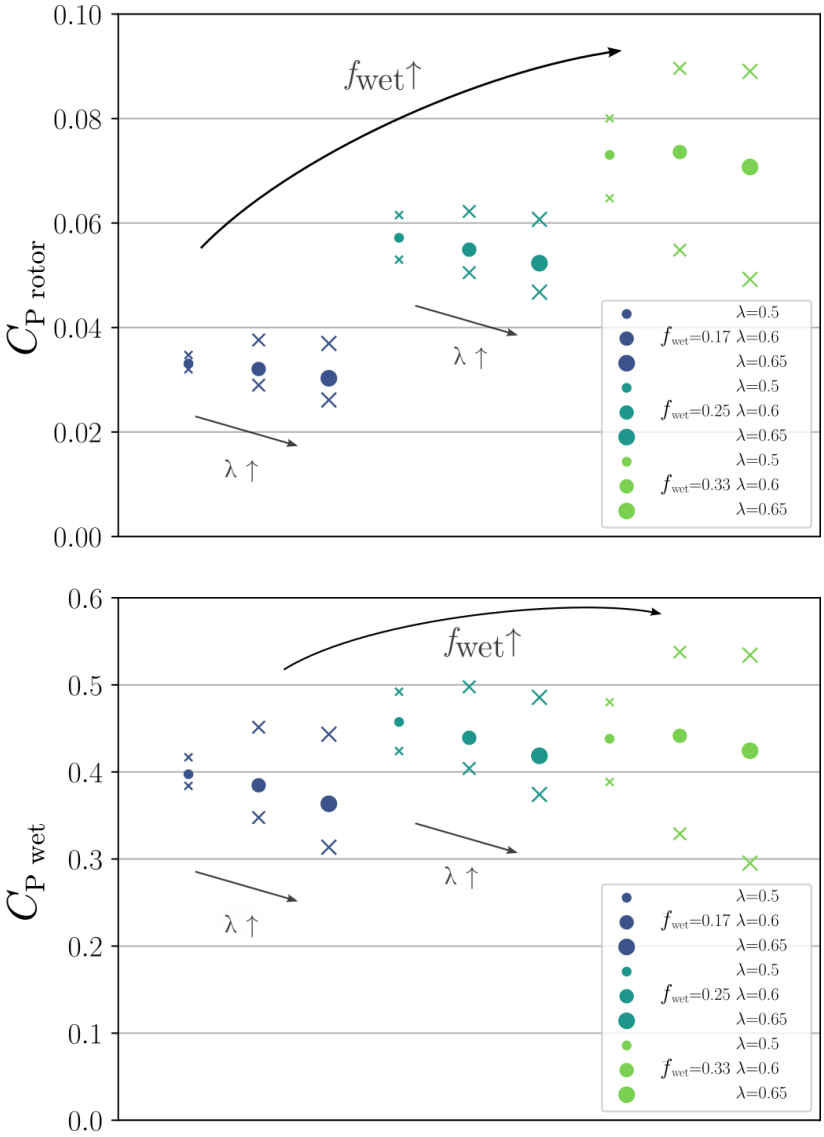

Figure 2.7: Time-averaged rotor-area power coefficient (top) and time-averaged wet-area power coefficient (bottom) for each of the nine cases, all running with 12 blades, U_∞=2 m s^{-1}. Round points stand for the time-averaged power coefficient developed, while the crosses indicate the mean deviation of the instantaneous power during the power cycle, above and below of the average.

Figure previously published in [73]

power peak in the vicinity of $\alpha^\star$=0 which is from here on termed *entry splash*, a positive contribution in the first two thirds of the power stroke, and a negative power phase in the final stage of the stroke, in which momentum is transferred from the blade to the water. Within the range of parameters explored here, when an increase in the immersion depth or a decrease in the tip speed ratio occur, it can be observed that:

- the entry splash is stronger and occurs earlier in the power stroke —even before the blade tip crosses the horizon line, which is the symptom of water building up ahead of the wheel;
- the power-producing phase has larger amplitude, occurs earlier in the stroke, and is more unsteady;
- as f_{wet} reaches 0.33, a negative power phase occurs in the last quarter of the stroke.

These traits are the symptoms of a change in the environment in which the blades are operating: within the range of parameters studied here, a deeper, slower wheel globally results in a higher water build-up immediately upstream of the wheel, and a higher dynamic pressure in the first third of the stroke.

Free-stream velocity

The second parameter of interest was the free-stream velocity: for each of three different incoming flow velocities (U_∞=2 m s^{-1}, 2.5 m s^{-1} and 3 m s^{-1}), a simulation was run at each of the same three tip speed ratios (λ=0.5, 0.6 and 0.65).

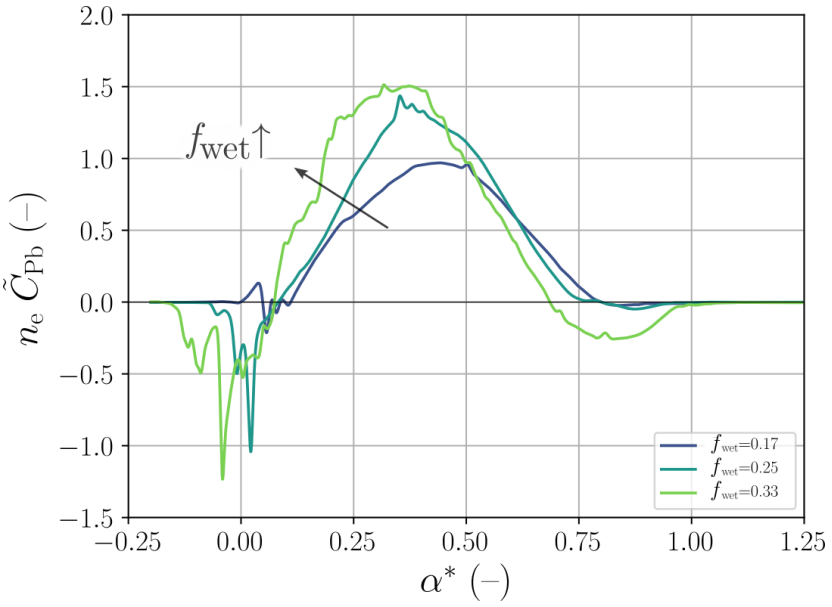

Figure 2.8: Blade power coefficient as a function of the non-dimensional stroke angle $\alpha^\star$, for three different depths. The three cases shown here were configured with λ=0.5, n_b=12 and U_∞=2 m s^{-1}. It is worth noting again that the reference $\alpha^\star$=0 is measured relative to the faraway horizon: water build-up immediately upstream of the wheel can be seen when the power curve starts at negative values of $\alpha^\star$.

Figure previously published in [73]

The time-averaged power output characteristics are presented in figure 2.9. The shaft power increases with the free-stream velocity; however the increase is not proportional to the increase in the cube of the velocity ($C_{\mathrm{P\ wet}}$ steadily decreases). The amplitude of the oscillations in the power curves also increases sharply.

At the blade level (figure 2.10), the increase in free-stream velocity results in two trends similar to these observed above when the immersion depth was increased:

- the entry splash is stronger and occurs earlier in the stroke;
- the power phase has greater amplitude, occurs earlier, and is more unsteady.

Additionally, it is noted that at high tip speed ratios, negative power occurs beyond $\alpha^\star$=1 (after the blade tip has risen above the horizon). Overall, those effects are the symptoms of the following trend observed within the range of parameters studied here: for a given tip speed ratio, as the incoming velocity is increased, the drop in the water surface altitude which takes place in between blades occurs both faster (in time) and sooner (within the stroke path).

Blade tip angle

Three different blade geometries were compared across experiments, varying the tip angle β from $-20°$ (the default angle on all other experiments) to $0°$ (straight, flat blades) and ultimately $+20°$ (as if the wheel had been flipped around). Since the intended objective was to reduce entry splash effects at high rotation velocities, for each value of β, a simulation was run at each of two tip speed ratios (λ=0.6 and 0.65).

The time-averaged power curves (figure 2.11) show an immediate, unmistakable detrimental effect of these geometrical modifications on the power coefficient compared to the baseline case, β=$-20°$.

At the blade level (figure 2.12) it can be observed that the increase in the tip angle results in:

- a shorter and much weaker entry splash;
- a noticeable drop in power during the main stroke, and especially,
- a pronounced negative power phase in the late part of stroke extending well beyond $\alpha^\star$=1 (the point at which the blade tip rises above the horizon line).

This last characteristic, which becomes more pronounced as the tip speed ratio is increased, allows for the visualization and the quantification of the energy cost of the pick-up of water by the departing blade. It is seen that with this particular set-up, this cost largely exceeds the benefit brought by the smoother entry into the water.

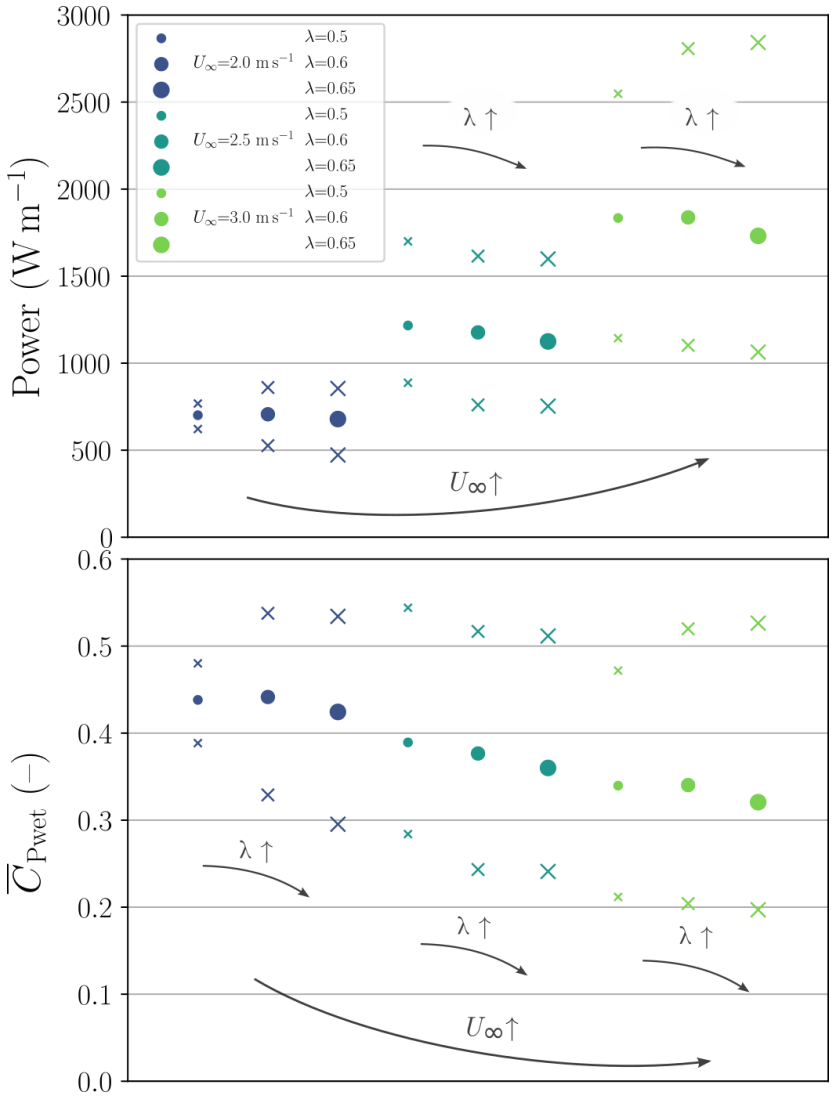

Figure 2.9: Power (time-averaged and per unit width) and time-averaged wet power coefficient for nine cases running at different rotation speeds and incoming velocities, all configured with n_{b}=12 and f_{wet}=0.33. Round points stand for the time-averaged power coefficient developed, while the crosses indicate the mean deviation of the instantaneous power during the power cycle, above and below of the average.

Figure previously published in [73]

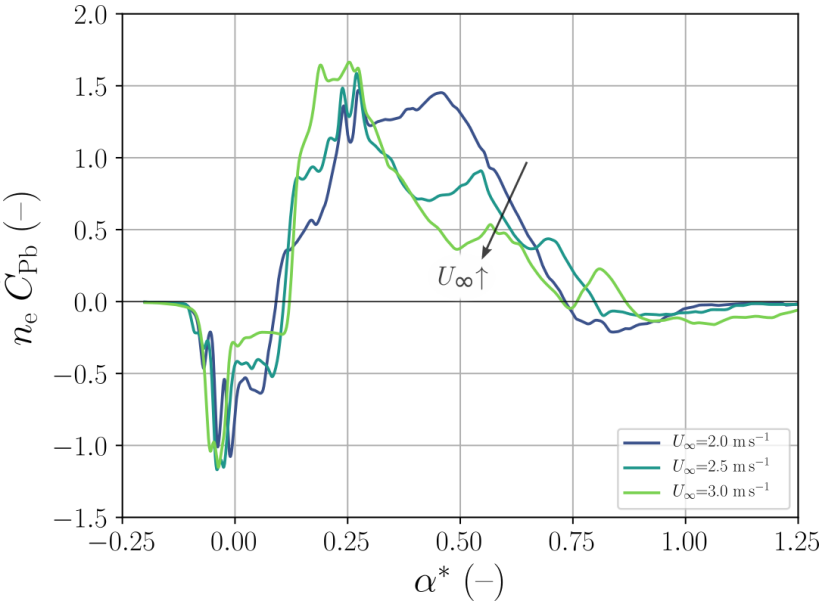

Figure 2.10: Blade power coefficient curves for three free-stream velocities. The three cases shown here were configured with λ=0.6, n_b=12 and f_{wet}=0.33.

Figure previously published in [73]

Number of blades

The final set of simulations focused on the effect of the number of blades. Four wheels with n_b=6, 8, 10, and 12 respectively were simulated in identical flow conditions. For each wheel, simulations were run at three different immersion depths (again, f_{wet}=0.17, 0.25 and 0.33).

The time-averaged power outputs for this experiment are gathered in figure 2.13. It can be seen that at low depth, an increase in number of blades leads to a smoother, higher power delivery. Nevertheless, this effect becomes lower as depth is increased, and ultimately, it reverses.

A precise description of the involved phenomenon can be found at the blade level. As n_b is increased, the power contributed by each blade is uniformly decreased over the entire stroke (figure 2.14a). At low depth, this decrease is more than compensated by the increase in the number of blades (figure 2.14b). However, an optimum is reached that depends on the depth. With too many neighbors, the blade power begins to feature a negative power phase in the late part of the stroke (figure 2.15a). Ultimately, the increase in n_e is unable to compensate the decrease in the average value of $\tilde{C}_{Pb}$ (figure 2.15b) and the net wet power coefficient decreases. An interesting side phenomenon observed here is that the strength of the entry splash always increases with n_e, for all the depths investigated in this experiment.

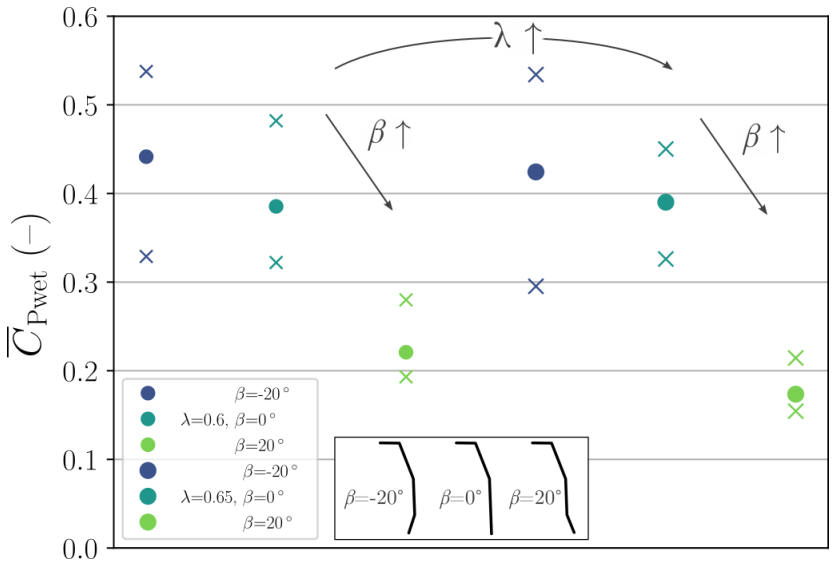

Figure 2.11: Time-averaged wet power coefficient for three values of blade tip angle β, each run for two values of tip speed ratio λ. All cases were configured with n_{b}=12 and f_{wet}=0.33 at U_{∞}=2 m s^{-1}. Round points stand for the time-averaged power coefficient developed, while the crosses indicate the mean deviation of the instantaneous power during the power cycle, above and below of the average.

Figure previously published in [73]

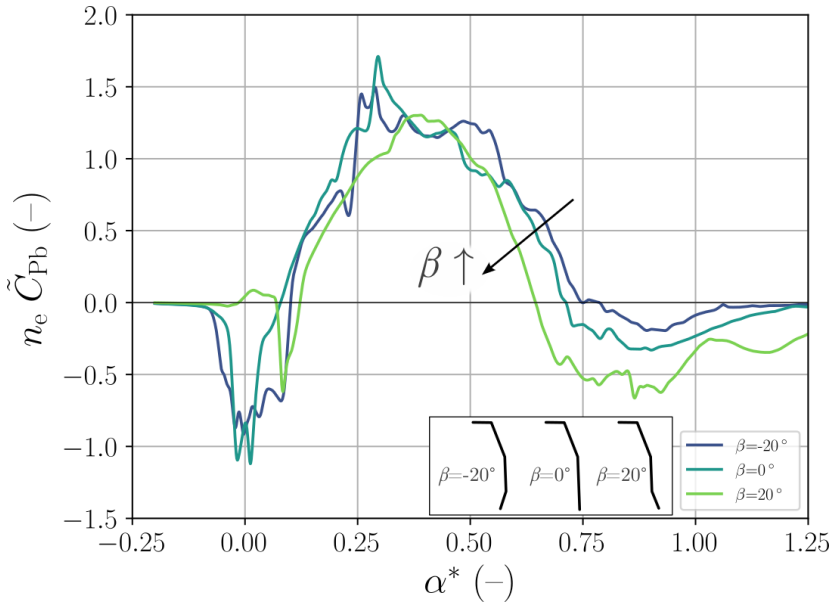

Figure 2.12: Blade power coefficient curves for three values of the tip angle β. All cases were configured with n_{b}=12, f_{wet}=0.33, U_{∞}=2 m s^{-1} and λ=0.65.

Figure previously published in [73]

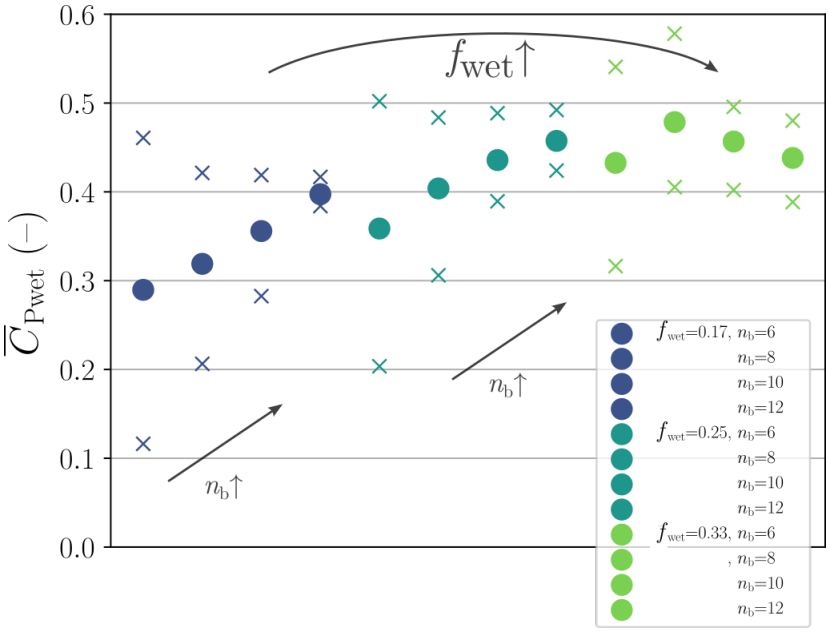

Figure 2.13: Time-averaged wet power coefficient for increasing number of blades at three different depths. All cases displayed were configured at U_∞=2 m s^{-1} and λ=0.5.

Figure previously published in [73]

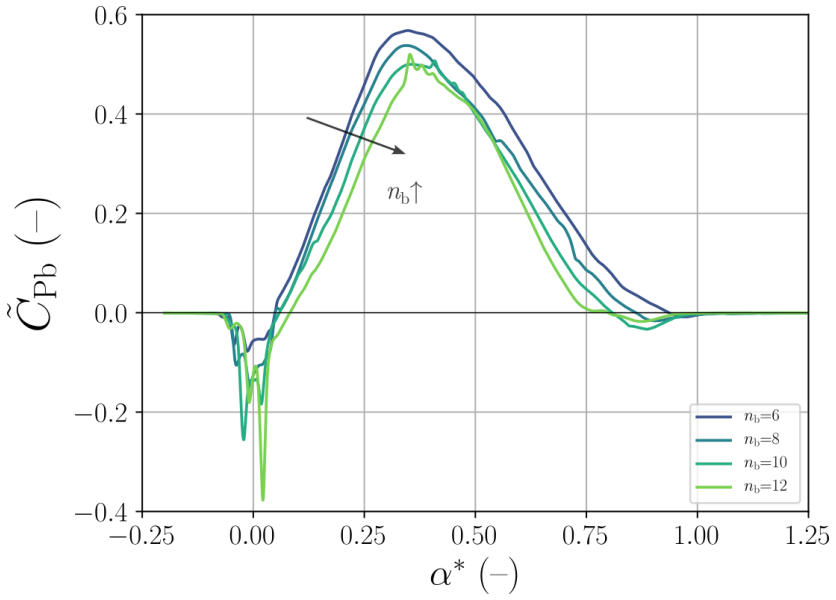

(a)

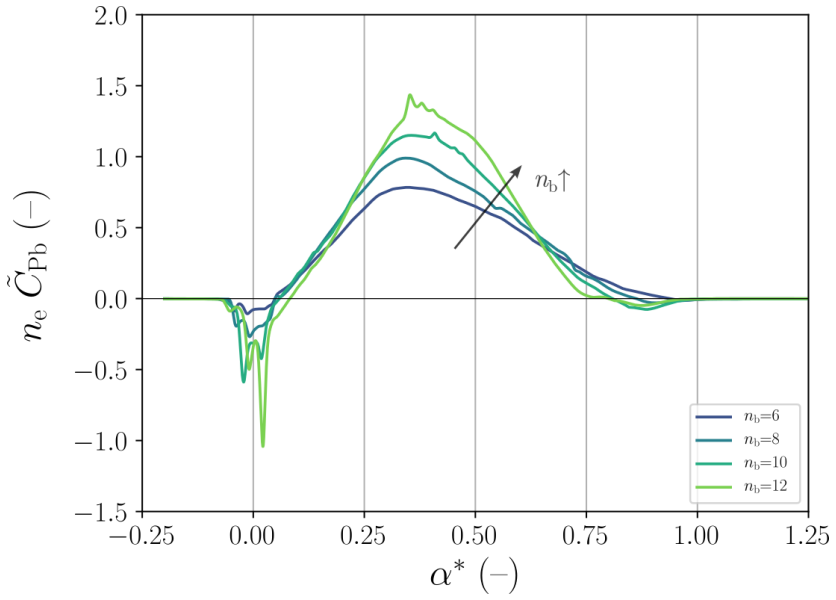

(b)

Figure 2.14: Blade power coefficient curves for increasing number of blades n_{b}, for constant wet radius f_{wet}=0.25. All cases displayed were configured with U_∞=2 m s^{-1} and λ=0.5.

Figure previously published in [73]

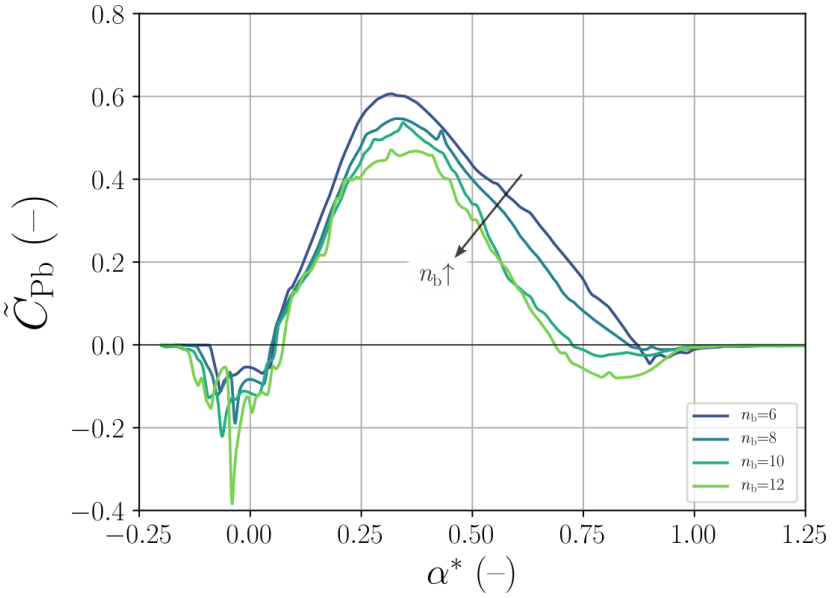

(a)

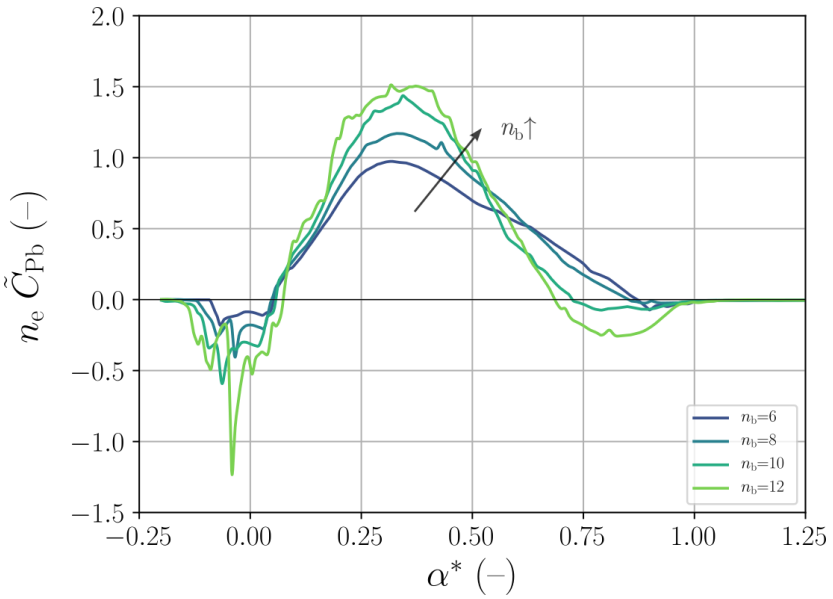

(b)

Figure 2.15: Blade power coefficient curves for increasing number of blades n_{b}, for constant wet radius f_{wet}=0.33. All cases displayed were configured with U_∞=2 m s^{-1} and λ=0.5. The reduced interaction between blades and smoother water flow between blades that are spaced further apart (for low values of n_{b}) translates as smoother curves on both graphs.

Figure previously published in [73]

2.6 Conclusions

This second chapter has provided insights on the challenges and opportunities associated with the numerical description of fluid flow in free-stream water wheels.

An account was first given of the complexity of the fluid flow physics, their modeling in CFD simulations, and of the need for relatively large simulation domains. These explain why three-dimensional simulations, at the time of writing of this thesis, constitute high-investment endeavors that remain too computationally expensive to carry out parametric studies.

Consequently, this systematic study —the first in literature, to the knowledge of the author— of the power characteristics of the free-stream water wheel was carried out using two-dimensional simulations. In these, the decomposition of the net power output of a free-stream water wheel in terms of the contribution of individual blades allows for an improved understanding of the dynamics of the machine. In particular, the parametrized $n_e\tilde{C}_{Pb}$ vs. $\alpha^\star$ curves are a useful tool for the analysis of the key mechanisms occurring at the blade level, and their systematic comparison across operating conditions. With this method, it is possible to pick up the effect on the blade mechanics of phenomena such as:

- blade entry splash and departure water pickup;
- shift in both entry splash and power stroke due to water build-up;
- interference between blades as a function of stroke distance.

With this tool, within the range of parameters studied in this chapter, the following phenomena could be identified, quantified, and better explained:

- deeper wheels, slower wheels, and wheels operating in faster flows feature higher power delivery (higher $C_{P\ rotor}$), at the cost of decreased efficiency (lower $C_{P\ wet}$) and higher oscillations in power delivery;
- increased depth and decreased tip speed ratios result in water build-up immediately upstream of the wheel, with generally detrimental effects on the power output;
- the energetic cost of water pickup by the departing blade largely exceeds the benefit of a smoother entry into the water brought by tilting the blade tip in the direction of rotation;
- an increased number of blades results in higher, smoother power delivery, up until interference effects reverse the trend.

The methodology detailed here constitutes an excellent basis for carrying out an optimization, using automated toolchains to manipulate well-parametrized simulations. After experimental validation of simulations is carried out in chapter 3, two such optimization studies will be presented in chapter 4.

Chapter 3

Experimental validation of simulations

3.1 Introduction

As with any research involving CFD simulations, a need exists to assess results obtained numerically against experimental measurements; this process should ideally involve the very same physical phenomena as in the original simulations.

In the literature, two experimental studies have been reported in conference proceedings on a free-stream water wheel, with focus on the geometry of its ducting apparatus [27, 28]. Further reports on similar experiments lack information about blockage ratio or ducting geometry [19, 36, 46], while numerous additional studies (e.g. [40, 55, 98]) are reported which lack even more essential information, making them wholly irreproducible. A need therefore exists for an experimental data set by which to assess the validity of the simulations presented in chapter 2.

In the present chapter, two series of experiments are presented, and then reproduced numerically for comparison. The first involves a purpose-built small-scale model operated in the channel of the University of Magdeburg. The second involves measurements on a mid-scale wheel carried out internally by project partner company Sibau GmbH, and post-processed independently for the purposes of this thesis.

The main results of section 3.2 of this chapter were published as part of a peer-reviewed journal article (reference [73]): O. Cleynen, E. Kerikous, S. Hoerner, and D. Thévenin. "Characterization of the performance of a free-stream water wheel using computational fluid dynamics". In: *Energy* 165 (2018), pp. 1392–1400. DOI: 10.1016/j.energy.2018.10.003

3.2 Comparison with small-scale laboratory device

Any experiment involving a free-stream water wheel must feature a flow of water with a free surface. In the LSS laboratory of the University of Magdeburg, a water channel designed by Stefan Hoerner was built specifically for such purposes (figure 3.1 left). It is able to deliver a 10 m-long stretch of free-surface water flow with cross-section $1.2 \times 0.6\,\mathrm{m}$ and mean surface velocity $0.53\,\mathrm{m\,s^{-1}}$. A 0.3 m-diameter, 0.25 m-wide wheel model with 10 blades was positioned near the surface using a traverse rail (figure 3.1 right).

Mechanical power was subtracted from the wheel using an electrical generator connected through reduction gearing (figure 3.2 left), and controlled with a chipboard and graphical user interface on a desktop computer. The torque exerted by the wheel on the shaft as well as its rotational speed were measured with a torque transducer with a frequency of 500 Hz. Frictional losses from the shaft leading to the transducer, measured by turning the wheel in reverse without water (with the generator running as a motor), were found to be insignificant.

Prior to the experimental measurements on the wheel, the distribution of velocity at the inlet of the test section was measured with a two-component Laser-Doppler (LDA) system, across the complete cross-section of the flow (figure 3.2 right), in order to provide accurate boundary conditions for the CFD simulations. During the power measurements, the LDA system was positioned upstream of the wheel, 0.1 m below the surface; it yielded two-component velocity measurements with a frequency of approximately 10 Hz.

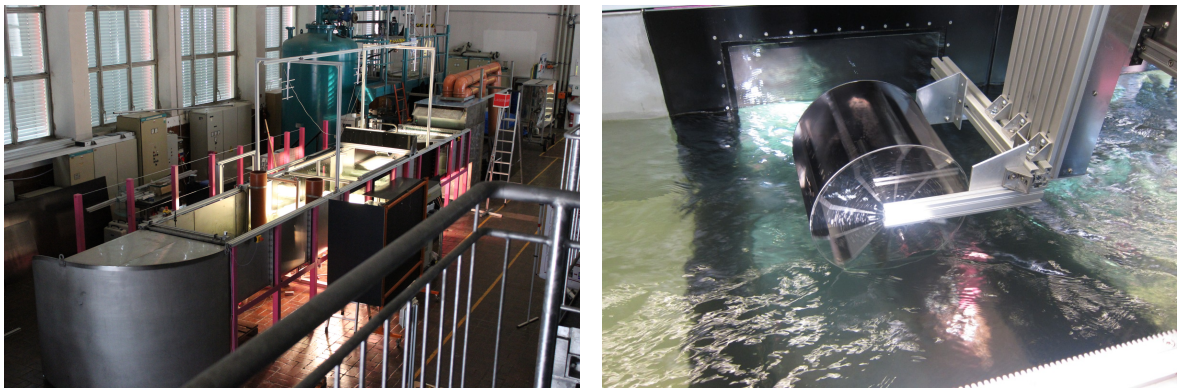

Figure 3.1: Left: the water channel of the LSS laboratory of the University of Magdeburg. Water from an underground pool enters the channel through the orange piping in the background. It then flows in an open, 10 meter-long stretch before returning to the pool (semi-cylindrical outlet in the foreground). Right: a 30-centimeter-diameter water wheel model operated in the water channel, positioned using a traverse rail system.

Right photo previously published in [73]

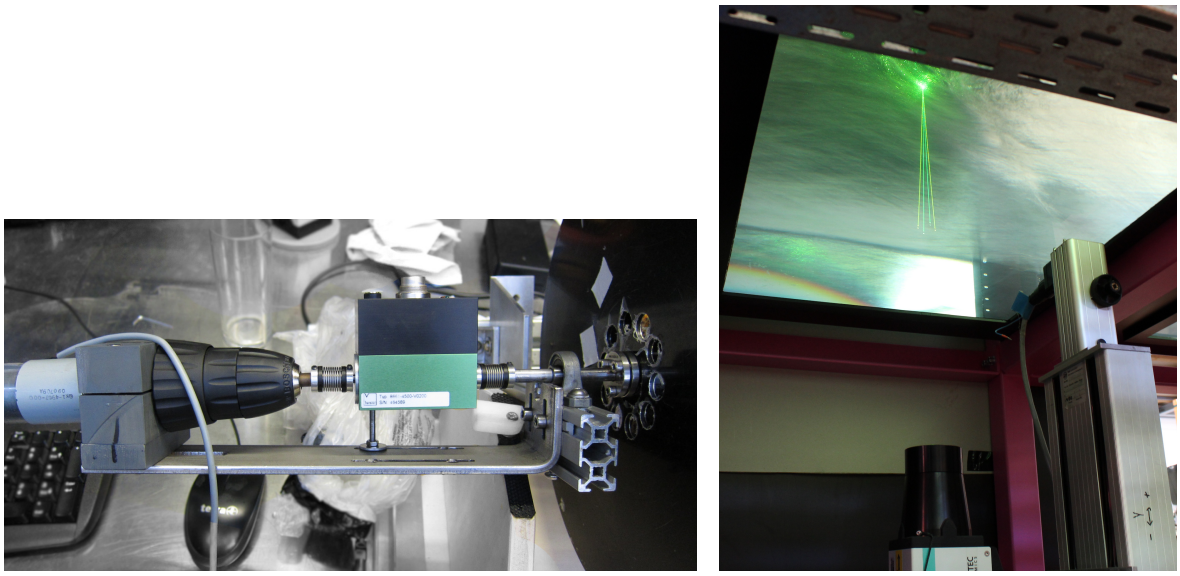

Figure 3.2: Left: apparatus used to measure the power produced by the model water wheel. Mechanical power is transmitted from the wheel (far right), through a torque transducer (center, green), a reduction gearbox (center left), and into an electrical motor (far left) operated as a generator. Right: Two-component LDA measurement device positioned below the channel. The four laser beams are visible through diffraction in the water passing above the glass window.

Measurements carried out jointly with Emeel Kerikous, co-author of publication [73]

Measurement values of shaft torque, rotational velocity and flow velocity were combined to produce power coefficient curves as a function of time. Runs at different rotation speeds, as well as runs with an empty water channel (with the generator operated as a motor, forcing the wheel to turn) allowed for the identification of four narrow frequency ranges added on top of the signal by the variable generator torque and flexible couplings. During the post-processing of measurement data, those frequencies were filtered out of the time-dependent data in order to reduce noise (reaching up to $\pm 35\,\%$ amplitude).

Challenges encountered during the measurements were all related to the relatively small size of the test wheel. The water channel is powered by four pumps with nominal power

8 kW each, whose 600 L s^{-1} output is discharged into a settling chamber, before flowing into the test section. By contrast, the mechanical power developed by the wheel is in the order of 0.5 W (0.6 % of the power as kinetic energy which is discharged into the channel inlet). Additionally, the incoming flow has nominal depth 60 cm; a 1 % change in this height subjects the wheel to a 12 % change in immersed depth. Oscillations in water velocity, related for example to the highly-turbulent flow in the settling chamber or to variations induced by the pump control system, therefore have a tremendous effect on the measurement of interest in this experiment. Careful calibration of the pump control systems and modifications carried out to the settling chamber outlet, in particular thanks to the work of LSS colleagues Emeel Kerikous and Stefan Hoerner, mitigated those issues. The final measurement uncertainty on the power coefficient values was calculated as ±5 %.

Parallel to the experiments, a three-dimensional simulation was set up. The simulation configuration was principally the same as these described in section 2.3 p. 49. An unsteady, incompressible, implicit segregated RANS solver was used in the Star-CCM+ software, with Volume-of-Fluid (VOF) and k-ω-SST solvers. The discretization was first-order in time, and the time step, chosen for each simulation so that the blade-passing period would be covered by an integer number of iterations, was $1.1 \cdot 10^{-3}$ s on average.

The domain (figure 3.3) reproduced a half (with a longitudinal symmetry mid-plane) 2 m-long section of the Magdeburg laboratory channel, meshed with 300k cells. This domain was joined through an overset interface to a polygonal, 450k-cell component containing the wheel blades and rotating together with them (figure 3.4). In order to increase accuracy while keeping the cell number under control, the mesh was refined dynamically at the phase interface five times for every blade-passing period, and only six of the blades (those in or close to the water surface) were actually modeled (the wheel position being reset at regular intervals). Close to the blades, the size of the cells was approximately 2 mm. The channel walls were set as no-slip surface boundaries, while the inlet velocity and turbulence intensity distributions were interpolated from cross-sectional measurements conducted with LDA in the channel (figure 3.3 right). Relative residuals were dropped to a satisfactory level (continuity $<5 \cdot 10^{-3}$, VOF $<2 \cdot 10^{-2}$, all others $<10^{-4}$) within 150 inner iterations per time step. A complete description of the flow was thus obtained (figure 3.5). The simulation, ran across 112 CPU cores, advanced at a rate of 15 s per week.

The measured and simulated power output of the wheel are compared as non-dimensionalized values in figure 3.6. The amplitude of the velocity oscillations could not be exactly reproduced in the CFD, due in particular to the steady boundary conditions. In three series of experiments and measurements, the best-fit polynomial curves displayed identical trends, with the simulated values on average 9 to 12 % below the measured values. Considering the complexity and the limitations of the procedure, this is a very satisfactory range.

After the above results were published in [73], a further comparison was carried out between flow field velocities obtained with two-component particle image velocimetry (in the horizontal and vertical planes) and those obtained in the same CFD simulations, in collaboration with Emeel Kerikous and Saketh Bharadwaj Kopparthy. At the time of writing, these results, which show excellent agreement, are in preparation for publication.

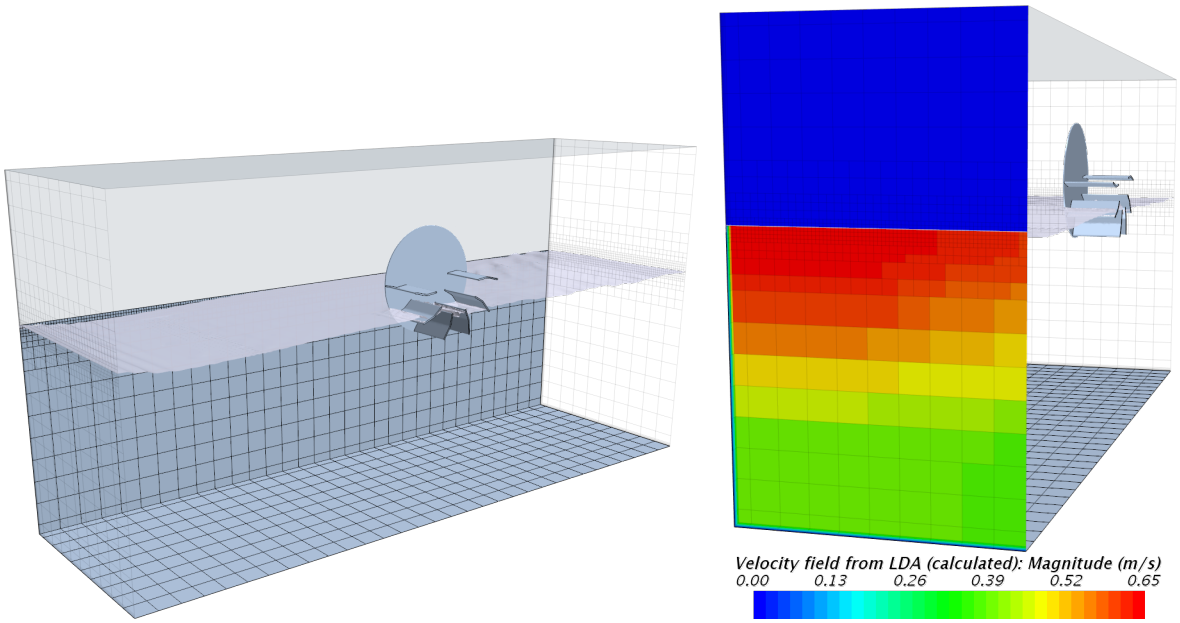

Figure 3.3: 3D numerical simulation of the water wheel tested in the water channel. Left: the simulation domain in whole, with the discretization grid visible on the channel walls. Water flows from left to right. Only one half of the channel is simulated, with the plane closest to the viewer configured as a symmetry plane. Right: the inlet of the domain (with water flowing from the foreground into the background). The plane is colored according to velocity; the magnitude of two components of the vectors was set according to the LDA measurements carried out at the entry of the channel.

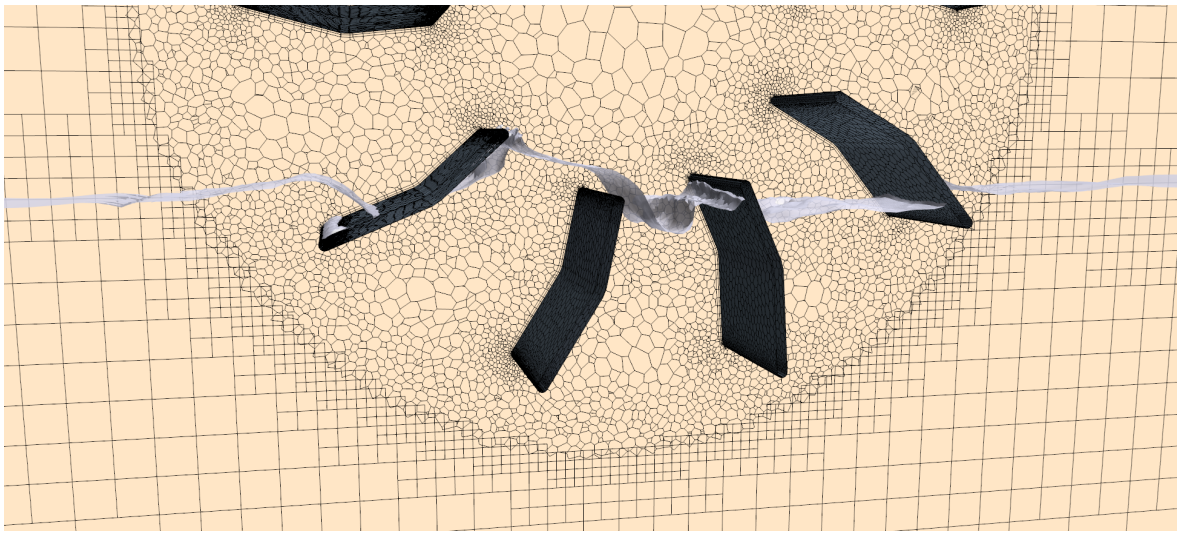

Figure 3.4: Close-up view of the mesh structure near the blades of the 30-centimeter diameter wheel model in the simulation. A vertical plane is laid along the flow direction, displaying the mesh structure. The rotating polygonal mesh is visible in the center, surrounded by the background structured mesh. The smallest cells in this view are 2 mm across. The water surface in a simulation with f_{wet}=0.33 is shown after 15 s of time has elapsed.

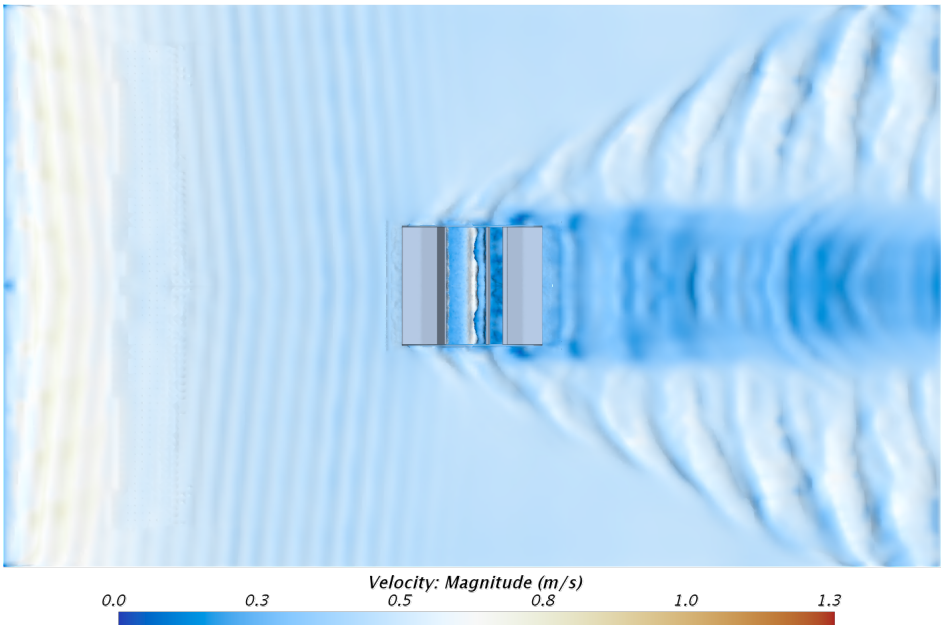

Figure 3.5: Velocity distribution on the free surface of the water after 15 s of physical time has elapsed. The color scale is set so that white corresponds to the nominal free-stream velocity ($0.6\,\mathrm{m\,s^{-1}}$), with lower and higher velocities denoted using blue and red respectively.

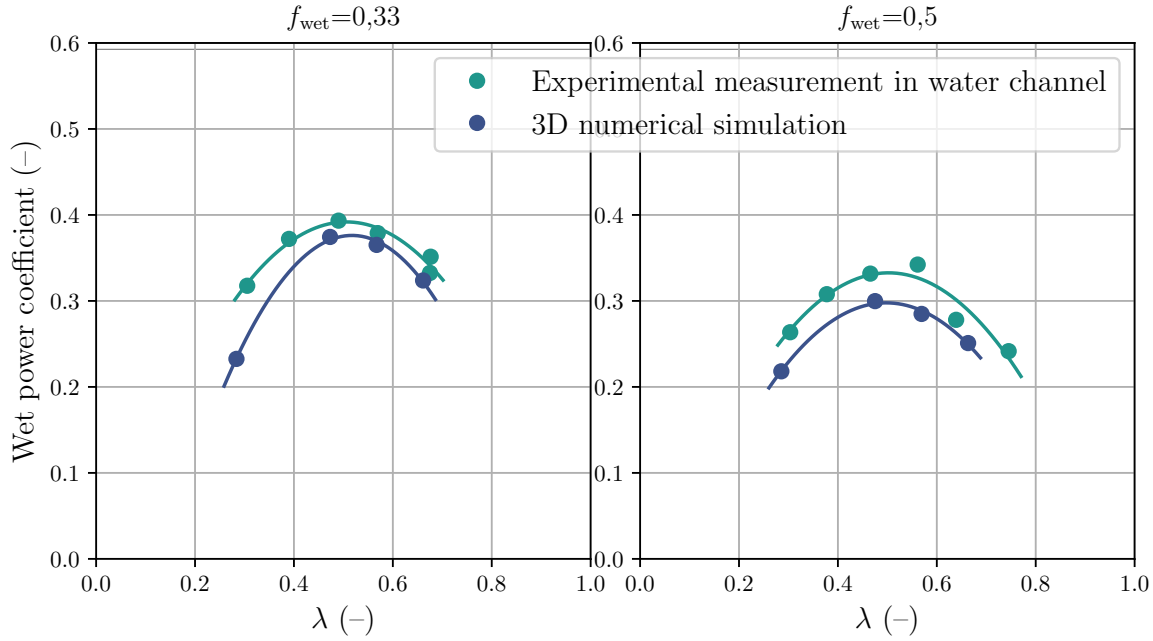

Figure 3.6: Wet-area shaft power coefficient of the 30-cm diameter water wheel model, as measured experimentally and as predicted by the 3D simulation, for 10 blades (n_b=10), incoming velocity $\overline{U}_\infty$=0.67 m s^{-1}. On the left, 33 % of the wheel radius is immersed in the water (f_{wet}=0.33), while on the right, f_{wet}=0.5. A second-order polynomial best-fit model is applied to each family of measurements.

Left figure previously published in [73]

3.3 Comparison with mid-scale device

3.3.1 The measurement campaign and its context

A series of experimental measurements were carried out around a mid-size (1.5 m-diameter) free-stream water wheel by the company Sibau Genthin GmbH in 2017. The raw results of this measurement campaign were made available to the author, and they provide an additional source of information with which to compare the numerical results obtained in the present work.

The measurement campaign was a project internal to Sibau Genthin GmbH. A 1.5 m-diameter, 1.4 m-wide wheel constructed out of steel was operated in between the hulls of a catamaran boat designed and built for such purposes (the *Vector 1*, figure 3.7), in a canal. The wheel construction was so that the blades' angle relative to the horizon could be easily modified. The campaign was carried out in order to investigate the blade angle which would maximize power, for purposes internal to the company. The measurements were never intended for comparison or publication; but access to raw measurement data was kindly granted to the author of this thesis one year later.

Figure 3.7: Photos of the *Vector 1* research catamaran. Left, the berthed boat; Right, installation of the mid-size free-stream waterwheel using a crane.

Both photos courtesy of Sibau Genthin GmbH, 2017

3.3.2 Procedure

The 1.5-by-1.4 m wheel was suspended at the center of the boat *Vector 1*, whose twin hulls are separated by a width of 5 m. The 12 blades of the wheel were all positioned at an angle β relative to the horizon; β was varied in four steps of 15° from 0° to 60°. For each angle β, the boat was operated at several speeds, ranging from 0.6 to 2.4 $\mathrm{m\,s^{-1}}$, as measured with a submerged nautical speedometer. For each speed, the wheel rotation speed was varied in 8 steps on average, resulting in tip speed ratios ranging from 0.1 to 1.

The wheel was connected through a chain (translation ratio 65.55) to a generator, whose characteristic was assumed constant at 3.45 $\mathrm{N\,m\,A^{-1}}$. The generator shaft rotation rate and electrical current were recorded, giving an indication of the power absorbed.

Overall, data was collected for 349 unique runs lasting about a dozen seconds each. For each of these, a record was made for the current, generator shaft rotation rate, water speed, as well as the wheel's geometrical configuration (two such records are shown in table 3.1 for illustration purposes). When grouped together according to free-stream velocity, these 349 runs result in 37 power curves. Videos captured with an action camera positioned between the hulls were available for approximately half of the runs.

Blade angle (β) deg	Current ($I_{\text{generator}}$) A	Rotation speed (ω_{shaft}) rpm	Water speed (U_∞) $\mathrm{m\,s^{-1}}$
30	0.47	168	1.29
30	0.54	260	1.29

Table 3.1: An extract from the raw data from the experiments carried out on the *Vector 1*, as they were made available to the author. Here, two records (out of a total of 349) are given, expressed in their original units and with the original significant digits.

3.3.3 Analysis

The mechanical design of the blade support is so that the tip radius R is changed when the angle β is varied, as shown in figure 3.8. During the experiment, an attempt was made to maintain the immersed depth approximately constant, at $L_{\text{wet}} \approx 0.125\,\mathrm{m}$, by varying the altitude of the wheel rotation axis accordingly.

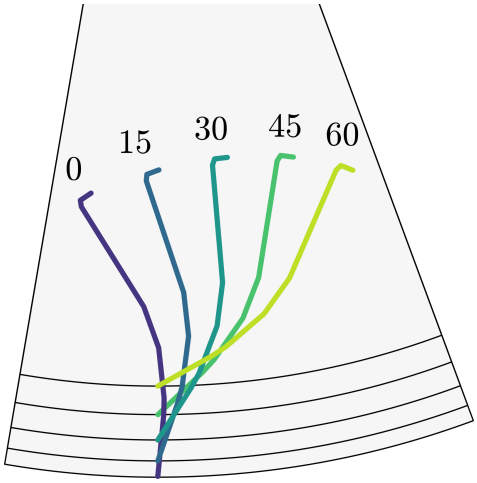

Figure 3.8: Diagram showing the different blade positions tested on the water wheel mounted on the *Vector 1*, using a segment of the wheel for a single blade (there are 12 blades in total). The flow is from left to right. The numbers indicate, in degrees, the value of the angle β between the blade tip segment and the zenith direction (as per fig. 2.5 p. 55)

Diagram created by the author, reverse-engineered from information provided by Sibau Genthin GmbH

Analysis of video footage from the measurement campaign reveals that the rotor axis altitude was not always adapted according to the blade angle. Post-processing of video stills allows for an estimation of the effective depth L_{wet}, albeit with relatively high uncertainty. The values for R and L_{wet} adopted henceforth for analysis are listed together with the corresponding wet radius fractions f_{wet} in table 3.2.

Blade angle (β) deg	Blade tip radius (R) m	Immersed depth (L_{wet}) cm	Corresponding f_{wet} –
0	0.79	14.5	0.183
15	0.777	13.1	0.169
30	0.759	10.1	0.133
45	0.737	10.8	0.146
60	0.712	6.6	0.093

Table 3.2: Geometrical properties of the wheel used in the experiments, when the blade angle β is varied. Values for radius were obtained through analysis of retro-engineered CAD drawings. Values for immersed depth were obtained using graphical analysis of video footage.

The rotation speed of the shaft, ω_{shaft}, is used to calculate the tip-speed ratio λ:

$$\lambda = \frac{B\ \omega_{\text{shaft}}\ R}{U_\infty} \tag{3.1}$$

where B is the translation ratio (here given as B=65.55);
and ω_{shaft} is the generator shaft rotation speed ($\text{rad}\,\text{s}^{-1}$).

No measurement of mechanical torque was carried out during the experiment; the power output of the wheel is instead recovered using the electrical characteristics of the generator, and non-dimensionalized according to the definition 1.8 p. 19 as follows:

$$C_{\text{P shaft, wet}} = \frac{C_{\text{useful, wet}}}{\eta_{\text{trans.}}\ \eta_{\text{el.}}} = \frac{\omega_{\text{shaft}}\ K_{\text{generator}}\ I_{\text{generator}}}{\eta_{\text{trans.}}\ \eta_{\text{el.}}\ \frac{1}{2}\ \rho\ L_{\text{width}}\ L_{\text{wet}}\ U_\infty^3} \tag{3.2}$$

where $K_{\text{generator}}$ is the generator constant (here given as K=3.45 $\text{N}\,\text{m}\,\text{A}^{-1}$);
$I_{\text{generator}}$ is the measured electric current (A);
$\eta_{\text{trans.}}$ is the mechanical efficiency of the transmission (–);
$\eta_{\text{el.}}$ is the conversion efficiency of the generator (–);
and L_{width} is the width of the wheel (m).

The rotor-area based power coefficient (def. 2.13 p. 54) is finally recovered as:

$$C_{\text{P shaft, rotor}} = C_{\text{P shaft, wet}}\ \frac{L_{\text{wet}}}{2\ R} \tag{3.3}$$

In this manner, non-dimensionalized power curves can be created for each of the 37 configurations. All available curves for the four lowest velocities (the cases most relevant for comparison with numerical results, as explained further down) are plotted in figure 3.9, where the individual measured points are shown together with a second-order least-squares trend curve.

It is visible in figure 3.9 that with the exception of the cases where β=0°, which consistently under-perform, the power output of the wheel is only very moderately affected by the blade angle. This moderate dependency is not consistent across flow velocities. The peak power occurs near $C_{\text{P rotor}}$=0.035 and λ=0.4 in most cases.

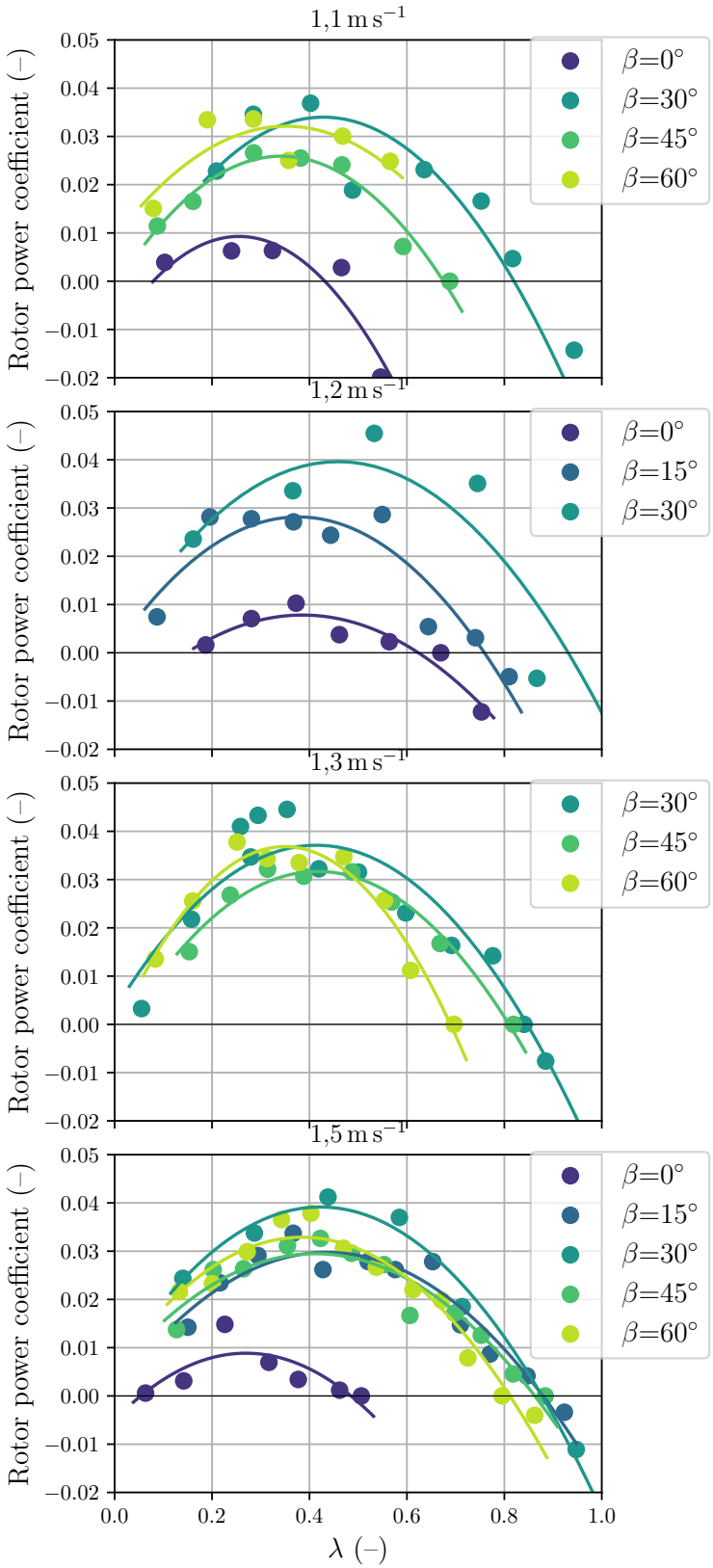

Figure 3.9: Power curves for 15 of the 37 configurations studied in the experimental campaign of company Sibau Genthin GmbH (non-dimensionalized as $C_{\mathrm{P\ shaft,\ rotor}}$). The four diagrams stand for four broad groups of free-stream velocities. Each data point is post-processed according to eqs. 3.1-3.3 using the corresponding source data, so that velocity is not kept perfectly constant within each diagram. Data is colored according to the value of the blade tip angle β, with color matching the diagram 3.8 p. 76. Trend curves are built with a least-squares second-order approximation.

Post-processing by author based on raw data provided by Sibau Genthin GmbH

3.3.4 Challenges in conducting experiments

Analysis of the raw measurement data, of the video footage made available to the author, and of the curves resulting from post-processing the data, reveals that significant challenges must be overcome when conducting such measurements. Weak points in the measurements and their post-processing can be listed as follows.

First, the water flow that feeds the wheel is not always uniform. The placement of the wheel in between of the two hulls of the *Vector 1* catamaran exposes it to the two symmetrical bow waves that they generate. Since the Froude number of the hulls remains below 0.2, those waves spread at an angle close to the Kelvin angle γ_{Kelvin}=19.5° from the bows. They therefore meet ahead of the wheel, and interfere with a wavelength which changes according to the speed. The bow waves not only influence the velocity distribution in the water incoming to the wheel blades, but also the height of the water surface, critically affecting the immersion depth L_{wet} and with it the mass flow of water directly available to the wheel. Review of video footage (available for 15 of the 37 configurations) reveals that the bow wave height is less than 1 cm for the lowest-speed cases, and of the order of 7 cm in the fastest cases. In some of these high-speed runs, the wheel is sometimes operating in the trough between waves, as shown in figure 3.10; in others, it is exposed to the crest.

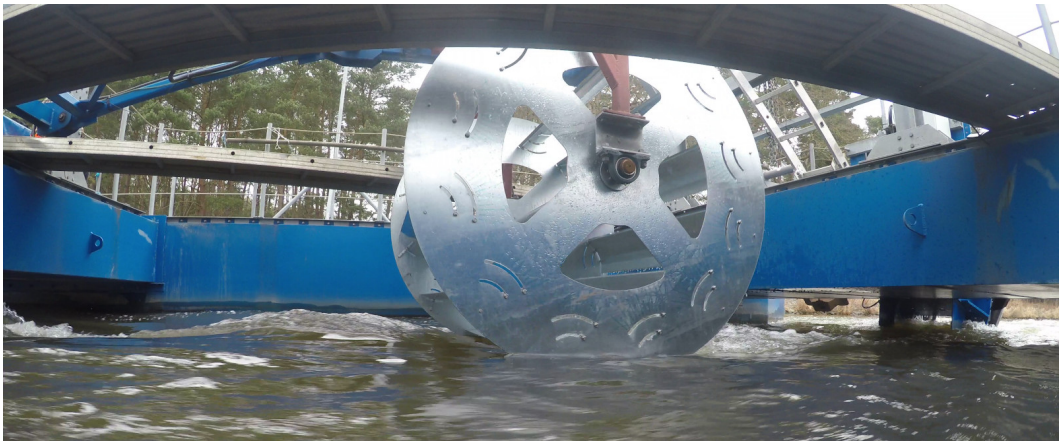

Figure 3.10: Still from a video recording carried out using an action camera during the experiment campaign. The camera is hoisted on the boat's port hull, pointing starboard; the flow relative to the wheel is from left to right in this image. In this case, the velocity is 2.1 $\mathrm{m\,s^{-1}}$. A large-amplitude stationary wave is visible immediately ahead of the wheel, while the wheel itself is operating in the stationary trough that follows the wave.

still image extracted from raw video footage provided by Sibau Genthin GmbH, 2017

Secondly, independently of bow wave effects, it is difficult to precisely set and control the immersed depth L_{wet}. This length was measured during installation (since the altitude of the rotation shaft must be suited to the blade position, as per table 3.2), but not monitored during the runs. Review of video footage, for example, indicates that the height of the rotation shaft was not changed when the blades' angle β was changed from 0° to 15°, resulting in an error of 1.3 cm in the depth (11 % of the nominal L_{wet}). In addition to manipulation and measurement errors, an error also likely arises from dynamic effects on the *Vector 1*, whose hulls displace 23 t of water; changes in water level at the wheel are possible if the boat squats into the water when underway

(increasing draft), and if thrust from the engine (which must compensate for the very strong changes in the drag exerted by the wheel) results in changes in pitch angle.

Finally, the power measurement is complicated by the lack of information about the direct mechanical power provided by the wheel. Instead, the electrical current delivered by the generator is the primary measure of output. The power delivered by the wheel is recovered using two assumptions: first, that the generator has constant characteristic (here given as K=3.45 N m A^{-1}) and constant efficiency (here assumed to be $\eta_{\text{el.}}$=90 %). This is unlikely to be true, especially when running far below speeds usually expected for generators (in this experiment, generator speeds as low as ω_{shaft}=58 rpm were recorded). The other assumption is that the chain transmission also has constant efficiency (here assumed to be $\eta_{\text{trans.}}$=95 %); this is also very unlikely. For example, when the wheel operates at high tip-speed ratios, the chain runs at normal speed but carries very little torque; mechanical losses may no longer meaningfully be expressed using an efficiency term in this regime.

In order to appreciate how these challenges influence the measurement results, an estimation of uncertainty is carried out in the following subsection. The hypotheses of constant generator and transmission characteristics are however not challenged, likely resulting in under-estimations of error at the lowest and highest tip-speed ratios.

3.3.5 Uncertainty estimation

The uncertainty in the power coefficient values obtained during the measurement campaign is estimated as per the JCGM's *Guide to the expression of uncertainty in measurement* [13] (henceforth called GUM), a long-established, well-documented, broadly-accepted set of guidelines.[1] The uncertainty (i.e. the estimation of the error) associated with each measurand, here written $\phi_{\text{measurand}}$, is expressed as a level of confidence, typically in terms of a standard deviation σ. This standard deviation can be calculated on the basis of repeated measurements (type A evaluation), or using engineering and physical insight about the experience (type B evaluation). In the end, the combined uncertainty on the final measurand (here the power coefficient) is expressed not as a min-to-max range, but in terms of a standard deviation which allows for the formulation of confidence intervals (e.g. the 95 % confidence interval is bound by $\pm 1.96\ \sigma$).

Here, the individual measurements for properties x_i conducted on the *Vector 1* are all assumed to be independent, and they combine to provide values for $C_{\text{P wet}}$ and λ through known functions f (equations 3.1 & 3.2). The propagation of the individual uncertainties $\phi_{\text{measurand}}$ on each final measurand is calculated, using a first-order approximation, using the following expression for the final combined uncertainty ϕ_{combined} (GUM 5.1.2):

$$\phi^2_{\text{combined}} = \sum_{i=1}^{N} \left(\frac{\partial f}{\partial x_i} \right)^2 \phi^2_{x_i} \tag{3.4}$$

The corresponding expressions for each term are therefore derived using derivatives of eqs. 3.2 & 3.1. As an example, the influence of the uncertainty ϕ_{U_∞} which is associated

[1] The GUM was prepared by a joint working group nominated by seven organizations, including the ISO and the BIPM. It was published in 1995 [13]; a lightly-updated version was prepared in 2008 and is available online [21].

with the velocity measurement on the power coefficient is:

$$\left(\frac{\partial f}{\partial x_i}\right)^2 \phi_{x_i}^2 \bigg|_{x_i=U_\infty} = \left(\frac{\omega_{\text{shaft}}\ K_{\text{generator}}\ I_{\text{generator}}}{\eta_{\text{trans.}}\ \eta_{\text{el.}}\ \frac{1}{2}\ \rho\ W\ L_{\text{wet}}}\ \frac{-3}{U_\infty^4}\right)^2 \phi_{U_\infty}^2 \tag{3.5}$$

The uncertainty for each term contributing to $C_{\text{P wet}}$ is quantified using the author's most reasonable engineering appraisal. They are listed in table 3.3.

measurand x_i	value	uncertainty	ϕ_{x_i}
$\eta_{\text{trans.}}$	0.95	95 % confidence interval: 0.05 $\eta_{\text{trans.}}$	$9.8 \cdot 10^{-2}\ \eta_{\text{trans.}}$
$\eta_{\text{el.}}$	0.9	95 % confidence interval: 0.1 $\eta_{\text{el.}}$	$0.196\ \eta_{\text{el.}}$
K_{gen}	$3.45\,\text{N m A}^{-1}$	95 % confidence interval: 0.1 K_{gen}	$0.196\ K_{\text{gen}}$
ω_{shaft}	reading	Systematic rounding error 1 rpm & 95 % confidence interval: 0.02 ω_{shaft}	$\frac{2\pi}{60}\frac{0.5}{3^{0.5}} + 1.02 \cdot 10^{-2}\ \omega_{\text{shaft}}$
I_{gen}	reading	Systematic rounding error 0.01 A & 95 % confidence interval: 0.02 I_{gen}	$\frac{0.005}{3^{0.5}} + 1.02 \cdot 10^{-2}\ I_{\text{gen}}$
U_∞	reading	Systematic rounding error $0.01\,\text{m s}^{-1}$ & 95 % confidence interval: 0.05 U_∞	$\frac{0.005}{3^{0.5}} + 2.55 \cdot 10^{-2}\ U_\infty$
L_{wet}	Table 3.2	95 % confidence interval: 2 cm	$1.02 \cdot 10^{-2}\,\text{m}$
R	Table 3.2	95 % confidence interval: 0.005 R	$2.55 \cdot 10^{-3}\ R$

Table 3.3: Uncertainties associated with each measurement involved in the computation of the power coefficient and tip-speed ratio using the raw data communicated to the author

Using the expressions for ϕ listed in table 3.3, the uncertainty $\phi_{C_{\text{P wet}}}$ is obtained as a function, using equation 3.4. In the six most relevant runs (used for comparison in the following section), the uncertainty on the wet power coefficient when the wheel was developing power was 0.054 on average (expressed in same quantity as the power coefficient itself). This uncertainty represented, on average, 15.4 % of the value of the power coefficient. This means that the 95 % confidence interval for $C_{\text{P wet}}$ is $\pm 0.3\ C_{\text{P wet}}$ on average.

3.3.6 Comparison with two-dimensional simulations

In order to carry out a comparison between experimental and numerical results, the cases where the experimental data was deemed to be the most reliable were selected. High velocities and extreme values of β were avoided, leaving two geometries and three velocities (six power curves) for a total of 53 data points. The configuration for each was reproduced in a two-dimensional simulation with the exact same characteristics as the family of simulations developed in section 2.4 p. 52 and later in chapter 4. The mesh and vorticity field for one such simulation is shown in figure 3.11. For each group of points, the velocity varied slightly from point to point; every time the recorded value was reproduced in the CFD simulation.

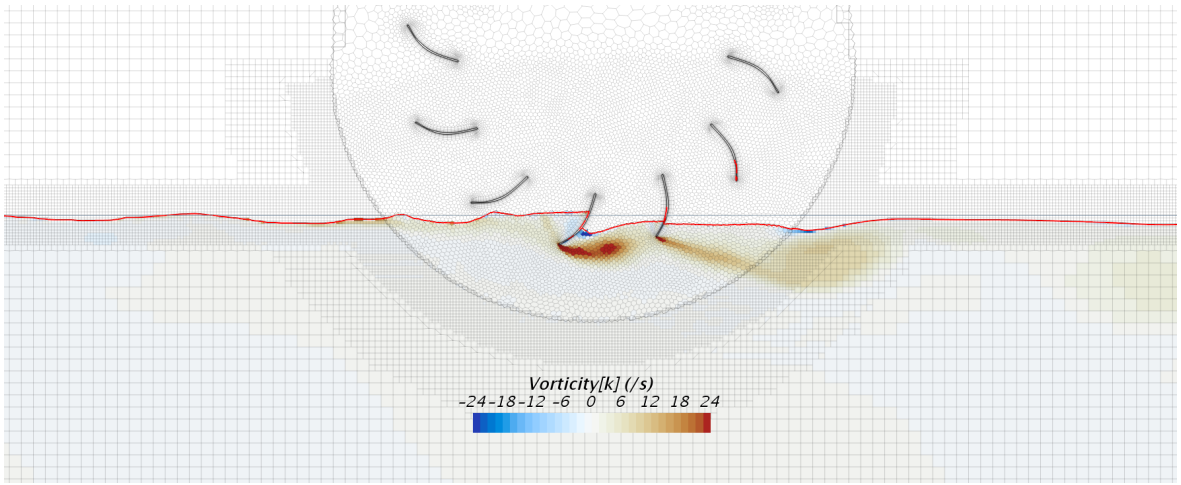

Figure 3.11: Flow field in one of the 53 two-dimensional simulations set up to mirror the conditions in the experiments on the *Vector 1*. In this case, the simulation is configured with β=45°, λ=0.16, U_∞=1.04 m s^{-1}. The simulation's physical and numerical setup is identical to these detailed in section 2.4. Color indicates vorticity in the water (color scale saturated at ±24 s^{-1}); the water surface is shown with a red line. In the background, the computation mesh (refined dynamically) is visible.

The results of both the simulations and the experiments are plotted together in figure 3.12, for a total of six power curves each. Trend curves (built using second-order polynomial models obtained with a least-squares algorithm) are shown for each group of points, and the experimental curves are plotted together with a shaded interval representing the 95 % confidence interval.

It can be seen in figure 3.12 that in the experiment, the angle β has a large effect on performance: peak power is decreased by 29 % on average when β is increased from 30 to 45°. Free-stream velocity also affects the experimentally-obtained power coefficient strongly, with peak performance increasing with free-stream velocity (relative increases approximately proportional to half of the increases in velocity). In the cases where β=30°, as the velocity is increased, multiple experimental measurement points distinctly exceed the Betz limit, suggesting that the generator efficiency or blade depth were underestimated. The optimal tip-speed ratio is everywhere close to λ=0.4.
By contrast, the power curves obtained in the two-dimensional simulations are insensitive to the blade angle β. Peak power coefficient decreases with increasing velocity (relative decreases approximately proportional to half of the increases in velocity). The optimal tip-speed ratio is everywhere close to λ=0.5.

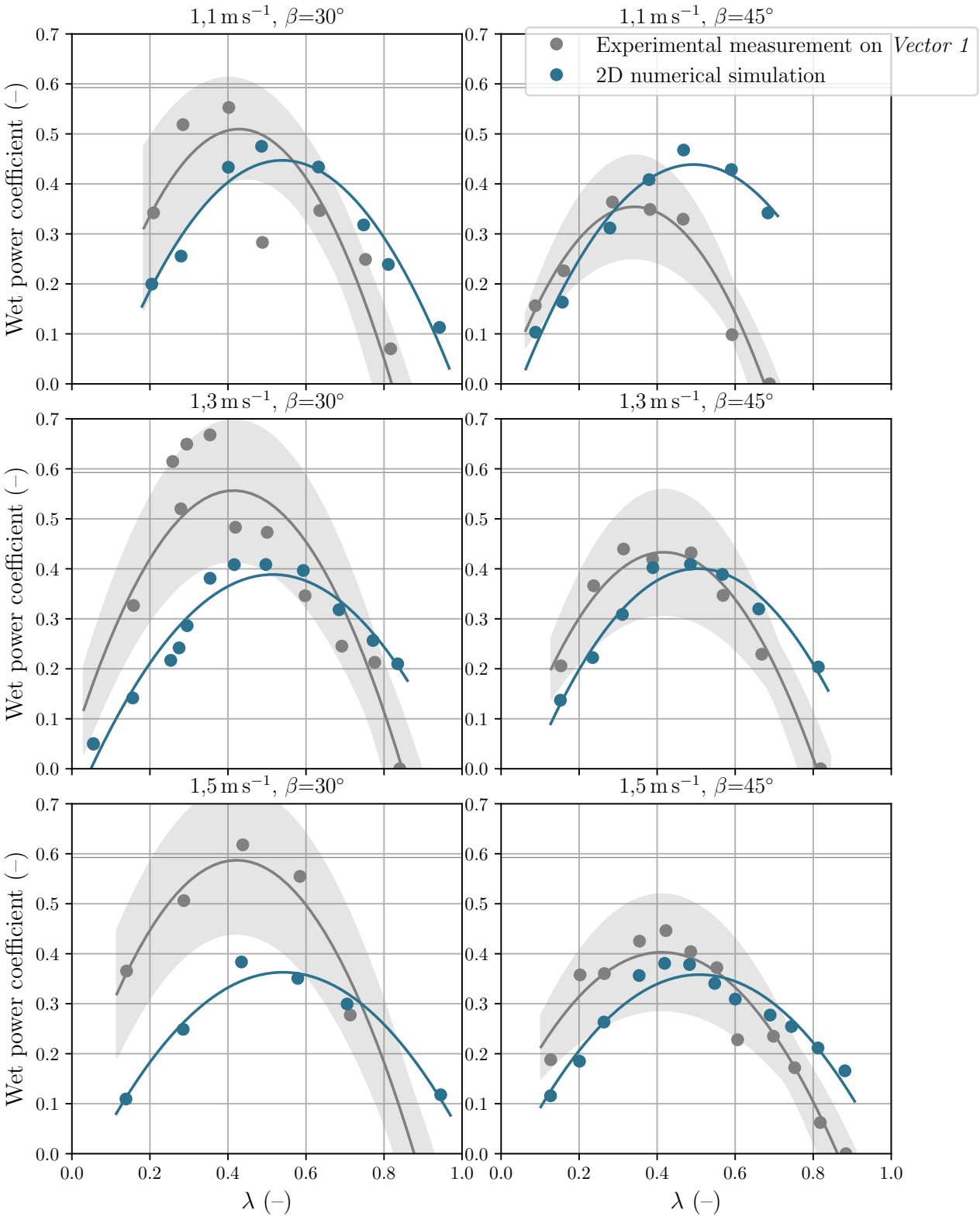

Figure 3.12: Power curves for both experimental measurements carried out onboard the *Vector 1*, and for two-dimensional CFD simulations corresponding to the same cases (all non-dimensionalized as the wet-area rotor power coefficient). The 95 % confidence interval on the experimental values for $C_{\mathrm{P\ shaft,\ wet}}$ and λ (calculated according to the procedure detailed in sec. 3.3.5) is shown as a gray area in the background. The six diagrams cover three free-stream velocities and two geometrical configurations. In every diagram, a horizontal line is drawn at the Betz limit ($C_{\mathrm{P\ wet}}$=16/27).

3.4 Conclusions

In the two attempts which have been presented in this chapter, the challenges of producing reliable measurements by which to assess the effectiveness of the models used in CFD simulations of water wheels are well illustrated.

One experiment was carried out in the laboratory for fluid mechanics of the University of Magdeburg. In order to provide a truly free-stream, free-surface flow, the blockage ratio must be minimized; in spite of the scale of the channel used in Magdeburg (a 15 m-long machine delivering 600 $\mathrm{kg\,s^{-1}}$), this strongly constrains the size of the testing model. It follows that the power output of a laboratory device becomes extremely sensitive to small variations in flow conditions. Consequently, the experiment requires sensitive measurement equipment (LDA, high-frequency torque & velocity measurement) and careful post-processing.

An important benefit of this small scale, however, is that it becomes possible to simulate the fluid flow using three-dimensional models with satisfactory mesh resolution. Comparison of numerical and experimental results indicates that the three-dimensional CFD simulations under-estimate the power output by approximately 10 %. This validates the methods used to describe fluid flow and power output in the numerical simulations developed in this thesis.

A completely different opportunity for comparison was presented to the author in the form of set of data from measurements carried out on a mid-scale (1.5 m-diameter) wheel by company Sibau Genthin GmbH. These measurements were never intended for publication; instead, they were conducted within Sibau for purposes internal to the company (determining the wheel configuration which would maximize electrical power in a given installation). In this sense, they constitute an independent source of information, tailored to the company's needs in research and development, and not to any need to demonstrate suitability or performance.

Measurements carried out in this context also come with drawbacks. The first is that it becomes difficult to assess a wheel's performance independently of the structure that supports it — in this case a 23-ton catamaran whose bow waves interact significantly with the dynamics of the wheel. Secondly, the experiment's original output (the electrical power directly produced by the generator, which is the one true output of interest to the company), when non-dimensionalized to enable comparison of the hydrodynamic properties of the wheel, becomes extremely sensitive to the quality of measurements. In this case, the generator's characteristics, wheel immersed depth, and water velocity dramatically affect values of the hydraulic power coefficient, which are of interest for comparison when considering the wheel's fluid dynamics. Much of the corresponding uncertainty could not be adequately evaluated during post-processing because of lack of information, and indeed, the results indicate unphysical performance in some places. Finally, the third drawback is the scale of the device, which renders three-dimensional simulations of the corresponding flow prohibitively expensive. Only two-dimensional simulations of the wheel were carried out in this case.

The result is that once the non-dimensional power curves are plotted together for both simulation and experiment (in figure 3.12), it is challenging to assess one against the other. On the one hand, experimental curves are presented, surrounded with a ±30 % uncertainty zone. While this confidence interval could easily be reduced with

higher-quality information about the experimental apparatus, it cannot account for much more subtle effects such as bow wave interference or draft changes due to the boat's squat. On the other hand, the absence of uncertainty values around the CFD curves must not be falsely interpreted: while the raw accuracy of the solver calculations is extremely high, the selection of each of the many physical and numerical models at hand (see sections 2.2.2 & 2.2.3) involves considerable uncertainty, not the least of which comes from the reduction to two-dimensional physics. Those uncertainties however cannot be calculated in a straightforward manner. As a result, the fact that the two sets of results agree only in broad, general terms, must not be considered worrying, considering the very satisfactory agreement found in figure 3.6. The numerical methods developed until here are therefore adopted for the rest of the work in this thesis.

Chapter 4

Optimal design for the free-stream waterwheel

4.1 Introduction

In chapter 2, a two-dimensional CFD model describing the power dynamics of the free-stream water wheel had been presented; this model and an associated methodology for analyzing performance were then used to carry out a parametric study involving 30 cases. In the present chapter, the same tools are put to use in two much larger-scale investigations, seeking to identify the free-stream wheel design(s) which will maximize power output.

To this effect, use is made of the laboratory's experience in studying hydraulic devices of various configurations [78, 84, 88, 99, 104, 105], and in their optimization [31, 32, 74, 89, 90]. Two major improvements are carried out, building on top of the tools developed in chapter 2. Firstly, the simulations are fully-parametrized, and a computational toolchain is set up so that they can be configured, sent to a distant cluster for computation, their output retrieved and post-processed in an automatic manner — this enabled over 2 400 CFD simulations to be investigated in this chapter. Second, the toolchain is coupled to an optimizer using a genetic algorithm. Instead of carrying out a systematic exploration of the complete domain (all combinations of input parameters), an attempt is made to travel intelligently through it, abandoning poorly-performing combinations, and investigating new evaluations derived from the top-performing ones. Although this method does not guarantee that the end-results truly constitute global optima in the mathematical sense, it allows for the exploration of much larger parameter ranges than a straight parameter study or manual optimization would.

Two distinct optimizations are carried out in this chapter. The first (sections 4.2 & 4.3) is a very large-scale study covering a broad range of radii, pointing towards not just one but a family of optimal wheels, depending on operator requirements. This work was published as a peer-reviewed journal article (reference [103]): O. Cleynen, S. Engel, S. Hoerner, and D. Thévenin. "Optimal design for the free-stream water wheel: a two-dimensional study". In: *Energy* (2021), p. 118880. DOI: 10.1016/j.energy.2020.118880

The second optimization features reduced scope, investigating a modification to the optimized wheels that improves the quality of their power delivery. This work (section 4.4) was performed by Abhishekkumar Shingala as part of his Master's thesis under the mentorship of the author [107]; at the time of writing, a journal article presenting the results is undergoing review (ref. [111]).

Finally, a brief, preliminary investigation is conducted which peers into the three-dimensional aspects of the fluid flow in two optimal-geometry wheels, pointing towards research questions to be answered in future work in order to overcome limitations associated with 2D simulations.

4.2 Setup for a computational optimization

4.2.1 Scope and objectives of optimization

A parametrized CFD model is used to optimize the design of a free-stream water wheel, with the objective of maximizing the generated shaft power. In installations operating

with significant blockage ratios, water height differences, or bed altitude differences, the efficiency should be measured according to flow properties both upstream and downstream of the machine, as has been covered in chapter 1. In the present case, the upstream conditions are sufficient to determine the power potential of the machine, using the shaft power coefficient $C_{\text{P shaft}}$.

In maximizing power, two competing objectives may be pursued, as already detailed in §2.5.1 p. 54. These are:

- Maximizing the wet shaft power coefficient, def. 2.11, repeated here:

$$C_{\text{P shaft, wet}} \equiv \frac{\dot{W}_{\text{shaft}}}{\frac{1}{2}\rho S_{\text{wet}} U_\infty^3} \tag{4.1}$$

- Maximizing the rotor-area power coefficient, def. 2.14, repeated here:

$$C_{\text{P shaft, rotor}} \equiv \frac{\dot{W}_{\text{shaft}}}{\frac{1}{2}\rho S_{\text{rotor}} U_\infty^3} \tag{4.2}$$

Here, these two objectives are pursued simultaneously; an attempt will be made in the next section to identify a Pareto front, and to describe which design parameter changes can be carried out to trade off between the two objectives.

4.2.2 Numerical models

The CFD model used in the present work has been extensively described in chapter 2 and validated against experimental data in chapter 3, as published in Cleynen et al. 2018 [73]. The 2D unsteady simulation contains a fully-parametrized description of a water wheel for automatic generation of cases; a picture of a representative simulation is displayed in figure 4.1.

The domain extends 13 m below the surface, 15 m upstream, and 20 m downstream of the wheel, in order to minimize boundary influence. The water height and velocity are monitored and averaged over six locations upstream of the wheel; these time-dependent values are used as input to eqs. 4.1 & 4.2 to evaluate the power coefficients. The moment resulting from shear and pressure on each blade is recorded at each time step and exported to enable post-processing.

A method was implemented to dynamically adjust the altitude of the wheel axis, as a function of the water level immediately upstream of the wheel, imitating in this manner the behavior of a real wheel installed on a floating installation. It was then observed that an unstable feedback loop was able to develop, whereby waves resulting from the upward and downward movement of the wheel would affect the water level measurement, in turn amplifying the movement in a self-reinforcing manner. In the light of the very large range of wheel diameters to be studied, it was not certain whether this issue could be reliably solved (e.g. using under-relaxation in the wheel movement specification) in all cases in an automated manner. The method was thus abandoned, and the wheel axis altitude remains fixed in all forthcoming simulations.

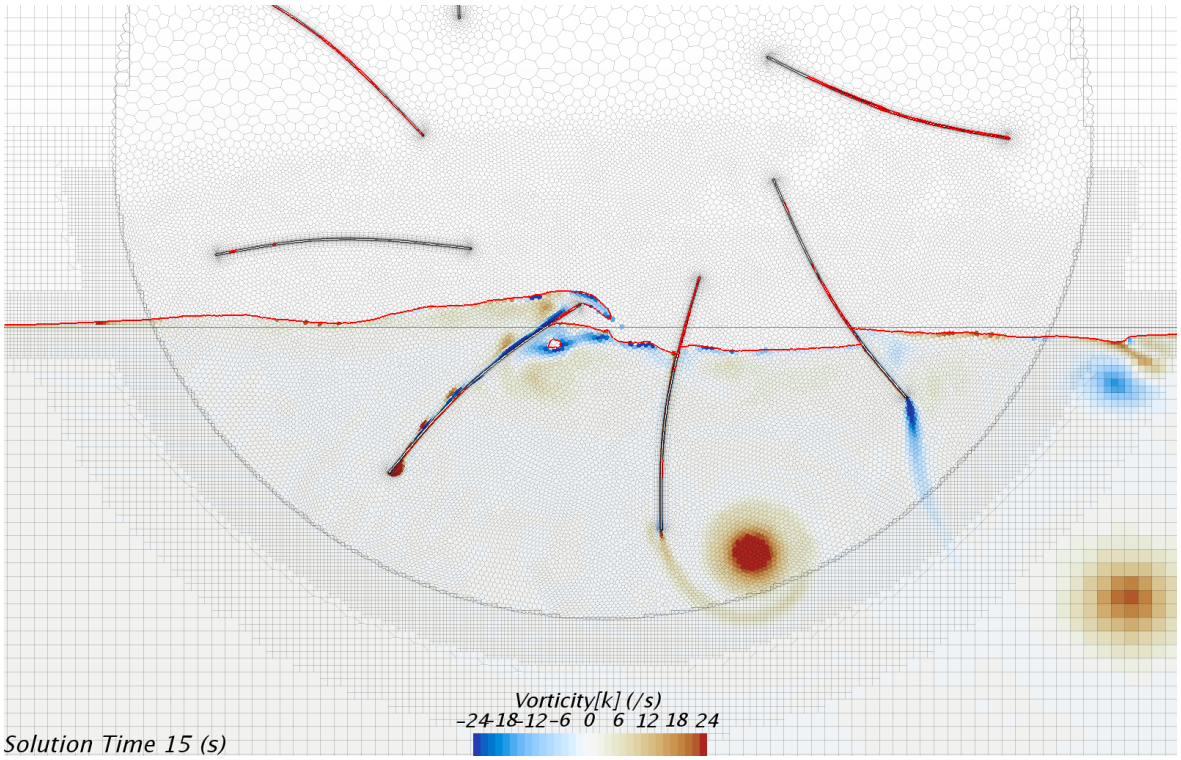

Figure 4.1: Fluid flow in one of the free-stream water wheels studied, with flow from left to right. Color stands for the local vorticity in the water, in the direction perpendicular to the plane (color scale saturated at $\pm 24\,\mathrm{s}^{-1}$). The interface between water and air is shown in red, and the horizon line is shown as a gray straight line. The locally-refined mesh is shown in the background. The flow domain extends far beyond the scene shown in the vertical and horizontal directions; and the diameter of this particular wheel (one among 1 900 studied in the optimization) is 2.4 m. Details about the CFD setup are given in chapter 2 and ref. [73].

Figure previously published in [103]

4.2.3 Parametrization of the free-stream water wheel

The design of the wheel is parametrized with five parameters:

- The radius R, which is varied in the range 0.4 m to 3 m;
- The number of blades n_b, which is varied in the range 5 to 32;
- The wet radius fraction f_wet, which is varied in the range 0.1 to 1 (an upper practical limit on f_wet is reached at 1, when the rotation axis sits at the water level);
- The blade geometry is defined based on a skeleton with angles β_1 and β_2, varied in the range $-30°$ to $+30°$. These angles are defined as shown in figure 4.2, with β_1 at the blade tip and β_2 at half-depth (the angle β_1 is the average of the angle between blade edge and horizon line during entry and during exit; β_2 is the equivalent at mid-depth). The blade itself is constructed with a 5 mm-thick relaxed spline joining the nodes of the skeleton.

Sensible value ranges for these parameters were determined in collaboration with project partner company Sibau Genthin GmbH, which is accumulating experience designing

and operating full-scale prototypes of such devices in Germany. The parameter ranges allow for an extremely varied population of designs (see e.g. fig. 4.3); this deliberately wide input parameter domain is deemed appropriate for a first optimization.

The water incoming velocity U_∞ is set at $1.2\,\mathrm{m\,s^{-1}}$ throughout the optimization (this value corresponds to the first quartile of the distributions of velocities on the river *Elbe* in Magdeburg, where this study was carried out). The tip-speed-ratio λ is fixed at 0.5, a value shown to be appropriate for this type of machine in chapters 2 and 3.

Three constraints are imposed on combinations of parameters, to avoid clearly impractical designs:

- The immersed depth L_{wet} is constrained in the range $0.2\,\mathrm{m}$ to $1\,\mathrm{m}$;
- The altitude of the rotation axis (relative to the horizon line) is constrained to remain below $2\,\mathrm{m}$, in order to limit the height of the rotor's center of gravity;
- The blade root is normally set above the water surface (at an altitude equal to $20\,\%$ of the immersed depth, as shown in figure 4.2); however, the root radius is constrained to never be below $0.2\,\mathrm{m}$, in order to prevent entrapment or constriction of air in between blades, leading to a strong performance reduction. In low-radius, high-depth wheel configurations, this constraint has the effect of making blades fully immersed (this effect is further investigated in section 4.4).

Several arbitrarily-selected examples of the geometries considered by the optimizer during the optimization process, all drawn according to the parametrization and constraints described above, are displayed in figure 4.3.

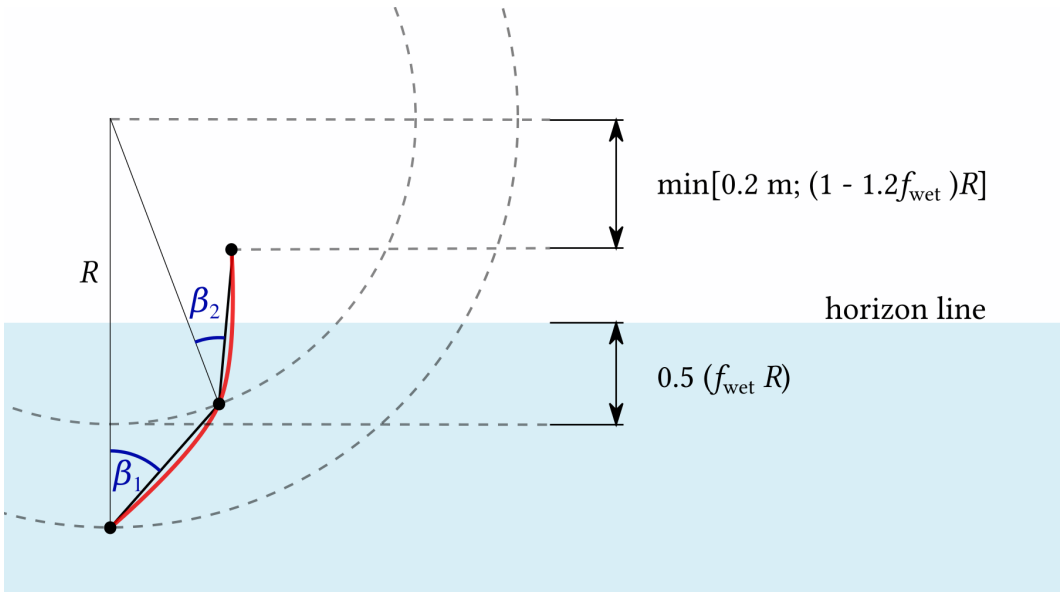

Figure 4.2: Schematic diagram detailing the geometry of a generic water wheel blade, as used in all simulations. The flow is from left to right. The blade itself (plotted in red) is a $5\,\mathrm{mm}$-thick relaxed spline joining three nodes. The nodes are linked together by a skeleton (plotted in black) consisting of two straight segments, the position of which is determined by the angles β_1 and β_2. The upper node is positioned at an altitude of $0.2 f_{\mathrm{wet}} R$ above the horizon line, unless this brings it within $0.2\,\mathrm{m}$ of the wheel center, as explained in the text.

Figure previously published in [103]

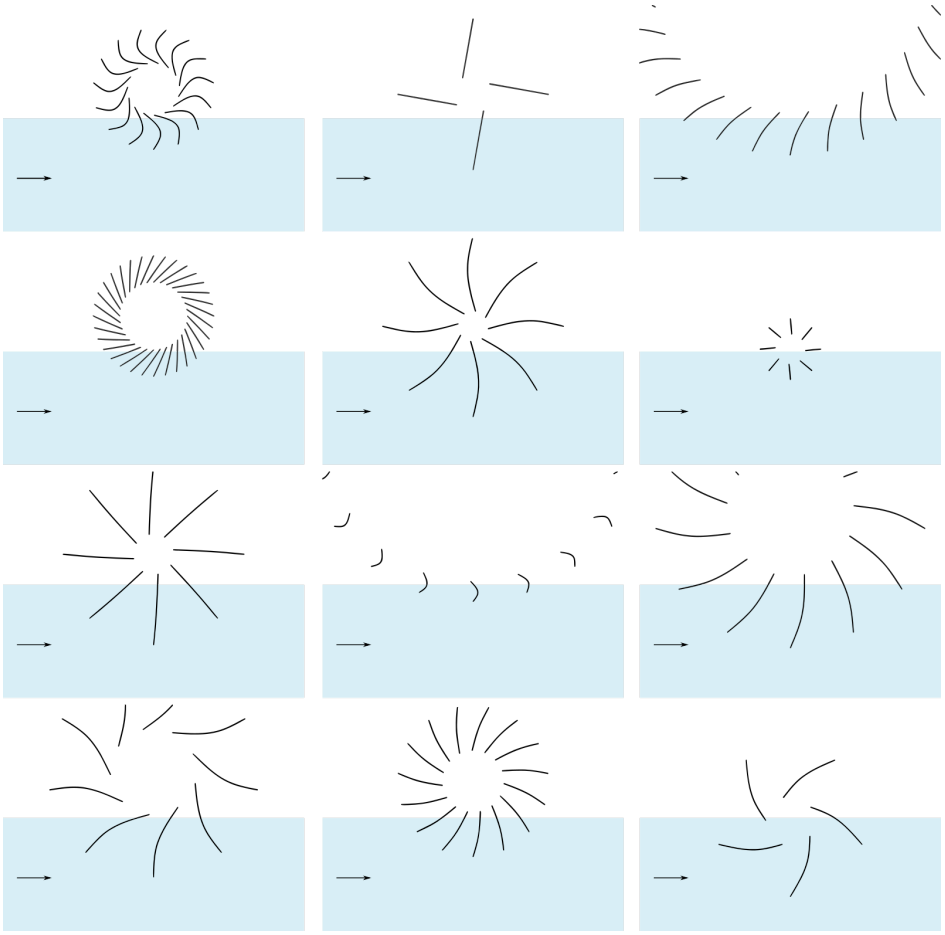

Figure 4.3: Some arbitrarily-selected geometries considered by the genetic optimizer, displayed at identical scale. The flow is from left to right; the thickness of the blades has been exaggerated in this diagram, for clarity. As per the constraints of the optimization, the diameters of the studied wheels ranged from 0.8 m to 6 m.

Figure previously published in [103]

4.2.4 Optimization process

The search for wheel configurations which maximize the wet- and the rotor-area power coefficients is carried out with an optimizer software distinct from the CFD simulation software. The Dakota 6.10 open-source toolbox [85] is configured with the `moga` genetic multi-objective algorithm to propose design parameters of candidate wheel designs in successive batches, based on the performance of previously-evaluated candidates. Since the objective is to produce practical, easily-implementable guidelines, the five input parameters are discretized with finite steps. The radius is varied in steps of 0.2 m, the wet radius fraction in steps of 0.05, the number of blades in steps of 1, and the two angles in steps of 5°. After constraints are applied, this results in 348 816 possible configurations.

The optimization is initialized with 200 designs spread uniformly in the input parameter space using a latin-hypersquare algorithm. A few configurations known to perform relatively well in previous investigations are also added to the initial population.

In each generation, the `moga` algorithm performs mutative parameter variations based on randomly-selected candidates; crossover is also performed on randomly-chosen groups of parent candidates. After the newly-created candidates are evaluated, individuals furthest from the Pareto front are rejected, and a new generation is started. The logic of the algorithm involved in creating each new generation from the previous one is described graphically in figure 4.4. It is further documented, together with a "sandbox" example case and lessons drawn from experience, on the author's website [87].

The principal settings of the `moga` algorithm used to obtain the first generation are listed in table 4.1. As the search progressed, separate optimizations were started with focus in specific areas of the parameter domain space, with less aggressive mutation parameters.

Each CFD computation ran on a 16-CPU node of a remote high-performance cluster (the *Neumann* cluster of the University of Magdeburg), until 15 seconds of physical time had been simulated. The computation time is contingent on the number of cells (itself strongly affected by the radius and number of blades), and varied between 9 and 36 hours. The two power coefficients were then averaged over the time period 3 s to 15 s and returned to the optimizer.

The optimization proper was run from a relatively low-power Linux desktop computer. Each evaluation was governed by a series of `bash` scripts, themselves configuring and launching in-house Python pre- and post-processing scripts, sending and retrieving files from the remote cluster, and submitting jobs to the cluster's queue system (`Slurm`) one at a time on a rolling basis, thereby minimizing total waiting time and optimizing the attribution of computing resources at a university-wide level. The excellent documentation and engineering insight provided by Sebastian Engel, from the laboratory for fluid mechanics of the University of Magdeburg, were instrumental in building this setup.

`crossover_type`	`shuffle_random`
`num_parents`	2
`num_offspring`	2
`crossover_rate`	0.5
`mutation_type`	`offset_normal`
`mutation_scale`	0.2
`mutation_rate`	0.5
`fitness_type`	`layer_rank`
`replacement_type`	`below_limit` = 5
`shrinkage_fraction`	0.75

Table 4.1: Main settings used to configure the `moga` genetic algorithm implemented in Dakota 6.10 in the first generation of the optimization. More conservative settings were used with reduced mutation amplitude as the optimization progressed.

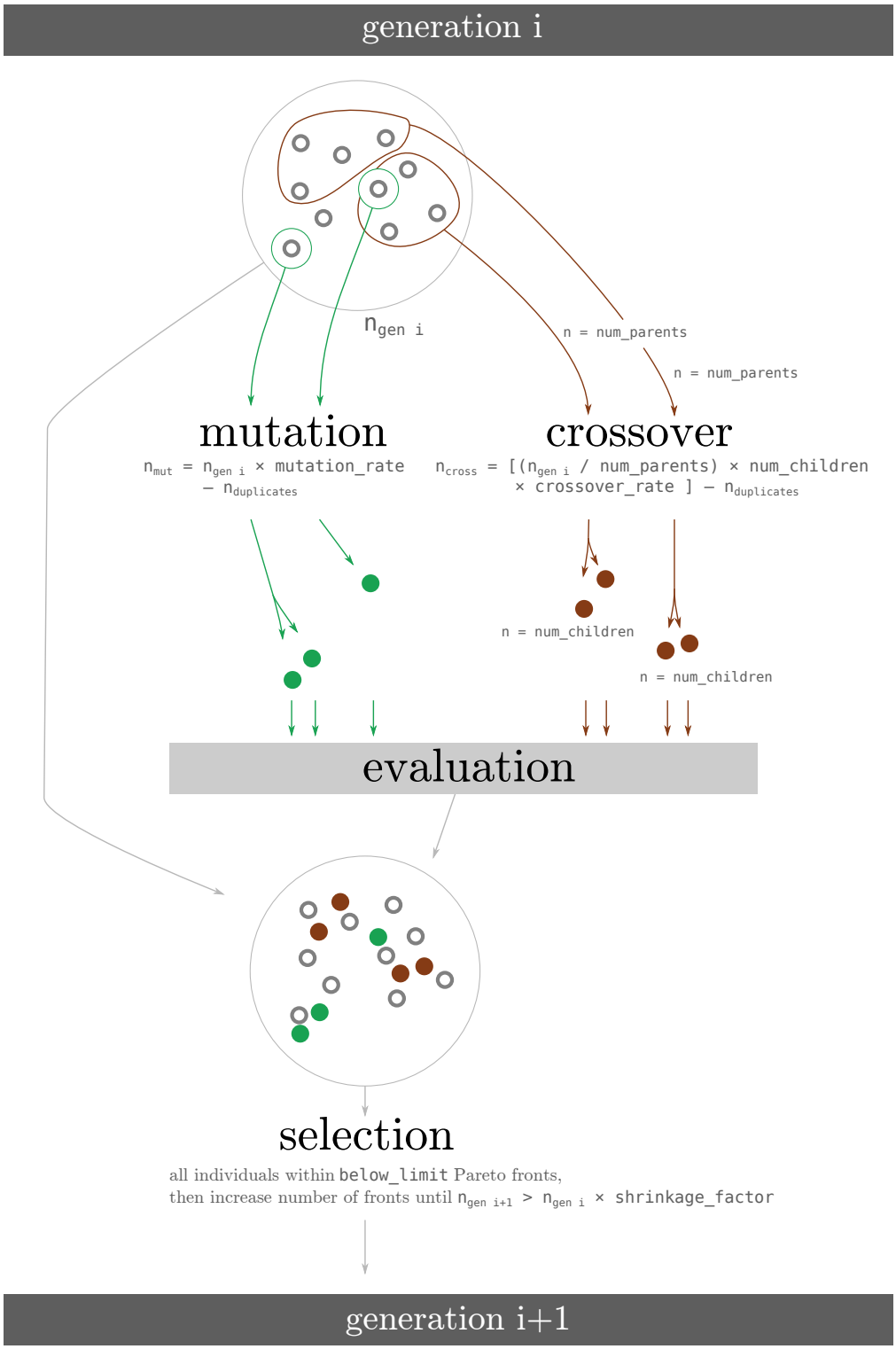

Figure 4.4: Structure of the main optimization loop of the `moga` genetic algorithm of Dakota 6.10. Beginning with generation `i`, the algorithm creates new individuals through two separate mechanisms: mutation and crossover. These are then sent for evaluation (in the present case, a series of scripts that submit a job request for the CFD computation on a distant cluster, then retrieve and post-process the results). The evaluated results are added to the group of individuals; the selection operation reduces this to a subset of high-performing individuals, that become the `i+1` generation.

Figure CC-BY-SA by the author, previously published in [86, 87]

4.3 Optimized family of 2D free-stream wheels

The optimization process described in the former section was brought to an end after 1939 evaluations were carried out, consuming a total of 432 000 CPU-hours over three months.

4.3.1 Resulting population

A map of the performance of all evaluated individuals is presented in figure 4.5. The wet radius fraction f_{wet} arithmetically determines the ratio between the wet and rotor power coefficients; since it was studied in discrete steps, the candidates are gathered in radial lines corresponding to individual values of f_{wet}. In this figure, multiple individuals with negative power output are not represented.

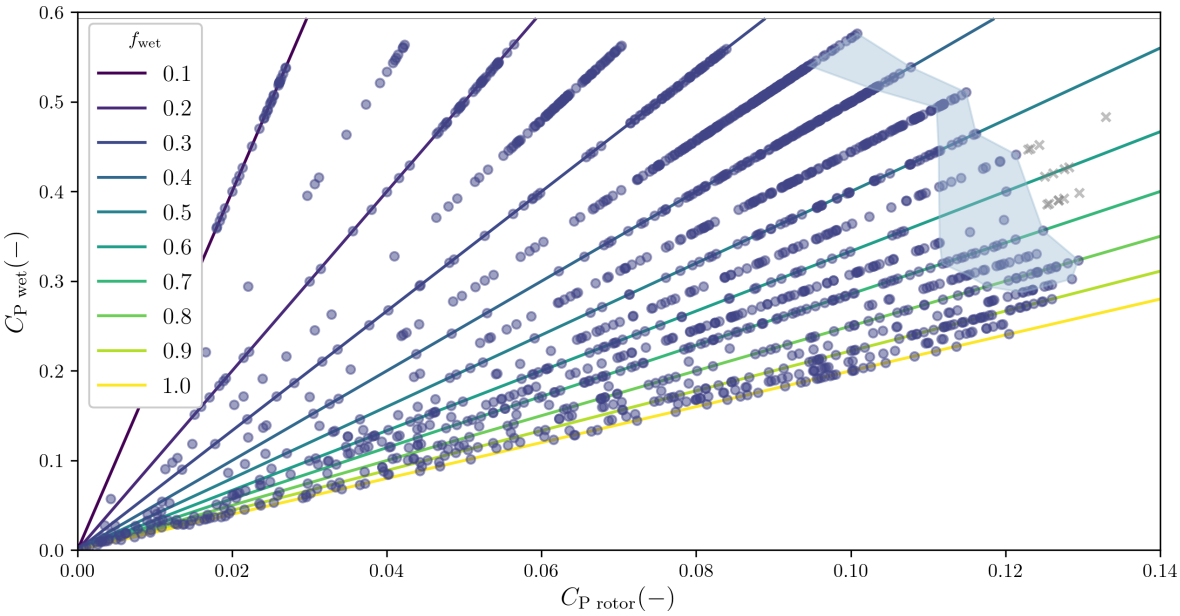

Figure 4.5: Performance of individual wheel configurations studied during the optimization, with the wet power coefficient on the vertical axis, and the rotor power coefficient on the horizontal axis. The power output of each individual was averaged over the time period 3 s to 15 s. Multiple individuals with negative power output stand outside the area displayed in the diagram. A horizontal line at y=0.593 denotes the Betz limit. Since f_{wet} was studied in discrete steps, individuals are clustered along diagonal lines, colored according to the corresponding values of f_{wet}. A group of rejected individuals, top right (see explanation in the text), is represented with gray crosses. The group highlighted in blue served as the basis for the determination of standard design rules, as detailed in section 4.3.3. The raw data presented in this figure, together with the corresponding geometrical configuration of individuals, is shared as supplementary material to ref [103].

Figure previously published in [103]

From the distribution of individuals in figure 4.5, it can be seen that the maximization of wet and rotor-area based efficiencies are clearly distinct and sometimes competing objectives. Individuals in the top left of the figure already feature relatively high wet-area performance, with their wet power coefficient approaching the Betz limit. Nevertheless, towards the right of the figure, individuals match that level of performance together with a five-fold increase of the rotor power coefficient.

In this figure 4.5, a number of high-performing individuals with f_{wet} ranging from 0.55 to 0.65 are represented with crosses. For those individuals, a particular effect is observed: the period of upstream-bound surface wave resulting from the entry of one blade is equal to the period separating two blades, so that the following blade always enters the water in the resulting trough. This strongly reduces the energy losses associated with the blades' entry in the water, and results in high performance; however, it is judged that this effect is unlikely to occur reliably in practice in real-world conditions, and so this group of individuals is arbitrarily removed from the population.

In the interest of facilitating further research, the dataset plotted in figure 4.5 is shared in a commented `csv` table as supplementary material to ref [103].

4.3.2 Design trends

Broad trends can be identified in the population covered by the optimizer in its search for optimal configurations. For each combination of radius and depth, several wheels of various blade geometry and blade number were evaluated; the best-performing wheel among these is selected. The results are plotted in figure 4.6, which presents a radius-depth design parameter map in which the performance is coded as color.

Broad performance trends can be extracted from the maps; in particular the following:

- Wet-area performance is best maximized using large wheels with high depths, but these depths are small relative to the radius. Depth-to-radius fractions (f_{wet}) below approximately 0.3 correspond to best wet-area performance;
- Rotor-area performance is best maximized using very small wheels with high relative depth (high f_{wet} values).

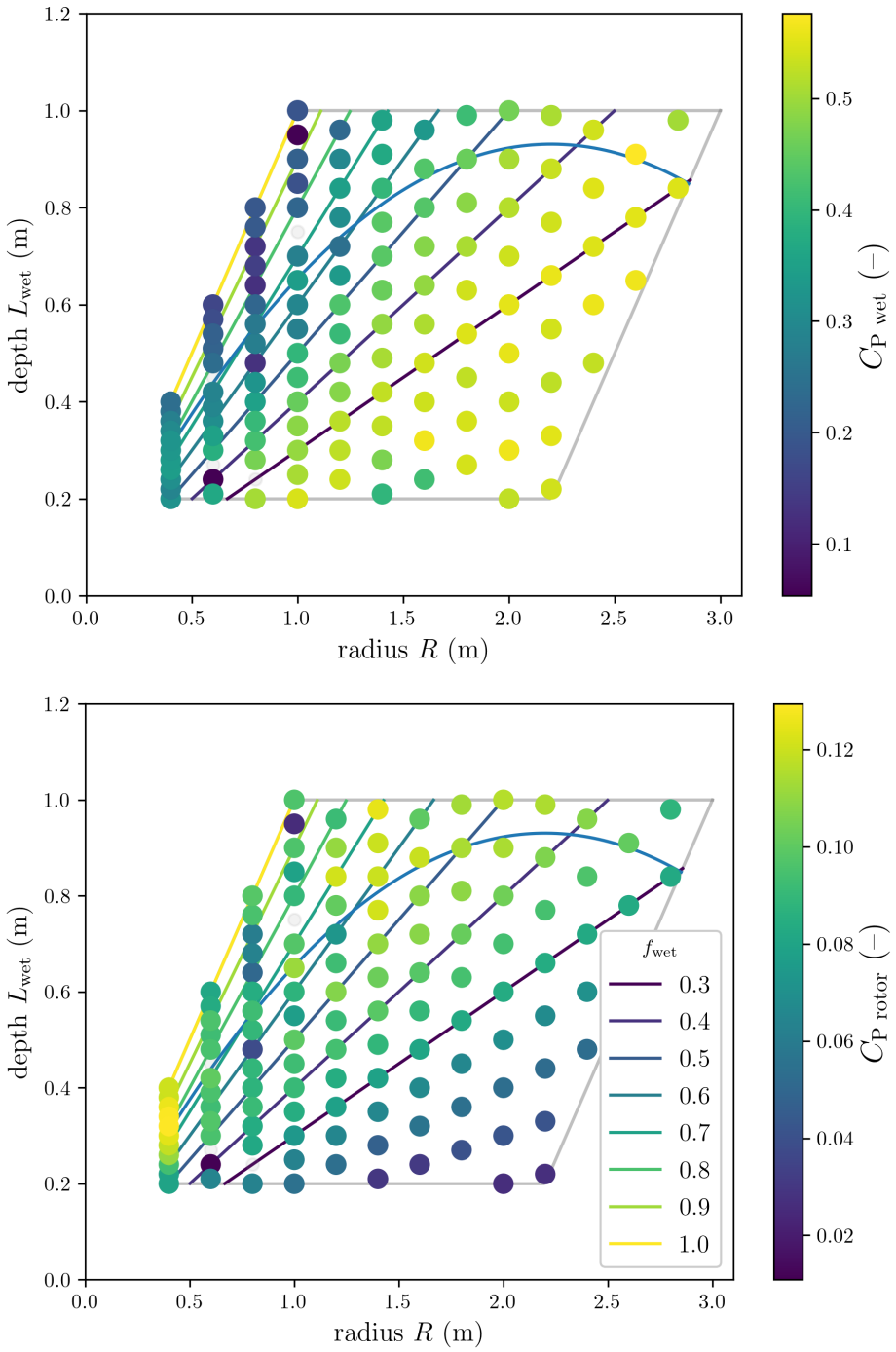

Figure 4.6: Design parameter map of the study. Both diagrams map radius (horizontal axis) against depth (vertical axis). For each combination, the best-performing candidate among all of the individuals evaluated during the optimization is selected, and its wet-area power coefficient (top) or rotor-area power coefficient (bottom) is coded as color. These individual points do not represent local maxima, because the optimizer was configured to search for global optima combining two objectives; nevertheless, broad trends can be extracted from the map. Radial lines in the background represent individual values of f_{wet}. The domain is limited by five constraints, clockwise from the top: maximum depth, maximum altitude of center of gravity, minimum depth, minimum radius, and maximum wet radius fraction. The superimposed parabola represents the solution to equation 4.6 presented in section 4.3.3 below.

Figure previously published in [103]

4.3.3 Design guidelines drawn from Pareto front

In an effort to combine best performance regarding both objectives simultaneously, those individuals highlighted in the blue area in figure 4.5 (a total of 118 individuals) are extracted. They correspond to the parameter range f_{wet}= 0.35 to 0.85 and are closest to the final Pareto front.

From here on, the focus is set on the characteristics and performance of this nearly Pareto-optimal group of individuals. In particular, an attempt is made to generalize their characteristics, and their performance is evaluated using stricter criteria, over a larger range of flow conditions.

The characteristics of the nearly Pareto-optimal individuals extracted previously are now examined in order to draw broad design guidelines. For each of the 11 wet radius fraction values of interest, a parallel coordinates plot of the corresponding individuals is derived; one example of such a diagram is shown in figure 4.7.

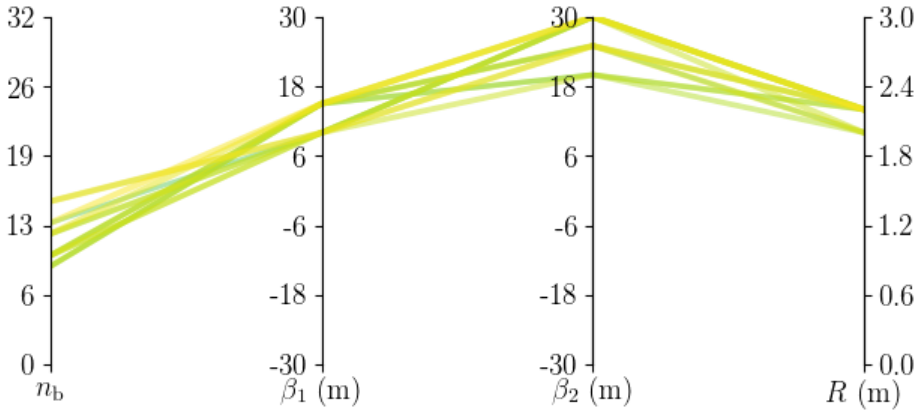

Figure 4.7: Parallel coordinates plot showing the combination of parameters corresponding to each individual of wet radius fraction 0.45 in the extracted Pareto group. The lines' thickness and color are coded according to performance, with thicker and lighter colors indicating higher values of rotor power coefficient, as evaluated during the optimization. The color map corresponds to that of figure 4.6b.

Figure previously published in [103]

The fact that in figure 4.7, lines remain grouped together, with little crossing, suggests that for this value $f_{\text{wet}} = 0.45$, there corresponds a single optimal value of each of the four remaining parameters. The trend is identical for the other ten values of f_{wet}, where each time the combinations of parameters corresponding to individuals remain broadly similar. These results suggest that it is possible to draw design guidelines with the wet radius fraction f_{wet} as the sole input parameter.

In a following step, the relationship between each of the four remaining parameters (R, n_b, β_1, β_2) and the wet radius fraction is examined. These relationships are plotted in figure 4.8. For each value of f_{wet}, the average value of the corresponding parameter in the extracted Pareto-optimal population is plotted, with a weight proportional to the rotor power coefficient. An area is also plotted in blue in the background, displaying the upper and lower median deviations of this parameter. The area surrounding f_{wet}=[0.6-0.65] is highlighted in red; following the arbitrary deletion of individuals there late in the optimization process (see sec. 4.3.1), this space features relatively few individuals.

The distribution of points in figure 4.8 suggests that broad guidelines can be drawn from the results, linking each of the parameters to f_{wet}. Trends are therefore drawn from the points in figure 4.8 and displayed there as orange lines. Since this type of machine is most likely to be used in low-budget, low-complexity applications, an attempt is made to extract trends that are mathematically as simple as possible. The guidelines produce a standard-optimal family of wheels, which is tentatively named the "Magdeburg" family of wheels, as follows:

Blade tip angle The angle β_1 is expressed in degrees as:

$$\beta_1 = \begin{cases} -68\ f_{\text{wet}} + 44 & \text{for } f_{\text{wet}} < 0.5 \\ 10 & \text{for } f_{\text{wet}} \geq 0.5 \end{cases} \tag{4.3}$$

Blade mid-depth angle The angle β_2 should remain around 25° for low values of f_{wet}, and around −10° for high values of f_{wet}. A third-order polynomial model produces, in degrees:

$$\beta_2 = 1\,476\ f_{\text{wet}}^3 - 2\,694\ f_{\text{wet}}^2 + 1\,488\ f_{\text{wet}} - 231 \tag{4.4}$$

Number of blades The number of blades is parametrized as the equivalent number of blades $n_{\text{e}} \equiv n_{\text{b}}\,[2\cos^{-1}(1 - f_{\text{wet}})]^{-1}$ (the average number of blades in contact with water, def. 2.19 p. 56): its value should be kept around 2.5. A guideline for the optimal value of n_{e} is expressed with one straight line and one third-order polynomial:

$$n_{\text{e}} = \begin{cases} 5.56\ f_{\text{wet}} + 1.04 & \text{for } f_{\text{wet}} < 0.5 \\ -198.3\ f_{\text{wet}}^3 + 438.6\ f_{\text{wet}}^2 & \\ \qquad -317.5\ f_{\text{wet}} + 77.7 & \text{for } f_{\text{wet}} \geq 0.5 \end{cases} \tag{4.5}$$

Wheel radius The optimal value of the radius, in meters, is expressed with the model:

$$R = \max\left[4.4 - 5.2\ f_{\text{wet}}; 0.4\right] \tag{4.6}$$

These four models are plotted as orange curves in figure 4.8. Additionally, solutions to eq. 4.6 are plotted as a blue line in figure 4.6.

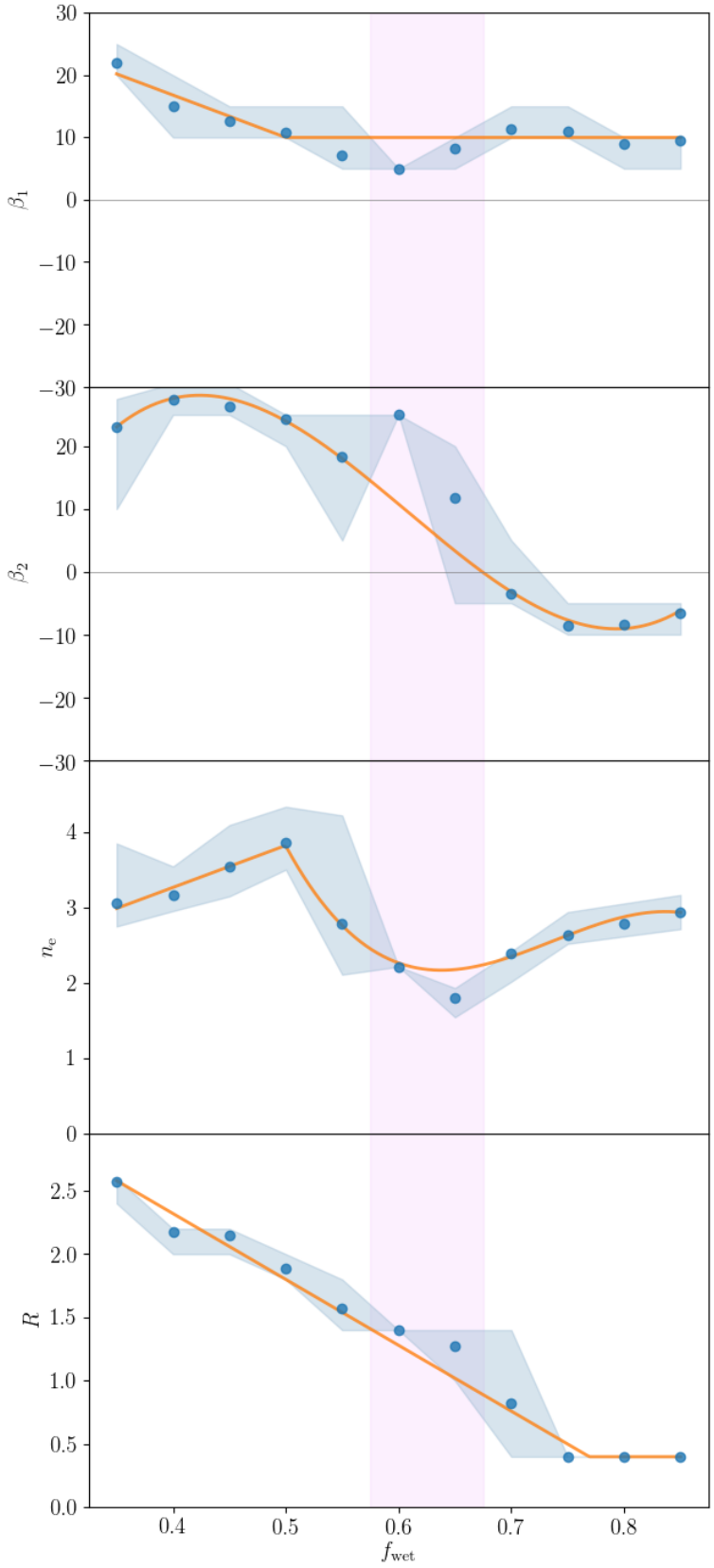

Figure 4.8: Distribution of the four parameters β_1, β_2, R and n_e (individual vertical axes) as a function of the parameter f_{wet} (horizontal axis), for the extracted Pareto-optimal population. The blue dots indicate the average of all the corresponding values in the population, weighted according to performance. The blue area is included between the upper and lower median deviations for each population. The zone highlighted in red indicates an area where relatively few individuals are available for analysis. Orange curves are trendlines corresponding to eqs. 4.3-4.6.

Figure previously published in [103]

4.3.4 Performance of optimal free-stream water wheel family

The performance of the wheels designed according to the "Magdeburg" model above is then evaluated, with an additional 39 000 CPU-hours invested. For this, CFD models for 11 wheels with f_{wet} ranging from 0.35 to 0.85 are created (with angles rounded to the nearest 5° and radii to the nearest 0.2 m, see fig. 4.9). To measure performance, instead of averaging the output power over 12 seconds, as was done during the optimization for computational cost reasons, higher standards are used, in order to ensure that the flow is well established. The power output is measured once the first 5 blades have passed through the water, and until the completion of the simulation, which is after 15 more blades have passed through the water. This standard for measuring power is kept for all remaining calculations in this work, resulting in simulations durations ranging from 16 to 86 s of physical time.

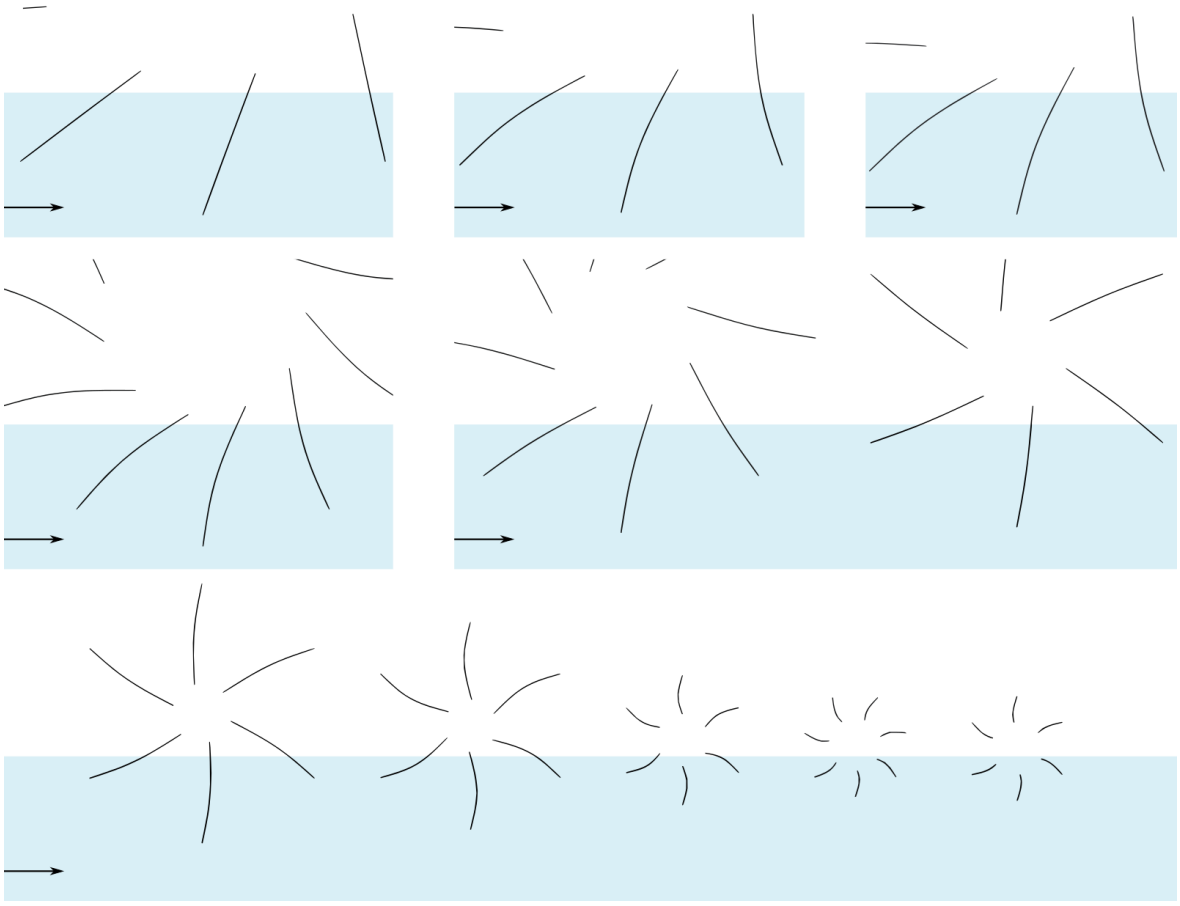

Figure 4.9: Eleven wheels constructed from the standard-optimal "Magdeburg" model, displayed at the same scale, ranging from f_{wet}=0.35 (top left, R=2.6 m, n_{b}=11) to f_{wet}=0.85 (bottom right, R=0.4 m, n_{b}=6). The flow is from left to right. In order to match realistic practical-world constraints, angles are rounded to the nearest 5° and the radii to the nearest 0.2 m.

Figure previously published in [103]

The performance of the newly-evaluated wheels is plotted in figure 4.10. Two features are immediately noticeable: first, the power output of low-f_{wet} wheels is markedly lower than that of similar wheels evaluated during the optimization (see figure 4.5). This is

due to the much more severe criteria used for measuring power output, which tend to affect deeper wheels. The second feature is that wheels with $0.55 < f_{\text{wet}} < 0.75$ perform very poorly. This disappointing result indicates that the model described above fails to provide a satisfying proposal in this region.

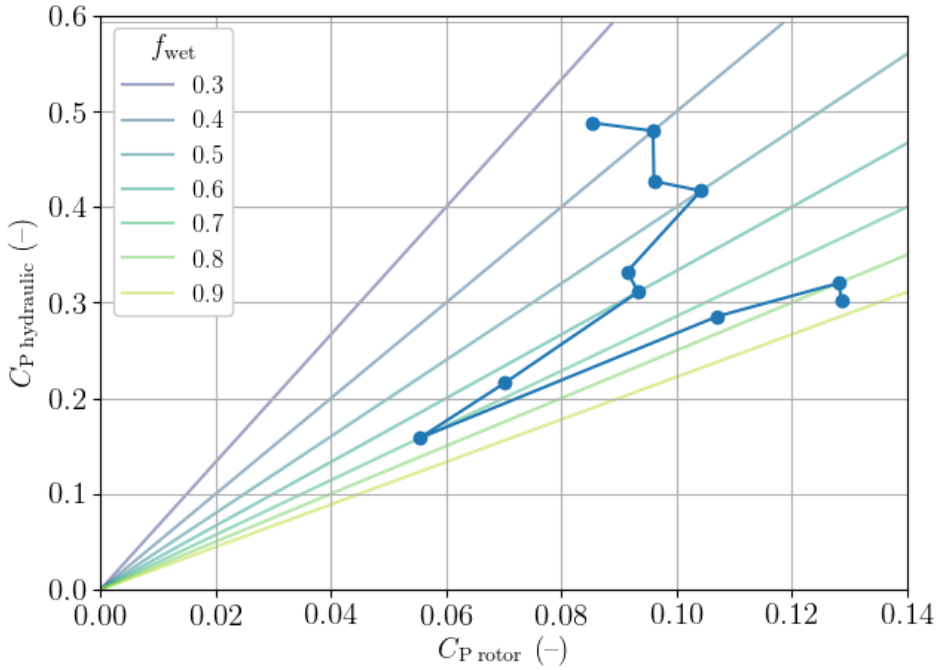

Figure 4.10: Performance of 11 wheels built after the "Magdeburg" standard-optimal model, as evaluated using criteria more thorough than during the optimization. Diagonal lines are once again plotted in the background, corresponding to individual values of f_{wet}.

Figure previously published in [103]

In order to assess the wheels' performance in operating conditions surrounding their design point, the tip-speed ratio λ and the incoming speed U_∞ are varied for four designs with f_{wet}=[0.35, 0.50, 0.65, 0.80]. The power curves obtained as a result are shown in figure 4.11.

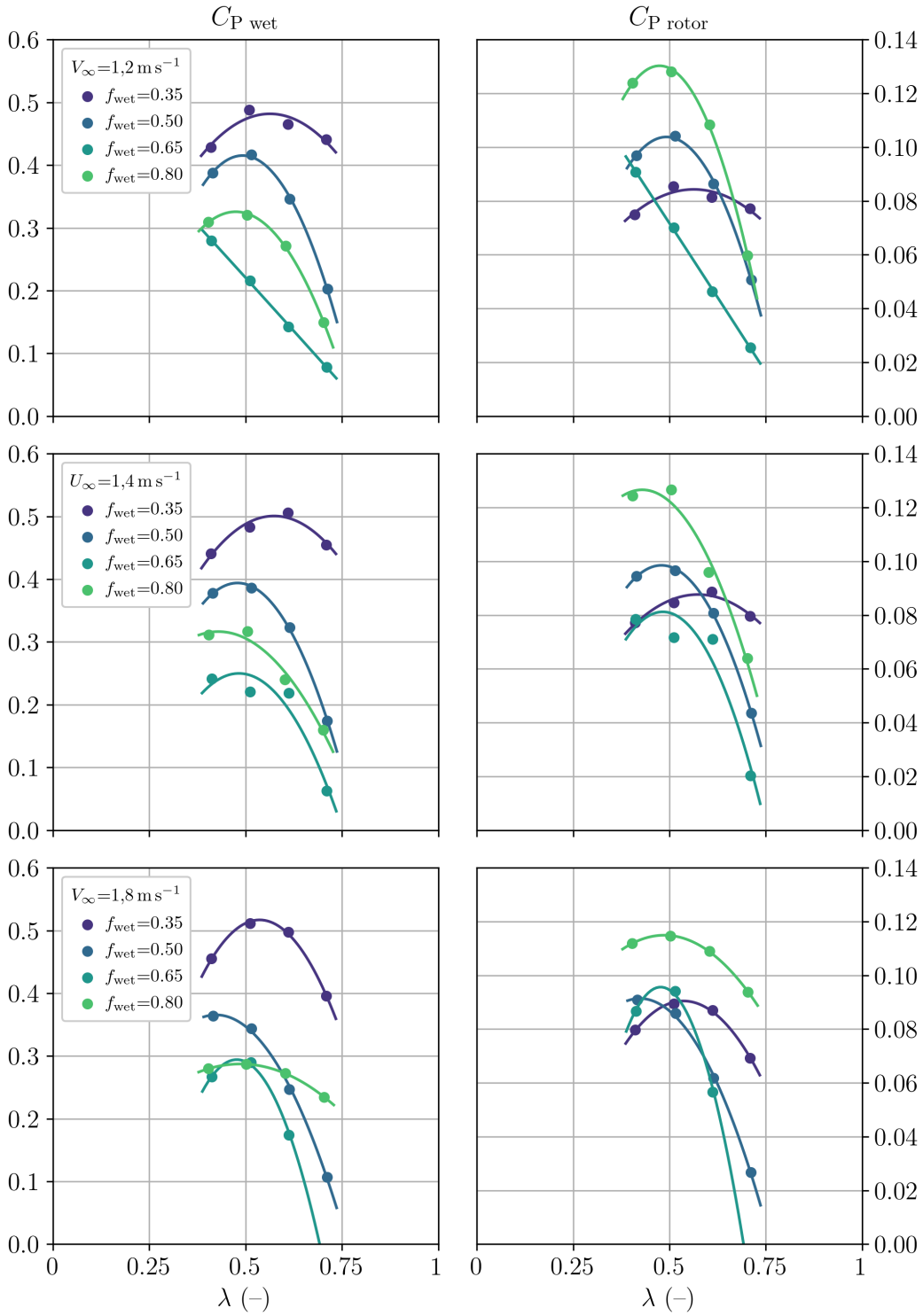

Figure 4.11: Performance of four standard-optimal "Magdeburg" wheels, each operated for three incoming water velocities and four tip-speed ratios. The wet power coefficient is plotted left, while the rotor power coefficient for the same cases is plotted right. The horizontal axes depict the tip-speed ratio λ. Four wheel configurations with f_{wet}=[0.35, 0.50, 0.65, 0.80] are studied (colored according to f_{wet}). The free-stream velocity U_∞ is 1.2 m s^{-1} in the top graphs, 1.4 m s^{-1} in the center graphs, and 1.8 m s^{-1} in the bottom graphs. Trend curves are plotted with second-order polynomials fitted with a regression algorithm.

Figure previously published in [103]

In figure 4.11, the trend lines were obtained using a regression second-order polynomial model. The point of maximum performance on these curves is extracted for each curve, and the resulting values are plotted in figure 4.12.

In figure 4.12, the main performance tradeoffs resulting from the proposed "Magdeburg" model are summarized at once. The trends are unequivocal: low-f_{wet} wheels feature higher wet-area performance and markedly higher power per unit width. One may consider the two extreme solutions proposed in that figure according to the model. Using predictions from the two-dimensional CFD simulations, averaged over the three studied velocities, these edge cases are as follows:

- Operators seeking to maximize power per unit of exposed area in the flow or per unit width of rotor (for example, those assigned a geographical installation area or a channel width in a given river with no limit on depth) should opt for a low-f_{wet} wheel. This translates into high-diameter, high-depth wheels with numerous blades. A large (5.2 m diameter, 11-blade) wheel immersed 91 cm into the river would feature high power per unit width ($C_{\text{P shaft, wet}} L_{\text{wet}}$=0.45 m), and a wet-area power coefficient of 0.5, at the cost of a relatively low rotor-area power coefficient of 0.085.

- Operators seeking to maximize power per unit area of the rotor (for example, those with a strong constraint on the diameter of the wheel or on cost of materials) should opt for a high-f_{wet} wheel. This translates into low-diameter, low-depth wheels with few blades. A compact (0.8 m diameter, 7-blade) wheel immersed 32 cm into the river would feature very low power per unit width ($C_{\text{P shaft, wet}}$ L_{wet}=0.1 m) and a reduced wet-area power coefficient of 0.3, but feature a higher rotor-area power coefficient of 0.13.
  These operators would therefore accept a four-fold (78 %) reduction in power per unit width and 40 % reduction in wet power coefficient, in order to secure a 53 % increase in power per unit rotor area. This is obtained because as one follows the model guidelines and the associated CFD predictions, the rotor diameter reduces more sharply than the developed power.

It must be stressed that these predictions are entirely based on two-dimensional fluid flow computations. An implicit assumption in those models is that no flow occurs in the third dimension (along the axis of rotation of the wheel). However, it is to be expected that edge losses occur, with flow deflected to the sides of the rotor; those losses are more likely to affect narrow, high-depth wheels. Additionally, surface disturbances associated with the floating structures supporting the rotor, also not reproducible in two-dimensional simulations, are likely to most affect the heaviest wheels. Both of those factors (discussed later in section 4.5) together suggest that in practice, as the wet radius fraction is reduced, the measured increase in power per unit width may be lower than predicted in figure 4.12.

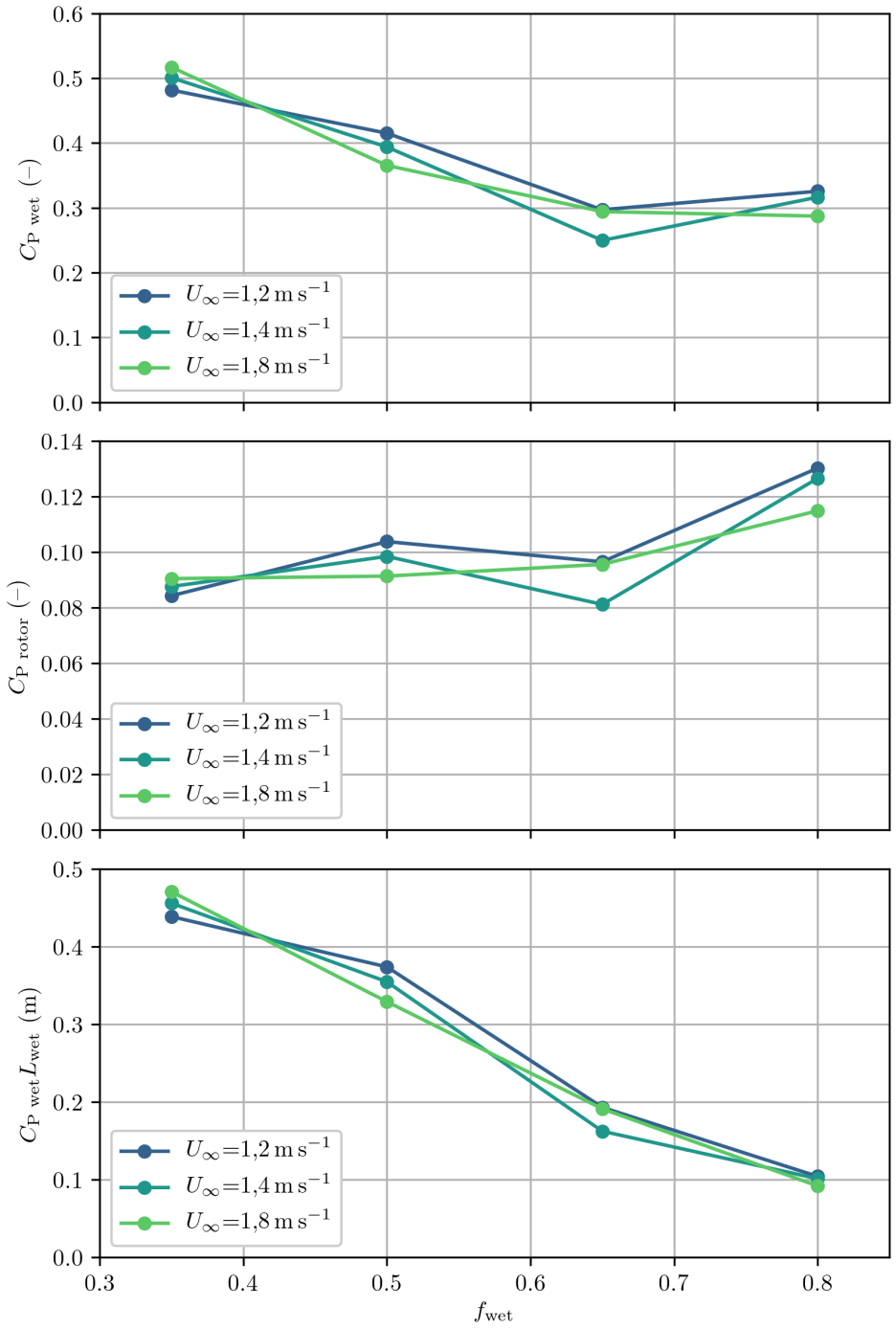

Figure 4.12: Performance of the "Magdeburg" standard-optimal family of wheels. Data points represent the best-efficiency point of each configuration, evaluated over four tip-speed ratios; data sets are grouped and colored according to free-stream velocity. The top graph shows the wet power coefficient $C_{\mathrm{P\ shaft,\ wet}}$; in the center is the rotor power coefficient $C_{\mathrm{P\ shaft,\ rotor}}$, and in the bottom graph shows the power per unit width, $C_{\mathrm{P\ shaft,\ wet}} L_{\mathrm{wet}}$.

Figure previously published in [103]

4.3.5 Performance mechanisms

Power stroke curves

The main mechanisms underlying the performance characteristics of the family of wheels presented above can be explored using blade power curves. Following the methodology established in chapter 2 (see §2.5.1 p. 54 & ref. [73]), it is possible to plot diagrams featuring non-dimensionalized expressions of the power developed by single blades along their stroke phase. The stroke angle α is non-dimensionalized as α^*, and the wet rotor power coefficient is recovered as the area under the curve of a $n_e \tilde{C}_{P\,b}$ vs. α^* diagram (eq. 2.21 p. 56 repeated here):

$$\overline{C_{P\ \mathrm{wet}}} = \int_0^{\frac{2\pi}{\theta}} n_e \tilde{C}_{Pb}\, d\alpha^* \tag{4.7}$$

$$\overline{C_{P\ \mathrm{rotor}}} = \int_0^{\frac{2\pi}{\theta}} \frac{1}{2} f_{wet} n_e \tilde{C}_{Pb}\, d\alpha^* \tag{4.8}$$

Such a diagram is plotted for selected configurations in the "Magdeburg" family of wheels, and shown in figure 4.13.

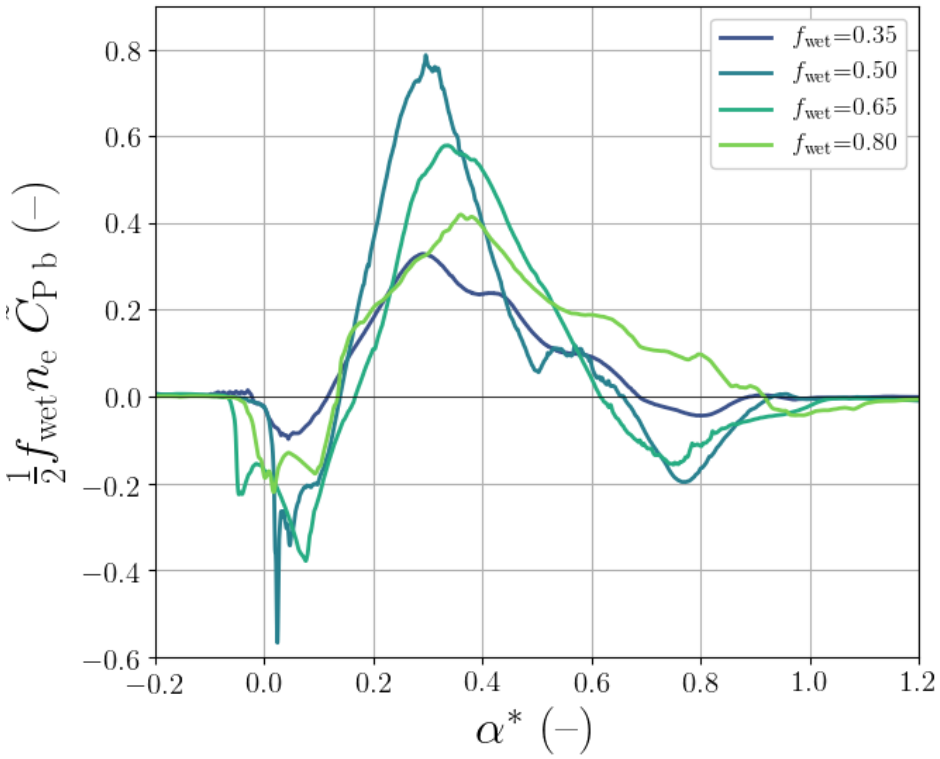

Figure 4.13: Blade power coefficient as function of the non-dimensional stroke angle α^*, for four different relative depths in the "Magdeburg" family. Each curve is constructed with average data resulting from 15 blades passing through the water. The net area under each curve in this diagram is equal to the rotor-based power coefficient $C_{P\ \mathrm{rotor}}$ of the wheel.

Figure previously published in [103]

The following trends are observed in figure 4.13:

- Low-f_{wet} wheels feature relatively smooth entry and exit from the water, with peak power occurring at one third of the stroke;
- As the wet radius fraction is increased and the radius is decreased, the energy losses associated with the entry and exit from the water rapidly increase. The power per unit rotor area increases as well, with a more pronounced, high-amplitude, wide peak;
- As the wet radius fraction is further increased towards smaller wheels, the delivery of power per unit rotor area becomes more uniform over the stroke, and features decreased cost of entry and exit. As f_{wet}=0.8 is reached, the blades provide power over more than 80 % of the stroke, and the cost of exit becomes very small.

Effect of blade root radius change

When designing parametrized rules for the design of the free-stream waterwheel (see sec. 4.2.3 p. 90), the root of the blade was positioned above the horizon, at an altitude equal to 20 % of the depth. It was observed that in deep wheels with numerous blades, this resulted in gaps between the roots so narrow that they would obstruct the movement of water between blades. Consequently, a limit was imposed on the height of the blade root (see fig. 4.2), so that an empty core of diameter 40 cm would always be present within each wheel. In some studied configurations, this restriction had the effect of making the blades fully-immersed at the nadir position, and this remains true in high-f_{wet} configurations of the "Magdeburg" model presented above.

Here, the effect of blade immersion is investigated for the first time. To this effect, the standard-optimal wheel with f_{wet}=0.5 is modified in four successive steps, with the radius of the blade root increased until it reaches mid-depth. The power characteristics of the modified wheels are then compared; they are presented in the following figures.

Figure 4.14 displays, as a function of blade root radius, first the wet power coefficient, and then the work ratio r_{ntg}, defined as the ratio of net to gross power produced by the blades:

$$r_{\text{ntg}} \equiv \frac{\int_0^{\frac{2\pi}{\theta}} \tilde{C}_{\text{P b}} \, \mathrm{d}\alpha^*}{\int_0^{\frac{2\pi}{\theta}} |\tilde{C}_{\text{P b}}| \, \mathrm{d}\alpha^*} \tag{4.9}$$

The work ratio, much like its equivalent in engine cycle design in thermodynamics, and similarly to the notion of margin in economics, is a measure of performance of a process; high work ratios indicate little work must be invested and spent internally for net work to be produced, and tend to translate into lighter, more reactive machines.

The two curves in figure 4.14 indicate that as the size of the blades is reduced, a slight decrease in power output and a strong increase in work ratio are observed. The wheel with the shortest blades features $L_{\text{root}}/L_{\text{wet}}$=0.5: compared to the reference standard-optimal configuration, this translates in a 58 % reduction in blade area, yet the power decreases by only 10 %, and the work ratio is increased by 80 % up to a value of 0.9. These results suggest that the immersed-blade design has tremendous potential, as it points towards lighter rotors subjected to reduced structural stresses.

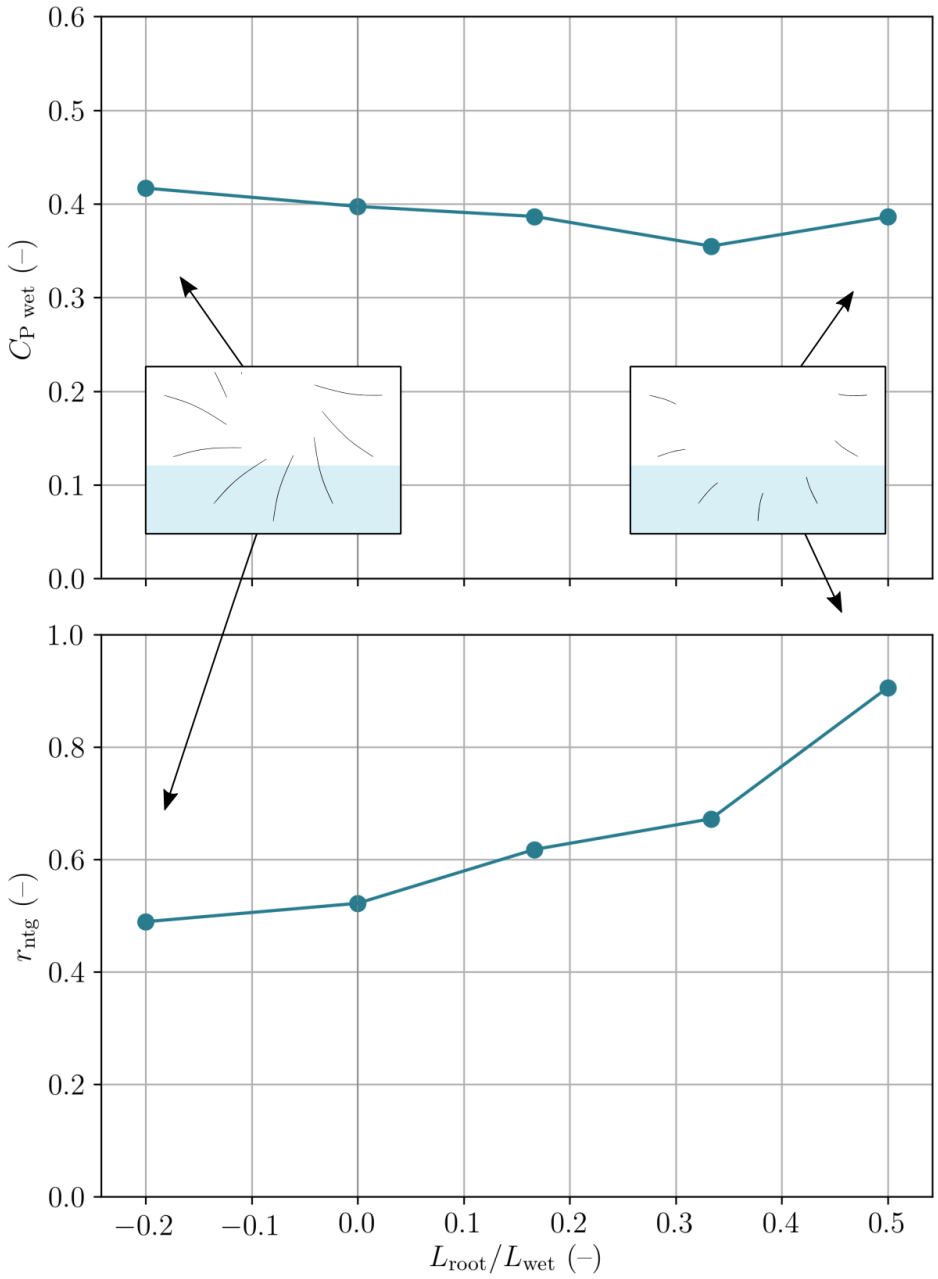

Figure 4.14: Performance of the "Magdeburg" wheel with f_{wet}=0.5, modified progressively (from left to right) as the radius of the blade root is increased. The bottom axis measures the depth L_{root} of the root of the blade (positive downwards), non-dimensionalized according to depth L_{wet}.

Figure previously published in [103]

A better understanding of this phenomena can be obtained from figure 4.15, where the blade power curves of the five wheels of interest are plotted together. There, it is seen that as the blade root radius is increased, the energy losses associated with both entry and exit from the water are reduced. The maximum torque is reduced, but the torque distribution over the stroke of the blade is widened. In fact, on the wheel with the shortest blades, maximum torque occurs at 75 % of the stroke (at this point, the blade operates in the wake of two blades further upstream), directly challenging the commonly-accepted notion that free-stream water wheels should necessarily be

drag-based machines. This trend calls for further investigation and suggests that blade root radius be included as an input parameter in further optimization studies.

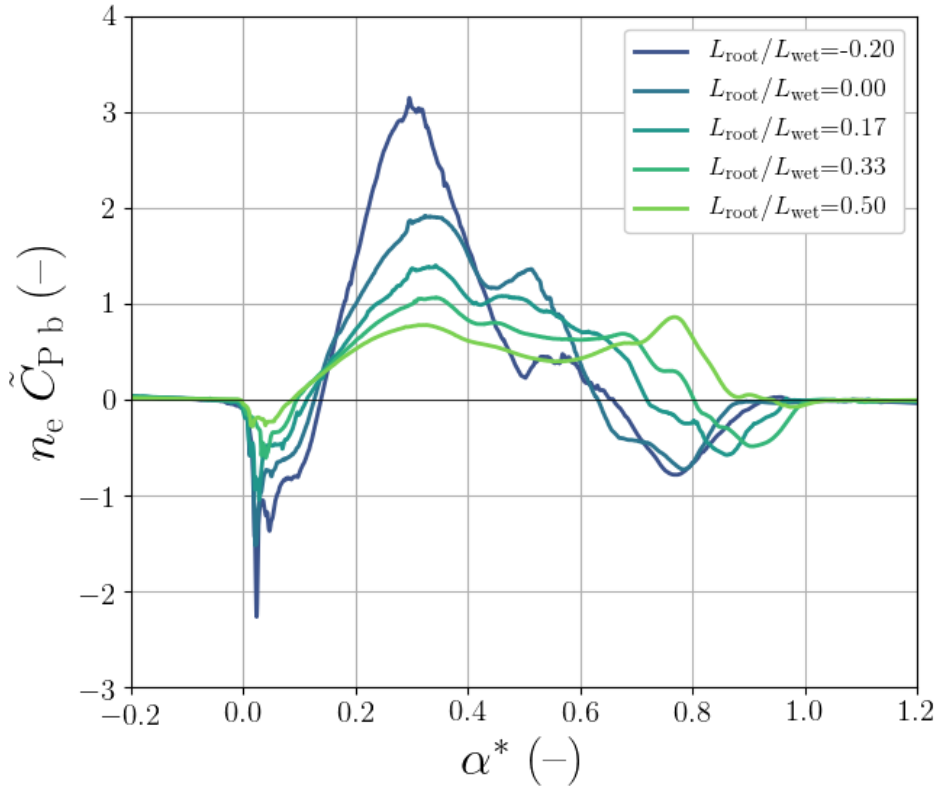

Figure 4.15: Blade power curves for each of the five cases displayed in figure 4.14. The plot displays non-dimensional power $n_e \tilde{C}_{P\,b}$ as a function of non-dimensional stroke angle α^*, so that the wet power coefficient $\overline{C_{P\,wet}}$ is recovered as the net area below each curve. Lighter color denotes increased blade root radius.

Figure previously published in [103]

This concludes this first exploration of the design parameter domain for the free-stream water wheel, which indicates that performance responds very strongly to changes in radius and relative depth. The broad trends are now clear that well-performing wheels feature either high radius and low relative depth, or low radius and high relative depth. A narrower optimization will be carried next, focusing on the "shortened-blade" modification that was proposed here.

4.4 Second 2D optimization: towards wheels with immersed blades

Following the optimization work presented in the section above and its publication in a peer-reviewed journal article [103], research was carried out in order to further study the effect of shortening the wheel's blades. Work towards this objective was performed by Abhishek Shingala as part of his Master's thesis under the mentorship of the author [107]. The present section is based on a journal article co-authored by the author (reference [111]), A. Shingala, O. Cleynen, A. Jain, S. Hoerner, and D. Thévenin. "Genetic optimization of a free-stream water wheel using 2D computational fluid dynamics simulations points towards design with fully-immersed blades". In: *Energies* (submitted) , which is, at the time of writing, undergoing peer review.

4.4.1 Setup of second optimization

The free-stream water wheel geometry considered in this work is largely similar to the geometry studied in section 4.2, and is shown in fig. 4.16. Notably, the altitude of the blade root (measured with L_{root}, the vertical distance from horizon line to root of the blade; positive downwards), is now a variable. The ratio of L_{root} to L_{wet}, already introduced in section 4.3.5, is now named the *cut radius fraction* Z_{cut}, and made one of the variables of interest:

$$Z_{\text{cut}} \equiv \frac{L_{\text{root}}}{L_{\text{wet}}} \tag{4.10}$$

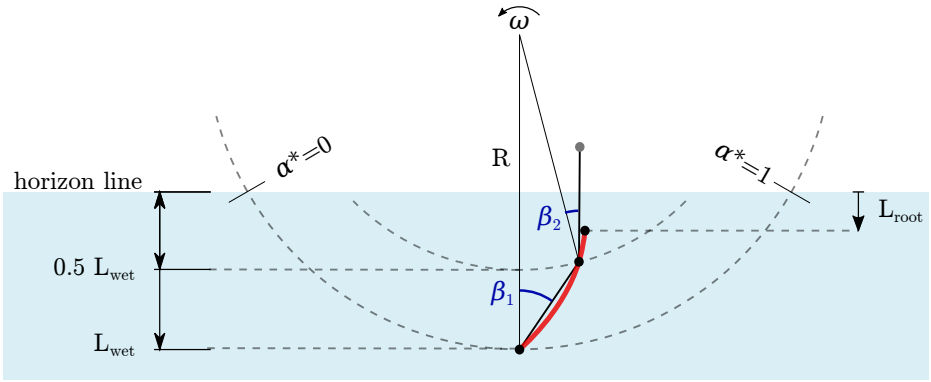

Figure 4.16: Schematic diagram of the parametrized water wheel geometry studied in this work, in which one blade is shown with a red thick spline (the number of blades is a variable in this study). This spline connects three points positioned using two angles β_1 and β_2, as in the optimization in the previous section (compare with figure 4.2 p. 91). In this new optimization, the altitude of these points is not modified, but the blade is "cut" (shortened) so that its root is located at a variable distance L_{root} from the horizon line. Water flows from left to right with free-stream velocity U_∞ and the wheel rotates in the anti-clockwise direction with angular velocity ω.

Figure from Shingala et al. submission [111]

This new, secondary optimization study has a much narrower focus than the one presented above, and aims at reducing internal energy losses associated with blade

entry and exit from the water. It considers a wheel with a given radius and depth; thus, the wet and rotor power coefficients vary monotonically together, and do not need to be considered both at once. By contrast, the quality of the power delivery is of great interest here. Therefore, the two objectives pursued simultaneously in this work are:

- Maximizing the work ratio r_{ntg} (def 4.9 p. 107);
- Maximizing the wet power coefficient $C_{\text{P shaft, wet}}$ (def 4.1 p. 89).

The parametrized CFD simulation used to evaluate candidates is only lightly modified compared to that used in section 4.2. The parametrization is modified so as to allow shortening the blades, refining the mesh at the root of the blade in the same way as at its tip, as shown in figure 4.17.

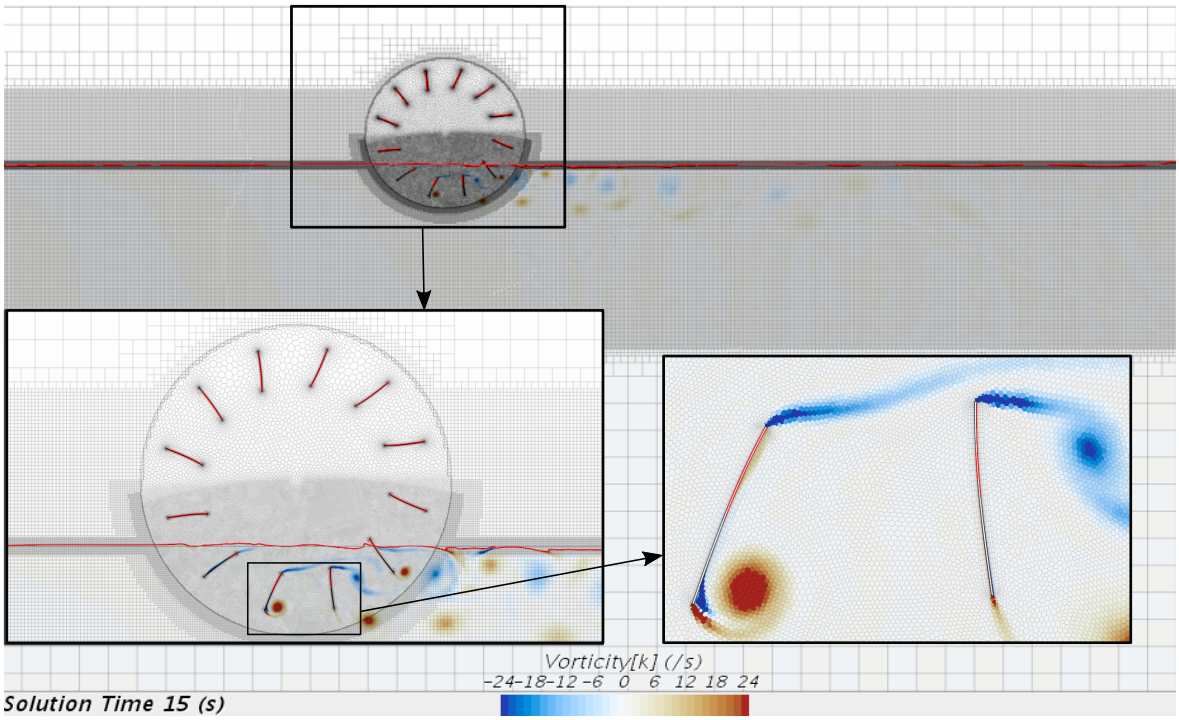

Figure 4.17: Flow field from an arbitrarily-selected simulation case in the optimization, displaying the rotating polygonal mesh rotating relative to the fixed trimmed background mesh after 15 s have been simulated. Water flows from left to right, and air is above the water surface (red line). Color denotes vorticity (with the color scale saturated at $\pm 24\,\text{s}^{-1}$). Closer visuals of the wheel and its immersed blades are also depicted.

Simulation run and figure prepared by Abhishek Shingala under mentorship by author [107], reproduced from Shingala et al. submission [111]

Results and experience gathered from the previous optimization are used to inform the choice of parameter ranges considered here. The wet radius fraction f_{wet} and the tip radius R, are kept constant at 0.5 and 1.8 m respectively, mechanically setting the wheel depth at L_{wet}=0.9 m. The free-stream inlet velocity U_∞ and tip-speed ratio are set to $1.2\,\text{m}\,\text{s}^{-1}$ and 0.5 throughout the optimization study. Values of Z_{cut} are taken in intervals of 0.1 from −0.2 (with the root of the blade protruding above the horizon, as with most conventional designs) to 0.9 (for which the blade occupies only 10 % of the wet frontal area), for a total of 12 discrete values. This range and those of the other

Parameter	Range	Interval
Number of blades (n_b)	[6, 15]	1
Beta1 (β_1), degrees	[0°, 25°]	5°
Beta2 (β_2), degrees	[10°, 30°]	5°
Cut radius fraction (Z_cut)	[-0.2, 0.9]	0.1
Tip radius (R), m	1.8	–
Wet radius fraction (f_wet)	0.5	–

Table 4.2: Range of input parameters for the present study, selected partly based on the results presented in section 4.2

input parameters, are summarized in table 4.2. Finally, after constraints were applied, the domain included 3 600 possible design configurations.

The software selected to carry out the optimization proper is, again, the `moga` genetic optimization module of Dakota 6.10 [85]. The chain of computing operations enabling the optimization is the same as described in section 4.2.

The optimization loop was initialized with a first generation of 100 candidates, 12 of which were based on geometries known to perform well in the previous study, while the other 88 were constructed using Dakota's latin-hypersquare algorithm (`lhs`).

The optimization was interrupted several times in order to adjust crossover and mutation settings, so as to keep the instantaneous Pareto front uniformly populated, a requisite for the genetic optimization to converge meaningfully. Details of the settings used for the optimization are listed in ref. [111]. When the present study completed, a total of 392 unique designs had been explored. The evaluation of these designs took a total of 66 000 CPU-hours over three months.

4.4.2 Results and analysis

Best-performing individuals

The performance of all candidates in each of the six generations is plotted in figure 4.18, where the horizontal and vertical axes respectively represent r_ntg and $C_{\mathrm{P\ wet}}$, the two objective functions to be maximized. There, candidates of later generations are depicted with smaller, lighter-colored dots. It can be observed from the figure that after the fourth generation, two groups of candidates, each favoring one objective, emerge. As the optimization reached the sixth generation, the performance of the selected individuals converged towards the top right of the figure.

Before the performance of the Pareto-optimal individuals is further analyzed, the dependence of individuals on the parameter Z_cut can be visualized; this is done in figure 4.19, where the data from figure 4.18 is shown colored according to values of Z_cut. Two groups of candidates, named as P1 and P2, are selected manually, based on their performance. Trends can be identified in the combination of input parameters possessed by each of these groups. Candidates from group P1 feature maximum $C_{\mathrm{P\ wet}}$; in general, wheels of group P1 feature fewer, long and inclined blades. By contrast, individuals from group P2 featured maximum work ratio and their blades are shorter, straighter and in greater number. Wheels of group P1 and P2 are displayed in figure 4.20.

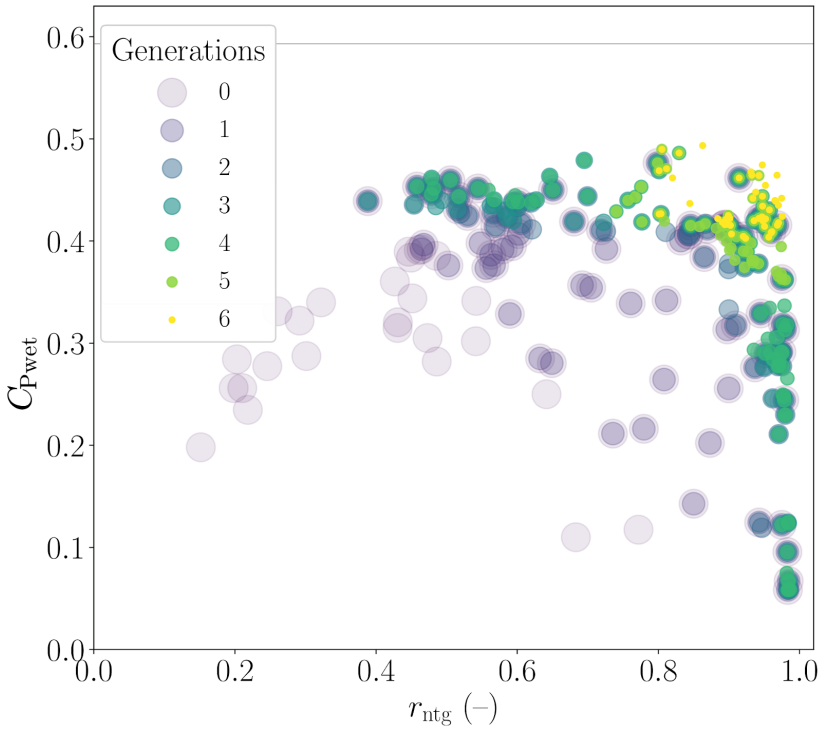

Figure 4.18: Performance of all cases evaluated during the optimization, colored according to generation, with wet-area power coefficient on the vertical axis and work ratio on the horizontal axis. A horizontal line at $y = 0.593$ indicates the Betz limit.

Figure from Shingala et al. submission [111]

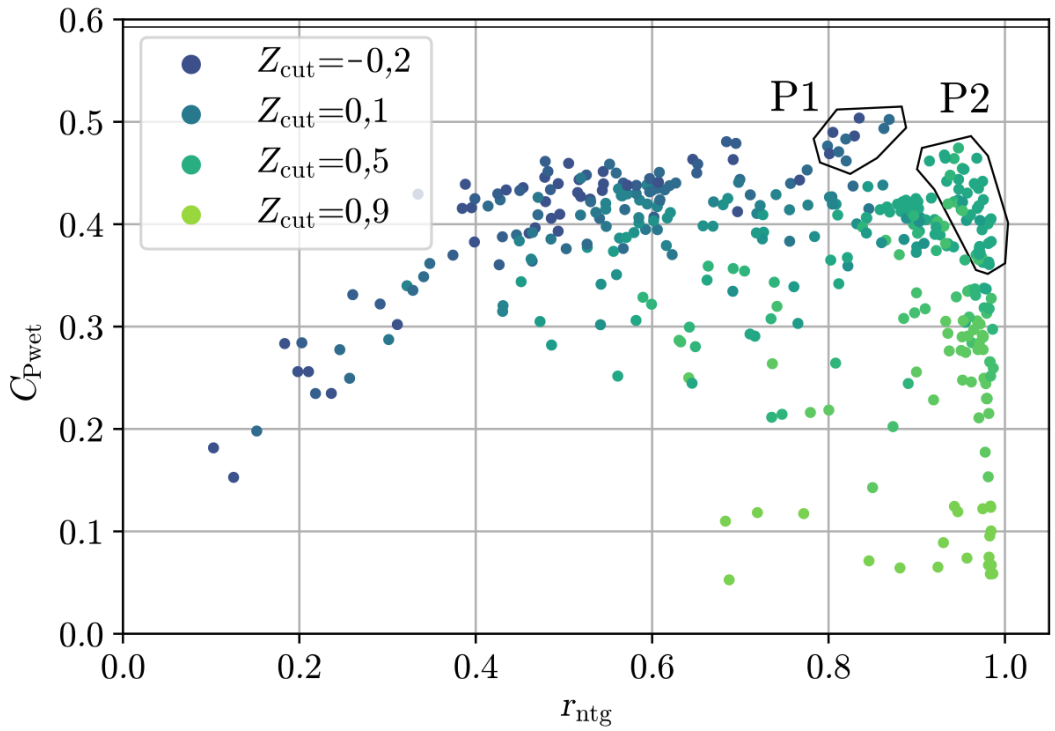

Figure 4.19: Scatter plot of all 392 evaluations, colorized with respect to their cut radius fraction (Z_{cut}). Two groups are identified manually, according to their performance and geometry. Group P1 features individuals with relatively high wet-area power coefficient, and also large blades (low values of Z_{cut}). In group P2, individuals have lower wet-area power coefficient and higher work ratio; they also feature short blades (high values of Z_{cut}).

Data reproduced from Shingala et al. submission [111]

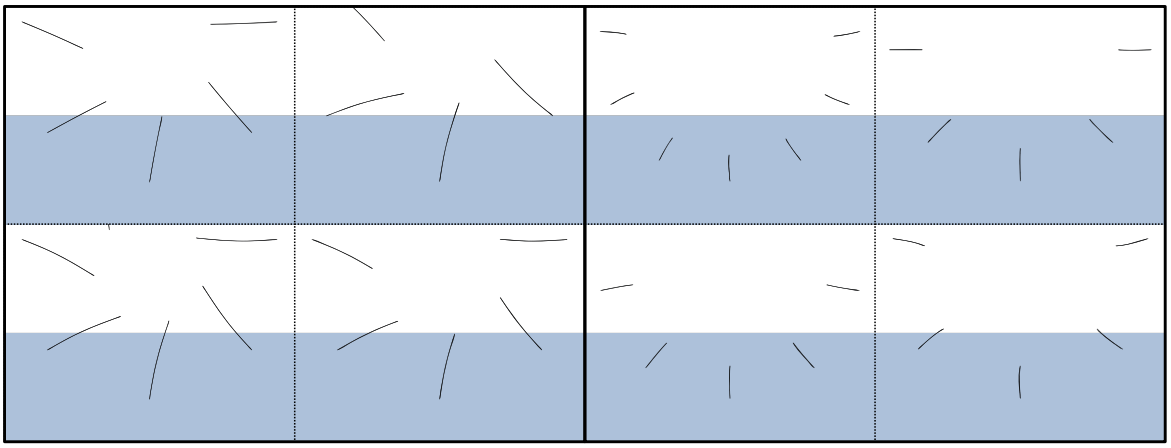

Figure 4.20: Geometries of water wheels from the broader Pareto front of the optimization. Shown on the left are four geometries from group P1; on the right, four geometries are depicted from P2 group. In this figure, blade thickness is slightly exaggerated for a clearer representation.

Figure reproduced from Shingala et al. submission [111]

In the present case, the outer-most layer of individuals from the Pareto optimal group is considered for further investigation. This Pareto front consists of five individuals (from here on designated f.1 to f.5), which are depicted together with their geometry in figure 4.21. There, the scale of both axes is so that only high-performing individuals are shown. From here on, these five Pareto-optimal candidates are further investigated, in order to converge towards one optimal design.

Detailed evaluation of top candidates

The analysis method described in section 4.3.4 is repeated here. During the optimization, power values had been extracted from CFD simulations after 3 s had elapsed (allowing the flow to settle down after initialization), and until 15 s had been simulated. In order to describe with even better accuracy the performance of the best candidates in the optimization, an additional 3 600 CPU-hours were invested by running these simulations over a longer duration of physical time. First, the power output is ignored until five blades have entered and left the water. Then, the power is extracted during a duration corresponding to 15 blades passing through the water. Time intervals obtained in this way vary according to the number of blades for each design configuration; cases with fewer blades require a longer amount of physical time. The durations considered to analyze power extraction in this study ranged from 16 to 71 s. The performance of the wheels evaluated in this detailed manner is plotted along with the results of initial evaluations into figure 4.22, where blue and green dots indicate initial and detailed evaluations, respectively.

It can be observed from figure 4.22 that the wet power coefficient and work ratio decreased noticeably for all designs, particularly so for design f.1: the average change in power is $-4.8\,\%$, except for case f.1, for which the change is $-12.2\,\%$. This detailed analysis suggests that the robustness of the evaluations in group P1 is lower in that group, due to very strong interactions with the free surface, with the formation of large waves and strong near-surface vortices, making accurate CFD evaluations very challenging. On the other hand, changes in r_{ntg} are much smaller, meaning that an

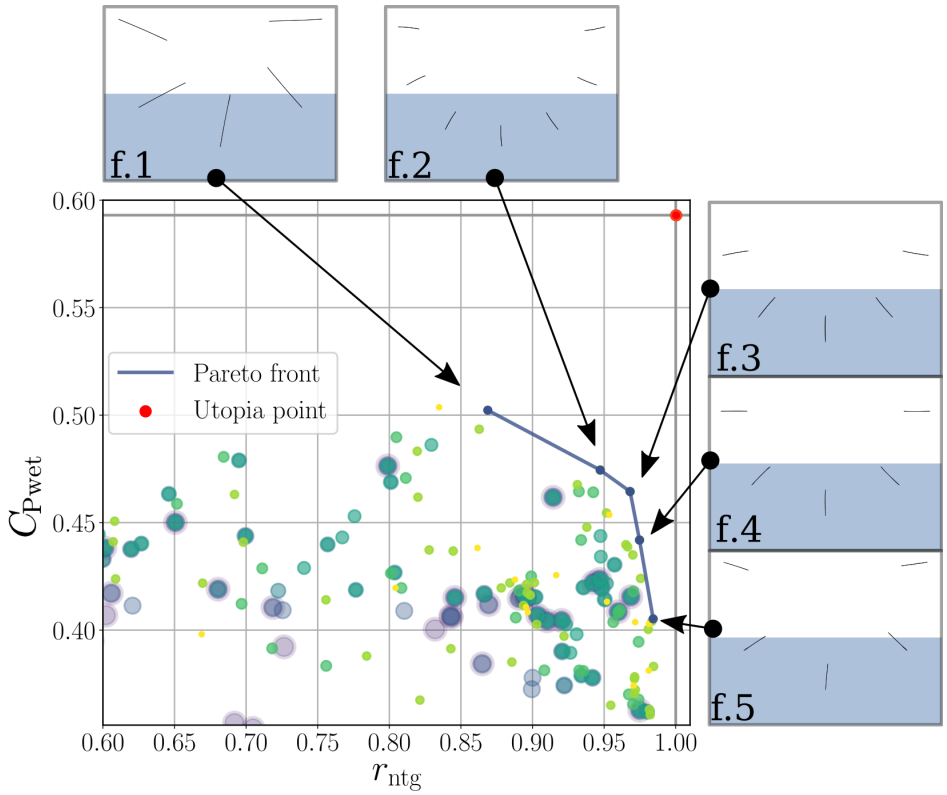

Figure 4.21: The top five best evaluations (Pareto front) of the optimization, connected with a thick blue line. The respective geometries are also depicted. Dots indicate evaluations, with their color and size indicating the generation they were produced in. The scales of both axes is such that only a portion of evaluated candidates are represented.

Figure prepared by Abhishek Shingala under mentorship by author [107], reproduced from Shingala et al. submission [111]

evaluation based on maximizing r_{ntg} leads to robust designs, highlighting the superiority of group P2 for practical applications.

The five top-performing simulations are then run for various values of tip-speed ratio λ, and their performance is then analyzed using non-dimensional blade stroke curves, a tool introduced in section 2.5.1 p. 54 and used already in § 2.5.2 & 4.3.5. The corresponding plots are shown in figure 4.23, sorted according to tip-speed ratio.

It can be observed from figure 4.23 that the power stroke curves of wheels f.2 to f.5 are largely similar. In contrast, for the f.1 water wheel, as visible from the dark blue line, the energy loss at entry and exit is distinctly larger, and it increases with tip-speed ratio. At the same time, peak blade power is also largest for design f.1. Therefore, this particular wheel induces much stronger fluctuations on the generator shaft, which translates as structural stresses.

At their optimal tip-speed ratio (figure 4.23(b)), the wheels with short blades, f.2 to f.5, produced power for 92 % of the stroke duration on average. Power is delivered in a regular manner, growing rapidly at first, and then maintaining a value close to the mean power delivery up until late in the stroke. At optimal rotation speed (λ=0.4), power is delivered up until $\alpha^{\star}$=0.9 (at which point the blade is 48° past the nadir point), when the blade is operating in the wake of two other blades further upstream. This is evidence that, as had been tentatively suggested in sec. 4.3.5, the optimum free-stream water

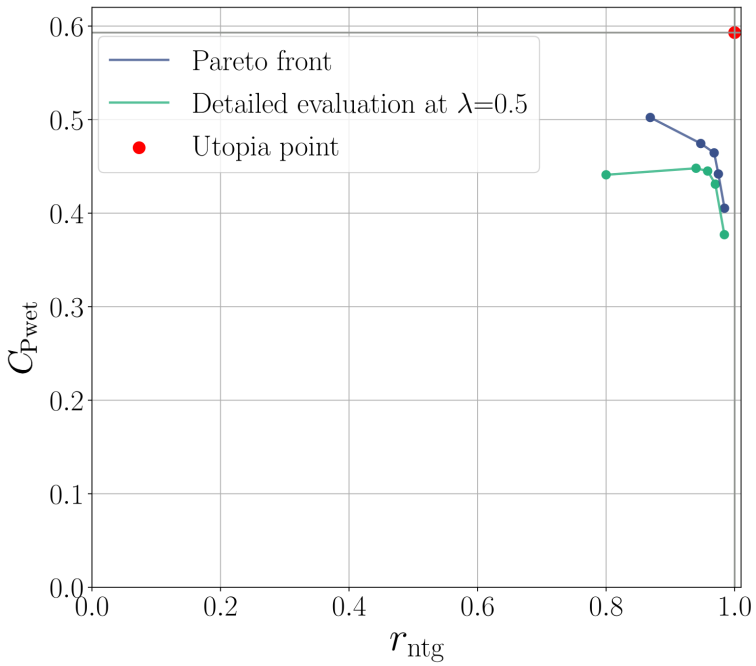

Figure 4.22: Performance of the top five designs (Pareto front) evaluated once with a standard duration of physical time (15 s, as with all individuals during the optimization), and once with thorougher criteria (as detailed in the text).

Figure prepared by Abhishek Shingala under mentorship by author [107], reproduced from Shingala et al. submission [111]

wheel is clearly not a purely drag-based machine. The optimization clearly indicates that for this radius and depth, wheels with fully-immersed blades (Z_{cut}=0.5) perform best, both from the point of view of net power output, and quality of mechanical power delivery.

Among the five wheels selected as part of the Pareto front, the three wheels f.2, f.3 and f.4 showed better performance compared to f.1 and f.5. Since these three wheels have very similar geometry and performance, the configuration with the lowest number of blades is selected, reducing construction cost and maximizing simplicity: therefore, the wheel f.4 is designated as the optimal design in this study.

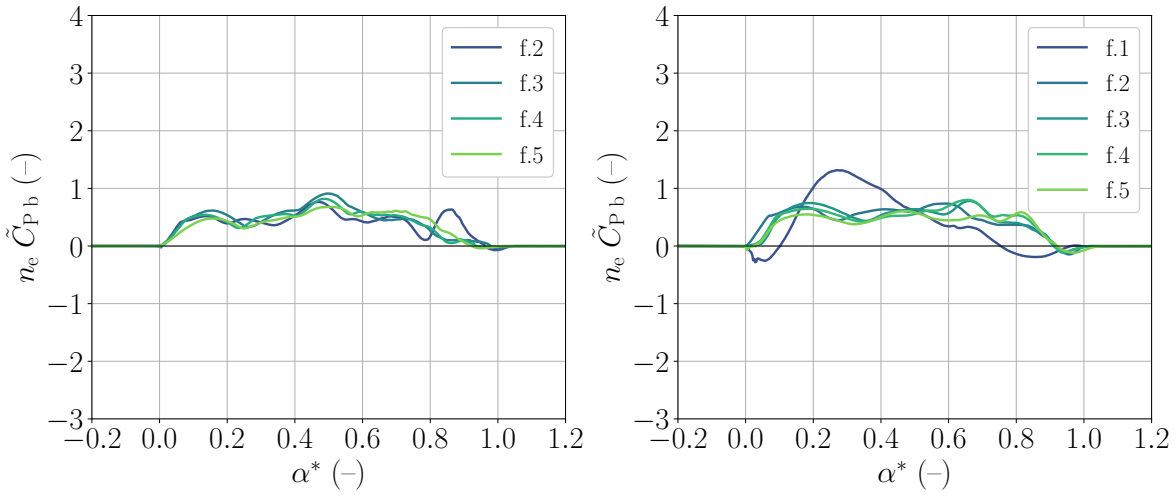

(a) λ=0.3

(b) λ=0.4

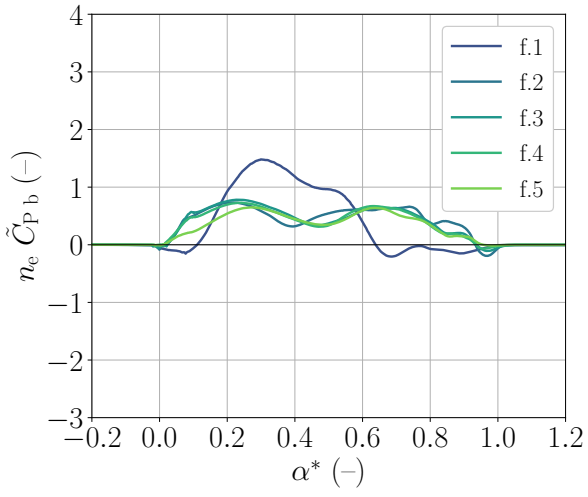

(c) λ=0.5

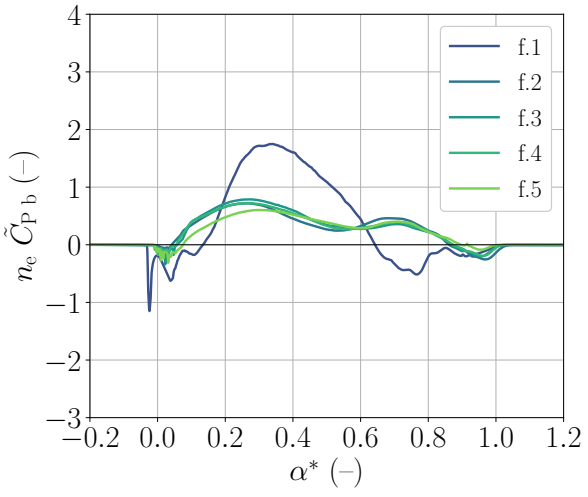

(d) λ=0.6

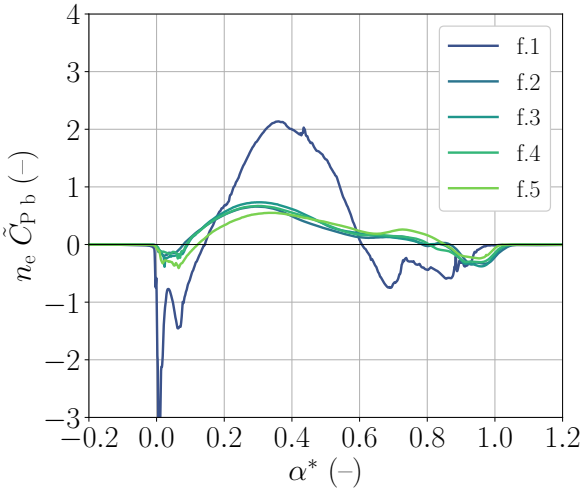

(e) λ=0.7

Figure 4.23: Non-dimensional blade power curves ($n_e \tilde{C}_{P,b}$) as a function of non-dimensional stroke angle ($\alpha^\star$) for the five Pareto-optimal wheels, plotted in separate diagrams for different tip-speed ratios. The part of the curves below the zero-line corresponds to energy transferred from the wheel to the water, which should obviously be avoided. In part a), the simulation corresponding to configuration f.1 could not be completed in time for publication.

Figure reproduced from Shingala et al. submission [111]

Comparison of optimized designs between different studies

A comparison of the best evaluations obtained here with those obtained previously in section 4.3 is carried out below.

The previous optimization study had considered a much larger domain, with wheel diameters ranging from 0.4 to 6 m in diameter, and 0.2 to 1 m in depth; the work ratio had not been considered. To address this very broad domain, a family of Pareto-optimal wheels (named "*Magdeburg*") had been proposed in section 4.3.3 p. 98. Within this family, the design configuration corresponding to f_{wet}=0.5 and R =1.8 m (the same input parameters as those of the study presented here) is presently considered, in order to compare its performance with result from the second optimization.

The geometries of the wheel selected from the previous optimization study and of the optimal wheel from the current study are shown in figure 4.24. The previous study constrained the geometry so that at this radius, the root of blades would remain above the water surface; while the current study finally recommends an immersed root blade.

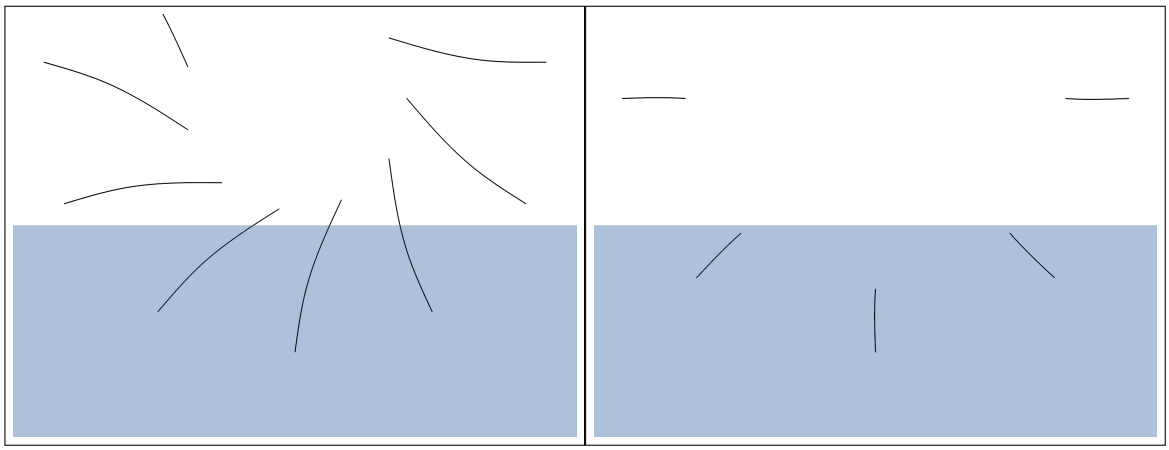

(a) Wheel from previous optimal family (b) Newly-optimized wheel

Figure 4.24: Sketch of the geometry of the optimal wheel selected out of the former optimization results for the given radius and depth (left), and the optimal wheel from the current study (right)

Figure prepared by Abhishek Shingala under mentorship by author [107], reproduced from Shingala et al. submission [111]

The performance of each wheel was evaluated at its respective optimum tip-speed ratio; the results are summarized in table 4.3.

It is observed from the results in table 4.3 that the work ratio of the optimized wheel obtained from the new study is 113 % higher than the wheel suggested by the guidelines in the previous optimization. Moreover, the wet- and rotor-area power coefficients are improved by 8 % and 8.2 % respectively. This improvement in the power output has the same order of magnitude as the uncertainty associated with carrying shorter evaluations during the optimization proper, compared to more detailed evaluations (as visible in figure 4.22 p. 116). Nevertheless, the improvement here is quantified by comparing two wheels with the same, rigorous method.

The total blade surface area per unit width for the new optimal wheel is 7.25 m^2/m, which is 71 % less than the area of the wheel proposed by the model in the previous study

Wheel selected out of previous optimization	Current optimal wheel, design f.4
Input variables $n_\mathrm{b} = 11$ $\beta_1 = 10°$ $\beta_2 = 25°$ $Z_\mathrm{cut} = -0.2$ $\lambda_\mathrm{optimal} = 0.5$	Input variables $n_\mathrm{b} = 8$ $\beta_1 = 0°$ $\beta_2 = 10°$ $Z_\mathrm{cut} = 0.5$ $\lambda_\mathrm{optimal} = 0.4$
Objective functions $C_\mathrm{P\ wet} = 0.42$ $C_\mathrm{P\ rotor} = 0.10$ $(r_\mathrm{ntg} = 0.45)$	Objective functions $C_\mathrm{P\ wet} = 0.45$ $(C_\mathrm{P\ rotor} = 0.11)$ $r_\mathrm{ntg} = 0.96$

Table 4.3: Comparison of the characteristics and performance of the two wheels shown in figure 4.24. On the left, one design among a family of optimal designs obtained in the previous optimization study (§4.3.4, ref. [103]), selected because its radius matches that of the new study. On the right, the optimum design obtained in the new optimization study. The performance of each wheel is evaluated at its optimum tip-speed ratio.

($25.1\,\mathrm{m}^2/\mathrm{m}$). This translates into substantial material savings, as well as a reduction in production cost and structural weight.

The performance of both wheels is compared in figure 4.25, using the approach introduced in section 2.5.1. In this figure, the green and red areas under the curve represent positive and negative contributions of power to the net shaft power, respectively.

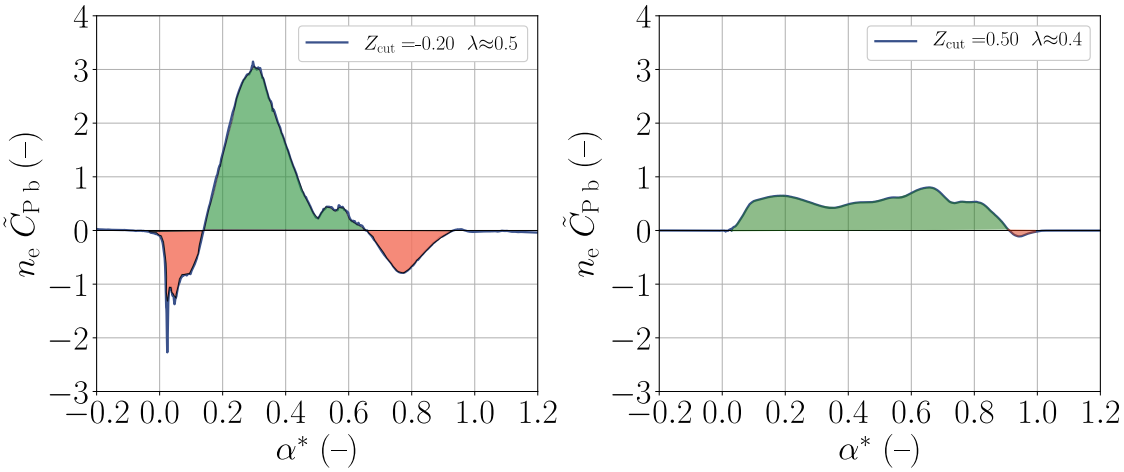

(a) Wheel selected from previous optimization (b) Optimal wheel from new optimization

Figure 4.25: Blade power curves ($n_\mathrm{e}\tilde{C}_\mathrm{P,\,b}$ vs $\alpha^\star$ curves, see 2.5.1) for results of the previous (left) and new (right) optimization studies.

Figure prepared by Abhishek Shingala under mentorship by author [107], reproduced from Shingala et al. submission [111]

It can be seen from figure 4.25a that in the wheel selected out of the previously-proposed optimal family of designs, considerable energy loss occurs due to the entry splash and blade exit. These occur for $\alpha^\star \in [0 - 0.14]$ and $\alpha^\star \in [0.66 - 1]$. The maximum torque occurs at around 35 % of the stroke, and large oscillations in power delivery are observed,

which is not desirable. By contrast, in the case of the new optimal wheel, losses have become almost insignificant (figure 4.25b). Power is produced consistently between $\alpha^\star$ values ranging from 0.01 to 0.92.

Thus, the concept of the immersed blade design is proven to be beneficial when maximizing performance of a free-stream water wheel with a radius of 1.8 m and a depth of 0.9 m, at least for the free-stream velocity of 1.2 $\mathrm{m\,s^{-1}}$ considered here. This suggests that the performance of wheel designs with other configurations may also be improved by increasing the blade root radius. This hypothesis is investigated in the following paragraphs.

Revised "Magdeburg" standard-optimal model

The optimization carried out in section 4.3 had led to proposed design guidelines covering a wide range of designs, in an attempt to cover broadly the Pareto front that appeared when maximizing simultaneously the pure wet-area performance (measured using $C_{\mathrm{P\ wet}}$) and the power density of the device (measured using $C_{\mathrm{P\ rotor}}$). Eleven wheel designs produced using these guidelines had then been evaluated in a detailed manner in section 4.3.4, revealing that their performance was not fully Pareto-optimal in this regard, especially for f_{wet} values between 0.55 and 0.75. In the light of the results obtained in this new optimization work while studying a more restricted parameter range, results from the former optimization can be revisited. To this end, eleven wheels built according to the "*Magdeburg*" guidelines were modified so that their blades were shortened with Z_{cut}=0.5. The flow through each of these wheels was simulated for five values of λ, and their performance was evaluated according to the same detailed method described in section 4.3.4 above, consuming a total of 29 000 CPU-hours.

The results from this new evaluation are described in figure 4.26. In fig. 4.26a, the vertical and horizontal axes display respectively the wet- and rotor-area power coefficients (the two objective functions that were to be maximized in §4.3). The gray dots are the wheels from the previous "Magdeburg" family, evaluated at λ=0.5, as first obtained in section 4.3. The blue dots indicate the performance of the modified wheels —identical in all respects except for their shortened blades— operated at their optimal tip-speed ratio (λ_{opt}=0.4 for most wheels). In this figure, it is seen that for all but the largest and smallest wheels, the power output of the wheels is significantly increased when the blades' size is reduced so that Z_{cut}=0.5.

In fig. 4.26b, the vertical axis again stands for the wet-area power coefficient, but the horizontal axis represents the work ratio. The performance of the same wheels (from both the first and the second optimizations) is displayed using the same color code. Since the work ratio was not considered as an objective function in the former optimization, it is not a surprise that neither curve resembles a Pareto front. Nevertheless, the effect of shortening the blades is very clear: the work ratio of all wheels is drastically improved, with eight of the short-bladed wheels reaching r_{ntg}>0.9.

These results make it unambiguous that reducing the length of the free-stream water wheel's blades, so that the blades become fully-immersed in the water during the power stroke, increases the performance of wheels with diameters and depths far below and above those of the wheel optimized in this second optimization. Even though this final investigation only identifies local optima, in the wait for a further optimization, the guidelines given in section 4.3.3 are hereby updated to add Z_{cut}=0.5 for every wheel.

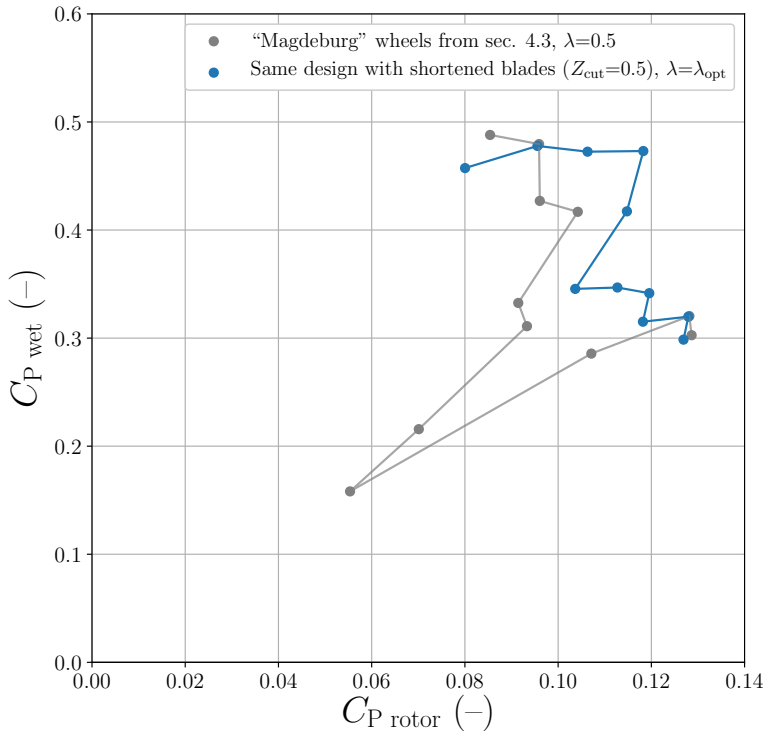

(a)

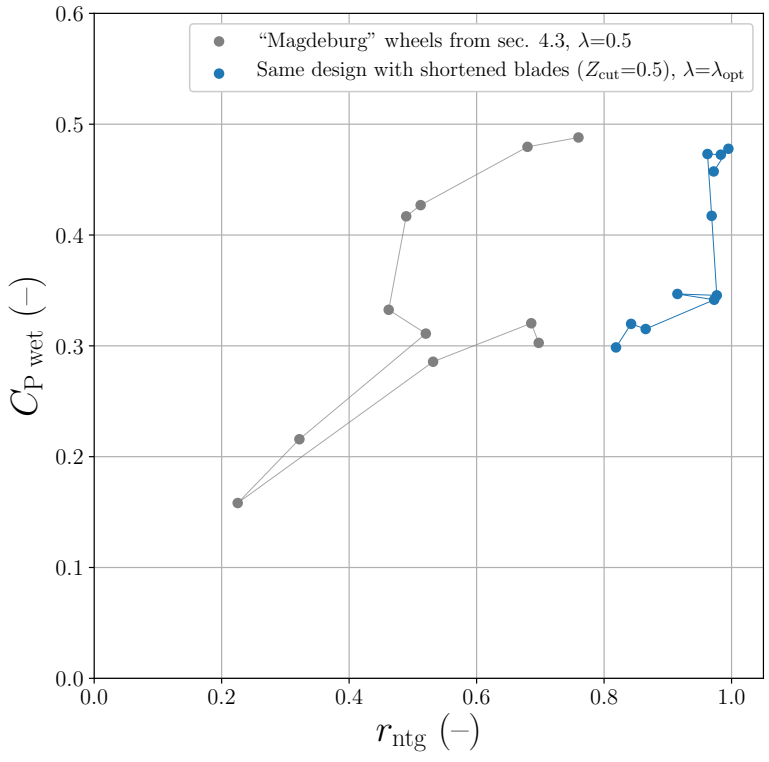

(b)

Figure 4.26: Performance of wheels of the "Magdeburg" family of designs, constructed in section 4.3 (published in [103]), compared to the same wheels modified with their blades shortened at Z_{cut}=0.5. In these two series of simulations, the wheels range from 6 m diameter (wheels with best $C_{P\ wet}$) down to 0.4 m diameter (wheels with best $C_{P\ rotor}$). Part a) displays the wheels' power output performance (wet- vs. rotor-area power coefficient), while part b) displays the wheels' wet-area power coefficient vs. work ratio r_{ntg}.

Figure reproduced from Shingala et al. submission [111]

4.4.3 Two-dimensional simulations: further work

The promising results brought by "simply halving" the blade geometries which had been obtained through the large-scale optimization in section 4.3.3 suggest that further improvements may be obtained by considering the parameter Z_{cut} and the objective function r_{ntg} in yet another optimization. The set of all evaluations completed so far (over 2 400) makes for an excellent database with which to suitably initialize a first generation, and inform the selection of parameter ranges of interest. In this way, an optimization with three simultaneous objectives (maximize $C_{\text{P wet}}$, $C_{\text{P rotor}}$ and r_{ntg}) could be run, searching across a still wider number of parameters (perhaps including the tip-speed ratio λ), with a credible chance of finally producing a true Pareto front to answer the water wheel design questions originally proposed in chapter 2.

On a less ambitious scale, the tools developed in the present chapter can be used to investigate other modifications. A potentially effective and relatively simple method for increasing the power output of free-stream water wheel is to use a deflector device; optimal geometries for similar turbines have already been devised using numerical tools [31, 89]. Work is underway which aims to identify an optimum deflector shape for the free-stream waterwheel using the very methods presented in the present article (figure 4.27).

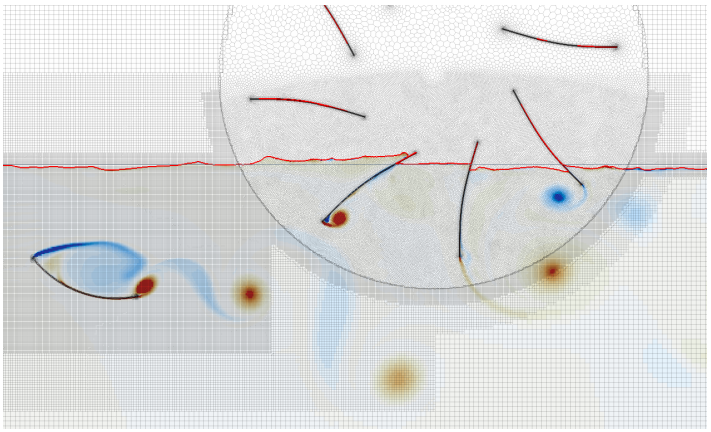

Figure 4.27: A two-dimensional CFD simulation based on the current work, also steered with a genetic optimizer, as part of the search for an optimal deflector shape to improve the power characteristics of the free-stream waterwheel. The color scale and visualization match those of figure 4.17 p. 111.

Simulation prepared and run by Aman Jain under mentorship by the author, reproduced from Shingala et al. submission [111]

Finally, it can be noted that the dynamics of the short-bladed wheel displayed in figure 4.25 indicate that the blades are developing power continuously during their stroke. This occurs as they deflect the flow upwards in the first third of their stroke, and downwards in the last third. As noted before, this is evidence that lift and not just drag contributes significantly to the power production. In turn, this suggests that a thick body may perform better in this role than a low-thickness blade. As done in the University of Magdeburg already for other types of turbines [90], a new optimization could be run to search for an optimal "thick-body" blade geometry, over which flow attachment and separation would occur at advantageous points in the power stroke, further improving performance.

4.5 Preliminary 3D models of free-stream wheels

The time span for the present thesis did not allow for in-depth numerical studies using three-dimensional models. Nevertheless, the results of preliminary works are presented in this final section. These include a simplified, porous-body model used for a first assessment of floater interference, and two full moving-rotor simulations used to describe three-dimensional flow around rotors.

4.5.1 Analysis

There are three main three-dimensional effects that affect the fluid flow around a free-stream water wheel, which two-dimensional descriptions cannot completely describe. These are, by order of decreasing importance:

Mass flow distribution The wheel blades exert a force on the water, decreasing its momentum and thereby its velocity. By virtue of mass conservation, this decrease velocity is compensated elsewhere by a velocity increase. In two-dimensional descriptions of the flow, just like one would observe in a real-world installation constrained by walls immediately left and right of the rotor, the water is accelerated below the wheel, and the same mass flow is obtained at every cross-section of the flow (per the mass balance equation solved in every cell). In a three-dimensional installation, water is also deviated to the sides of the installation, thereby depriving it of part of the available mass flow. In that sense, the two-dimensional simulations used up to here "feed" the wheel with an exaggerated mass flow and likely overestimate its power output.

Floater interference In a floating installation, the rotor, as well as the mechanical and electrical equipment which it connects to, must be supported by a floater system of some kind. A suitable position for those floaters is to each side of the rotor, which make two-dimensional studies unable to take them into account. Their displacement is expected to influence the power available to the wheel, and may affect the blade power stroke dynamics, as already reported during experimental investigations in section 3.3.

Wave propagation In two-dimensional descriptions, surface waves created by the entry and exit from the water of the blades propagate only upstream and downstream; while in three-dimensional cases, they can spread laterally as well. This likely translates into an exaggeration of the amplitude of those waves and their influence on the power delivery in 2D simulations.

Preliminary studies of floater interference are presented in the following subsection; while preliminary studies of the effect of mass flow distribution are carried out later in section 4.5.3.

4.5.2 Floater interference and blockage ratio

An influence of the floater installation on the power delivery of the mid-scale experimental installation mounted on the *Vector 1* catamaran was already observed in the campaign

described in section 3.3. There, the ship's very large mass (23 ton) when considering the modest size of the wheel (1.5 m diameter) and the high speeds pursued probably exaggerated that influence compared to those to be found in a more realistic free-stream installation.

In order to investigate this effect more closely, a series of three-dimensional simulations was built, derived from the complete model presented in section 2.3. These were set up and run by Farooq Hussain as part of his Master's thesis under the mentorship of the author: F. Hussain. "Numerical investigation of the ducting of free-surface hydraulic devices". Master's thesis. University Otto von Guericke of Magdeburg, Germany, Laboratory of fluid dynamics, 2018 (reference [75]). Results derived from selected parts of this work are presented here.

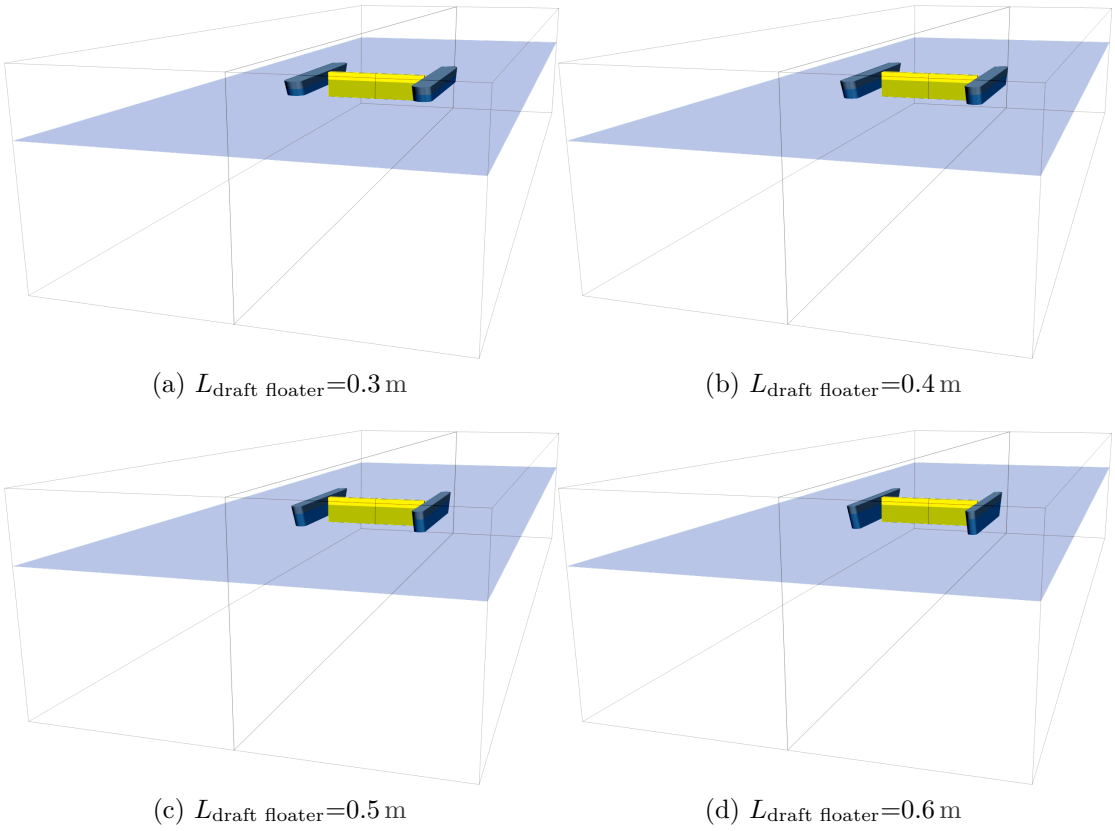

(a) $L_{\text{draft floater}}$=0.3 m (b) $L_{\text{draft floater}}$=0.4 m

(c) $L_{\text{draft floater}}$=0.5 m (d) $L_{\text{draft floater}}$=0.6 m

Figure 4.28: Four of six floater geometries studied using the porous body family of three-dimensional simulations. Seen each time are the domain edges, the water surface (water flows from foreground towards the background), the yellow porous body and gray floaters. The representation of the bodies is mirrored through the longitudinal center plane, which is set as a symmetry (zero-gradient) plane in the simulation. The floater static buoyancy is maintained constant across simulations.

Simulations prepared and run by Farooq Hussain under mentorship from the author [75]

A family of 3D simulations was prepared to carry out parametric studies. Because of the extremely high computational costs involved in describing the flow close to moving blades, a simplified approach was adopted: the wheel's hydraulic power subtraction was modeled using a porous body (a set of mesh cells configured to act as a momentum sink). The block of porous cells was sized so it would feature the same frontal area as the blades it abstracted for. Its inertial and viscous resistance properties were adjusted to $15 \cdot 10^3\,\mathrm{kg/m^4}$ and $5 \cdot 10^3\,\mathrm{kg\,m^{-3}\,s^{-1}}$ respectively — these values ensured that velocity

distributions 1 m upstream and downstream of the rotor axis were closest to those extracted from the moving-blade simulation from section 2.3.

The domain was set to be 29 m long and 3.7 m deep, with a central plane of symmetry splitting the installation in halves. The free-stream velocity was set as $1.5\,\mathrm{m\,s^{-1}}$. A 5.6 m-long floater was installed next to the porous body, its geometry parametrized so that its draft (immersed depth) could be changed by modifying its width, while keeping the static buoyancy constant. After mesh size independence of the main metrics of interest (flow rate through and force exerted on the porous body) was observed, the final mesh contained approximately one million cells.

The first investigation of interest quantifies the influence of floater draft on the extracted hydraulic power. To this effect, the floater geometry was altered in several steps, reaching up to $L_{\text{draft floater}}$=0.6 m, as shown in figure 4.28. Each time, the hydraulic power absorbed by the porous body was calculated (as multiple of the drag force and surface-averaged axial velocity) and non-dimensionalized. The results are presented in figure 4.29.

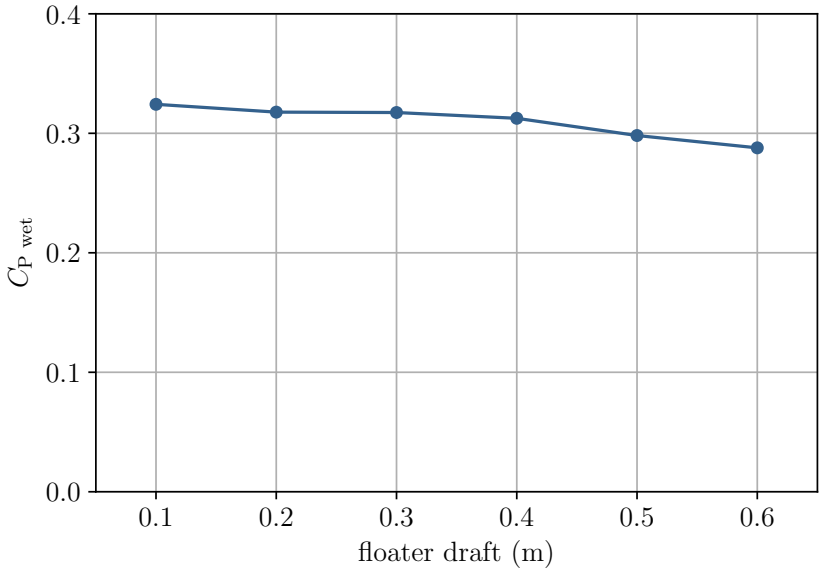

Figure 4.29: The hydraulic (wet-area) power coefficient of the porous body, as a function of the floater draft, for simulations illustrated in figure 4.28

Data from simulations prepared and run by Farooq Hussain under mentorship from the author [75]

From figure 4.29, it is observed that duct draft has a modest influence on the hydraulic power extracted in the simulations. A decrease of 0.036 power coefficient (−11 %) is observed as $L_{\text{draft floater}}$ is increased from 0.1 m (wide, "flat" shallow floaters) to 0.6 m (narrow, deep-reaching floaters). This observation, which may run counter to intuition (one might expect on the contrary that inhibition of three-dimensional flow structures around the floater may lead to improved power extraction), must however be taken with caution: the porous resistance properties were kept constant across simulations. As has been discussed in chapter 1, changes in ducting may affect not just the available power, but the relative flow velocity required to achieve it (see e.g. figure 1.7 p. 26). To ensure that only a series of maxima is displayed in figure 4.29, an iterative process varying porous resistance and seeking for maximum extracted power would be needed.

In the second investigation, the duct with $L_{\text{draft floater}}$=0.4 m (illustrated in figure 4.28b) was selected, and the depth of the domain was varied, in order to vary the blockage ratio (ratio of frontal area of device to water inlet area). In this way, the blockage ratio was varied from 5 to 14 % in nine steps; each time, the extracted hydraulic power was quantified and non-dimensionalized. These results are plotted in figure 4.30.

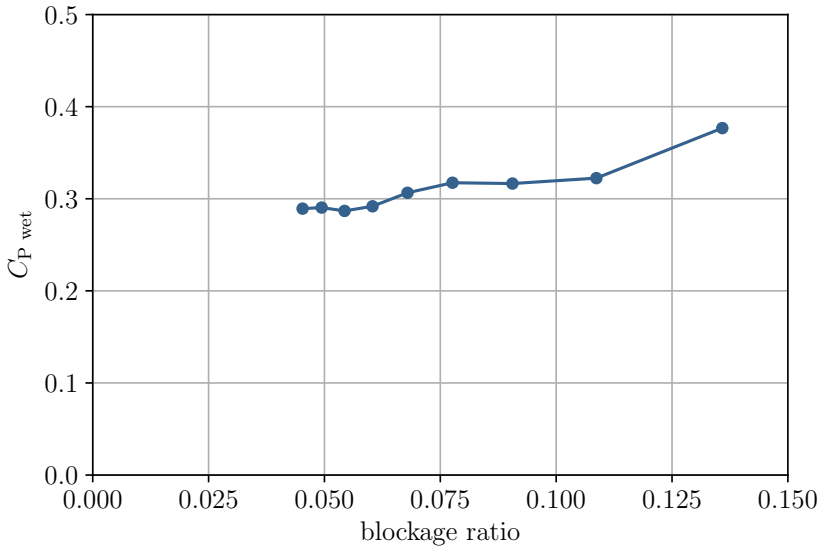

Figure 4.30: The hydraulic (wet-area) power coefficient of the porous body, as a function of the blockage ratio in the 3D simulation

Data from simulations prepared and run by Farooq Hussain under mentorship from the author [75]

In figure 4.30, it is seen that even low values of blockage ratio affect the hydraulic power extracted by the porous body. As the blockage ratio is reduced from 13.6 % down to 4.5 %, the power coefficient drops by 0.087 (−23 %) — a considerable decrease.

Again, in these two relatively simple investigations, the cautionary remarks written above apply: the porous body properties should be iteratively adapted in order to seek local maxima. Nevertheless, results suggest that the combined effects of blockage ratio and volume distribution of the floaters is substantial, warranting their investigation in future work.

4.5.3 Three-dimensional flow around rotors

In the final investigation of this thesis, two preliminary, three-dimensional simulations of wheels are presented. The geometry for these two wheels is taken from the updated "Magdeburg" family from section 4.4. Wheel "A" is a 0.8 m-diameter wheel with depth 0.32 m, maximizing power per unit rotor area. Wheel "B" on the contrary is designed to maximize power per unit of wet area, and features a 4 m-diameter with a depth of 0.94 m. As shown in figure 4.31, the two wheels are modeled in 3D simulations similar to those described in section 2.3 p. 49, with only the blades in their lower section actually taken into account for fluid flow calculations.

The mesh is refined in three successive phases, allowing for the flow to settle progressively, in order to decrease computational costs. A view of the mesh structure for case B is provided in figure 4.32. In their finest configuration, the simulations for cases A

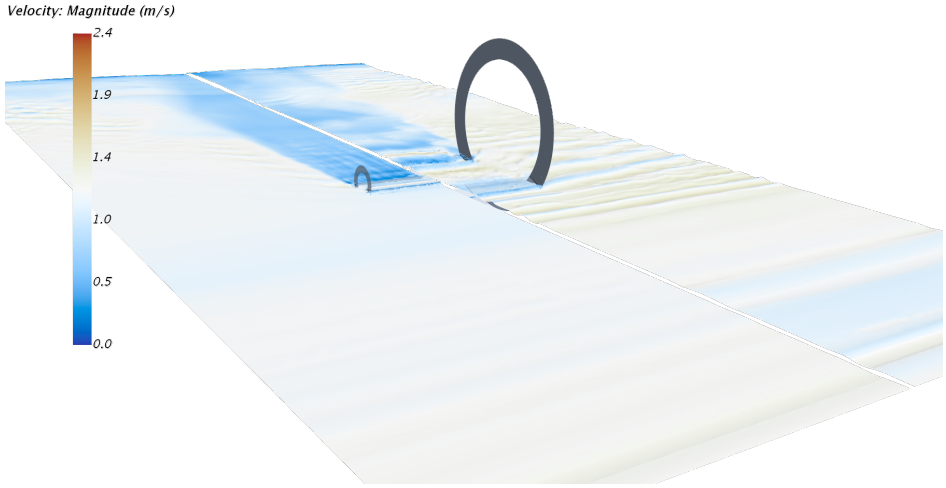

Figure 4.31: Overview of the final two three-dimensional simulations carried out in this work, represented together in a single image for comparison. The flow is from the foreground towards the background, with water colored according to its velocity (the color scale is centered around the free-stream velocity U_∞=1.2 m s^{-1}, in white). On the left, case A (designed to maximize power per unit rotor area). On the right, case B (designed to maximize power per unit of wet area).

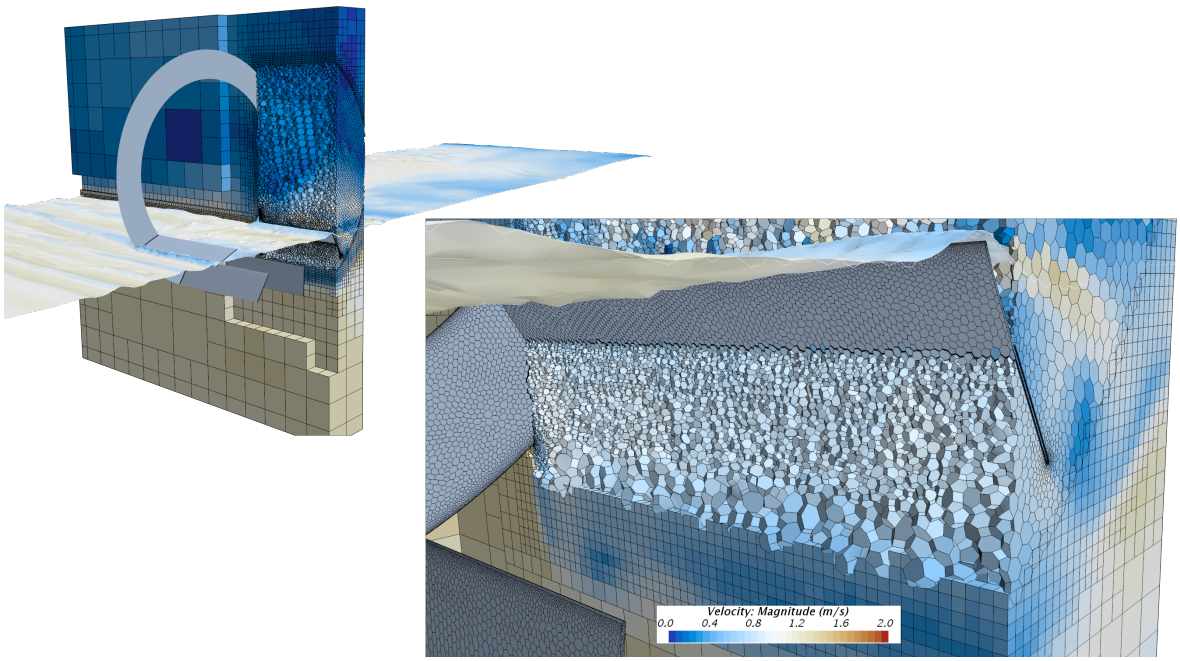

Figure 4.32: Mesh structure of the simulation for case B (left: overview; right, close-up view). A cross-flow block of cells encompassing one blade is shown, revealing the structure of the static and rotating meshes used to compute the flow. The surface of the cells and of the water is colored according to velocity.

and B feature 1.4 and 3.2 million cells respectively. All numerical settings are otherwise identical to these presented in section 2.3.

Unfortunately, after over 7 100 CPU-hours invested in both calculations in three successive mesh refinement steps, the main metrics in the simulations (velocities near the rotor, moments exerted on blades) fail to exhibit mesh size independence. While the wet-area power coefficients reach realistic values (0.23 and 0.35 for cases A and B respectively), the uncertainty associated with those values is too high to make any meaningful comparison

with those obtained in the two-dimensional simulations. Instead, in the scope of the time available for the work in this thesis, a brief outlook into the three-dimensionality of the flow is given below.

The first investigation quantifies the mass flow in a series of vertical, cross-flow planes, all positioned 2 m downstream of one another, as shown in figure 4.33. These planes reach down to the channel bed surface, but are only exactly as wide as the rotor.

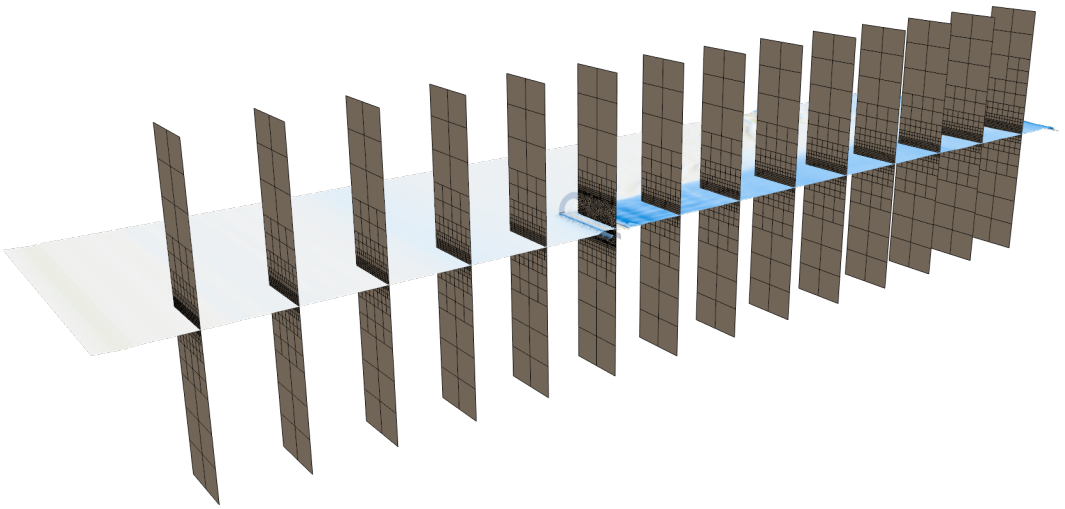

Figure 4.33: A series of 14 cross-flow sections positioned in the simulated domain, for case A. The mass flow through each of these planes, as a fraction of the mass flow in the first plane, is plotted in figure 4.34.

For each of the planes, the mass flow is extracted after the simulation has stabilized. The values are expressed as a fraction of the mass flow in the plane in the most upstream position. This data, for both cases A and B, is reported as a function of the planes' flow-wise position in figure 4.34.

In figure 4.34, it is visible that mass deficit occurs already 2 to 4 m upstream of the rotors, and is never really recovered in the following 16 m downstream. As expected, the effect is much pronounced for wheel B, which not only extracts 4.5 times more power, but also results in higher blockage ratio.

The two curves indicate how much of the mass flow in the path of each wheel is affected by its presence, and deviated to the sides. In a way, they indicate how much of the mass flow in the two-dimensional simulations ought to be "removed" from the domain at different flow-wise positions if a strict equivalence with three-dimensional simulations were to be kept.

A further visualization of the mass balance issue associated with two-dimensional simulations is provided with figure 4.35. There, a longitudinal plane is seen slicing through the two 3D simulations, with flow from left to right, just like in the 2D simulations from the sections above. In this plane, the mass flux in the direction of the rotor axis —towards and away from the viewer— is plotted as a scalar field. The values in these two images are by definition zero in the 2D simulations, so that again the three-dimensionality of the flow is highlighted.

In figure 4.35, it becomes apparent that the spatial resolution of the mesh used is largely insufficient to properly account for the flow. Indeed, very high gradients of the mass

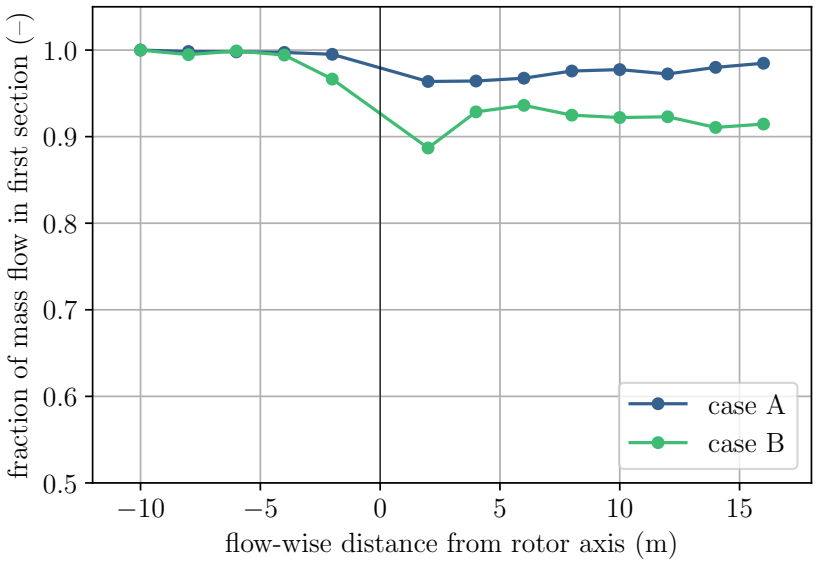

Figure 4.34: The mass flow passing through each of the planes displayed in figure 4.33, expressed as a fraction of the mass flow in the plane furthest upstream. On the horizontal axis is the flow-wise position relative to the rotor axis (positive downstream). Data for the planes immediately in the wake of the rotor B displayed significant oscillation in time, and time-averaged values were adopted for display here.

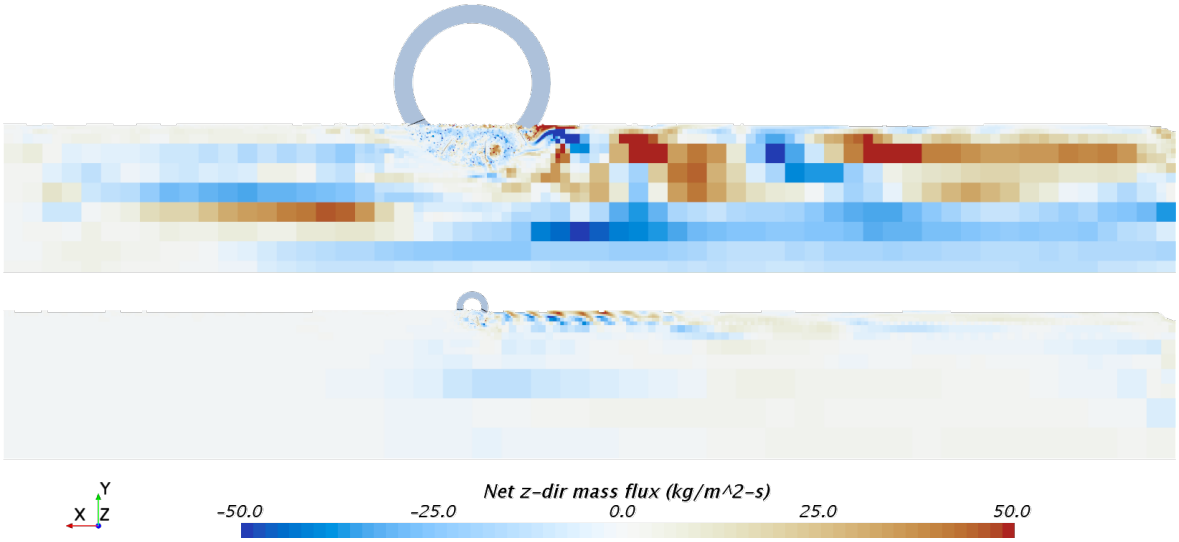

Figure 4.35: For case B (top) and case A (bottom), the mass flux in the direction of the wheel axis is plotted in a plane positioned 10 cm away from the symmetry plane of the wheels. The flow is from left to right. The color scale (saturated at $\pm 50\,\mathrm{kg\,m^{-2}\,s}$) is so that red color (positive values) indicates flow away from the viewer, while blue color (negative values) towards the viewer.

fluxes are observed, not just in regions that bear little influence over the power dynamics (in the far wake of the wheels), but also within moderate distance upstream and below the rotors. This highlights the need for careful investment of further computational resources into finer spatial discretization.

Figure 4.36 provides a final opportunity to visualize the three-dimensional effects at play in free-stream water wheel flows. There, isosurfaces of vorticity are shown, viewed from below and downstream of the rotor. Only vorticity in the x- (streamwise) and y- (vertical) directions is considered. Vorticity in the direction of the wheel axis, which is

associated with the power production, is ignored: it is already very well accounted for by two-dimensional simulations (and z-vorticity was indeed often used to describe flow in these simulations in the last three chapters). The result is that the flow patterns that cannot be captured in the 2D simulations are singled out in this figure.

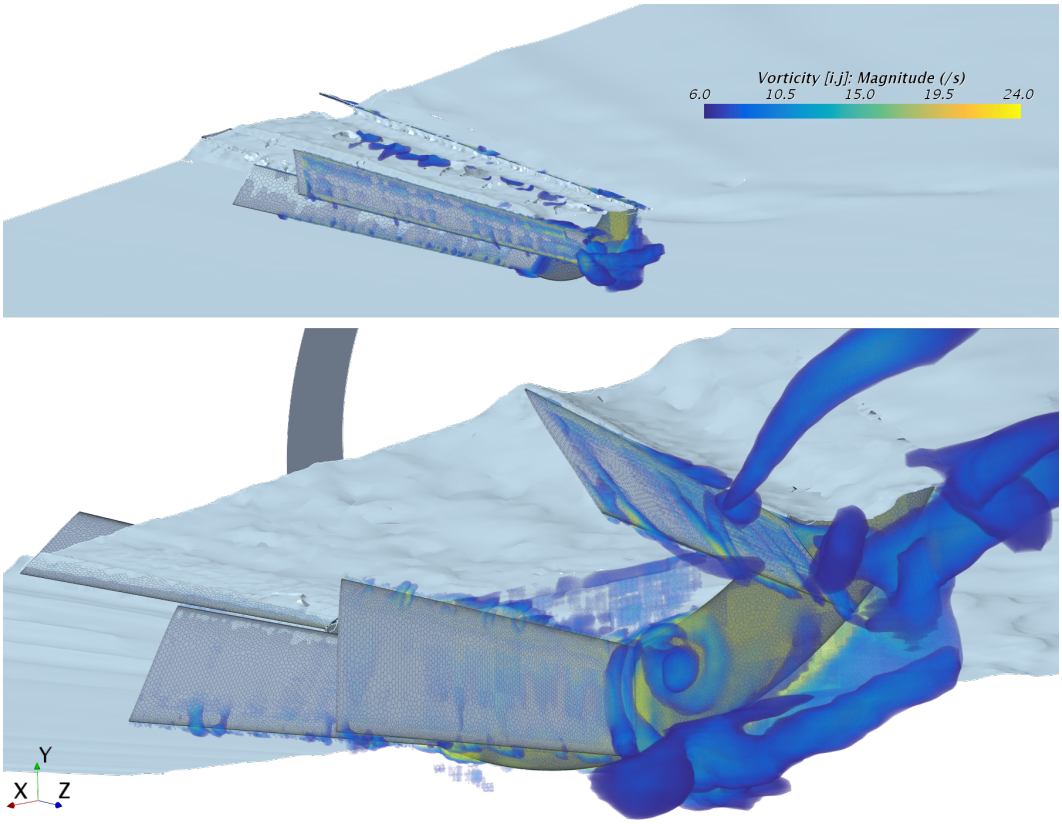

Figure 4.36: Isosurfaces of vorticity in the water immediately below the wheel for case A (top) and case B (bottom), with both images at exactly the same scale. Flow is from left to right. Here, only vorticity in the x and y directions is shown; vorticity in the z-direction (parallel to the axis of the wheel), which is associated with the power production, is omitted. For clarity, only vorticity between 6 and 24 s^{-1} is visualized.

The flow patterns in figure 4.36 indicate complex cross-plane flow, in particular for wheel B. As expected, sheets of vorticity are visible along and in the wake of the flat surface boundary layers. Large vortices, with their axis chiefly in the flow direction, appear near the tip and side edges of the blade at the nadir point. Interaction with the z-direction vortices emanating at the blade root and tip (rendered invisible in the figure) seems to break these up into multiple smaller structures. In videos created from multiple instances of the view during the transient simulations, numerous smaller structures appear and dissipate as the blades travel.

Again, a concern stemming figure 4.36 is that the spatial discretization (presented earlier in figure 4.32) is still deemed insufficient to correctly describe water flow around the blades: several relatively large structures in this figure stretch across areas with large mesh size gradients. Nevertheless, the patterns revealed in this figure are evidence that non-trivial flow occurs in the third, axis-wise dimension, very close the blades.

4.5.4 Open research questions

As evidenced in the section above, there is a pressing need for the development of a three-dimensional CFD model for a free-stream water wheel in which the mesh is everywhere fine enough to capture flow patterns relevant to power production. These are, in particular, flow in the direction parallel to the wheel axis far upstream, below and downstream of the rotor, as well as three-dimensional flow below and immediately behind the blades.

If this model is well parametrized and computational resources are available to run these simulations with acceptable rate of progress, the following open questions could be investigated:

- How do the power curves of the wheels compare to those obtained in 2D simulations? If there are significant differences, do they depend on the wheel geometry?
- Are the hydraulic power predictions which are carried out using porous-body models accurate? If so, can they be calibrated and further developed to run an optimization of floater geometry using comparatively inexpensive 3D simulations? In this way, can the geometry of the floaters be adapted so as to increase power by channeling more flow towards the rotor?
- How does blade geometry in the direction of the wheel axis influence the power output? Can the smoothness of the power delivery be increased by using helically-shaped rotor geometries? Can increases in power be obtained by varying the blade tip angle β or even the depth of the blade root L_{root} along the rotor axis direction?

4.6 Conclusions

This last chapter has tackled the problem of optimizing the design of the free-stream water wheel. For this, based on the work carried out in the former chapters, a first optimization —the first in the literature, to the best knowledge of the author— was carried out. Steered by the genetic algorithm of an optimizer, this optimization was deliberately driven across extremely wide ranges of parameters; for example, the diameter was allowed to grow from 0.8 to 6 meters. After nearly 2000 iterations and three months of computations, a wealth of data had been returned (configurations for many different Pareto-optimal or near-Pareto-optimal wheels) requiring careful analysis. An attempt to abstract away this complexity was made by constructing a family to address the two conflicting objectives of the optimization, only with limited success.

Despite this, the results allows to quantitatively quantify the conundrum associated with the design of the optimum wheel. Operators constrained in installation width or area should adopt high-radius, high-depth wheels; while operators constrained in rotor size or installation depth should deploy low-radius, low-depth wheels. Compared to the former, the latter will concede to a four-fold decrease in power per unit width and a 40 % reduction in wet-area performance in order to gain a 50 % increase in power per unit rotor area. This trade-off is well visualized using blade-level graphical descriptions of performance developed in previous work.

A second optimization was then conducted, based on the very same computing toolchain and infrastructure. In addition to featuring slightly different objectives, it was much purposefully narrower in scope. Predictably, it converged much more easily, delivering a configuration for a single optimal individual: a wheel whose blade geometry maximizes both power output and smoothness of power delivery. This design features fully-immersed blades and results in a 113 % increase in work ratio, while still improving the wet and rotor power coefficients by 8 %, compared to the wheel suggested by the previously-established design guidelines. Its configuration translates into a 71 % reduction in total blade area, corresponding to significant reduction in weight, bulk, and material usage.

Applying the same immersed-blade modification to the complete set of wheel designs obtained in the former optimization reveals that performance is markedly improved in nearly every case, whether measured in terms of wet-area power coefficient, rotor power coefficient, or work ratio. In this manner, the two-dimensional work presented in this chapter, after half of a million CPU-hours of computational time invested, unambiguously indicates that the optimal free-stream water wheel design has fully-immersed blades, which produce power for most of the power stroke in a continuous fashion. This shows that lift, in addition to drag, contributes to energy conversion mechanism for these machines. Future work should make further use of the tools presented, seeking to identify the configuration of blades with thicker geometry that take the best advantage of these mechanics.

Finally, preliminary investigations are carried out with three-dimensional simulations. Clearly, these simulations are still in their infancy: the local coarsening of the mesh required to carry these out given the time and resources available for this thesis prevents the accurate quantification of the phenomena of interest here. Nevertheless, they account well for lateral mass flow deflection, blade edge losses, and floater-induced disturbances. They thus point the way forward for further research, which will need to rise beyond the simplifications inherent to two-dimensional CFD computations.

Conclusion

This thesis has covered four main aspects of the optimization of free-stream water wheels.

In the first chapter, a theoretical analysis of the achievable performance in floating or bypass hydropower installations was carried out. The one-dimensional model describing the fluid flow through hydraulic devices presented there is able to quantify the device operating speed required to attain full load efficiency, and the corresponding maximum hydraulic power. It was shown that it allows both to evaluate any device's real-life performance, benchmarking it against reference values anchored in physical principles, and to provide design guidance. These results are obtained at a computing cost several orders of magnitude smaller than those associated with full description of the flow using CFD methods.

The second chapter has presented numerical models of the fluid flow in free-stream water wheels. A systematic study of the power characteristics of this type of machine was carried out using two-dimensional simulations. Two conflicting performance requirements were identified: generating high power per unit submerged frontal area ($C_{\mathrm{P\ wet}}$), and high power unit frontal rotor area ($C_{\mathrm{P\ rotor}}$). It was shown the decomposition of the net power output in terms of the contribution of individual blades allows for an improved understanding of the dynamics of the machine, highlighting the influence of key design parameters (relative depth, number of blades, blade geometry) on its performance.

The third chapter has illustrated the challenges of producing reliable measurements by which to assess the effectiveness of the models used in CFD simulations of water wheels. One experiment was carried out on a small-scale wheel, necessitating sensitive measurement equipment and careful post-processing. A simulation of the same flow using a three-dimensional model with satisfactory mesh resolution under-estimated the corresponding power output by only approximately 10 %, validating the methods used to describe fluid flow and power output in the numerical simulations developed in this thesis.
A different opportunity for comparison was presented to the author in the form of set of data from measurements carried out on a mid-scale (1.5 m-diameter) wheel by an external actor. The non-dimensionalization of those results for comparison translates into large (±30 %) uncertainty. Additionally, only two-dimensional simulations were carried out for comparison. Consequently, although the two sets of results agree only in broad, general terms, this is not seen as a reason to distrust the numerical tools used in this thesis.

The fourth and final chapter has tackled the problem of optimizing the design of the free-stream water wheel. For this, two optimizations steered by a genetic algorithm

were carried out. The first was deliberately driven across extremely wide ranges of parameters. As a result, the main design conundrum associated with the design of the free-stream wheel was quantified as follows: operators constrained in installation width or area should adopt high-radius, high-depth wheels; while operators constrained in rotor size or installation depth should deploy low-radius, low-depth wheels. A four-fold decrease in power per unit width and a 40 % reduction in wet-area performance must be conceded in order to gain a 50 % increase in power per unit rotor area.
The second optimization was much narrower in scope and focused on improving the quality of power delivery through the shortening of the blades. For the single wheel radius considered, a 113 % increase in work ratio combined with a 71 % reduction in total blade area (corresponding to significant reduction in weight, bulk, and material usage) was obtained.
Overall, after the investigation of 2 400 different wheel configurations, the results unambiguously indicate that the optimal free-stream water wheel design features fully-immersed blades which produce power for most of the power stroke in a continuous fashion. This shows that lift, in addition to drag, contributes to energy conversion mechanism for these machines.

Finally, preliminary investigations were carried out with three-dimensional simulations. While still insufficiently resolved to make accurate predictions, they allow for the visualization of lateral mass flow deflection, blade edge losses, and floater-induced disturbances. They point the way forward for further research, which will need to rise beyond the simplifications inherent to two-dimensional CFD computations.

List of publications

As per University regulations, a list of publications of the author is presented here, as of May 2022:

Textbook

[102] O. Cleynen. *Thermodynamique de l'ingénieur*. French. 3rd ed. Thermodynamique.fr (O. Cleynen), 2021. ISBN: 9781794848207. URL: https://thermodynamique.fr/.

Peer-reviewed articles

In review:

[111] A. Shingala, O. Cleynen, A. Jain, S. Hoerner, and D. Thévenin. "Genetic optimization of a free-stream water wheel using 2D computational fluid dynamics simulations points towards design with fully-immersed blades". In: *Energies* (submitted).

Published:

[63] O. Cleynen, S. Hoerner, and D. Thévenin. "Characterization of hydraulic power in free-stream installations". In: *International Journal of Rotating Machinery* 2017 (2017). DOI: 10.1155/2017/9806278.

[73] O. Cleynen, E. Kerikous, S. Hoerner, and D. Thévenin. "Characterization of the performance of a free-stream water wheel using computational fluid dynamics". In: *Energy* 165 (2018), pp. 1392–1400. DOI: 10.1016/j.energy.2018.10.003.

[78] S. Müller, O. Cleynen, S. Hoerner, N. Lichtenberg, and D. Thévenin. "Numerical analysis of the compromise between power output and fish-friendliness in a vortex power plant". In: *Journal of Ecohydraulics* (2018), pp. 86–98. DOI: 10.1080/24705357.2018.1521709.

[88] S. Hoerner, S. Abbaszadeh, T. Maître, O. Cleynen, and D. Thévenin. "Characteristics of the fluid-structure interaction within Darrieus water turbines with highly flexible blades". In: *Journal of Fluids and Structures* 88 (2019), pp. 13–30. DOI: 10.1016/j.jfluidstructs.2019.04.011.

[97] O. Cleynen, G. Santa-Maria, M. Magdowski, and D. Thévenin. "Peer-graded individualized student homework in a single-instructor undergraduate engineering course". In: *Research in Learning Technology* 28 (2020). DOI: 10.25304/rlt.v28.2339.

[99] S. Hoerner, C. Bonamy, O. Cleynen, T. Maître, and D. Thévenin. "Darrieus vertical-axis water turbines – deformation and force measurements on bioinspired highly-flexible blade profiles". In: *Experiments in Fluids* 61.141 (2020). DOI: 10.1007/s00348-020-02970-2.

[103] O. Cleynen, S. Engel, S. Hoerner, and D. Thévenin. "Optimal design for the free-stream water wheel: a two-dimensional study". In: *Energy* (2021), p. 118880. DOI: 10.1016/j.energy.2020.118880.

[104] S. Hoerner, S. Abbaszadeh, O. Cleynen, C. Bonamy, T. Maître, and D. Thévenin. "Passive flow control mechanisms with bioinspired flexible blades in cross-flow tidal turbines". In: *Experiments in Fluids* 62.5 (2021), pp. 1–14. DOI: 10.1007/s00348-021-03186-8.

[105] S. Hoerner, I. Kösters, L. Vignal, O. Cleynen, S. Abbaszadeh, T. Maître, and D. Thévenin. "Cross-flow tidal turbines with highly flexible blades — experimental flow field investigations at strong fluid–structure interactions". In: *Energies* 14.4 (2021). DOI: 10.3390/en14040797.

[106] D. Powalla, S. Hoerner, O. Cleynen, N. Müller, J. Stamm, and D. Thévenin. "A computational fluid dynamics model for a water vortex power plant as platform for etho- and ecohydraulic research". In: *Energies* 14.3 (2021). DOI: 10.3390/en14030639.

[109] O. Cleynen, D. Powalla, S. Hoerner, and D. Thévenin. "An efficient method for computing the power potential of bypass hydropower installations". In: *Energies* 15.9 (2022). DOI: 10.3390/en15093228.

[110] D. Powalla, S. Hoerner, O. Cleynen, and D. Thévenin. "A numerical approach for active fish behaviour modelling with a view toward hydropower plant assessment". In: *Renewable Energy* (2022). DOI: 10.1016/j.renene.2022.02.064.

Conference talks

In print:

[96] O. Cleynen, S. Hoerner, D. Powalla, and D. Thévenin. "First assessment of a turbine's fish passability with combined probe measurements and numerical simulations". In: *Proceedings of the IAHR 2020 Congress*. Lausanne, Switzerland, 2020.

Published:

[54] O. Cleynen, S. Hoerner, and D. Thévenin. "Performance mapping of ducted free-stream hydropower devices". In: *Proceedings of the 4th IAHR Europe Congress*. Liège, Belgium, 2016, p. 284. ISBN: 9781138029774.

[57] N. Lichtenberg, O. Cleynen, and D. Thévenin. “Numerical investigations of a water vortex hydropower plant implemented as fish ladder – Part I: The water vortex”. In: *Proceedings of the 4th IAHR Europe Congress*. Liège, Belgium, 2016, p. 277. ISBN: 9781138029774.

[64] O. Cleynen, E. Kerikous, S. Hoerner, and D. Thévenin. “Influence of flotation bodies on the power characteristics of a free-stream water wheel”. In: *Proceedings of the 9th International Conference on Computational and Experimental Methods in Multiphase and Complex Flow (Multiphase Flow IX)*. Vol. 60. Tallinn, Estonia, 2017. DOI: 10.2495/MPF170071.

[65] S. Hoerner, C. Bonamy, T. Maître, O. Cleynen, and D. Thévenin. “Strongly-coupled fluid-structure-interaction with large deformations on a flexible hydrofoil under forced oscillation”. In: *Proceedings of the 12th OpenFoam Workshop*. Exeter, UK, 2017. oai: hal-01917888.

[67] S. Müller, O. Cleynen, and D. Thévenin. “Numerical investigation of the influence of a guide wall in a fish-friendly weir”. In: *International Conference on Engineering and Ecohydrology for Fish Passage*. Corvallis, Oregon (USA), 2017. Chap. Session B2: Fishway Design & Efficiency II, p. 15.

Non-profit work 2007-2009

Conference talks given as leader of ’*GNU/Linux Matters*’ non-profit organization:

[15] O. Cleynen. “Overtaking proprietary software without writing code”. In: *Proceedings of the 24th Chaos Communication Congress (24c3)*. Berlin, Germany, Dec. 2007.

[16] O. Cleynen. “Proprietäre Software übernehmen ohne Code zu schreiben”. German. Keynote of Ubucon 2007. Krefeld, Germany, Nov. 2007.

[22] O. Cleynen. “The Blonde and the Scruffy Coder: tackling gender imbalance in the open-source community”. Talk at the 2009 Chemnitzer Linux Tage. Chemnitz, Germany, Mar. 2009.

Nomenclature

Δ	net difference
α	in chapter 1, kinetic energy correction factor [—]
α	in chapters 2-4, angular position of blade along stroke (fig. 2.5) [rad]
α^*	non-dimensional stroke angle (fig. 2.5) [—]
β	blade geometry angle, fig. 2.5 [°]
β_1	blade angle at tip, fig. 4.2 [°]
β_2	blade angle at mid-depth, fig. 4.2 [°]
ϵ	turbulent dissipation rate [$\mathrm{J\,kg^{-1}\,s^{-1}}$]
η	efficiency, defs. 1.4-1.6 & 3.2 [—]
λ	tip speed ratio, def. 2.15 [—]
μ	viscosity [$\mathrm{Pa\,s}$]
μ_T	turbulent viscosity, see §2.2.2 [$\mathrm{Pa\,s}$]
ω	in §2.2.2 only: specific turbulent dissipation rate [$\mathrm{s^{-1}}$]
ω	rotor rotational speed [$\mathrm{rad\,s^{-1}}$]
ϕ	uncertainty, expressed as standard deviation (as per the GUM, see ref. [13])
ρ	density [$\mathrm{kg\,m^{-3}}$]
σ	standard deviation
θ	stroke angle, def. 2.17, fig. 2.5 [rad]
A_A	actuator frontal area [$\mathrm{m^2}$]
A_f	device frontal area [$\mathrm{m^2}$]
A_ref	Reference area for power coefficient [$\mathrm{m^2}$]
B	chain translation ratio [—]
b	width of rectangular channel [m]

C_{P} power coefficient (def. eq. 1.8) [—]

$C_{\mathrm{P\ dry}}$ Power coefficient based on the rotor area [—]

C_{Pb} single-blade wet power coefficient [—]

$C_{\mathrm{P\ wet}}$ Power coefficient based on the immersed area [—]

$\tilde{C}_{\mathrm{Pb}}$ single-blade wet power coefficient averaged over several blades [—]

e specific mechanical energy [$\mathrm{J\,kg^{-1}}$]

e_k specific kinetic energy [$\mathrm{J\,kg^{-1}}$]

[Fr] Froude number [—]

f_{wet} wet radius fraction, def. 2.16 [—]

g gravitational acceleration [$\mathrm{m\,s^{-2}}$]

h height from bed to water surface, positive upwards [m]

$H_{\mathrm{eff.}}$ effective head (def. in section 1.3) [m]

$I_{\mathrm{generator}}$ measured electric current [A]

k turbulent specific energy [$\mathrm{J\,kg^{-1}}$]

K_{D} drop coefficient (def. 1.16) [—]

$K_{\mathrm{generator}}$ generator constant [$\mathrm{N\,m\,A^{-1}}$]

K_{D0} static drop coefficient (def. 1.21) [—]

K_{D2} loss coefficient, def. 1.20 [—]

L_{root} depth of root of blade, positive downwards (figure 4.16) [m]

L_{wet} immersion depth of rotor (figure 2.5) [m]

L_{width} width of rotor [m]

$\dot{m}$ mass flow [$\mathrm{kg\,s^{-1}}$]

n_{b} number of blades on rotor [—]

n_{e} equivalent number of blades on rotor, def. 2.19 [—]

O_{water} volume fraction of water (eq. 2.6) [—]

p pressure [Pa]

Q Lanchester correction factor (cf. footnote p. 56 & [50]) [—]

q volume flow per unit width [$\mathrm{m^2\,s^{-1}}$]

[Re] Reynolds number [—]

R	in chapter 1, size ratio (def. 1.23) [—]
R	in chapters 2-4, wheel radius (figure 2.5) [m]
R_1	radial position of pivot point for blade tip in fig. 2.5 [m]
r_{ntg}	work ratio ("net to gross")), def. 4.9 [—]
S	Reference area for power coefficient [m^2]
T	generic parameter used for clarity
u	local fluid velocity [$\text{m}\,\text{s}^{-1}$]
U_∞	free-stream velocity [$\text{m}\,\text{s}^{-1}$]
$\dot{\mathcal{V}}$	volume flow rate [$\text{m}^3\,\text{s}^{-1}$]
$\vec{V}$	fluid velocity vector field [$\text{m}\,\text{s}^{-1}$]
$\dot{W}$	mechanical or electrical power [W]
x_i	generic measurand
Z_{cut}	cut radius fraction, def 4.10 [—]
y^+	non-dimensional distance away from wall [—]
z	altitude of bed, positive upwards [m]

Subscripts

A	actuator
alt.	due to altitude
av.	averaged in space
hydraulic	refers to mechanical energy lost by water
hyd.	abbreviation for hydraulic
max.	maximum
opt.	optimum
loss	integral effect of pressure losses
rotor	reference area is frontal area of rotor
shaft	refers to mechanical energy transferred in the rotor shaft
wet	reference area is frontal area exposed to water
+	immediately upstream of actuator surface
-	immediately downstream of actuator surface
∞	far-field incoming conditions

Superscripts

bar	average in time
arrow	vector

Sign conventions

Lengths are measured positive upwards and downstream.

Numbers

The decimal separator of numbers is a dot; the thousand separator is a thin space; exponents are separated with a median dot. For example, $1.23456 \cdot 10^5 = 12\,345.6$

Bibliography

[1] A. Parent. “Sur la plus grande perfection possible des machines dont un fluide est la force mouvante”. French. In: *Histoire de l’Académie Royale des Sciences, année 1704* (1704), pp. 116, 323.

[2] F. Redtenbacher. *Theorie und Bau der Wasserräder*. In German. Verlag von Friedrich Bassermann, 1846.

[3] F. W. Lanchester. “A contribution to the theory of propulsion and the screw propeller”. In: *Naval Engineers Journal* 27.2 (1915), pp. 509–510.

[4] W. Müller. *Die Wasserräder*. In German. 2nd ed. Verlag Moritz Schäfer, 1939.

[5] S. Yokosi. “The structure of river turbulence”. In: *Bulletin of the Disaster Prevention Research Institute* 17.121 (2 1967), pp. 1–29. URL: https://hdl.handle.net/2433/124737.

[6] W. Jones and B. Launder. “The calculation of low-Reynolds-number phenomena with a two-equation model of turbulence”. In: *International Journal of Heat and Mass Transfer* 16.6 (1973), pp. 1119–1130. DOI: 10.1016/0017-9310(73)90125-7.

[7] W. F. Noh and P. Woodward. “SLIC (simple line interface calculation)”. In: *Proceedings of the fifth international conference on numerical methods in fluid dynamics*. Enschede, Netherlands, 1976, pp. 330–340. DOI: 10.1007/3-540-08004-X_336.

[8] K. H. Bergey. “The Lanchester-Betz limit (energy conversion efficiency factor for windmills)”. In: *Journal of Energy* 3.6 (1979), pp. 382–384. DOI: 10.2514/3.48013.

[9] C. W. Hirt and B. D. Nichols. “Volume of fluid (VOF) method for the dynamics of free boundaries”. In: *Journal of Computational Physics* 39.1 (1981), pp. 201–225. DOI: 10.1016/0021-9991(81)90145-5.

[10] D. C. Wilcox. “Reassessment of the scale-determining equation for advanced turbulence models”. In: *AIAA Journal* 26.11 (1988), pp. 1299–1310. DOI: 10.2514/3.10041.

[11] F. R. Menter. “Two-equation eddy-viscosity turbulence models for engineering applications”. In: *AIAA Journal* 32.8 (1994), pp. 1598–1605. DOI: 10.2514/3.12149.

[12] P. J. Roache. “Perspective: a method for uniform reporting of grid refinement studies”. In: *Journal of Fluids Engineering* 116.3 (1994), pp. 405–413. DOI: 10.1115/1.2910291.

[13] BIPM, IEC, IFFC, ISO, IUPAC, IUPAP, OIML. *Guide to the expression of uncertainty in measurement*. 1st ed. International Organization for Standardization (ISO), 1995. ISBN: 9267101889.

[14] M. Denny. "The efficiency of overshot and undershot waterwheels". In: *European Journal of Physics* 25.2 (2004), p. 193. DOI: 10.1088/0143-0807/25/2/006.

[15] O. Cleynen. "Overtaking proprietary software without writing code". In: *Proceedings of the 24th Chaos Communication Congress (24c3)*. Berlin, Germany, Dec. 2007.

[16] O. Cleynen. "Proprietäre Software übernehmen ohne Code zu schreiben". German. Keynote of Ubucon 2007. Krefeld, Germany, Nov. 2007.

[17] G. A. M. van Kuik. "The Lanchester–Betz–Joukowsky limit". In: *Wind Energy* 10.3 (2007), pp. 289–291. DOI: 10.1002/we.218.

[18] G. Müller, S. Denchfield, R. Marth, and B. Shelmerdine. "Stream wheels for applications in shallow and deep water". In: *Proceedings of the 32nd IAHR World Congress*. Vol. 32. 2. Venice, Italy, 2007, p. 707.

[19] S. R. Turnock, G. U. Müller, R. . Nicholls-Lee, S. Denchfield, S. Hindley, R. Shelmerdine, and S. Stevens. "Development of a floating tidal energy system suitable for use in shallow water". In: *Proceedings of the 7th European Wave and Tidal Energy Conference*. Porto, Portugal, 2007.

[20] G. T. Houlsby, S. Draper, and M. L. G. Oldfield. *Application of linear momentum actuator disc theory to open channel flow*. OUEL report 2296/08. University of Oxford, Department of Engineering Science, 2008.

[21] Joint Committee for Guides in Metrology (BIPM, IEC, IFFC, ISO, IUPAC, IUPAP, OIML). *Evaluation of measurement data – Guide to the expression of uncertainty in measurement. JCGM 100:2008 – GUM 1995 with minor corrections*. 1st ed. 2008. URL: https://www.bipm.org/documents/20126/2071204/JCGM_100_2008_E.pdf.

[22] O. Cleynen. "The Blonde and the Scruffy Coder: tackling gender imbalance in the open-source community". Talk at the 2009 Chemnitzer Linux Tage. Chemnitz, Germany, Mar. 2009.

[23] M. Khan, G. Bhuyan, M. Iqbal, and J. Quaicoe. "Hydrokinetic energy conversion systems and assessment of horizontal and vertical axis turbines for river and tidal applications: a technology status review". In: *Applied Energy* 86.10 (2009), pp. 1823–1835. DOI: 10.1016/j.apenergy.2009.02.017.

[24] A. Al Sam. "Water wheel CFD simulations". Master's thesis. Lund University, Sweden, Department of energy sciences, 2010.

[25] M. H. Mohamed, G. Janiga, E. Pap, and D. Thévenin. "Optimization of Savonius turbines using an obstacle shielding the returning blade". In: *Renewable Energy* 35.11 (2010), pp. 2618–2626. DOI: 10.1016/j.renene.2010.04.007.

[26] M. Shives and C. Crawford. "Overall efficiency of ducted tidal current turbines". In: *Proceedings of OCEANS 2010 MTS/IEEE*. Seattle, USA, 2010, pp. 1–6. DOI: 10.1109/OCEANS.2010.5664426.

[27] W. M. J. Batten and G. U. Müller. "Potential for using the floating body structure to increase the efficiency of a free stream energy converter". In: *Proceedings of the 34th IAHR World Congress*. Brisbane, Australia, 2011, pp. 2364–2371. ISBN: 9780858258686.

[28] W. M. Batten, F. Weichbrodt, G. U. Müller, J. Hadler, C. Semlow, M. Hochbaum, S. Dimke, and P. Frohle. "Design and stability of a floating free stream energy converter". In: *Proceedings of the 34th IAHR World Congress*. Brisbane, Australia, 2011, pp. 2372–2379. ISBN: 9780858258686.

[29] T. Burton, N. Jenkins, D. Sharpe, and E. Bossanyi. *Wind Energy Handbook*. John Wiley and Sons, 2011. ISBN: 9780470699751.

[30] J. Hadler and K. Broekel. "Low head hydropower — its design and economic potential". In: *Proceedings of the World Renewable Energy Congress*. Linköping, Sweden, 2011, pp. 1464–1471. DOI: 10.3384/ecp110571464.

[31] M. H. Mohamed, G. Janiga, E. Pap, and D. Thévenin. "Optimal blade shape of a modified Savonius turbine using an obstacle shielding the returning blade". In: *Energy Conversion and Management* 52.1 (2011), pp. 236–242. DOI: 10.1016/j.enconman.2010.06.070.

[32] M. H. Mohamed, G. Janiga, E. Pap, and D. Thévenin. "Multi-objective optimization of the airfoil shape of Wells turbine used for wave energy conversion". In: *Energy* 36.1 (2011), pp. 438–446. DOI: 10.1016/j.energy.2010.10.021.

[33] P. F. Pelz. "Upper limit for hydropower in an open-channel flow". In: *Journal of Hydraulic Engineering* 137.11 (2011), pp. 1536–1542. DOI: 10.1061/(ASCE)HY.1943-7900.0000393.

[34] W. M. J. Batten and G. U. Müller. *HYLOW end of project publishable summary*. Project report. HYLOW, 2012.

[35] Y. Liu and Y. Peymani. "Evaluation of paddle wheels in generating hydroelectric power". In: *Proceedings of the ASME 2012 International Mechanical Engineering Congress and Exposition*. Houston, USA, 2012, pp. 675–684. DOI: 10.1115/IMECE2012-85121.

[36] F. Weichbrodt, S. Dimke, J. Hadler, and P. Fröhle. "Großmaßstäbliche Modellversuche mit einem schwimmenden Energiewandler". German. In: *Dresdner Wasserbauliche Mitteilungen – 34. Dresdner Wasserbaukolloquium*. Dresden, Germany, 2012, pp. 291–299.

[37] P. F. Pelz and M. Metzler. "An analytic approach to optimize tidal turbine fields". In: *IOP Conference Series: Materials Science and Engineering*. Vol. 52. 5. 2013, p. 052019. DOI: 10.1088/1757-899X/52/5/052019.

[38] H. Toya, T. Yuji, and T. Kusakabe. "Experimental study on a hydraulic power generator with floating turbine". In: *Proceedings of the 2013 International Conference on Electrical Machines and Systems (ICEMS)*. Busan, Korea, 2013, pp. 242–245. DOI: 10.1109/ICEMS.2013.6754418.

[39] L. Chen and W.-H. Lam. "Slipstream between marine current turbine and seabed". In: *Energy* 68 (2014), pp. 801–810. DOI: 10.1016/j.energy.2014.02.083.

[40] T. P. Kumara. "Analysis of floating type water wheel for pico hydro systems in Sri Lanka". Master's Thesis. KTH Royal Institute of Technology, Sweden, Department of Building, Energy and Environmental Engineering, 2014.

[41] Y. Li. "On the definition of the power coefficient of tidal current turbines and efficiency of tidal current turbine farms". In: *Renewable Energy* 68 (2014), pp. 868–875. DOI: 10.1016/j.renene.2013.09.020.

[42] Y. Nishi, T. Inagaki, Y. Li, R. Omiya, and K. Hatano. "Research on the flow field of undershot cross-flow water turbines using experiments and numerical analysis". In: *Proceedings of the 27th IAHR World Congress*. Vol. 22. 6. Montreal, Canada, 2014. DOI: 10.1088/1755-1315/22/6/062006.

[43] M. Sánchez, R. Carballo, V. Ramos, and G. Iglesias. "Energy production from tidal currents in an estuary: A comparative study of floating and bottom-fixed turbines". In: *Energy* 77 (2014), pp. 802–811. DOI: 10.1016/j.energy.2014.09.053.

[44] O. S. Akinyemi, T. L. Chambers, and Y. Liu. "Evaluation of the power generation capacity of hydrokinetic generator device using computational analysis and hydrodynamic similitude". In: *Journal of Power and Energy Engineering* 3.08 (2015), pp. 71–82. DOI: 10.4236/jpee.2015.38007.

[45] O. S. Akinyemi and Y. Liu. "CFD modeling and simulation of a hydropower system in generating clean electricity from water flow". In: *International Journal of Energy and Environmental Engineering* 6.4 (2015), pp. 357–366. DOI: 10.1007/s40095-015-0180-2.

[46] S. Baker, A. Cornett, and M. Kluijver. "3D modelling and optimization of a hydrokinetic power generation barge". In: *Proceedings of the 11th European Wave and Tidal Energy Conference, EWTEC*. Nantes, France, 2015.

[47] J. J. Cartelle Barros, M. Lara Coira, M. P. de la Cruz López, and A. del Caño Gochi. "Assessing the global sustainability of different electricity generation systems". In: *Energy* 89 (2015), pp. 473–489. DOI: 10.1016/j.energy.2015.05.110.

[48] L. Daróczy, G. Janiga, K. Petrasch, M. Webner, and D. Thévenin. "Comparative analysis of turbulence models for the aerodynamic simulation of H-Darrieus rotors". In: *Energy* 90 (2015), pp. 680–690. DOI: 10.1016/j.energy.2015.07.102.

[49] N. Kolekar and A. Banerjee. "Performance characterization and placement of a marine hydrokinetic turbine in a tidal channel under boundary proximity and blockage effects". In: *Applied Energy* 148 (2015), pp. 121–133. DOI: 10.1016/j.apenergy.2015.03.052.

[50] G. A. M. van Kuik, J. N. Sørensen, and V. L. Okulov. "Rotor theories by professor Joukowsky: momentum theories". In: *Progress in Aerospace Sciences* 73 (2015), pp. 1–18. DOI: 10.1016/j.paerosci.2014.10.001.

[51] W.-H. Lam, L. Chen, and R. Hashim. "Analytical wake model of tidal current turbine". In: *Energy* 79 (2015), pp. 512–521. DOI: 10.1016/j.energy.2014.11.047.

[52] Y. Nishi, T. Inagaki, Y. Li, and K. Hatano. "Study on an undershot cross-flow water turbine with straight blades". In: *International Journal of Rotating Machinery* 2015 (2015). DOI: 10.1155/2015/817926.

[53] E. Quaranta and R. Revelli. "Performance characteristics, power losses and mechanical power estimation for a breastshot water wheel". In: *Energy* 87 (2015), pp. 315–325. DOI: 10.1016/j.energy.2015.04.079.

[54] O. Cleynen, S. Hoerner, and D. Thévenin. "Performance mapping of ducted free-stream hydropower devices". In: *Proceedings of the 4th IAHR Europe Congress*. Liège, Belgium, 2016, p. 284. ISBN: 9781138029774.

[55] J. R. Gandhi, H. Jha, S. N. Jha, and D. S. Patel. "Renewable energy based floating power generator (rivers and canals)". In: *International Journal of Engineering Research and Applications* 6 (2016), pp. 49–52.

[56] M. Leschziner. *Statistical turbulence modelling for fluid dynamics – demystified. An introductory text for graduate engineering students*. Imperial College Press, 2016. ISBN: 9781783266616.

[57] N. Lichtenberg, O. Cleynen, and D. Thévenin. "Numerical investigations of a water vortex hydropower plant implemented as fish ladder – Part I: The water vortex". In: *Proceedings of the 4th IAHR Europe Congress*. Liège, Belgium, 2016, p. 277. ISBN: 9781138029774.

[58] I.-H. Liu, J. Riglin, W. C. Schleicher, and A. Oztekin. "Flow past a plate in the vicinity of a free surface". In: *Ocean Engineering* 111 (2016), pp. 323–334. DOI: 10.1016/j.oceaneng.2015.11.009.

[59] S. Paudel. "Experimental and numerical study of Dethridge wheel for pico-scale hydropower generation". PhD thesis. Technische Universität Darmstadt, Germany, Department of Civil and Environmental Engineering, 2016.

[60] S. Paudel and N. Saenger. "Dethridge wheel for pico-scale hydropower generation: an experimental and numerical study". In: *Proceedings of the 28th IAHR Symposium on Hydraulic Machinery (IOP Conference Series: Earth and Environmental Science)*. Vol. 49. 10. Grenoble, France, 2016, p. 102007.

[61] W. Tian, J. H. VanZwieten, P. Pyakurel, and Y. Li. "Influences of yaw angle and turbulence intensity on the performance of a 20 kW in-stream hydrokinetic turbine". In: *Energy* 111 (2016), pp. 104–116. DOI: 10.1016/j.energy.2016.05.012.

[62] N. F. Yah, M. S. Idris, and A. N. Oumer. "Numerical investigation on effect of immersed blade depth on the performance of undershot water turbines". In: *Proceedings of the 3rd International Conference on Mechanical Engineering Research (ICMER 2015)*. Vol. 74. Kuantan, Malaysia, 2016. DOI: 10.1051/matecconf/20167400035.

[63] O. Cleynen, S. Hoerner, and D. Thévenin. "Characterization of hydraulic power in free-stream installations". In: *International Journal of Rotating Machinery* 2017 (2017). DOI: 10.1155/2017/9806278.

[64] O. Cleynen, E. Kerikous, S. Hoerner, and D. Thévenin. "Influence of flotation bodies on the power characteristics of a free-stream water wheel". In: *Proceedings of the 9th International Conference on Computational and Experimental Methods in Multiphase and Complex Flow (Multiphase Flow IX)*. Vol. 60. Tallinn, Estonia, 2017. DOI: 10.2495/MPF170071.

[65] S. Hoerner, C. Bonamy, T. Maître, O. Cleynen, and D. Thévenin. "Strongly-coupled fluid-structure-interaction with large deformations on a flexible hydrofoil under forced oscillation". In: *Proceedings of the 12th OpenFoam Workshop*. Exeter, UK, 2017. oai: hal-01917888.

[66] S. Müller. "Numerical investigation of the flow in a vortex power plant in consideration of the river continuity". Master's thesis. University Otto von Guericke of Magdeburg, Germany, Laboratory of fluid dynamics, 2017.

[67] S. Müller, O. Cleynen, and D. Thévenin. "Numerical investigation of the influence of a guide wall in a fish-friendly weir". In: *International Conference on Engineering and Ecohydrology for Fish Passage*. Corvallis, Oregon (USA), 2017. Chap. Session B2: Fishway Design & Efficiency II, p. 15.

[68] Y. Nishi, K. Hatano, and T. Inagaki. "Study on performance and flow field of an undershot cross-flow water turbine comprising different number of blades". In: *Journal of Thermal Science* 26.5 (2017), pp. 413–420. DOI: 10.1007/s11630-017-0956-1.

[69] E. Quaranta. "Investigation and optimization of the performance of gravity water wheels". PhD thesis. Politecnico di Torino, Italy, 2017. DOI: 10.6092/polito/porto/2674225.

[70] E. Quaranta and R. Revelli. "CFD simulations to optimize the blade design of water wheels". In: *Drinking Water Engineering and Science* 10.1 (2017), p. 27. DOI: 10.5194/dwes-10-27-2017.

[71] A. Skrypnik. "Numerical simulation of energy transfers in a helically-corrugated pipe heat exchanger". Master's thesis. University Otto von Guericke of Magdeburg, Germany, Laboratory of fluid dynamics, 2017.

[72] A. Bohne. "Analytische und numerische Untersuchung eines Oberflächenwirbels". German. Bachelor's Thesis. University Otto von Guericke of Magdeburg, Germany, Laboratory of fluid dynamics, 2018.

[73] O. Cleynen, E. Kerikous, S. Hoerner, and D. Thévenin. "Characterization of the performance of a free-stream water wheel using computational fluid dynamics". In: *Energy* 165 (2018), pp. 1392–1400. DOI: 10.1016/j.energy.2018.10.003.

[74] L. Daróczy, G. Janiga, and D. Thévenin. "Computational fluid dynamics based shape optimization of airfoil geometry for an H-rotor using a genetic algorithm". In: *Engineering Optimization* 50.9 (2018), pp. 1483–1499. DOI: 10.1080/0305215X.2017.1409350.

[75] F. Hussain. "Numerical investigation of the ducting of free-surface hydraulic devices". Master's thesis. University Otto von Guericke of Magdeburg, Germany, Laboratory of fluid dynamics, 2018.

[76] N. Müller and J. Stamm. "Errichtung eines 1:1 Labormodells für ethohydraulische Untersuchungen an einem Wasserwirbelkraftwerk". German. In: *Dresdner Wasserbauliche Mitteilungen (Heft 60)*. Germany, Dresden: Technische Universität Dresden, Institut für Wasserbau und technische Hydromechanik, 2018, pp. 123–132.

[77] N. Müller, J. Stamm, and F. Wagner. "A water vortex power plant as ethohydraulic test site". In: *Proceedings of the 5th IAHR Europe Congress*. Trento, Italy, 2018. DOI: 10.3850/978-981-11-2731-1_282-cd.

[78] S. Müller, O. Cleynen, S. Hoerner, N. Lichtenberg, and D. Thévenin. "Numerical analysis of the compromise between power output and fish-friendliness in a vortex power plant". In: *Journal of Ecohydraulics* (2018), pp. 86–98. DOI: 10.1080/24705357.2018.1521709.

[79] M. H. Nguyen, H. Jeong, and C. Yang. "A study on flow fields and performance of water wheel turbine using experimental and numerical analyses". In: *Science China Technological Sciences* 61.3 (2018), pp. 464–474. DOI: 10.1007/s11431-017-9146-9.

[80] L. Orunova. "Experimental investigation of the fluid dynamics of a Rubens tube". Master's thesis. University Otto von Guericke of Magdeburg, Germany, Laboratory of fluid dynamics, 2018.

[81] E. Quaranta. "Stream water wheels as renewable energy supply in flowing water: theoretical considerations, performance assessment and design recommendations". In: *Energy for Sustainable Development* 45 (2018), pp. 96–109. DOI: 10.1016/j.esd.2018.05.002.

[82] J. Wahrlich. "Entwicklung eines Optimierungskonzeptes für schwimmende Wasserräder als Leistungseinheit eines Fluss-Strom-Flottillenkraftwerkes". German. Master's thesis. University Otto von Guericke of Magdeburg, Germany, Laboratory of fluid dynamics, 2018.

[83] W. Warjito, D. Adanta, S. A. Arifianto, S. B. Nasution, and B. Budiarso. "Effect of blades number on undershot waterwheel performance with variable inlet velocity". In: *Proceedings of the 4th International Conference on Science and Technology (ICST)*. Yogyakarta, Indonesia, 2018, pp. 1–6. DOI: 10.1109/ICSTC.2018.8528714.

[84] S. Abbaszadeh, S. Hoerner, T. Maître, and R. Leidhold. "Experimental investigation of an optimised pitch control for a vertical-axis turbine". In: *IET Renewable Power Generation* 13.16 (2019), pp. 3106–3112. DOI: 10.1049/iet-rpg.2019.0309.

[85] B. M. Adams, L. Bauman, W. Bohnhoff, K. Dalbey, M. Ebeida, J. Eddy, M. Eldred, P. Hough, K. Hu, J. Jakeman, J. Stephens, L. Swiler, D. Vigil, and T. Wildey. *Dakota, a multilevel parallel object-oriented framework for design optimization, parameter estimation, uncertainty quantification, and sensitivity analysis: version 6.10 user's manual (Sandia Technical Report SAND2014-4633)*. 2019. URL: https://dakota.sandia.gov//sites/default/files/docs/6.10/Users-6.10.0.pdf.

[86] O. Cleynen. *File:Dakota genetic optimization.svg*. Dec. 2019. URL: https://commons.wikimedia.org/wiki/File:Dakota_genetic_optimization.svg.

[87] O. Cleynen. *Genetic optimization with Dakota 1/3: The optimization loop*. Dec. 2019. URL: https://ariadacapo.net/blog/2019-12-18-genetic-optimization-with-dakota-1-3-the-optimization-loop/.

[88] S. Hoerner, S. Abbaszadeh, T. Maître, O. Cleynen, and D. Thévenin. "Characteristics of the fluid-structure interaction within Darrieus water turbines with highly flexible blades". In: *Journal of Fluids and Structures* 88 (2019), pp. 13–30. DOI: 10.1016/j.jfluidstructs.2019.04.011.

[89] E. Kerikous and D. Thévenin. "Optimal shape and position of a thick deflector plate in front of a hydraulic Savonius turbine". In: *Energy* 189 (2019), p. 116157. DOI: 10.1016/j.energy.2019.116157.

[90] E. Kerikous and D. Thévenin. "Optimal shape of thick blades for a hydraulic Savonius turbine". In: *Renewable Energy* 134 (2019), pp. 629–638. DOI: 10.1016/j.renene.2018.11.037.

[91] N. Müller, C. Jähnel, J. Stamm, and F. Wagner. "Analyse der Strömung in einem Wasserwirbelkraftwerk hinsichtlich des Fischabstiegs". German. In: *Wasserwirtschaft* 9/2019 (2019), pp. 60–63. DOI: 10.1007/s35147-019-0227-z.

[92] D. Powalla. "Numerical investigation of the hydraulic and ecological characteristics of a power-producing fish gateway". Master's thesis. University Otto von Guericke of Magdeburg, Germany, Laboratory of fluid dynamics, 2019.

[93] E. Y. Setyawan, S. Djiwo, D. H. Praswanto, P. Suwandono, and P. Siagian. "Design of low flow undershot type water turbine". In: *Journal of Science and Applied Engineering* 2.2 (2019), pp. 50–55. DOI: 10.31328/jsae.v2i2.1184.

[94] A. Tomporowski, A. Al-Zubiedy, J. Flizikowski, W. Kruszelnicka, P. Bałdowska-Witos, and J. Rudnicki. "Analysis of the project of innovative floating turbine". In: *Polish Maritime Research* 26.4 (2019), pp. 124–133. DOI: 10.2478/pomr-2019-0074.

[95] F. Wagner, P. Warth, M. Royan, A. Lindig, N. Müller, and J. Stamm. "Laboruntersuchungen zum Fischabstieg über ein Wasserwirbelkraftwerk". German. In: *Wasserwirtschaft* 9/2019 (2019), pp. 64–67. DOI: 10.1007/s35147-019-0228-y.

[96] O. Cleynen, S. Hoerner, D. Powalla, and D. Thévenin. "First assessment of a turbine's fish passability with combined probe measurements and numerical simulations". In: *Proceedings of the IAHR 2020 Congress*. Lausanne, Switzerland, 2020.

[97] O. Cleynen, G. Santa-Maria, M. Magdowski, and D. Thévenin. "Peer-graded individualized student homework in a single-instructor undergraduate engineering course". In: *Research in Learning Technology* 28 (2020). DOI: 10.25304/rlt.v28.2339.

[98] D. Dewatama, M. Fauziah, H. Safitri, and S. Adhisuwignjo. "Design and implementation: portable floating pico-hydro". In: *Proceedings of the 1st Annual Technology, Applied Science, and Engineering Conference (IOP Conference Series: Materials Science and Engineering)*. Vol. 732. 1. Batu, Indonesia, 2020. DOI: 10.1088/1757-899X/732/1/012049.

[99] S. Hoerner, C. Bonamy, O. Cleynen, T. Maître, and D. Thévenin. "Darrieus vertical-axis water turbines – deformation and force measurements on bioinspired highly-flexible blade profiles". In: *Experiments in Fluids* 61.141 (2020). DOI: 10.1007/s00348-020-02970-2.

[100] Y. Nishi, K. Hatano, T. Okazaki, Y. Yahagi, and T. Inagaki. "Improvement of performance of undershot cross-flow water turbines based on shock loss reduction". In: *International Journal of Fluid Machinery and Systems* 13.1 (2020), pp. 30–41. DOI: 10.5293/IJFMS.2019.13.1.030.

[101] Y. Nishi, Y. Yahagi, T. Okazaki, and T. Inagaki. "Effect of flow rate on performance and flow field of an undershot cross-flow water turbine". In: *Renewable Energy* 149 (2020), pp. 409–423. DOI: 10.1016/j.renene.2019.12.023.

[102] O. Cleynen. *Thermodynamique de l'ingénieur*. French. 3rd ed. Thermodynamique.fr (O. Cleynen), 2021. ISBN: 9781794848207. URL: https://thermodynamique.fr/.

[103] O. Cleynen, S. Engel, S. Hoerner, and D. Thévenin. "Optimal design for the free-stream water wheel: a two-dimensional study". In: *Energy* (2021), p. 118880. DOI: 10.1016/j.energy.2020.118880.

[104] S. Hoerner, S. Abbaszadeh, O. Cleynen, C. Bonamy, T. Maître, and D. Thévenin. "Passive flow control mechanisms with bioinspired flexible blades in cross-flow tidal turbines". In: *Experiments in Fluids* 62.5 (2021), pp. 1–14. DOI: 10.1007/s00348-021-03186-8.

[105] S. Hoerner, I. Kösters, L. Vignal, O. Cleynen, S. Abbaszadeh, T. Maître, and D. Thévenin. "Cross-flow tidal turbines with highly flexible blades — experimental flow field investigations at strong fluid–structure interactions". In: *Energies* 14.4 (2021). DOI: 10.3390/en14040797.

[106] D. Powalla, S. Hoerner, O. Cleynen, N. Müller, J. Stamm, and D. Thévenin. "A computational fluid dynamics model for a water vortex power plant as platform for etho- and ecohydraulic research". In: *Energies* 14.3 (2021). DOI: 10.3390/en14030639.

[107] A. Shingala. "Optimization study on the blades of a free-stream water wheel using computational fluid dynamics and a genetic algorithm". Master's thesis. University Otto von Guericke of Magdeburg, Germany, Laboratory of fluid dynamics, 2021.

[108] S. Sukhorukov. "Parameter study of the performance of a vortex power plant". Master's thesis. University Otto von Guericke of Magdeburg, Germany, Laboratory of fluid dynamics, 2021.

[109] O. Cleynen, D. Powalla, S. Hoerner, and D. Thévenin. "An efficient method for computing the power potential of bypass hydropower installations". In: *Energies* 15.9 (2022). DOI: 10.3390/en15093228.

[110] D. Powalla, S. Hoerner, O. Cleynen, and D. Thévenin. "A numerical approach for active fish behaviour modelling with a view toward hydropower plant assessment". In: *Renewable Energy* (2022). DOI: 10.1016/j.renene.2022.02.064.

[111] A. Shingala, O. Cleynen, A. Jain, S. Hoerner, and D. Thévenin. “Genetic optimization of a free-stream water wheel using 2D computational fluid dynamics simulations points towards design with fully-immersed blades”. In: *Energies* (submitted).